Numerical and Experimental Investigations on the Performance Improvements of Parabolic Trough Solar Thermal Collector for Medium Temperature Applications

DOCTOR OF PHILOSOPHY

SHAJAN S.

Register No. D-TKM18JAN005

Department of Mechanical Engineering

TKM College of Engineering, Kollam

APJ ABDUL KALAM TECHNOLOGICAL UNIVERSITY

Thiruvananthapuram

2023

Numerical and Experimental Investigations on the Performance Improvements of Parabolic Trough Solar Thermal Collector for Medium Temperature Applications

Submitted in partial fulfillment of the
requirements of the degree of

DOCTOR OF PHILOSOPHY

SHAJAN S.

Register No. D-TKM18JAN005

Supervisor:

Dr. BAIJU V.

Department of Mechanical Engineering

TKM College Of Engineering, Kollam

APJ ABDUL KALAM TECHNOLOGICAL UNIVERSITY

Thiruvananthapuram

2023

DECLARATION

I declare that this written submission represents my ideas in my own words and where others' ideas or words have been included, I have adequately cited and referenced the original sources. I also declare that I have adhered to all principles of academic honesty and integrity and have not misrepresented or fabricated or falsified any idea/data/fact/source in my submission. I understand that any violation of the above will be cause for disciplinary action by the University and can also evoke penal action from the sources which have thus not been properly cited or from whom proper permissions have not been taken when needed.

SHAJAN S

Register No. D-TKM18JAN005

Date: 18.03.2023

CERTIFICATE

It is certified that the work contained in the thesis titled "**Numerical and Experimental Investigations on the Performance Improvements of Parabolic Trough Solar Thermal Collector for Medium Temperature Applications**" by **Shajan S.**, has been carried out under my supervision and that this work has not been submitted elsewhere for a degree.

Dr. Baiju V.
(Research Supervisor)
Assistant Professor
Department of Mechanical Engineering
TKM College of Engineering
Kollam, Kerala.

Date : 18.03.2023
Place : Kollam

ACKNOWLEDGEMENT

I wish to record my deep sense of gratitude and profound thanks to my research supervisor, **Dr. Baiju V**., Assistant professor, Department of Mechanical Engineering, TKM College of Engineering, Kollam, for his keen interest, inspiring guidance, constant encouragement during all stages of this work, to bring this thesis into fruition. I would also take this opportunity to express my indebtedness and profound feeling of admiration to, **Dr. T. A. Shahul Hameed**, the Principal, TKMCE for allowing me to use all the facilities to pursue my research. I am thankful to **Dr. Udayakumar J.**, Dean (Research), for his scholarly advice and valuable criticisms during the review of this work and for his support in submitting the thesis in time. I thank **Dr. Dileep P. N.**, Professor and Head, Department of Mechanical Engineering, for his timely intervention whenever required. I want to thank **Dr. Jose Prakash**, **Dr. K. K. Abdul Rasheed**, and **Dr. N. K. Mohammed Sajid**, former HODs, for their support and motivation. I am thankful to my Doctoral Committee Chairman, **Dr. Salih A.**, IIST, Thiruvananthapuram, and Doctoral Committee members **Dr. Mahesh Kumar P.**, GEC, Kannur; **Dr. Joy Varghese**, CET; **Dr. Mohammed Sadikh**, TKMCE and **Dr. Rijo Jacob Thomas**, TKMCE for their timely advice and valuable criticisms during the reviews of this work. I am very much thankful to **Dr. Krishnakumar T. S.**, **Dr. Leena R.**, and **Dr. Sheeba A.**, faculties of Department of Mechanical Engineering, for their valuable support during the research.

It will be an injustice to my conscience if I don't mention the name of **Mr. Jayakumar K.**, Workshop Superintendent; **Mr. Shibu Kumar P. B.**, **Mr. Shajahan S.**, **Mr Afsal S.**, Technical staffs of Mechanical Workshop , who has rendered a lot of help in the fabrication of the experimental setup. I also express my deep gratitude to the amicable staff of the Mechanical Workshop for their priceless help while doing the experiments. In this context, I fondly remember the timely support and help extended by my co-researchers, **Mr. Asif Shah**, **Mr. Abhishek P.**, **Mr. Krishna Raj V.**, and **Mr. Syamkumar G**. I also thank the **faculty** of the Department of Mechanical Engineering, TKMCE, for their valuable support throughout the course of my research work. I acknowledge the AICTE for granting the QIP Scholarship; **Dr. Anu V Thomas** (QIP Coordinator), and the **staff** of the TKM College office for the help rendered for the effort taken to get QIP scholarship. Finally, and most importantly, I would like to extend my deepest gratitude to my **beloved parents**, my dear life partner **Saritha T.**, my daughter **Rupika S**., and my son **Bharadwaj S. S.** for their lifetime support and encouragement.

Shajan S

Abstract

The environmental repercussions of harmful emissions caused by conventional energy fuels such as petroleum and coal are a significant concern in today's globe. A parabolic trough collector (PTC) is a promising solar energy harvesting technology that provides thermal energy. In conventional PTC receivers, solar fluxes are significantly non-uniform, which can cause high local temperatures and large temperature gradients, posing serious challenges to safety and efficiency. One approach for increasing the service life and dependability of a PTC is to reduce the receiver tube's circumferential temperature difference that increases with the concentration ratio. This study investigates the design and development of a PTC with a secondary reflector for medium temperature applications and its experimental performances. Tonatiuh, a Monte Carlo ray-tracing based optical simulation tool, is used to obtain the power output and heat flux profiles on the receiver tube surface. Response surface methodology has been used to examine and select the desired configuration of the solar collector system, and the findings have been analysed using ANOVA. The results showed that the uniformity of heat flux distribution has significantly enhanced after the secondary reflector is installed in its most suitable location, compared to the solar collector without the secondary reflector. Therminol® 55 (TH55) oil-based hybrid nanofluids with graphene nanoplatelets and alumina nanoparticles are prepared by two-step method with different concentrations. Compared to the base fluid, the hybrid nanofluid appears to have an 18.72% increase in thermal conductivity at 65°C. A CFD analysis results show that at 0.1 kg/min mass flow rate, the hybrid nanofluids average convection heat transfer coefficient has enhanced by 21.88%. The experimental results revealed that the efficiency of the PTC with the secondary reflector obtained a greater than 6.0 % improvement over conventional PTCs. With a flow rate of 7.5 lpm, the PTC using hybrid nanofluid demonstrated an increase of 4.05 % in average thermal efficiency compared to the PTC using TH55. Overall this study proposes a new design approach of a solar PTC and a new hybrid nanofluid as its heat transfer fluid for efficient operation of PTC systems.

Table of Contents

Acknowledgements i

Abstract iii

Table of contents v

List of figures xi

List of tables xvii

Abbreviations, notations, and nomenclature xix

Chapter 1: Introduction 1

1.1 Classification of solar thermal collectors 5

1.1.1 Non-concentrating solar collectors 6

1.1.1.1 Flat plate collectors 6

1.1.1.2 Evacuated tube collectors 7

1.1.2 Concentrating solar collectors 8

1.1.2.1 Solar power towers 8

1.1.2.2 Linear Fresnel collectors solar power towers 8

1.1.2.3 Parabolic dish collectors 9

1.1.2.4 Parabolic Trough Collectors (PTC) 10

1.2 Problem definition 12

1.3 Aim and scope of the work 13

1.4 Summary 14

Chapter 2: Literature Review 15

2.1 Background of the research 15

2.1.1 Features of solar PTC components 16

2.1.2 Heat transfer augmentation in PTC 24

2.1.2.1 Heat transfer enhancement through modified absorber geometry and flow inserts 24

2.1.2.2 Heat transfer enhancement through advanced Heat Transfer Fluids (HTFs) 26

2.1.2.3 Heat flux distribution augmentation in PTCs 36

2.2 Summary 39

Chapter 3: Objectives and Methodology 41

3.1 Broad objective 41
3.2 Specific objectives 41
3.3 Research approach and methodology 42
3.4 Conceptual framework 44
3.5 Outline of the thesis 45
3.6 Summary 46
Chapter 4: Design of Parabolic Trough Collector with Secondary Reflector for Uniform Heat Flux Distribution 47
4.1 Theoretical background 47
4.2 Methodology 49
4.2.1 Parameters of the primary concentrator and the receiver tube 50
4.2.2 Parameters of secondary reflector and design of experiment 53
4.2.3 MCRT model of PTC 57
4.2.4 Modelling paradigm 59
4.2.5 Validation of MCRT methodology 61
4.2.6 Computational Fluid Dynamic (CFD) analysis 61
4.3 Results and discussion 65
4.3.1 Ray tracing and heat flux analysis 65
4.3.2 Development of model and statistical testing 67
4.3.3 Validation of the model 70
4.3.4 Parametric effects 71
4.3.5 Response optimisation 74
4.3.6 CFD simulation 76
4.4 Summary 79
Chapter 5: Structural Analysis and Construction of the PTC with Secondary Reflector
5.1 Materials and methodology 81
5.2 Wind load 83
5.3 Determination of drag coefficient 83
5.3.1 Pressure and velocity field around the collector 87
5.4 Structural stability analysis of the PTC 89
5.4.1 Load calculation 89
5.4.2 Modelling of the PTC support structure 90
5.4.3 Boundary conditions 90

5.4.4 Mesh convergence study 91
5.4.5 Numerical analysis with varying load conditions 92
5.4.5.1 Analysis of mechanical behaviour at different wind angles 93
5.5 Construction of the PTC 95
5.5.1 Support structure 95
5.5.2 Main base 95
5.5.3 Solar tracking 96
5.5.4 Receiver tube and secondary reflector 97
5.5.5 HTF storage system 97
5.6 Apparatus and instrumentation 98
5.7 Summary 100
Chapter 6: Preparation and Experimental Characterisation of Hybrid Nanofluid 101
6.1 Nanofluid preparation methods 101
6.2 Stability of nanofluids 103
6.3 Thermophysical and transport properties of nanofluids 104
6.4 Selection of materials for the present study 104
6.5 Materials and methodology 108
6.5.1 Materials used 108
6.5.2 Experimental study 109
6.5.3 Nanofluid preparation 110
6.5.4 Thermal conductivity measurement 111
6.5.5 Viscosity measurement 113
6.5.6 Specific heat measurement 113
6.5.6.1 Temperature history (T-history) method 114
6.5.6.2 Method of measurement and analysis 115
6.5.6.3 Thermal delay method 118
6.5.6.4 T-history experimental setup 120
6.5.6.5 Validation of experimental setup 121
6.6 Experimental results and discussion 121
6.6.1 X-ray powder diffraction 122
6.6.2 Scanning Electron Microscopy (SEM) 123
6.6.3 Optimisation of synthesis procedure of the hybrid nanofluid 124

6.6.3.1 Influence of ultrasonication time 124
6.6.3.2 Influence of OA dispersant on stability of the nanofluids 125
6.6.3.3 Thermophysical properties 127
6.6.3.3.1 Viscosity 127
6.6.3.3.2 Thermal conductivity 128
6.6.4 Transmission Electron Microscopy (TEM) 130
6.6.5 Dispersion stability analysis using UV –vis. spectroscopy 132
6.7 Thermophysical properties 133
6.7.1 Thermal conductivity 133
6.7.2 Viscosity 138
6.7.3 Specific heat 141
6.7.4 Density of nanofluids 144
6.8 Thermophysical property models 145
6.8.1 Thermal conductivity model 145
6.8.2 Viscosity model 146
6.8.3 Specific heat model 147
6.9 Summary 150
Chapter 7: Numerical Analysis of Heat Transfer Performance of Hybrid Nanofluid 153
7.1 Theoretical background 153
7.2 Model description 155
7.3 Governing equations 156
7.4 Thermophysical properties of the fluids 157
7.5 Boundary conditions 159
7.6 Grid independence study 160
7.7 Model validation 161
7.8 Results and discussion 163
7.9 Summary 169
Chapter 8: Experimental Study on the Thermal Performance and Heat Transfer Characteristics of the PTC 171
8.1 Experimental methodology 171
8.2 Performance analysis of the PTC 173
8.3 Uncertainty analysis 174

8.4 Performance parameters 175
8.5 Determination of Direct Normal Irradiation (DNI) 175
8.6 Results and discussion 176
8.6.1 Inlet and outlet temperatures 179
8.6.2 Heat gain of the PTC with and without secondary reflector 183
8.6.3 Efficiency of the PTC with and without secondary reflector 184
8.7 Performance prediction of the PTC 188
8.8 Exergy analysis 189
8.9 Summary 193

Chapter 9: Numerical Modeling of the PTC and Thermal Performance Evaluation of Hybrid Nanofluid

9.1 Mathematical model of the receiver tube 195
9.1.1 Heat transfer through HTF 197
9.1.2 Heat transfer in the absorber tube 199
9.1.3 Solar energy absorbed 200
9.1.4 Heat transfer model for the tank and connecting pipes 203
9.2 Material properties 204
9.3 Numerical procedure 205
9.4 Model validation 207
9.5 Results and discussions 209
9.5.1 Inlet and outlet temperatures of HTFs 209
9.5.2 Effect of flow rate and nanoparticles on heat gain 212
9.5.3 Effect of nanofluid and mass flow rate on thermal efficiency 215
9.6 Economic evaluation of the PTC system 219
9.7 Summary 221

Chapter 10: Summary, Conclusions and Scope for Future Work

10.1 Summary 223
10.2 Conclusions 225
10.3 Recommendations for future works 230

List of publications based on the research 231
Appendices 233
List of References 241

List of Figures

Fig. No:	Figure caption	Page No:
1.1	Worldwide primary energy consumption in the year 2020	2
1.2	Installed renewable energy (excluding hydro) capacity of India	3
1.3	Installed renewable energy breakup of India as on January 2022	3
1.4	Map showing the annual DNI across India	4
1.5	Temperature ranges of solar thermal systems	5
1.6	Solar collectors (a) flat plate collector, (b)evacuated tube collector, (c) solar power tower, (d) linear Fresnel collector	7
1.7	Parabolic dish collector	9
1.8	A mini PTC made by Runh Power Corporation Limited, China for industrial application	10
1.9	Typical Schematic diagram of SEGS plant	11
2.1	Schematic of a receiver tube	18
2.2	Schematic diagram of a sun-tracking mechanism	22
2.3	Modified receivers of the parabolic solar collectors	25
2.4	Boiling point and specific heat of ethylene glycol-based water solutions	28
3.1	Conceptual framework of the investigation	44
4.1	Schematic of a conventional parabolic trough collector	48
4.2	Receiver tube of a PTC	49
4.3	Summary of the procedure	52
4.4	Parameters of a PTC	53
4.5	Receiver tube positions (a) above the focal axis (b) at the focal axis (c) below the focal axis	54
4.6	Schematic diagram of a PTC with a secondary booster reflector	55
4.7	Geometry to determine the location of the receiver tube (a) minimum limit, (b) maximum limit	56
4.8a	Comparison of different sunshapes used in optical simulation	59
4.8b	Ray independent study	59
4.9	Comparison of LCR profile for a round receiver tube	61
4.10	Grid convergence test	63
4.11	Final mesh obtained after mesh convergence study (a) cross section, (b) lateral view	65

4.12	PTC with concentrated radiations (a) without secondary reflector (b) with secondary reflector	66
4.13	Radiation flux (W/m^2) in receiver's surface (a) without secondary reflector (b) with secondary reflector	66
4.14	Experimental results and predicted values (a) uniformity (b) total power	69
4.15	Uniformity of heat flux distribution with (a) receiver tube position (b) width of the secondary reflector	71
4.16	Interaction effect of receiver position and secondary reflector configuration on heat flux uniformity (a) response surface plot and (b) contour plot	72
4.17	Distribution of heat flux when (a) f'=14.2 mm and W_s=13.225mm (b) f'=28.1 mm and W_s=41.6625 mm (c) f'=42.0 mm and W_s=70.0 mm	73
4.18	Effect of power output with (a) receiver tube position and (b) width of secondary collector	73
4.19	Interaction effect of receiver position and secondary reflector configuration on power output (a) response surface plot and (b) contour plot	74
4.20	Response surface plot showing the desirable parameter values	75
4.21	Contour plots for desirability predictions (a) desirability, (b) uniformity, (c) total power	75
4.22	Heat flux distribution (kW/m^2) on the receiver tube's surface, (a) without secondary reflector (b) with secondary reflector, at the outlet of the tube	76
4.23	Temperature contour at different cross sections of the receiver tube without secondary reflector for 3 lpm	77
4.24	Temperature contour at different cross sections of the receiver tube with secondary reflector for 3 lpm	78
5.1	Support structure of the PTC	82
5.2	Wind shear corresponding to different α values	84
5.3	Computational domain (a) front view (b) top view	84
5.4	Mesh at the collector surface	85
5.5	Mesh at the central plane	86
5.6	Discretised computational domain of the wind flow	86
5.7	Inlet velocity based on wind power law	87
5.8	Variation of velocity around the collector	87
5.9	Velocity vector around the collector	88

5.10	Contours of static pressure (top view)	88
5.11	Pressure coefficient contour around the PTC collector	89
5.12	Wind directions for the analyses (a) 30°, (b) 45°, (c) 60°, (d) 90°	91
5.13	Mesh independence study	92
5.14	Discretised computational domain of the PTC structure	92
5.15	Pressure applied on the PTC surface when wind direction is 90°	93
5.16a	Deformation of the collector for wind direction is 90°	93
5.16b	Maximum shear elastic strain for wind direction is 90°	93
5.17	Equivalent stress for different wind directions (a) 30°, (b) 45°, (c) 60°, and (d) 90°	94
5.18	Factor of safety for wind direction (a) 45°, (b) 90°	94
5.19	Main frame and support structure	96
5.20	(a) Gear arrangement and (b) dial indicator for solar tracking	96
5.21	HTF storage tank and weather station	97
5.22	Schematic of the experimental setup	99
5.23	Constructed PTC experimental setup	100
6.1	One-step preparation process of nanofluids	102
6.2	Two-step preparation process of nanofluids	103
6.3	Relations between nanofluid properties and design parameters of nanoparticles and base fluid	105
6.4	Comparison of thermophysical properties of therminol oils and water (a) specific heat, (b) thermal conductivity and (c) density	106
6.5	Schematic diagram of the hybrid nanofluid preparation	110
6.6	Schematic diagram of the thermal conductivity measurement setup	112
6.7	Comparison of the experimental and reported values for thermal conductivity of TH55	113
6.8	Schematic of the experimental setup for the T-history method	116
6.9	Cooling curves of phase change material and reference fluid, according to the original T-history method	117
6.10	Schematic diagram of measurement processing in thermal delay method	119
6.11	Experimental arrangement of the T-history method	120
6.12	(a) cooling history of TH55 and glycerine (b) specific heat of TH55	121
6.13	XRD pattern of (a) Al_2O_3 nanoparticles (b) XRD pattern of GNP	122
6.14	SEM images of Al_2O_3 nanoparticles (a) 3500x magnification (b) 7000x magnification	123
6.15	SEM images of GNP (a) 3500x magnification (b) 7000x magnification	123
6.16	Viscosity as a function of ultrasonication duration for the hybrid nanofluids at 30°C	124

6.17	Thermal conductivity of hybrid nanofluids at 30°C for different ultrasonication time	125
6.18	UV-Vis spectrum of hybrid nanofluids with and without OA dispersant	126
6.19	Viscosity of the base fluid and hybrid nanofluids	128
6.20	Thermal conductivity of the base fluid and hybrid nanofluids	129
6.21	Thermal conductivity of the samples vs storage time at 65°C	129
6.22	TEM images of Al_2O_3-GNP suspension (a) scale bar is 100nm, (b) scale bar is 20 nm	131
6.23	SAED pattern of GNP	131
6.24	UV spectrographs of TH55-GNP/Al_2O_3 hybrid nanofluid	132
6.25	Variations of (a) thermal conductivity of mono-nanofluids and (b) percentage of thermal conductivity enhancement of mono-nanofluids at various particle loadings under the influence of temperature	133
6.26	Variations in thermal conductivity ratio and volume fractions (a) mono-nanofluids, (b) GNP mono and hybrid fluids	135
6.27	(a) Thermal conductivity of mono and hybrid nanofluids and (b) percentage enhancement in thermal conductivity	136
6.28	Effect of temperature on viscosity for different nanofluids at 50/s shear rate	139
6.29	Relative viscosity of nanofluids as a function of temperature	141
6.30	Effect of shear rate on viscosity for different nanofluids at 80°C	141
6.31	Reduction in specific heat as compared with the base fluid	142
6.32	Specific heat of nanofluids at different temperatures	143
6.33	Density variations with temperature	145
6.34	Comparison of hybrid nanofluid thermal conductivity value between present data and proposed model	146
6.35	Comparison of viscosity between the experimental data and correlation output	147
6.36	Comparison of specific heat of experimental data and correlation output	148
7.1	Schematic of the PTC with receiver tube	155
7.2	HTF flowing in the receiver tube of PTC	155
7.3	Properties of TH55 (a) density (b) specific heat (c) thermal conductivity (d) viscosity	158
7.4	Computational domain and boundary conditions for the analysis	159
7.5	Enlarged view of the discretised domain	160
7.6	Grid convergence study	160
7.7	Validation of present model with Graetz's number correlation for convective heat transfer coefficient at (a) x = 0.25m, (b) x = 0.5m, (c) x = 0.75m, (d) x = 1.0m, (e) x = 1.25 m, (f) x = 2.0 m	162

7.8	Percentage deviation of h between the model and correlation results	163
7.9	(a) heat transfer coefficient versus axial location for different flow fates (b) ratio of heat transfer coefficients with discharge at various points along the tube axis	165
7.10	Average convection heat transfer coefficient of the base fluid and the hybrid nanofluid	166
7.11	Surface temperature of the fluid along the tube axis	167
7.12	Difference between the surface temperature of TH55 and hybrid nanofluid	167
7.13	Thermal diffusivity of TH55 and hybrid nanofluid as a function of temperature	168
8.1	Ambient weather station WS2902A	172
8.2	The photograph of the experimental setup	173
8.3	PTC receiver (a) without secondary reflector, (b) with secondary reflector	174
8.4	Hourly incident solar radiation on the days of the experiments (a) Day 1 (b) Day 2, (c) Day 3, (d) Day 4, (e) Day 5, (f) Day 6	177
8.5	Ambient temperature and wind speed on the days of experiments (a) Day 1, (b) Day 2, (c) Day 3, (d) Day 4, (e) Day 5, (f) Day 6	178
8.6	Inlet and outlet temperatures of the HTF (a) Day 1, (b) Day 2, (c) Day 3	179
8.7	Inlet and outlet temperatures of the HTF (a) Day 4, (b) Day 5, (c) Day 6	180
8.8	Outlet temperature of the HTF for the experimental days	180
8.9	Maximum receiver surface and HTF temperatures (a) Day 1, (b) Day 2, (c) Day 3, (d) Day 4, (e) Day 5, (f) Day 6	181
8.10	Average irradiation and average fluid temperatures	182
8.11	Useful heat gain by the HTF (a) Day 1, (b) Day 2, (c) Day 3, (d) Day 4, (e) Day 5, (f) Day 6	183
8.12	Average and instantaneous efficiencies (a) Day 1, (b) Day 2, (c) Day 3, (d) Day 4, (e) Day 5, (f) Day 6	185
8.13	Efficiencies of PTC on evaluated days	186
8.14	Average HTF temperature of experimental days and predicted by the model for varying metereological data	189
8.15	(a) Exergetic losses for the PTC, (b)Exergetic destruction for the PTC	191
8.16	(a) PTC exergy efficiency, (b)Exergy efficiency for different solar hours	192
9.1	Heat collecting element of the PTC along with the stencil considered	196
9.2	Complete energy interaction for an elemental section of the receiver tube	197

9.3	Intercept factor for the proposed PTC	201
9.4	Stratified tank model considered	203
9.5	Temperature dependant properties of TH55	205
9.6	Flow chart for solving the problem	206
9.7	Time-dependent study	207
9.8	Grid independent study	208
9.9	Model validation (Day 5)	208
9.10	Weather data on the evaluated day (a) global and DNI radiation, (b) wind speed and ambient temperature	209
9.11	Inlet and outlet fluid temperature of HTFs for different flow rates (a) TH55, (b) nanofluid	210
9.12	Outlet HTF temperatures at different flow rates (a) 2.5 lpm, (b) 5.0 lpm, (c) 7.5 lpm	211
9.13	Outlet fluid temperature of TH55 and hybrid nanofluids	212
9.14	Instantenious useful heat gain of working fluids at different flowrates (a) 2.5 lpm, (b) 5.0 lpm, (c) 7.5 lpm	213
9.15	Heat gain and heat loss of TH55 (a) 2.5 lpm, (b) 5.0 lpm, (c) 7.5 lpm	214
9.16	Heat gain and heat loss of hybrid nanofluid (a) 2.5 lpm, (b) 5.0 lpm, (c) 7.5 lpm	214
9.17	Instantenious and daily average efficiencies for different flow rates (a) 2.5 lpm, (b) 5.0 lpm, (c) 7.5 lpm	216
9.18	Daily average outlet temperatures and efficiencies for different flowrates	217
9.19	Hybrid nanofluid outlet temperatures for different mass flow rates	218
9.20	Average outlet temperature of hybrid nanofluid with different mass flow rates	219

List of Tables

Table No:	Table Title	Page No:
1.1	Solar thermal energy concentrators	6
2.1	Solar parabolic trough systems characteristics in literature	22
2.2	Characteristics of commonly used thermal oils and molten salts	30
2.3	Thermal properties of usual nanoparticles	32
4.1	Physical parameter of the primary collector and receiver	53
4.2	Coded levels of experimental design	57
4.3	Experimental configurations for ray tracing	57
4.4	Optical errors considered in the present study	64
4.5	Validation of numerical study	64
4.6	CCD matrix and results for uniformity and total power	67
4.7	ANOVA for uniformity	69
4.8	ANOVA for total power	70
4.9	Confirmation between experimental and predicted results	70
4.10	Objectives and constraints for the desirability of parameters and responses	76
5.1	Bill of materials	82
5.2	Measuring instruments specification	99
6.1	Thermophysical property-based preference position of nanomaterials	107
6.2	Chemical and physical data of TH55 oil	108
6.3	Characteristics of selected nanomaterials	109
6.4	Comparison among four common thermal analysis methods	115
6.5	Effect of surfactant addition on the hybrid nanofluid	149
6.6	Thermophysical properties of obtained HTFs	149
6.7	Comparison of thermophysical properties of the proposed hybrid nanofluid with the existing literature	150
7.1	Properties of water	161
7.2	Convective heat transfer coefficient enhancements in PTCs	166
7.3	Comparison of thermal properties of TH55 and developed fluid	168
8.1	Chemical and physical data of TH55	172

8.2	Experiment details	173
8.3	Daily average efficiency of the PTC with and without secondary reflector	186
8.4	Thermal efficiency of PTCs with secondary reflectors	187
9.1	Constants in Zukhaskas Correlation	200
9.2	Factors affecting intercept factor and optical properties considered	201
9.3	PTC performance with TH55 and hybrid nanofluid as the HTF	216
9.4	Themal efficiency enhancement of PTCs with oil based hybrid nanofluids	219
9.5	Cost incurred in the manufacturing of the present PTC	220

Abbreviations, Nomenclature, and Notations

Abbreviations

CCD	Central Composite Design
CFD	Computational Fluid Dynamics
CSP	Concentrating Solar Power
CSR	Circumsolar Ratio
DNI	Direct Normal Irradiance
DOE	Design of Experiments
DSC	Differential Scanning Calorimetry
GNP	Graphene Nanoplatelets
HTF	Heat Transfer Fluid
LCR	Local Concentration Ratio
MCRT	Monte Carlo Ray Tracing
OA	Oleic Acid
PTC	Parabolic Trough Collector
PV	Photovoltaic
RSME	Root Mean Square Error
RSM	Response Surface Methodology
SEM	Scanning Electron Microscopy
TEM	Transmission Electron Microscopy
TH55	Therminol® 55
XRD	X-Ray Diffraction

NOMENCLATURE

A_a	Collectors projected aperture area (m^2)
C_c	Geometric concentration ratio (-)
C_d	Drag coefficient (-)
C_p	Specific heat capacity (J/(kg K))
D	Receiver diameter (m)

DNI	Direct normal irradiance (W/m^2)
d_n	Day number (-)
F_w	Wind force (N)
f	Focal length of the primary collector (m)
f'	Distance to receiver centre from the focal point (m)
G_k	Production rate of k [kg/(ms^3)]
G_ε	Production term in ε equation [kg/(m·s^4)]
h	Convective heat transfer coefficient [W/(m^2.K)]
I	Intensity of direct (beam) solar radiation (W/m^2)
I_g	Global radiation incident on the Earth surface (W/m^2)
I_o	Solar radiation just outside the atmosphere (W/m^2)
P_w	Wind load (Pa)
k	Thermal conductivity [W/(m.k)]
k	Turbulent kinetic energy (m^2/s^2)
L	Length of the solar collector (m)
Le	Entrance length (m)
r	Radius of receiver tube (m)
r_r	Rim radius of the collector (m)
S_T	Energy source term (W/m^3)
S_k, S_ε	User-defined source terms
T	Temperature (K)
t	Time (s)
u_i, u_j	Averaged velocity components (m/s)
V_w	Wind speed (m/s)
W_a	Collector's aperture width (m)
W_p	Half aperture of the primary reflector (m)
W_S	Half width of secondary reflector (m)
W_{-S}	Width of the secondary reflector (m)
Y_k	Contribution of fluctuating dilatation [kg/(m.s^3)]
Y_ε	Destruction term of turbulent dissipation (kg/m.s^4)

NOTATIONS

α	Thermal diffusivity (m^2/s)
ε	Turbulent dissipation rate (m^2/s^3)
η	Collector thermal efficiency
φ_r	Collector rim angle (degrees)
ρ	Fluid density (kg/m^3)
ρ_a	Density of air (kg/m^3)
θ	Radial angular displacement (mrad.)
θ_m	Half acceptance angle (degrees)
θ_z	Zenith angle (degrees)
μ	Dynamic viscosity [kg/(m.s)]
μ_t	Turbulent viscosity [kg/(m.s)]
δ_{ij}	Intermolecular distance
δ	Declination of the sun (degrees)
ω	Hour angle (degrees)
σ	Surface tension (kg/m)
σ_k	Turbulent Prandtl number for k
σ_ε	Turbulent Prandtl number for ε
Γ	Day angle (radians)

Chapter 1

Introduction

Increasing population, economic activity, and urbanisation have led to increasing demand for energy and electricity. Due to the depleting nature and environmental and health-related effects of the consumption of conventional energy sources like petroleum and coal, the globe is facing significant hurdles in delivering a clean and sustainable energy supply to the mass population. Global warming and the impacts of environmental issues have been significantly exacerbated by increased greenhouse gas emissions from fossil fuels. The intensified global warming, rising sea levels, ozone layer depletion, frequent and intense drought, and melting of polar ice caps are some of the signs and consequences of the changing climate. According to the statistical review of world consumption of primary energy in 2020, as shown in Fig.1.1, fossil fuels such as oil, natural gas, and coal still account for a significant share of the global primary energy needs. Renewable energy has recently grown rapidly in many regions around the world. The net-zero emission scenario by 2050 will require significant innovation efforts to rapidly deploy available renewable energy technologies and develop novel and improved technologies [1].

A significant portion of global energy available is used in heat transfer systems, both industrial and residential. In industrialised nations, around 40% of the total energy is consumed by buildings, 30% by industries and the remaining 30% for transportation [2]. Thermal energy is the primary or transitional energy source used to generate

electricity from fossil fuels, nuclear energy, and alternative energy sources. Hence, improving the efficiency of the heat transfer processes and equipment has been a significant research focus in recent years to reduce the level of heat consumed.

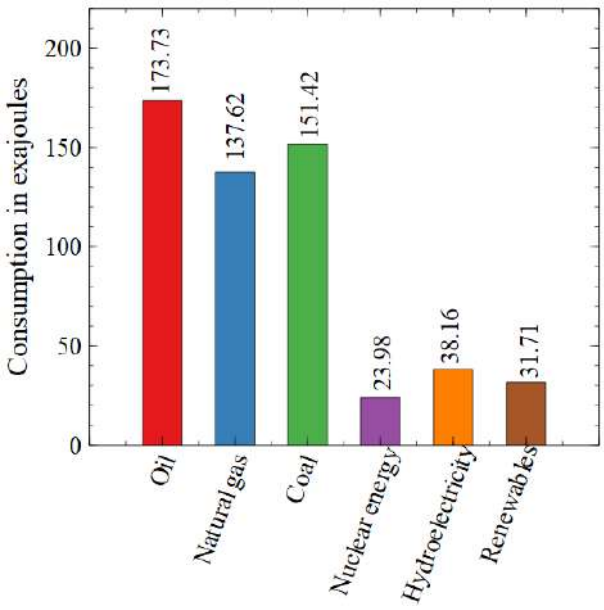

Fig. 1.1: Worldwide primary energy consumption in the year 2020 [3]

Many renewable energy sources can be utilised as a replacement for fossil fuels. Renewable energy generated from natural recourses such as solar, wind, biomass, tidal, hydro, and geothermal energies is an excellent alternative to conventional fossil fuels. As a part of its commitment to clean energy, India has aimed to have 40% non-fossil fuel electricity by 2030. As of March 2021, the country's renewable energy generation capacity was 94.4 GW [4], 24.15% of the total generation capacity of 390.791 GW. As of January 2022, the total installed capacity of renewable energy (excluding hydro) in the country increased to 105.85 GW, representing 26.395 % of the nation's total power supply (Fig. 1.2). With hydroelectric energy also taken into consideration, the nation's renewable energy capacity was 158.12 GW as of April 2022 ranked 4th in the world [5]. Figure 1.3 shows the breakdown of installed renewable capacity (excluding hydro) as of January 2022, with solar power holding the majority share of 50.3%. India target to install over 450 GW of renewable energy capacity by 2030, with solar accounting for approximately 280 GW (more than 60%).

The most significant advantage of solar energy as related to other types of energy is that it is clean and can be delivered without ecological problems like pollution, greenhouse effect and global warming, even if the associated costs are a little higher. Moreover, solar power costs have steadily declined over the last few decades. As per the International Energy Agency reports, by 2050, solar energy is forecasted to grow into the world's leading source of electric power, with around 45% of the world's energy demand [6].

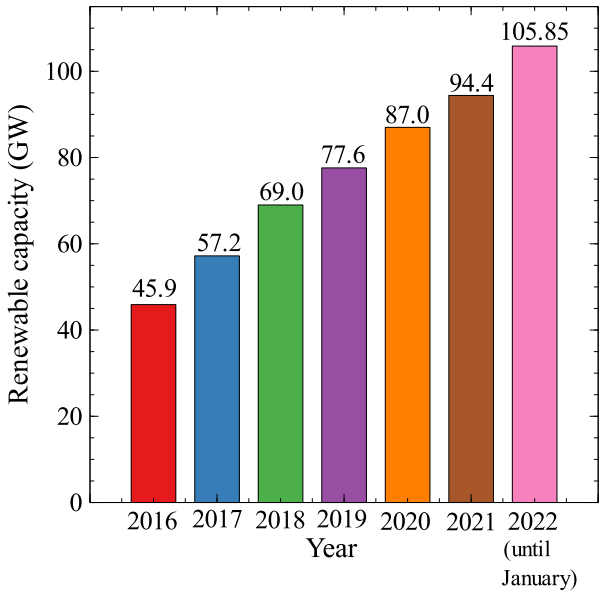

Fig. 1.2: Installed renewable energy (excluding hydro) capacity of India [4]

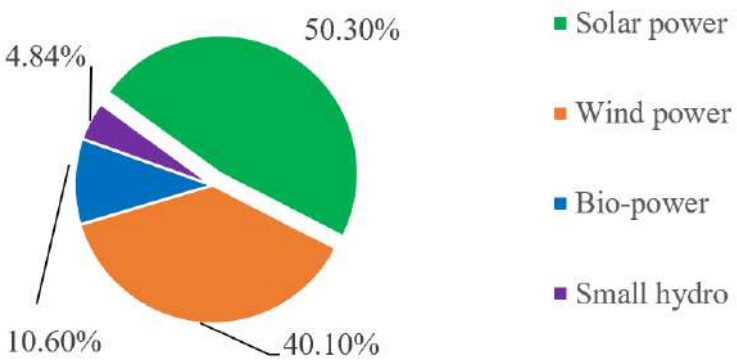

Fig. 1.3: Installed renewable energy breakup of India as on January 2022 [4]

Solar energy received on the Earth's surface is, amounting to approximately 1.5 x 10^{18} kWh/year in the form of electromagnetic radiation [7], which is about 10,000 times the world's present yearly energy consumption. According to the World Energy Council, the amount of energy emitted from the sun is called the solar constant, and the value of this constant is 1367 W/m^2. It makes solar energy as one of the promising renewable energy sources. So the use of solar energy and its technologies have received much attention. India is one of the best solar recipients with relatively abundant availability due to its favourable location in the solar belt (400 S to 400 N). Despite of this immense potential of solar energy resources, technical, economic, and institutional challenges exist to its effective utilisation. High capital costs, the limited ability to transform all energy in sunlight into usable energy, and gradual declination of the performance of the solar thermal systems over time due to structural deformation are the critical drawbacks of solar energy technologies. Besides, large areas are required to harvest hundreds of kWs of solar energy. As a result, significant R & D attempts are still needed to address these issues.

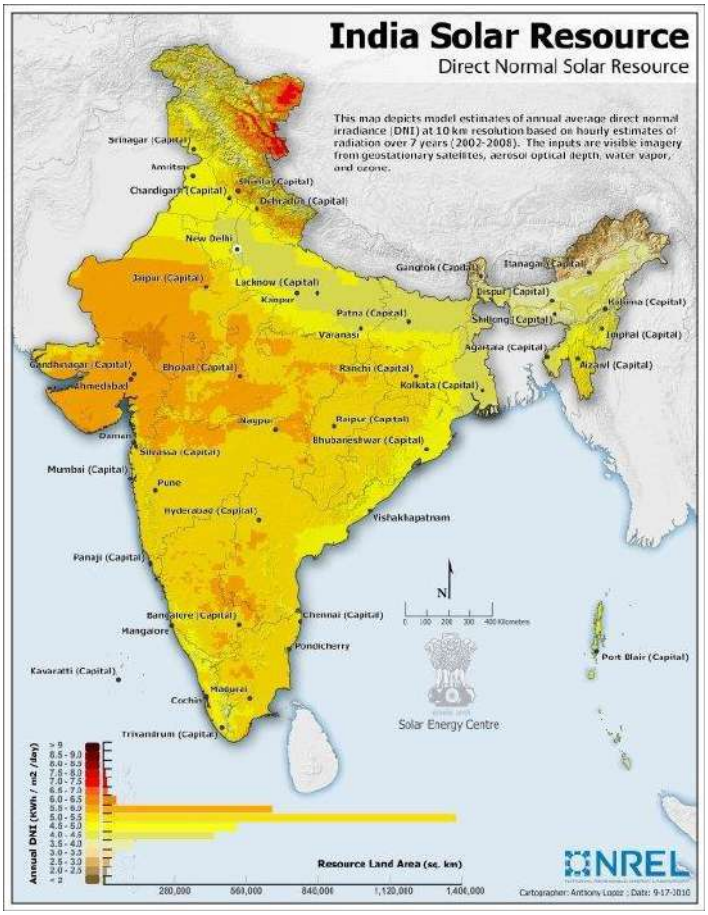

Fig. 1.4: Map showing the annual DNI across India [8]

There are currently two dominant technologies in the solar power industry: Concentrated Solar Power (CSP) and photovoltaic (PV). A solar PV to generate a single kilowatt (kW) requires around 10 square meters of land. An alternative way for the land-constrained and densely populated state like Kerala would be to install smaller CSP systems, especially for thermal energy applications. The application of such technologies can be helpful in domestic, agricultural, and commercial sectors. The CSP systems harness the Direct Normal Irradiance (DNI) component of solar irradiance. As a result, locations with DNI of greater than 1800 kWh/m^2 per year are appropriate for commercial CSP power generation installation at temperatures around 400°C [9]. The yearly solar irradiance levels across India are depicted in Fig. 1.4. It can be seen from Fig.1.4 that Kerala receives an average DNI of 4 to 5.5 kWh/m^2 per day [10], which is more than enough for the deployment of small-scale, medium temperature (<200°C) CSP technologies.

1.1 Classification of solar thermal collectors

A solar collector captures solar irradiation energy as heat, which is transmitted to its Heat Transfer Fluid (HTF). The heat absorbed by the HTF can be used for either industrial/domestic process heating applications or stored in thermal energy storage units for later use. Figure 1.5 shows the maximum attainable temperature ranges of commonly used solar thermal systems. A comprehensive list of solar thermal energy collectors is listed in Table 1.1.

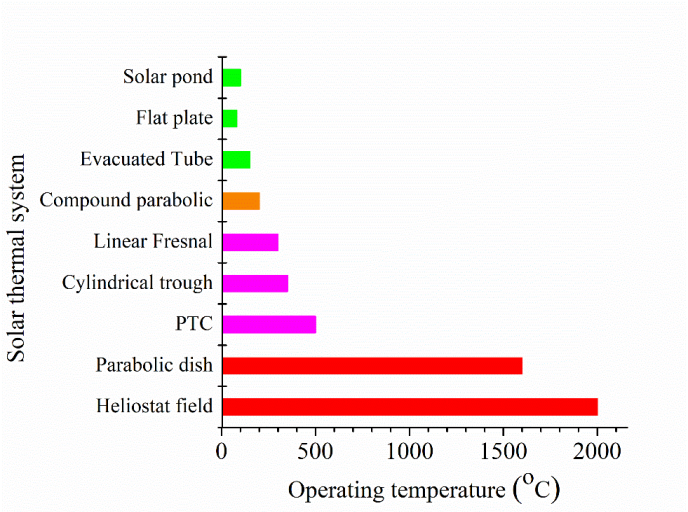

Fig. 1.5: Temperature ranges of solar thermal systems [11]

Table 1.1 Solar thermal energy concentrators [11]

Reflector type	Movement type	Absorber	Temperature range (°C)	Concentration ratio
Flat plate collector	Stationary	Flat	30 - 80	1
Compound Parabolic - collector		Tubular	60 - 240	1 - 5
Evacuated tube collector		Flat	50 - 200	1
Tracking compound - parabolic collector	Single-axis tracking	Tubular	60 - 300	5 -15
Parabolic trough collector		Tubular	60 - 400	15 - 85
Cylindrical trough - collector		Tubular	60 - 300	15 - 50
Linear Fresnel reflector		Tubular	60 - 250	10 – 50
Parabolic dish collector	Double-axes tracking	Point	100 - 1500	600 – 2000
Heliostat field collector		Point	150 - 2000	300 - 1500

Solar collectors are often categorised into two groups such as non-concentrating and concentrating solar collectors. CSP collectors have a bigger concentrator than the absorber, while the non-concentrating collectors have the same sizes.

1.1.1 Non-concentrating solar collectors

Non-concentrating solar collectors are often used for low or medium energy requirements such as solar water heating. The amount of hot water a solar water heater provides is heavily influenced by design and environmental factors such as direct and diffused radiation, outdoor temperature, wind velocity, etc. Commonly used solar water heaters are flat-plate collectors and evacuated tube collectors.

1.1.1.1 Flat-plate collectors

Flat-plate collectors consist of a metal enclosure with insulated edges and bottom, a clear transparent cover (glass), and a selectively coated absorber plate. Solar radiation absorbed by the absorber plate is transferred to the fluid circulating through the tubes. The schematic of the cross-section of a simple flat plate collector is demonstrated in Fig.

1.6 (a). These collectors usually heat the liquid to a temperature considerably less than the boiling point of water. They are best suited for applications where the demand temperature is between 50°C to 70°C.

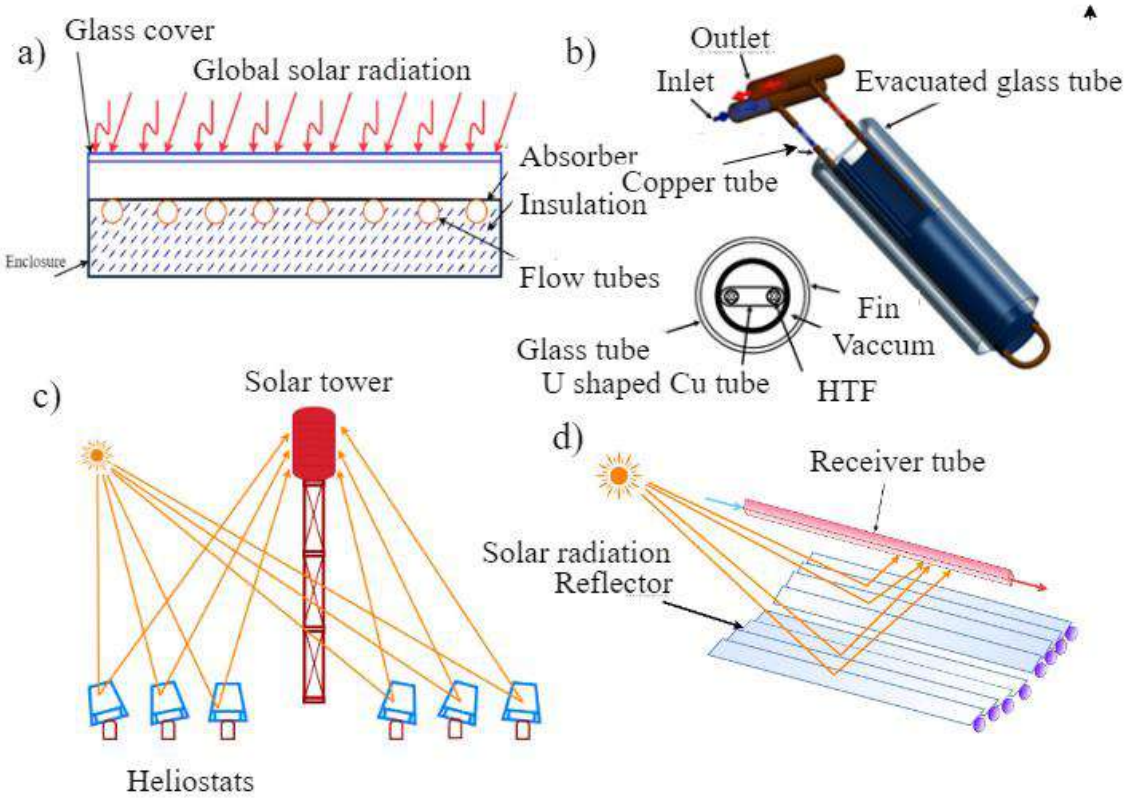

Fig. 1.6: Solar collectors (a) flat plate collector, (b) evacuated tube collector, (c) solar power tower, (d) linear Fresnel collector

1.1.1.2 Evacuated tube collector

Evacuated tube solar collectors are popular and have a greater temperature range than flat plate collectors, ranging from 50°C to 130°C. The heat pipes surrounded by vacuum glass tubes significantly reduce the convection and conduction heat losses. So, as compared to flat-plate collectors, evacuated tube collectors have high thermal efficiency. As the water boils, it delivers the absorbed heat to the collector header. It is captured by water or working fluid circulating the top of the heat pipe and stored in a storage vessel or transferred elsewhere in the system. Because of their cylindrical

construction, evacuated tubes are less sensitive to solar angle and orientation. This allows sunlight to flow at an optimal angle throughout the day- from sunrise to evening. The schematic diagram with the cross-section of the evacuated tube collector is shown in Fig. 1.6(b).

1.1.2 Concentrating solar collectors

In CSP systems, solar energy is harvested into thermal energy by concentrating solar insolation. Reflectors or concentrators focus the beam solar radiations into a point or small area, which is then converted into heat. Based on their optical principles, CSP technologies are classified as either point focus concentrators or linear focus concentrators. Parabolic trough and linear Fresnel collectors are linear focus collectors, but the parabolic dish and solar towers (heliostat field) come under the category of point focus collectors.

1.1.2.1 Solar power towers

Solar power tower or central receiver (Fig. 1.6(c)) consists of a number of sun-tracking mirrors known as heliostats that focus solar radiations on a receiver mounted at the top of a tower. These point focusing can achieve concentration ratios of up to 2000. The HTF is heated to a high enough temperature to produce steam, eventually spinning a turbine to generate power. In these systems, water/steam, molten salt, liquid sodium, or air can be used as the HTF for large plants ranging from 100 to 200 MW.

1.1.2.2 Linear Fresnel collectors

The Linear Fresnel Receiver (LFR) is a line-focused CSP system with adequate thermal performance, and hence is regarded as an attractive and beneficial option for harvesting solar energy. This mirror-based device works on the same theory as a Fresnel lens, which employs flat plane mirrors to follow the sun and reflect radiation onto a

receiver. As illustrated in Fig. 1.6(d), these mirrors concentrate the incident solar radiation onto a metallic receiver tube located above the mirrors.

The mirrors are moved such that they always reflect the solar radiation onto the heat transfer tube. The mirrors are grouped into multiple sets to enhance optical and ground-use efficiency, each with its receiver. This enables a larger mirror packing density, improving optical efficiency while reducing land consumption. The concentration ratio ranges from 10 to 50, and the working temperature ranges from 50°C to 300°C. Despite the parabolic collector's high efficiency, the LFR benefits from a lower investment cost and fewer mechanical issues during operation.

1.1.2.3 Parabolic dish collectors

Parabolic dish solar concentrators are point-focused systems that collect the direct incoming solar energy onto a small receiver area. The intensity of the sun's energy is increased many times on the order of 1000 times by focusing the radiation on a small location. As shown in Fig. 1.7, a parabolic solar dish collector resembles a huge satellite TV or radar dish in appearance; however, it is considerably smaller than a long trough collector.

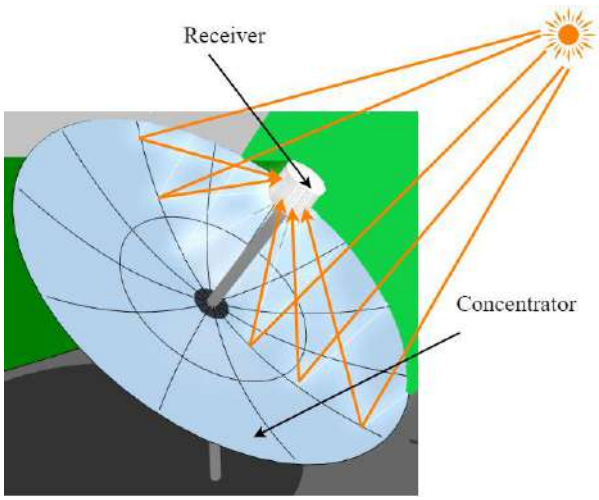

Fig. 1.7 Parabolic dish collector

1.1.2.4 Parabolic trough collectors (PTC)

A PTC consists of a group of reflectors made by forming a thin plate of reflective material (usually silvered acrylic) into a parabolic shape to focus sun rays onto an absorber tube or receiver that is mounted in the focal line of the parabola (Fig. 1.8). To achieve this, the parabola's symmetry plane (optical axis) has to be in line with the incoming solar radiation. In other words, to maximise the solar heat gain, a tracking mechanism has to be used to align the collector with respect to the sun's changing position. One-axis tracking is usually adequate, allowing the use of lengthy concentrator modules. A Heat Transfer Fluid (HFT) is circulated through the absorber tube to absorb the solar heat. The HTF is pumped to a heat exchanger, where the thermal energy is transferred to water or steam.

The parabolic concentrator can focus the beam radiations from 30 to 100 times its normal intensity on the receiver tube, known as the PTC concentration ratio. PTCs can transfer heat energy to the working fluids at temperatures ranging from 50°C to 500°C, the temperature range at which many industrial and domestic processes occur.

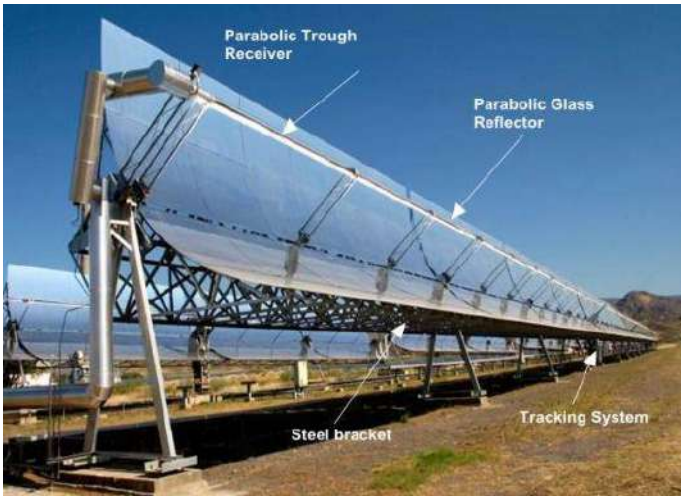

Fig. 1.8: A mini PTC made by Runh Power Corporation Limited, China, for industrial application

Solar PTC systems are categorised into two classes. The first is a mature technology primarily employed in the generation of electricity. It can reach temperatures of up to 550°C [12]. The schematic diagram of the SEGS plant, presently the world's biggest parabolic trough-based solar thermal energy facility, is depicted in Fig. 1.9 and is located in the Mojave desert in the United States. With a temperature range of 70°C to 200°C, the second group includes applications such as solar heating, space cooling, water desalination, soil disinfection, industrial process heat, and so on.

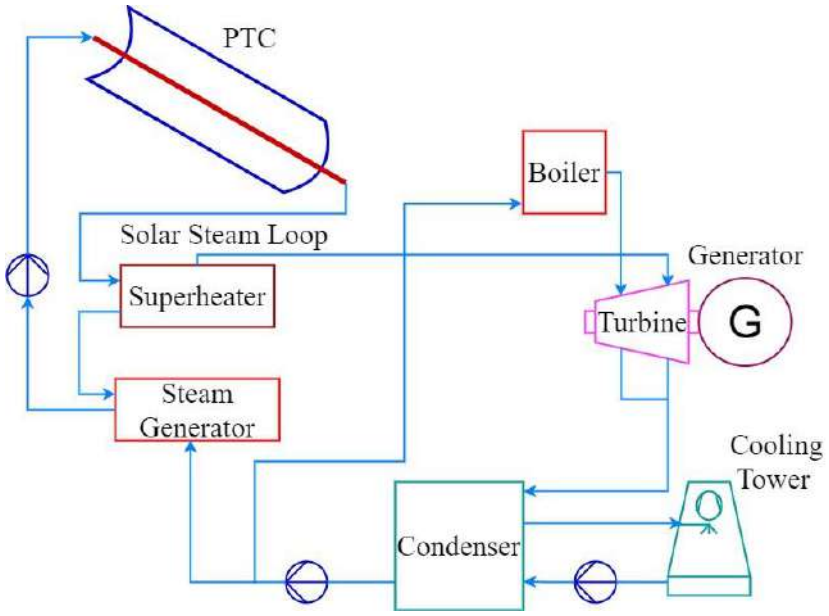

Fig. 1.9: Typical Schematic diagram of SEGS plant [10]

Among the solar power technological innovations, the PTC is one of the most popular and hopeful research areas for solar power extraction. It is widely used with different kinds of working fluids for medium/low-temperature solar energy extraction. However, it has poor thermal performance and issues due to the excessive uneven heat flux distribution. Some solutions to alleviate these problems include structural modification of collectors, innovative heat transfer fluids application, and homogenisation of uneven heat flux distribution.

1.2 Problem definition

The receiver tube is a vital component of a PTC system, which has a substantial role in the system's overall efficiency. Receiver tubes are affected by a high uneven heat flux distribution caused by the non-uniform heat flux induced by concentrated solar irradiation [13]. Furthermore, large concentration ratios have been recommended, resulting in a greater circumferential temperature gradient and high local peak temperature spots in the receiver tube. Because of the local peak temperature and high-temperature gradient, the large heat fluxes on the receiver surface would exacerbate the irreversibility of heat transfer. Hence, the PTC's performance and receiver's durability would suffer due to these adverse operational conditions of large circumferential temperature gradient. On the other hand, it might induce thermal twisting of the tube and consequent cracking of its glass envelope, decreasing the receivers' service life.

To address the aforementioned issues, various thermal enhancement approaches have been extensively used to improve the heat transfer of PTCs. It was shown that properly applying a secondary reflector over the receiver tube is highly effective in enhancing the heat flux uniformity on PTC receivers. The position of the receiver tube about the primary reflector's actual focal axis and the secondary reflector's geometry and size all play a significant role in improving the solar heat flux distribution over the circumference of the tube. A well-established approach for designing a PTC with a secondary reflector is currently unavailable. A PTC with an improperly designed secondary reflector may result in a greater difference in flux distribution and eventually system failure. Hence, the proper design of the PTC with a secondary reflector is also essential for the performance enhancement and long service life of the PTC system.

A PTC's performance is also greatly influenced by the thermophysical properties of the HTF, along with the non-uniform heat flux distribution on the receiver tube. The receiver temperature is substantially greater than the HTF temperature because of the weak convective heat transfer coefficients between the receiver surface and the HTF flow. Many scientists have acknowledged the method for heat transfer augmentation to reduce the temperature gradient by using various working fluids. Nanofluids have gained a lot

of interest in the last decade because they promise to improve the thermal performance of a PTC. In recent years, a novel class of HTFs known as hybrid nanofluids, consisting of two solid nanoparticles dispersed in a conventional HTF, has been developed and extensively explored. Hybrid nanofluids are expected to have better thermophysical properties than base fluids and mono-nanofluids containing single nanoparticles. However, further research is needed to investigate; the proper combinations of hybrid nanoparticles, their mass concentration ratio, dispersion stability, and the physics that contribute to thermal transport enhancement. Experimental and numerical studies are essential to comprehend the thermophysical characteristics and heat transfer behaviour under different flow conditions.

The ability of the receiver tube to withstand thermal bending, the rigidity of the parabolic trough support structure against self-weight and wind load, and the profile accuracy of the parabolic reflector all have a significant impact on properly concentrating direct solar radiations onto the receiver tube. PTCs that provide adequate stiffness, usually built on the terraces of buildings, can enhance optical performance and minimize the harm caused by severe winds, which are increasingly prevalent in densely populated states such as Kerala due to changing climatic conditions. Hence, in addition to the optical design of the PTC, the design for the structural stiffness against extreme loads must also be considered.

1.3 Aim and scope of the work

A rapid transition to renewable energy has become of great importance worldwide to mitigate the problem of climate change and manage emissions. It is beneficial to reduce environmental pollution by utilizing renewable energy sources, not only for large-scale energy production but also for standalone systems. Renewable energy systems are less competitive than conventional energy conversion technologies due to their intermittent nature and comparatively high maintenance requirements. However, these renewable energy limitations surpass fossil fuels due to their abundant resources and environmentally favourable characteristics. Among various clean, renewable resources, solar energy is widely accepted as an attractive and feasible option, owing to its abundant distribution, safety, and ability to serve as a source for others. The PTCs are the most proven CSP technologies available up to now.

In conventional PTCs, the solar heat radiation distribution on the receiver tube is highly non-uniform, which is one of the primary causes of receiver failures and the poor thermal performance of the system. The majority of PTC failures reported are due to the induced stresses and bending of the receivers due to the uneven expansion of the tubes with this non-uniform heat flux distribution. A secondary reflector placed somewhere near the receiver tube can be used to homogenise the solar heat flux distribution over the circumference of the receiver tube. Additionally, an HTF with enhanced heat transfer characteristics can improve the heat transfer and lower the temperature gradient. With these, structural stiffness appears an attractive option for enhancing PTC's thermal performance.

Therefore, this work aimed to develop a systematic and simple design approach for a PTC with a secondary reflector that will result in more even distribution of the heat flux on the receiver and conduct extensive outdoor tests of the developed unit and develop and apply a hybrid nanofluid that prompt higher thermal performance.

1.4 Summary

India has very limited conventional energy resources in comparison to its massive population and constantly emerging economy. India, however, has a great potential for renewable energy, especially solar power, as it receives an abundance of sunshine throughout the year. As India seeks to increase its energy supply, solar power is an avenue it has yet to explore. Solar energy is a useful energy source for securing energy security and meeting energy demand without significantly straining non-renewable resources. This chapter concludes that solar energy could prove to be the most effective alternative to conventional sources of energy. This chapter also presents a general overview of the solar thermal collectors, the problem statement, the aim and scope of the work presented, and the investigation's significant contribution. An in-depth review of the previous work published in the literature is presented in the next chapter.

Chapter 2

Literature Review

This chapter presents a critical literature review on PTCs, focusing on heat transfer augmentation methods, heat transfer fluids, and thermal and structural performance factors in the design and analysis of PTC systems. It begins with a review of features of PTC system components that have a significant role in the performance of collectors. The review includes experimental and numerical investigations with a focus on PTC performance and enhancement methods.

2.1 Background of the Research

The primary role of a solar thermal collector is to gather and process solar insolation into heat energy and thus transfer this energy into a working fluid that can be water, gas or oil. High capital costs and the limited ability to transform all energy in sunlight into useful energy are the key drawbacks of solar energy technologies, as large areas are required to harvest hundreds of kWs. Concentrated solar collectors have been used to resolve the constraint of the low energy density of solar radiation by achieving high temperatures. Several parameters can influence the performance of CSP-based parabolic solar thermal collectors. Research on the influence of these factors on optical loss, thermal loss and other losses is necessary.

The optical loss is mainly caused by the materials of the trough components, such as reflector, absorber tube and glass cover, as well as the errors in the geometric precision of the solar concentrators. The characteristics of component materials must be considered in the design of parabolic collectors to ensure their optimal performance. Inadequate focusing of the solar radiation onto the absorber and shadowing are other significant reasons for low optical efficiency. Various materials and methodologies of thermal performance enhancements are generally used in parabolic solar collector systems to reduce thermal losses. A wide variety of methods for improving thermal performance are available, including the use of advanced absorber materials and working fluids, the use of nanofluids, the use of phase change materials for heat energy storage, the application of inserts into the receiver tubes, and the modification of absorbers' geometry. Over the past years, a significant number of theoretical and numerical research has focused on different ways to improve optical and thermal efficiency of the PTC in order to access and enhance the performance of PTC systems. Such studies investigate the performance of parabolic trough concentrator systems by using different materials for their trough, support structure, reflective material, absorber, selective coating and working fluids. For investigators involved in contributing to the advance of parabolic trough solar collectors, it is essential to choose the right material combinations for collector components.

2.1.1 Features of solar PTC components

The PTC's fundamental components are the parabolic trough reflector, a reflector support structure, an absorber or receiver tube with a suitable selective coating, a glass envelope for the receiver tube and a precise sun tracking system that includes the drive, sensors and controls.

Brooks *et al.* [14] constructed an accurate stainless steel trough reflector mounted on a torque tube structure with a mixture of less sophisticated and improved technology. In 2012 Venegas-Reyes *et al.* [15] developed a light but robust aluminium structure for low-enthalpy steam and hot water production. Forman *et al.* [16] prepared a high-strength concrete support structure, ensuring structural stiffness and keeping the centre of gravity horizontally levelled while tracking the sun.

Various research and reports on polymers as solar collector materials have been carried out. Synthetic rubber materials like polyethylene, polypropylene and a group of Ethylene-Propylene-Diene-Monomers (EPDM) are the most suitable polymer materials for absorber design. Because of its high specific strength, specific stiffness, and high resistance at elevated temperatures and acid corrosion compared to traditional glass troughs, efforts were made over the past decade to construct the parabolic trough collector with composite surfaces using synthetic fibres. Commonly used fibres are glass, boron, aramids and graphite. GFRP (Glass Fibre Reinforced Polymer) is a material with proven properties under severe outdoor weather conditions. Kalogirou *et al.* [17] described the construction of fibreglass cloth and polyester resin-based parabolic trough with good stiffness to weight ratio. Valan Arasu and Sornakumar [18] proposed fibreglass reinforced polymer-based 90^{o} rim angle solar trough that resulted in a high strength-to-weight ratio and cost reduction. Sagade *et al.* [19] developed a fibreglass reinforced plastic parabolic trough with an aluminium foil reflecting surface and a glass enveloped mild steel receiver coated with black epoxy.

Despite the low density and high specific strength, poor fibre matrix adhesion is one of the limitations of natural fibre polymer composites. Therefore, chemical treatment is vital to ensure the mechanical properties for ensuring the utilisation of natural fibre polymer composites. Cotton, jute, flax and sisal are the commonly used natural fibres. The mirror or reflected surfaces of the concentrator is made from various raw materials such as aluminium, stainless steel or low iron glass to reduce the absorption losses. The mirror's solar-weighed reflectivity and price, durability, and wear characteristics are essential in selecting the collector mirrors. PTCs' most frequently used reflective surface is stainless steel, glass mirror, polished aluminium, silver mirror film, and acrylic mirror.

Parabolic troughs are usually installed on framework structures that allow tracking of the sun. The support structure of the solar collector is the major carrier of wind load and structurally supports the parabolic trough. In trough plants, this support structure can be constructed from space frame or torque box designs using steel, aluminium or other more strength materials. Trusses, torque tubes, torque boxes, monocoques, stamped profiles, polymer sections, and moulded composite material structures were some of the

options for the parabolic structure. Chafie *et al.* [20] designed and produced a galvanised iron metal frame consisting of parabolic ribs and a torque box attached by a cylindrical rod to the trough support. A high-strength, stiff and light-weighted concrete parabolic shell mounted on circular segments of new rocker bearings instead of the steel frames is described by Forman *et al.* [16]. Fu *et al.* [21] studied the influence of cross-section sizes for torque box and cantilever beams in the support structure of the parabolic trough. They optimised the torque box, cantilever beams and weight of the parabolic trough collector structure using the wind-structure interaction technique in the CFX module of ANSYS Workbench software. Solargenix has created a PTC with a full aluminium frame that fits the LS-2 collector's size and characteristic parameters [22]. Abengoa developed the 'Space Tube' technology in 2012, in association with Rioglass Solar Inc. and Eucomsa SA, which has higher rigidity and better optical accuracy and can function as much as 550°C.

The receiver/absorber is the element of the PTC system that absorbs and transform solar radiation into heat energy. It has of an absorber tube, an associated glass envelope made of borosilicate glass, and insulations at its end. Current absorbers are usually made of either stainless steel, copper, or mild steel tube covered with a selective surface for improved solar absorptance and low emission coefficient. Thus decreasing thermal losses transfers solar heat to a working fluid. Therefore, the key parameters that affect the collector performance are the emissivity and absorptivity of the absorber tube material. The receiver is the critical element of parabolic trough systems and usually accounts for 30% of the component cost of solar field construction [23]; a schematic diagram is shown in Fig. 2.1 [24].

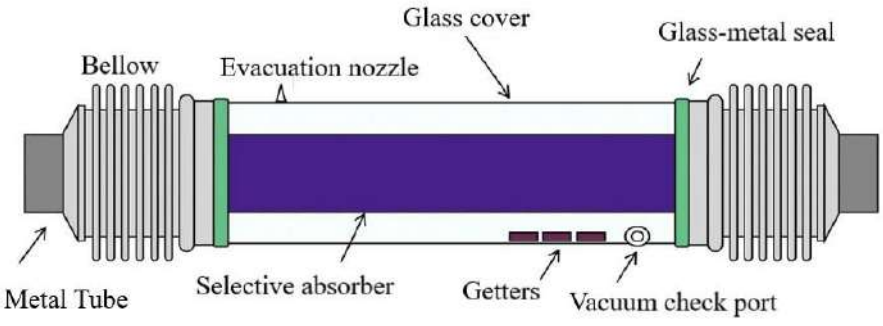

Fig. 2.1: Schematic of a receiver tube [Courtesy of Flagsol]

Several studies have shown that the heat flux distribution on the absorber is not uniform around the surface of the absorber tube [25]. The non-uniform distribution of heat flux on the absorber tube can affect the distribution of thermal stress, which leads to increased optical error and decreasing service life. Thus the non-uniform distribution of heat flux should be kept below safe levels to ensure the longer service life of the absorber tube. This can be accomplished by maintaining optimal flow rates through the absorber tube and incorporating heat transfer enhancement techniques. As copper's thermal conductivity is several times larger than steel, thermal stress and temperature gradient distribution in copper are more uniform. As a result, copper absorbers show lower peak deflection than iron. On the other hand, due to its higher modulus of elasticity, steel will recover its original position more easily than copper after removing the thermal load. Copper absorber tubes are, therefore, not ideal for applications at very higher temperatures. However, as the mass flow rate increases, the uneven surface temperature distribution decreases results in a decrease in maximum deflection.

The selection of the absorber tube diameter is also essential to attain a high intercept factor corresponding to higher heat gain. Nevertheless, because of its increased convective surface area, a larger receiver tube may cause an increase in heat loss. A small diameter of the absorber leads to excessive fluid friction. A fraction of the radiation reflected by the reflector will not meet on the tube. The concentration factor will be reduced with more heat losses on the tube. To ensure enough radiation is received with minimum heat losses, the appropriate determination of the absorber tube diameter is significant. The absorber tube of line concentrating collectors is usually coated with selective coatings to increase optical absorptivity in the solar spectral region and minimise the energy re-emission in the infrared spectrum region [26], which has a high impact on the heat gain of the absorber tube. The selective coatings are stable and appear to remain as long as the vacuum is preserved over time. However, some coating deterioration usually begins to occur once the selective coatings are exposed to air. The selective absorber coatings are classified into different types based on the absorptivity of solar radiation and the structure of the coatings, such as optical interference coating, the structure of the coatings, multi-grade coating, semiconductor coating, metal-ceramic

coating and porous coating. Ease of fabrication, application and reparability is the main attraction of paint coatings as selective surfaces.

Because of the high absorptivity and low emissivity, black oxide copper and nickel-chrome plating are useful for solar applications. When choosing paint coatings, the key factors are film thickness, pigment volume fraction, pigment dispersion in the matrix, and pigment size [27]. Many methods are there for producing low-cost spectrally selective absorber surfaces, but the most preferred in recent decades are sputtering and painting [28]. The interest in the high-quality vacuum-deposited coating has grown more recently due to its high reproducibility and good homogeneity.

The majority of the absorber tubes have an evacuated glass envelope to minimise convective heat loss between them. The vacuum pressure for a fully evacuated glass enveloped absorber tube is approximately 0.013 Pa [29]. The anti-reflective layer covers the glass cover to lower heat losses due to infrared radiation. Due to the important role of the glass envelope for solar absorbers, many studies on the glass envelope have been conducted. Wang *et al.* [30] studied the effect of a glass cover on heat flux distribution over the absorber surface. They proposed a glass envelope with an elliptic–circular cross-section for an absorber tube to minimise the heat flux variation on the absorber surface and reduce the thermal stress. Giovannetti *et al.* [31] developed and manufactured a glass cover with high transmissivity and low emissivity. As an absorber envelope, borosilicate is the most frequently used glass material [32].

The PTC receiver consists of an annular vacuum space between the metallic absorber tube and glass envelope to minimise convective heat transfer from the absorber tube. The vacuum in the annular space between the absorber tube and glass envelop results in the best absorber tube heat transfer performance. However, maintaining a vacuum in the annulus for a more extended period is the main problem. Due to the disintegration of synthetic oil at higher temperatures, the hydrogen absorbed by the stainless steel absorber tube naturally permeates from the working fluid. Thus the presence of hydrogen raises the annular pressure and decreases the absorber efficiency

[33], although the annulus pressure is adequately low (<100 Pa). Oxidation of vacuumed absorber tube due to the air leakage affects the emittance of selective coatings. Burkholder [33] modelled and evaluated the prediction of the thermal characteristics of the absorber tubes with argon, hydrogen and gas mixtures such as hydrogen- argon and hydrogen–xenon.

The solar tracker, a mechanism that moves the collector in-line with the sun's position throughout sunlight hours, increases the energy gathered. The quantity of solar radiation acquired by the solar collector relies upon the time of the day, which similarly applies for the month as well as the season. Numerous studies show that with the use of solar tracking, the collection of solar energy systems can be increased by around 20 -50% [34]. A schematic block diagram of an active sun-tracking mechanism is shown in Fig. 2.2.

Depending on the degrees of freedom of the tracking mechanism, the tracking systems for PTCs can be of 1-axis solar tracking system and, for higher accuracy, 2-axis solar tracking system. The main disadvantage of the 1-axis tracking mechanism is that it can only follow the sun's daily movement and cannot follow the yearly movement. Solar energy accepted on the concentrator by the 2-axis tracker is higher because of the decreased angle of incidence. However, because of the lower cost and ease of installation, the majority of parabolic systems use single axis solar tracking. When the orientation of the PTC axis is N-S (E-W tracking system), the annual incident energy obtained on the collector surface is prominent, resulting in greater annual collector efficiency and lower auxiliary energy requirements. The single-axis tracker usually follows the east-west movement of the sun, while the two-axis tracker also follows the changing altitude angle of the sun. Stern *et al.* [35] designed and constructed a 1-axis solar tracker that provides 20% more energy in a typical year than a fixed axis device. Table 2.1 represents the experimental configurations of small parabolic solar collectors that have been reported in the literature.

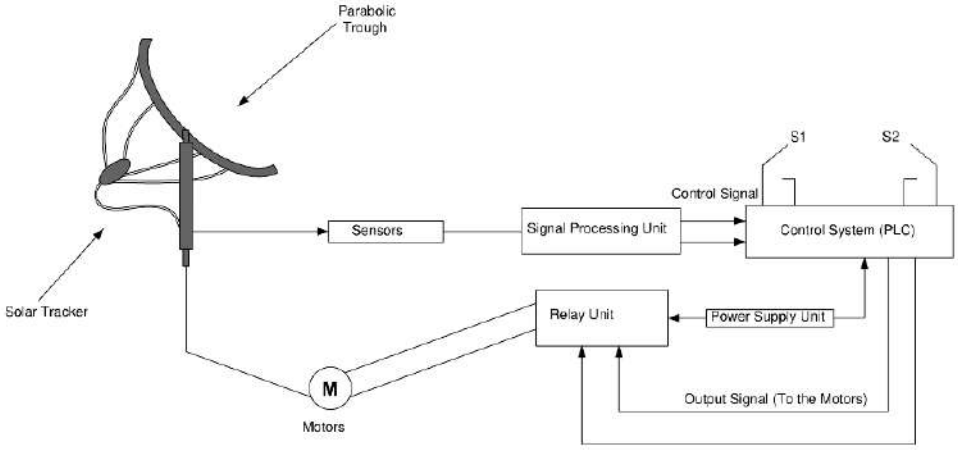

Fig. 2.2: Schematic diagram of a sun-tracking mechanism

Table 2.1 Solar parabolic trough systems characteristics in literature

Year	Author	Reflector material/Area of the trough (m^2)/rim angle	Receiver tube material /dia. (m)	Working fluid	Efficiency	Application	Ref.
1936	Abbot			steam	15.5% overall system efficiency	0.37 kW solar-powered steam engine	[36]
1938	Abbot			steam	11.7% actual efficiency	Produce steam at 225^0C steam engine)	[37]
2007	Valan Arasu *et al.*	GFRP and SOLARFLEX foil /1.0/ 90º	Copper tube coated black paint/ 0.0128 d_o	water	Optical efficiency 69.4%	Hot water generation (75ºC max.)	[18]
2012	Venegas-Reyes *et al.*	Steel & Al foils / 5.8/ 45º	Copper tube coated with Zynolyte paint/ 0.0254 d_o	water	60% maximum	Low-temperature applications (90ºC max.)	[15]
2013	Mohamed *et al.*	Stainless steel / 2.4 / 90°	Galvanized steel/	Water	Ave. collector	-	[39]

			0.0254 d_i		efficiency 37%		
2014	J.Maced o-Valencia *et al.*	Medium density fibreboard & Reflective Al sheet /-/96^o	Copper/ 0.012 d_i	water	50.57% max	Low-temperature applications	[40]
2015	Rizwan *et al.*	Highly polished Al sheet/ - /95^o	Copper/ 0.013d_i	water	Efficiency 53.4% max.	Water distillation (104^{o}C max.)	[41]
2016	Wang *et al.*	-/5.77/80.2°	TP304H steel/0.0 65 d_i	Al_2O_3/synt hetic oil nanofluid		-	[42]
2017	Mohame d	Stainless steel/ 2.4 /90^o	Galvaniz ed steel/ 0.0254 d_i	water	Collector efficiency 42% max.	Hot water generation	[39]
2017	Murtuza *et al.*	Aluminized silver-finished sheet/ 7.5/-	Stainless steel/0.5 08	Water	-	103°C outlet temperature .	[43]
2018	Subrama ni *et al.*	Anodized aluminium reflector /1.6/80°	Copper (black carbon mat finish coating/-	Water-based Al_2O_3 nanofluid	Collector efficiency 55.8% max.	-	[44]
2018	Bilal *et al.*	Stainless steel/ 2.1/-	Cu/0.023 di	Thermic oil	-	-	[45]
2019	Mewes *et al.*	Stainless steel/ 0.6/ -	Copper tube painted black / 0.022	-	-	Melting of plastic waste (211^{o}C max.)	[46]
2020	Abed *et al.*	Stainless steel/32/95°	Stainless steel/ 0.066 d_i	Therminol based SiO_2 nano- fluid	9.18% enhancem ent in thermal efficiency		[47]
2021	Nain *et al.*	Stainless steel/1.68/-	Copper U tube /0.058 d_i	Air	14.68% at 4.55 kg/hr	Space heating	[48]
2022	Sami *et al.*	/4.4/94°/-	/0.114 d_i	Air	-	Desiccant dehumidific ation	[49]
2022	Shaker *et al.*	Glass/39/-	Steel/0.0 66 d_i	Syltherm/ Al_2O_3 nanofluid	Efficiency increased by 5% at 350 K		[50]

2.1.2 Heat transfer augmentation in PTC

The effective heat transfer from the receiver not only leads to enhanced thermal performance but also reduces the problems of non-uniform heat flux. As a result, many investigations focus on the effective heat transfer from the receiver to the HTF using different methods. Experimental and analytical investigations on thermal enhancement using different techniques have been undertaken, as detailed in the coming sections.

2.1.2.1 Heat transfer enhancement through modified absorber geometry and flow inserts

The temperature gradient over the surface of the receiver tube has improved in many concepts with customised receiver geometry and the inclusion of things inside the flow, such as dimples, inserts, fins, and protrusions. Wang *et al.* [51] performed a simulation of the receiver tube by inserting high porosity metal foams within the tube to obtain an enhanced temperature distribution. Ghasemi and Ranjbar [52] found that the inclusion of porous rings within the receiver tubes impressively improves the heat transfer coefficient. At the same time, Bellows and Tzivanidis [53] used geometry modification inserts with star shapes that revealed an increase in thermal efficiency.

Figure 2.3 shows some absorber modifications that have been reported in the literature of PTCs. However, high-pressure drops in many of the concepts examined significantly restrict these modifications. Jaramillo *et al.* [54] enhanced the heat transfer in the absorber by introducing a twisted tape into the receiver, which changes the flow pattern to improve the heat transfer rate between the receiver and the working fluid. Sani *et al.* [55] designed a wavy stripped absorber tube to increase the inner surface of the tube to increase the turbulence of the flow and mix the flow better to enhance the heat transfer rate. Khanna *et al.* [56] studied the effect of the bimetallic tube (stainless steel and copper) to improve the thermal performance of the absorber. Huang *et al.* [57] investigated different receiver tube modifications using dimples, protrusions and helical fins. They

proved that dimpled tubes showed much better results for improving the thermal efficiency of parabolic trough absorbers.

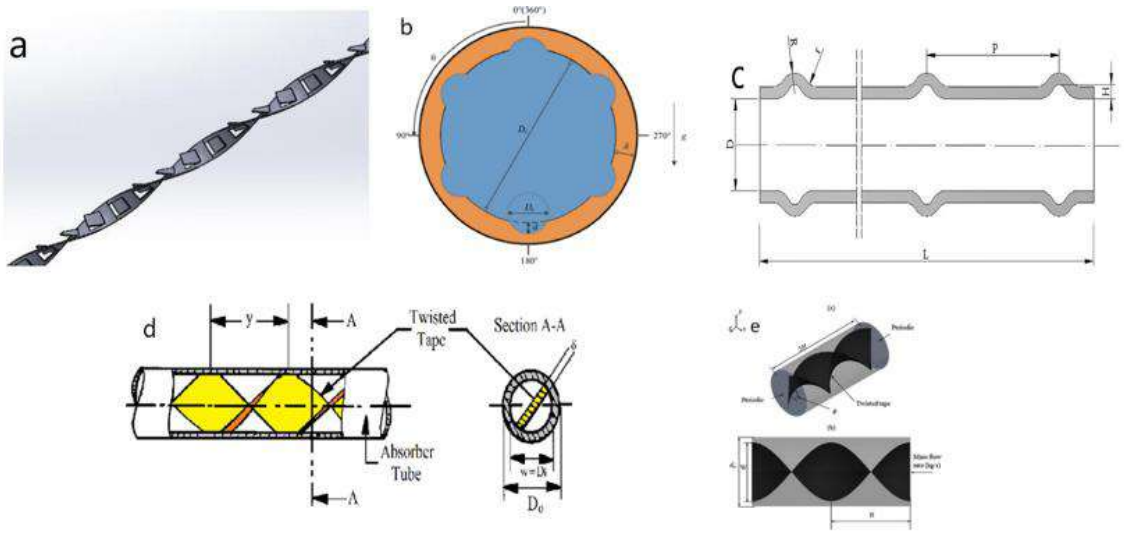

Fig. 2.3: Modified receivers of the parabolic solar collectors (a) perforated louvred twisted tape (b) dimpled absorber tube (c) Symmetric outward convex corrugated absorber tube rings (d) Twisted tape inserts (e) wall detached twisted tape [58]

To examine the overall efficiency of a PTC system, Okongwo *et al.* [59] examined three different types of inserts such as linear fins, twisted tape, and converging-diverging pipe using Therminol VP1oil-based alumina nanofluid. The results revealed that the converging-diverging receiver has the highest thermal efficiency and exergetic efficiency of about 66% and 38%, respectively. Khan *et al.* [60] modified the receiver tube with internal longitudinal fins and numerically determined the solar collector efficiency with water/Al_2O_3 nanofluid as 72.10%, using the Engineering Equation Solver. When the receiver tube is redesigned with a twisted tape insert, it acquired a greater thermal efficiency of 72.26 %. Literature studies have shown that the geometry, dimensions, and location of the inserts used significantly affect the heat transfer on the absorber.

2.1.2.2 Heat transfer enhancement through advanced Heat Transfer Fluids (HTFs)

The critical element of a concentrated solar thermal power technology is the HTF, as its overall efficiency depends on thermal energy. Due to their applicability and temperature requirements, it is necessary to identify the types of HTFs with distinct advantages and appropriate operating temperatures to select the correct working fluids for solar systems. In recent years, many studies have concentrated on heat transfer fluid selection, which performs a crucial function in the overall performance of the collector. There are several types of working fluids, including water, ethylene glycol, thermal oil, and air, and applications with molten salts (primarily nitrate salts) have been developed and tested in recent years.

Due to their low thermal conductivity in the order of 0.609, 0.258 and 0.145 W/(m. K), respectively, the heat transfer performance of traditional HTFs such as water, ethylene glycol and oil is essentially poor. As part of the R&D effort to increase the thermal performance of CSPs, new HTFs with significantly higher thermal conductivities and enhanced heat transfer characteristics will be developed. The selection of a working fluid requires knowledge of the physical properties of each fluid under different thermal conditions. Thermophysical properties are the main factors for achieving maximum heat transfer with minimum input energy and cost. An ideal thermal oil should have good thermal stability, safely and successfully function in all temperature ranges of interest, be chemically compatible with the system's tubing components, have low toxicity, and be environmentally friendly.

The heat transfer rate between the solar absorber and HTF interface depends on the fluid properties such as density, viscosity, thermal conductivity and specific heat. The lowest temperature at which a CSP plant operation can be started depends on oil viscosity, and it should be low, particularly at the lower end of the temperature range. The exact low-end operating temperature at which an HTF can operate in CSP applications is the temperature corresponding to a viscosity (typically 2000 cP) below which rotodynamic pumps can no longer circulate the oil. HTF viscosity also affects the friction losses and

the required pumping energy. The heat transfer medium should be non-flammable, non-corrosive and non-toxic as well. No HTF can come across all these measures equally well, and every selection is a compromise. However, the most recent advances can provide most of the above requirements and surpass the traditional heat transfer fluids. Making the proper selection would increase performance and make your heat transfer device more reliable. The working fluids commonly used in parabolic trough collectors are detailed below.

Water is the most widely used working fluid in PTC studies which usually operates in medium and high-temperature applications. In water-operated CSP plants, the pressure of around 80 bar should be maintained to hold the liquid phase of water at extreme temperatures. Corrosion of tubing and system components and freezing in the winter are other major disadvantages of water. Absorber tubes of solar collectors may fail due to overheating caused by scaling and mineral deposit formation. Mineral deposition on absorber tube surfaces causes corrosion hazards and reduces its heat transfer capability. Compared to oil, steam can be produced at temperatures of more than 500°C. In addition, water leaks are not endangered by either fire or pollution.

Adding glycols to water can solve many problems such as freezing, boiling and corrosion associated with water as an HTF by lowering the freezing point, raising the boiling temperature, and reducing corrosion as an inhibitor. The boiling temperature of ethylene glycol-based water solutions increases with the volume concentration of ethylene glycol. However, the specific heat of ethylene glycol-based water solutions is less than that of clean water, and it reduces with an increase in temperature, as shown in Fig. 2.4. The degradation of water-based glycol fluids, on the other hand, necessitates the replacement of the HTF every three to five years. When a glycol solution is subjected to a bulk temperature in the range of 121°C for an extended period, fluid degradation increases, further reducing the life of the HTF. Ethylene glycol has superior thermophysical characteristics than other ordinary glycols, but due to its relatively higher toxicity is not usually used with domestic hot water applications.

On the other hand, propylene glycol-based fluids are favoured in circumstances where there is a chance of contact with food or beverage goods. It is also worth noting that the freezing point of ethylene glycol/water solutions is considerably less than those of propylene glycol/water solutions for the same concentrations. Choosing a proper inhibited glycol solution can minimise the corrosion of metals in the fluid line and retards the degradation process.

Thermal oil includes Therminol, Dowtherm, Syltherm and Sandotherm. Nowadays, most parabolic trough thermal applications use thermal oils, such as Therminol VP1, Therminol 55, and Syltherm 800, the most popular and dependable solutions [61]. These oils are preferred for the working temperature from 200°C to 400°C, and the devices need not be pressurised to temperatures of up to 350°C. Still, most of them have limitations due to low density and decomposition temperature, high vapour pressure, flammability, and low chemical stability [62]. Thermal stability of synthetic oils, eg. typically Therminol VP1 at higher temperatures, is better, therefore acting as a safeguard against degradation if the upper working temperature is surpassed.

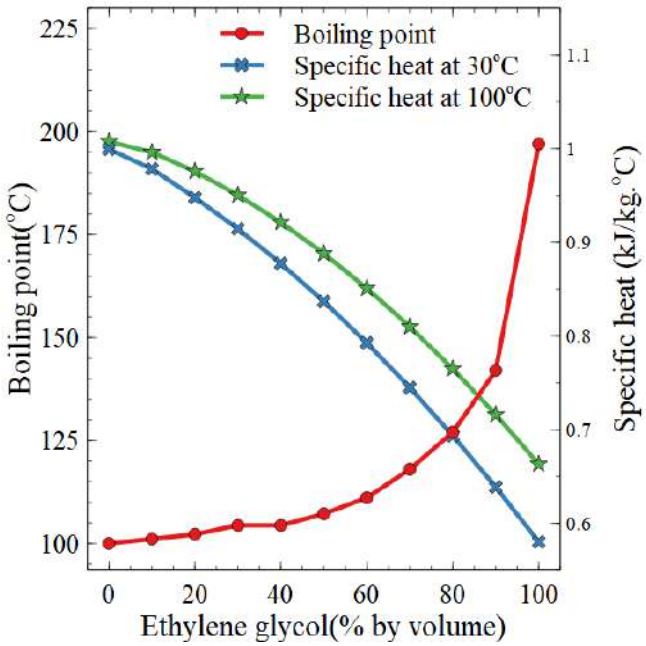

Fig. 2.4: Boiling point and cP of ethylene glycol-based water solutions [63]

Silicone-based HTFs offer many advantages for CSP applications due to their very low freezing and very high boiling points. Properly engineered silicone oils withstand temperatures up to 425°C for long periods, and retaining their low viscosity even at -40°C avoids the need for freeze protection [64]. They are non-corrosive to components and environmentally acceptable. Silicones have a low heat capacity and require more pumping power due to their high viscosity. They are more likely to leak, even through microscopic holes in a loop. Silicones are incompatible with neoprene, butyl rubber, and Teflon.

Because of their desirable properties at elevated temperatures, molten salts are primarily ionic nitrate salts used in high-temperature heat transfer applications. They remain in a liquid stage over a wide range of temperatures and are suitable as HTFs for high temperatures from 250°C to 600°C. High heat capacity, high thermal conductivity, high density, and small vapour pressure even at high temperatures are the unique characteristics of molten salts, which are essential features of a heat transfer/storage fluid. Compared to synthetic oil, molten salts are cheaper and more environmentally friendly than synthetic and mineral oils. However, the main challenge that needs to be addressed is maintaining the entire solar field of a CSP plant above 250°C during the solar downtime/night due to the high melting point of molten salts [65]. Eutectic mixtures of two or more salts help reduce the melting point while maintaining a very high boiling point. Molten alkali nitrate salts, especially the eutectic blend of sodium and potassium nitrate, are extensively used in CSP plants as thermal transportation/storage medium. Blending two different salts together drops the melting point, thereby allowing lower operating temperatures and reducing the chances of freezing.

Solar salt ($NaNO_3$ and KNO_3,60:40 wt%) is the most common salt used as HTF in solar devices. HITEC is a registered $NaNO_3/KNO_3/NaNO_2$ mixture containing respectively 7:53:40 wt% with a liquid temperature range of 149°C to 538°C. Lithium nitrate is the additional component in the quaternary mixtures. Another distinct advantage of molten salts is their ability to lower the size of the thermal storage container due to their high specific heat capacity. The major demerit of molten salt is necessary for secondary facilities to resolve the freeze-up and blockage of pipelines during winter. Due to high working temperatures of 600°C, high heat capacity and high thermal stability,

molten salts were widely researched as a promising candidate for the next generation solar thermal technology. A comparison between the main properties of commonly used thermal oils and molten salts is shown in Table 2.2.

Table. 2.2 Characteristics of commonly used thermal oils and molten salts [66]

Heat transfer fluid	**Temperature range (°C)**	**Thermal conductivity (W/(m K))**	**Average Specific heat (kJ/(kg K))**	**Density (kg/m^3)**
Synthetic oil	250 -350	0.11	2.3	900
Silicone oil	300 - 400	0.10	2.1	900
Hitec solar salt	220 - 600	-	1.5	1900
HitecXL solar salt	120 - 500	0.52	1.4	1992
Nitride salt	250 - 450	0.57	1.5	1825
Nitrate salt	265 - 565	0.52	1.6	1870
Liquid sodium	270 - 530	71	1.3	850
Carbonate salts	450 - 850	2	1.8	2100

Liquid metals are currently being proposed as attractive high-temperature HTFs and TES media, particularly for CSP systems. They are associated with extensive chemical stability at temperatures beyond 900°C, high thermal conductivity and low viscosity. Compared to other HTFs, liquid metals deal with very high outlet fluid temperatures within stable liquids up to their significantly higher boiling point (ie. for Na-883°C at 1 bar) [67]. Ultimately, these properties allow higher maximum solar fluxes on the absorber and, hence, greater heat transfer efficiency. However, liquid metals have not been used in CSP applications until now due to the necessity for complex handling and distinct requirements of the components, flammability and strong corrosion of structural materials. Compatibility concerning corrosion and mechanical strength of structural materials with liquid metals is one of the major issues for its commercial implementation

in CSP plants. With the advancements in R & D on these HTF technologies, many engineering limitations have been resolved. Liquid metals are a small group of metals categorised into three classes, namely, alkali metals, heavy metals, and fusible metals. Primarily investigated liquid metals are liquid Na, liquid Na-K, liquid Pb-Bi, liquid Cd-Bi, liquid Sn-Bi, and liquid Ca-Cu [68]. The use of nanofluids to improve solar thermal system performance is an emerging area for HTFs.

Nanofluid is a colloidal mixture prepared by suspending nanoparticles less than 100nm such as metals, oxides, ceramics, or nanostructured carbon materials into a base fluid such as water, oils, ethylene glycol or molten salts. Metallic nanoparticles have better thermal conductivities than metal oxides; hence they were the first choice. Metal oxides, on the other hand, provide superior chemical stability due to their ability to resist oxidation and lower densities. They are presently the most often utilised family for nanofluid synthesis [69]. The most common nanoparticles are made from metallic nanoparticles (e.g. Au, Fe, Cu, Al, Zn, and Ag), metallic oxide nanoparticles (e.g. SiO_2, TiO_2, CeO_2, Al_2O_3, Fe_2O_3, CuO, and ZnO) [70], and carbon-based nanoparticles (e.g. carbon nanotube (CNT, MWCNT, SWCNT, graphite nanoparticle, and grapheme) [71]. However, along with this advancement in nanofluids, the scientific community is deeply interested in hybrid nanofluids . Minea and El-Maghany [72], and Munkhbayar *et al.* [73] reported a relative increase in the thermal conductivity of hybrid nanofluid as compared to a single nanoparticle in a base fluid.

The application of nanoparticles significantly improves the thermophysical and thermodynamic properties of the traditional HTF, thus improving the exergy and energy efficiencies of the solar collector and thereby reducing the solar field area. The various factors that determine the effectiveness of a nanofluid as HTF are nanoparticle material, size, shape, concentration, type of base fluid, temperature, mass flow rate and nanofluid stability. The stability of nanofluids can be enhanced with the addition of surfactant and ultrasonic processing [74]. Nanofluids have superior extinction, transmissivity, and absorption coefficients because of their better optical properties than traditional HTFs. Brownian motion of the nanoparticles within the HTF is primarily responsible for the surprisingly higher heat transfer capacity of the nanofluids relative to that of the base

fluids. The utilisation of nanofluids in CSP technologies makes a significant enhancement in thermal performance. Table 2.3 provides the thermal properties of typical nanoparticles.

Table. 2.3 Thermal properties of usual nanoparticles [75]

Nanoparticle	Density (Kg/m^3)	Specific heat capacity [J/(kg. K)]	Thermal conductivity [W/(m/K)]
Cu	8933	397	393
CuO	6000	551	33
Fe_2O_3	5180	670	6.9
TiO_2	4230	692	8.4
Al_2O_3	3960	773	40
SiO_2	2200	765	1.4

Numerous experimental studies on nanoparticles are reported using metals, non-metals, metal oxides, carbides, nanoplatelets, and nanotubes. Most researchers reported a significant rise in the thermal conductivity, about 30% for these engineered fluids [76]. In solar thermal systems, Al_2O_3 nanofluids are found to have excellent stability at high temperatures. Wang *et al.* [42] experimented the influence of Al_2O_3 nanoparticles on the thermophysical properties of synthetic oil numerically. It was observed that the performance of the PTC solar systems was significantly higher for the nanofluid as HTF than the base fluid. Mostafizur *et al.*[77] investigated the effect of Al_2O_3, and MWCNT on the thermal conductivity of radiator coolant hybrid nanofluid. The results showed that the thermal conductivity of the nanofluids with coolant oil is higher than that of water-based nanofluids with the same weight fractions and under the same conditions. Heris *et al.* [78] investigated the improvements in heat transfer of Al_2O_3/water and CuO/water nanofluids. The results showed that the heat transfer improvement of the base fluid with the dispersion of Al_2O_3 is more than the addition of CuO nanoparticles. Mostafizura *et al.* [79] studied the thermal conductivity of nanoparticles such as Al_2O_3, SiO_2 and TiO_2 in methanol and reported that the Al_2O_3-based nanofluid has the highest thermal conductivity. Theoretical investigation performed by Tyagi *et al.* [80] reported a 10% improvement in efficiency with Al_2O_3water-based nanofluid as compared to the base

fluid. The literature reveals that Al_2O_3 nanoparticles provide better heat transfer characteristics and are ideal for applications in solar thermal technologies.

Carbon nanotubes and graphene are the most often used carbon-derivative nanoparticles in the literature, followed by nanoscale graphite, diamond, carbon black and fullerenes. Structures of the most employed carbon-based nanomaterials like spherical fullerene, carbon nanotubes, graphene, and diamond are zero-D, 1D, 2D, and 3D carbon crystalline allotropes of carbon. Graphene, atom-thick monocrystalline graphite, exhibited remarkable heat transport properties and was proven to be a promising nanomaterial for HTFs for thermal energy storage and direct absorption solar collectors. GNP possesses a large surface area, high thermal conductivity, better stability, and low specific gravity than metal oxide nanoparticles. These materials have an outstanding thermal conductivity of around 5000 W/(mK) [81], which is higher than the thermal conductivity of carbon nanotubes.

Iranmanesh *et al.* [82] studied the effect of graphene/distilled water nanofluid as the HTF of an evacuated tube solar collector. Their findings illustrated that using 0.1 wt.% of GNP increases the thermal efficiency up to 90.7%. Doping methanol with 0.1 wt.% GNP suspension improved its thermal conductivity by 19%[83]. Yanwei Hu *et al.* [84] proposed a graphene-ethylene glycol aqueous nanofluid using two-step method. They reported that the prepared nanofluid has good stability and reliability. According to investigations, graphene-based nanofluids have superior heat transport properties and conductivity than other carbon-based materials. Besides, recent studies reveal that the addition of highly conductive particles such as GNP and Al_2O_3 improves the performance of HTFs and thermal energy storage materials used in PTCs. Various researchers' findings suggested that graphene nanoplatelets (GNP) could be a promising candidate for solar thermal energy harvesting applications.

Most of the studies on the application of nanomaterials in PTCs reported the use of mono-nanomaterials. The fast growth of nanotechnology has opened up a new way for typical heat transfer fluids (HTF) to develop nanofluids, which can significantly enhance the performance of thermal systems. As a result, there is a lot of research going on in this sector to enhance the thermophysical properties of the working fluids. Recently, dispersion of two or more nanoparticles (Hybrid) in base HTFs has been the subject of

numerous heat transfer engineering investigations to improve the heat transfer properties. The hybrid nanoparticles, a mixture of two or three nanoparticles in correct proportion, will enhance the thermal and rheological properties of the fluid. The enhanced characteristics of hybrid nanofluids make them an appropriate substitute for mono-nanofluids in many applications, including solar energy. Hybrid nanofluids showed better thermal conductivity than mono-nanofluids containing individual nanoparticles separately. A few experimental studies on thermal conversion performance revealed the superiority of hybrid nanofluids over mono-nanofluids and base fluids. The feasibility of using hybrid nanomaterials in solar thermal systems has already been proven. Thus, further investigations need to be carried out to explore its application in PTCs with thermal oils. Moreover, there is not much research done on the heat transfer properties of hybrid nano-based HTFs except for a few on water-based hybrids.

Nanofluids can be synthesised either by the one-step or two-step process. The one-step technique uses wet chemistry procedures, including plasma arc, spraying or sputtering, and laser or electric ablation [85]. The fabrication and dispersion of the nanoparticles in the base fluid are carried out concurrently. The two-step approach requires two distinct procedures, such as fabrication followed by dispersion using various stabilising methods. Even though the dispersion stability of nanoparticles in one-step synthesised nanofluid is superior, the process is complex and expensive [73]. Most researchers use two-step synthesis because of its more effortless production procedure and have better capability to improve thermophysical properties than one-step synthesis. Mohammadpoor *et al.* [63] developed Cu-based nanofluids using both one-step and two-step techniques and investigated the fluids' thermophysical characteristics and dispersion stability. They reported that nanofluids developed in one-step process were shown to be more stable than fluids developed in two-step process, but the nanofluids fabricated in two-step technique have better heat transport properties.

Dispersion stability of nanoparticles plays a vital role in the resulting thermophysical properties of nanofluids. Because of their large surface energy, nanoparticles agglomerate gradually over time. Brownian motions of the nanoparticles lead to Van der Walls forces of attraction between the particles, causing clustering and agglomeration. The aggregation of nanoparticles leads to sedimentation, which reduces the thermal conductivity of nanofluids. The primary limitation of two-step synthesised

nanofluids is the deterioration of expected thermal properties due to their short time dispersion stability. Various methods for enhancing the stability of nanofluids include mechanical agitation, magnetic stirring, ultrasonication, pH regulation, use of dispersants, functionalisation of nanoparticles, and so on [69].

Ultrasonication is a popular approach used by researchers to stabilise nanofluids. High frequency (>20kHz) sound waves induce nanoparticles to disperse evenly in the base fluid with no modification in nanoparticle surface properties. Krishnakumar *et al.* [86] followed the ultrasonication method while synthesising Al_2O_3 nanofluid with different concentrations of Al_2O_3 nanoparticles in ethylene glycol, fabricated by two-step technique. Sanukrishna and Jose Prakash [87] prepared TiO_2-PAG nanolubricant by the same method. Increased ultrasonication duration gives a more homogeneous nanofluid up to a certain point, after which more ultrasonication degrades dispersion stability due to sedimentation at excessive ultrasonication [85].

According to the review, a lot of effort has been put in over the last few decades to conduct both experimental and numerical studies. Heat transfer by convection rises moderately with oxide nanoparticles, but viscosity also rises. With metallic nanoparticles, a very small increase in particle concentration results in almost constant viscosity, but significant heat transfer improvements are observed. Temperature and particle volume fraction both affect the effective thermal conductivity of carbon nanofluid, but temperature has a greater effect than particle volume fraction. However, heat transfer by convection rises considerably with the increasing volume fraction of nanoparticles. Generally, volume fractions of nanoparticles between 0.1 and 6% have been studied in the literature. The usual nanoparticle diameter ranges from 10 nm to 200nm [75]. Tyagi *et al.* [80] describe a steady-state heat transfer model for a nanofluid-based solar collector, which shows a slight increase in efficiency with increasing nanoparticle size. High costs of nanoparticles, handling and preparation of nanofluids, the stability of nanofluids, wall erosion and sedimentation due to different solar receiver designs are significant drawbacks that challenge the usefulness of nanofluids as heat transfer fluids. High solar absorption and high stability with low abrasion are the features of the best heat transfer nanofluid. It is vital to make the exact option of heat transfer fluids for solar collectors due to their suitability and temperature demands**.**

2.1.2.3 Heat flux distribution augmentation in PTCs

The parabolic trough reflector and receiver tube are the two critical components of conventional PTCs based on CSP technology. In conventional PTCs, solar radiation is concentrated on the lower periphery of the receiver tubes, while the rest of the surface receives direct solar radiation. This results in a non-uniform distribution of heat flux around the receiver tube's circumference. The non-uniform distribution of heat flux over the circumference of the PTC receiver tubes is the primary cause of receiver failures and its performance degradation [88]. These include: (i) the non-uniform heat flux distribution around the absorber wall causes the receiver to deflect away from the parabolic trough's focal axis, lowering the system's optical efficiency. (ii) the local peak temperature caused by the non-uniform heat flux may deteriorate the spectral selective coating on the evacuated absorber tube surface, lowering the spectral concentration and increasing heat and vacuum loss due to hydrogen permeation. Thus, it is obvious that the non-uniform distribution of heat flux should be kept below safe levels to ensure a long service life for the receiver tube.

Mitigating non-uniformity in concentrated flux distributions is a critical area of research to which more attention is given. Fathabadi [89] proposed a mathematical model for designing a solar collector that provides the required flux distribution around the receiver tube. The model can develop concentrators with varying aperture areas and geometries to achieve the desired flux distribution. Demagh *et al.* [90] developed an S-shaped/sinusoidal receiver tube for PTCs with a higher intercept factor than conventional linear receiver tubes. The study demonstrates that improving the flux distribution across the tube can help to reduce the receiver tube bending. Few studies have discussed the unequal flux distribution using the Monte Carlo Ray Tracing (MCRT) method [91].

Even though numerous heat transfer investigations have been conducted, they failed to take into account the effects of uneven heat distribution on the surface of the heating element. They presupposed a uniform distribution of heat flux around the absorber tube

surface [92]. Investigations for reducing the circumferential heat flux gradient are necessary for avoiding failures and extending the life of the receiver tubes. Recently, the performance of a PTC with a secondary reflector was investigated. This configuration increases the collector's optical efficiency by balancing the flux distribution around the receiver with the highest total heat output [93]. According to the studies, adding a secondary reflector to the PTC lowers end losses and raises the concentration ratio. Abdelhamid *et al.* [94] studied a solar collector with a compound parabolic booster reflector. They reported an outlet temperature of 638 K. Wang, He, and Cheng [95] conducted a evaluation on secondary reflectors and discovered that using an additional reflector improved the temperature uniformity across the receiver circumference while sacrificing 4% of optical efficiency.

Rodriguez and Rosengarten [96] investigated flat plate secondary reflectors for PTCs with longer focal lengths and an 80° rim angle. They found that the collector's concentration ratio is increasing by approximately 80% with the addition of a secondary reflector. Minaeian *et al.* [97] numerically investigated and optimised various geometric parameters of secondary reflectors in terms of flux density and flux uniformity. They compared optical properties of circular, flat, few segmented, and parabolic secondary reflectors. They found that a few flat segmented collectors could boost flux to 87.9%, while parabolic secondary reflectors provided the best flux uniformity. Bellos and Tzivandis [93] proposed a vertical booster reflector mounted on the longitudinal edge of the trough to reduce end losses and make use of the additional irradiation that falls directly on it. Hack *et al.* [98] proposed a novel adaptive approach for optimising secondary reflector shape, and this design outperforms other secondary reflector designs. Balaji *et al.* [99] performed an optical analysis of parabolic and an involute secondary reflector used in a linear Fresnel collector. They discovered that the parabolic profile had a 2.83% increase in optical efficiency over the involute reflector. Bharti *et al.* [100] investigated a parabolic secondary reflector experimentally and observed an increased working fluid outlet temperature. The results indicated that a parabolic secondary reflector increases the maximum thermal efficiency of a PTC by 6.5% over a PTC without a secondary reflector.

The literature review indicates that further investigation of the implimentation of a

secondary reflector to uniform the heat flux distribution over the receiver tube is necessary to improve the system's performance. Furthermore, the review indicates that the design of a secondary reflector has a significant effect on the PTC's performance. The position of the receiver tube with respect to the primary collector's focal axis, as well as the position and size of the parabolic secondary reflector, are the most critical parameters affecting the optical and thermal performance of these PTCs. Without careful design, the use of a secondary reflector can result in a more severe non-uniform heat flux distribution than a conventional collector and even structural failure of the receiver tube. Consequently, a properly designed PTC with a secondary reflector is essential to a long-lasting and reliable solar collector.

The important aspects influencing the efficiency of a solar parabolic collector are the structural, optical, and thermal performance. To improve reliability, and the structural and optical performance, the proper selection of components of PTC is required. HTF is another critical attribute, and research has shown that using nanofluids as an HTF could significantly enhance thermal performance. Nowadays, hybrid nanoparticles are used in HTF to achieve improved heat transport. Despite numerous studies on improving heat transfer and various thermal transport enhancement approaches proposed, heat flux distribution in PTC receivers has received little attention. Furthermore, most of the research on the thermal behaviour of PTCs considers uniform heat flux around the periphery of the concentrators' receiver, despite the fact that the actual heat flux distribution is non-uniform. To be more specific, PTCs must, as is obvious, be carefully designed and constructed if they are to provide reliable energy delivery over periods of many years.

Hence, this research focuses on the design and experimental performance analysis of a PTC, that combines a secondary reflector and a conventional PTC. This research develops and proposes a new systematic approach for the design of a PTC with a secondary reflector with improved heat flux distribution against a targeted output power. In order to improve the thermal performance, an experimental and numerical study of the fabrication of an oil-based hybrid nanofluid is performed. The hybrid nanofluid has the

potential to replace the conventional HTFs for medium-temperature heat transfer applications.

2.2 Summary

Parabolic trough solar collector system is the most extended solar technology for electricity generation, industrial process heat generation, space heating, heat-driven refrigeration and cooling and domestic hot water production. The important aspects influencing the efficiency of a solar parabolic collector are the structural, optical, and thermal performance. The right selection of the PTC component materials can enhance structural as well as optical performance and increase service life. The performance and safety of standalone rooftop PTC are greatly enhanced by a stiff support structure. HTF is another important attribute, and research has shown that using nanofluids as an HTF could significantly enhance thermal performance. Nowadays hybrid nanoparticles are used in HTF to achieve improved heat transport. Considering the numerous studies on improving heat transfer and the various thermal transport improvement approaches suggested, the heat flux distribution in PTC receivers has not received significant attention. Furthermore, most research on the thermal behaviour of PTCs in the research consider uniform heat flux around the periphery of the concentrators' receiver, despite the fact that the actual heat flux distribution is non-uniform.

This chapter contributes an in-depth review of various heat transfer and heat flux distribution augmentation methods of PTCs. The different PTC component materials have been described and the advantages and demerits of each material is discussed. The gaps identified in this review reveal a lack of established design procedure for a PTC with a secondary reflector for a more uniform heat flux distribution. Added to this, an engineered hybrid nanofluid made of suitably selected components can enhance the thermal performance of the PTCs. The definition of the problem, objectives and research approach and methodology are described in the next chapter.

Chapter 3

Objectives and Methodology

In this chapter, the objectives of the study are presented, the methodology used to execute the research is outlined, including the conceptual framework, and the organisation of the thesis report is explained.

3.1 Broad objective

This investigation aims to design and develop a medium temperature PTC with improved heat flux distribution around the receiver tube and develop an advanced hybrid nanofluid-based HTF for enhanced thermal performance of the system. Specifically, the broad objective intends to design and develop a medium temperature PTC having sufficient structural rigidity with improved heat flux distribution around the receiver tube and develop an advanced hybrid nanofluid based HTF for the enhanced thermal performance of the system. The broad objective motivates the following specific objectives of the present investigation.

3.2 Specific objectives

Specific objectives for achieving the broad objective are stated below:

1. To conduct a comprehensive literature review in the area of PTCs and HTFs.

2. To investigate the effect of secondary reflector geometry and its desirable location on the optical and thermal performance of the parabolic trough collector.
3. To identify suitable hybrid nanoparticles for thermal properties and to develop the best combination and composition of hybrid nanoparticles in thermal oil through experimental investigations.
4. To numerically evaluate the heat transfer performance of the hybrid nanofluid employed in PTC with and without secondary reflector.
5. To design, fabricate and conduct performance investigations of PTC with and without a secondary reflector.
6. To create a numerical model to predict the performance of the parabolic trough collector using hybrid nanofluid and compare it to Therminol®55 (TH55) as the heat transfer oil.

3.3 Research approach and methodology

A literature review on the state-of-art of the PTC technology and advanced HTFs is carried out to critically examine the topic by reviewing the research articles from reputed international journals and books. The knowledge gained from the literature review inspires the design of a novel PTC with a secondary reflector. As a result, this research work proposed a systematic design procedure for a PTC with improved heat flux distribution for targeted output power. The design-points for the optical simulations of the PTC configurations are developed using a classical Design of Experiments (DOE) approach based on Central Composite Design (CCD). Tonatiuh, a Monte Carlo Ray Tracing (MCRT) based optical simulation software, is used to conduct a ray-tracing analysis of the secondary reflector. Response Surface Methodology (RSM) has been used to examine and select the desirable configuration of the PTC system, and the findings have been analysed using ANalysis Of VAriance (ANOVA). Computational Fluid Dynamics (CFD) analysis is conducted using ANSYS Fluent 2020 R1 for the collector with a secondary reflector and the collector without a secondary reflector, based on the flux distribution acquired from the MCRT analysis. ANSYS Workbench 2020 R1 has been used to conduct a numerical analysis to ensure structural rigidity under severe wind load conditions for the concentrator and its support structure. Besides wind load, the gravity effect of the PTC is also considered during the mechanical testing of the PTC

support structure. Development and construction of the experimental rig are completed at Mechanical Engineering Workshop.

After a comprehensive literature review on HTFs and nanofluids, a novel hybrid nanofluid for medium temperature solar applications has been developed by two-step method of nanofluid preparation. The desired procedure for synthesising the hybrid nanofluid is first examined in terms of ultrasonication time, addition of surfactant, and nanofluid properties. Thermophysical properties such as thermal conductivity, dynamic viscosity, and specific heat are determined experimentally over a different range of temperatures and solid concentrations. The transient hot-wire technique, cone-and-plate rheometer, and T- history methods are used to evaluate thermal conductivity, viscosity, and specific heat of nanofluids, respectively. Moreover, based on the experimental data, correlations for predicting the hybrid nanofluid's thermal conductivity, dynamic viscosity, and specific heat capacity in terms of solid concentration and temperature are developed using the non-linear least square method. A CFD analysis based on finite volume method has also been conducted to study the heat transfer behaviour of the developed hybrid nanofluid. For the numerical test, a simple pipe flow with heat flux input is considered, and ANSYS fluent is used to run the simulation. TH55 and the experimentally developed hybrid nanofluid are compared on the basis of their properties. The flow rate is varied, and corresponding indices such as the heat transfer coefficient, surface temperature, fluid temperature, and diffusivity are calculated.

Finally, the PTC with and without the secondary reflector with TH55 oil as the heat transfer fluid (HTF) has been experimented with from September to January (2021-2022). Performance analysis is carried out under outdoor experimental conditions at TKM College of Engineering, Kollam, at a latitude of 8.8932°N and a longitude of 76.6141°E. Numerical results are used to validate the observed outputs. The experiments are conducted at different flow rates under actual outdoor weather conditions.

Finally, a numerical code is developed to predict the performance of the PTC using hybrid nanofluid and compare it to TH55 as the working fluid. The code is developed based on finite volume method in C++ language. The method assumes a 1-D approach with empirical correlations are used for modelling the heat transfer coefficient and is validated using the experimental data. Performance indices, including the overall

3.4 Conceptual framework

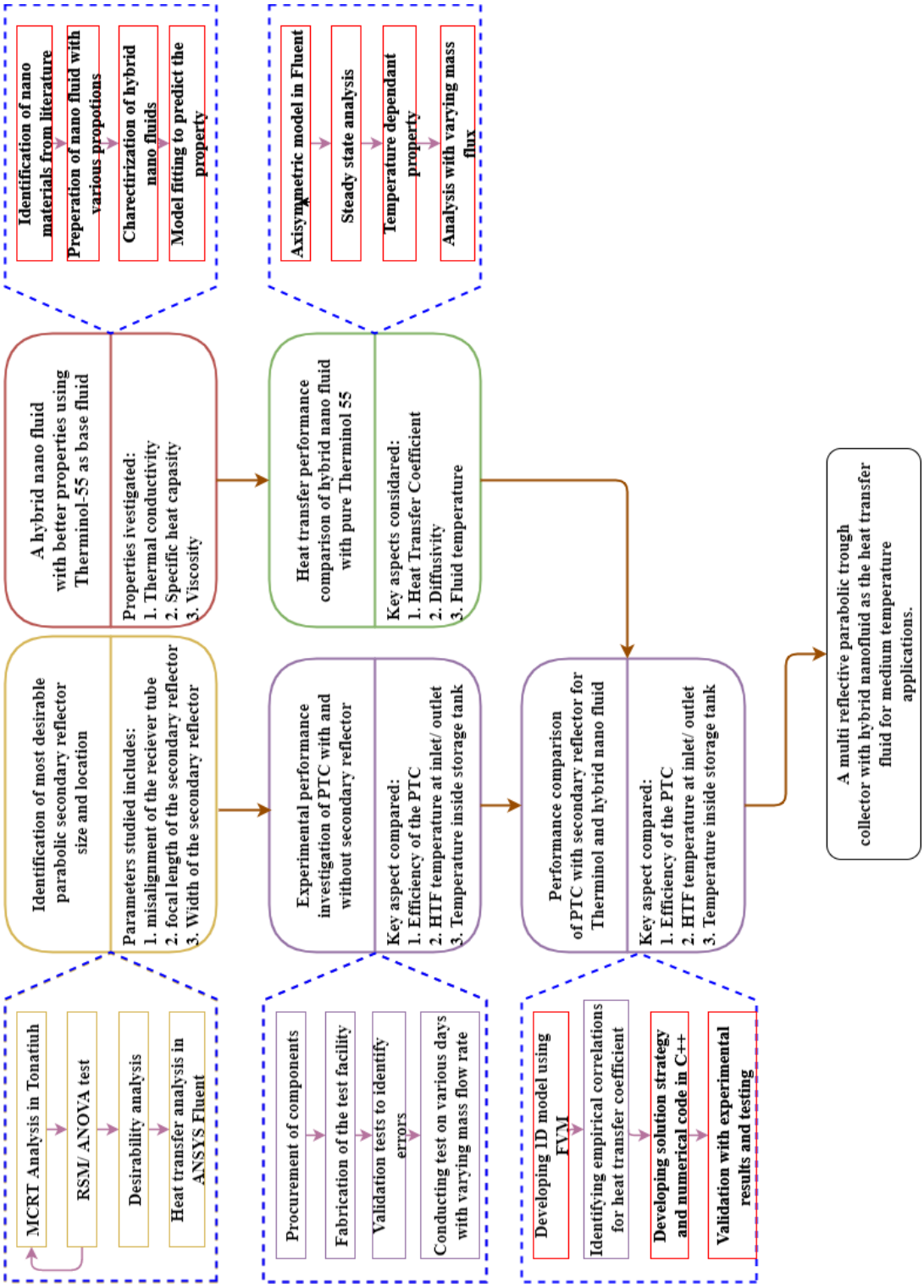

Fig. 3.1: Conceptual framework of the investigation

efficiency, outlet temperature, inlet temperature and tank temperature, are compared for both the HTFs. For all numerical investigations, validation has been accomplished using

mesh independent studies and comparing the numerical results with the experimental data or numerical results reported in relevant research available in the literature.

The illustrative diagram that describes the conceptual framework of the present investigation is shown in Fig. 3.1. It shows the series of actions to be carried out in this research and the relationships between the specific objectives and the broad objective.

The co-concepts involved in the framework are,

1. Design and development of a PTC with a secondary reflector with better heat flux distribution
2. Fabrication and evaluation of the experimental setup with and without secondary reflector and validation of the numerical model.
3. Identification of the most desirable HTF and nanoparticles and development of the hybrid nanofluid
4. Verification of the heat transfer performance of the hybrid nanofluid in comparison to the TH55 oil.
5. Development and validation of the numerical code for the PTC with secondary reflector and its validation with the experimental results.

The final result will be an improved medium temperature PTC with a secondary reflector and hybrid nanoparticle-based HTF.

3.5 Outline of the thesis

There are ten chapters in this thesis. Chapter 1 begins with an introduction that justifies and highlights the problem posed, defines the topic and explains the scope of the work presented in this thesis. Chapter 2 provides an critical literature review on PTCs, including the development of the technology and its applications. In addition, this chapter discusses the previous studies carried out regarding the advancements in PTC technologies and their HTFs. Chapter 3 presents the objectives of this research, as well as the research approach and methodology used to carry out this study.

Chapter 4 presents the design of a PTC with a secondary reflector that has an enhanced heat flux distribution than the conventional PTCs. This chapter proposes a new systematic design procedure for a PTC with a secondary reflector against a target output power. In Chapter 5, the structural performance of the PTC has been analysed using finite element numerical simulations. The study is carried out by considering the severe wind load that the PTC structure may experience over its operating life. Afterwards, the chapter describes the method used to fabricate the designed PTC.

After a detailed description of selecting the appropriate base fluid and nanomaterials to develop the hybrid nanofluid, Chapter 6 discusses the development and experimental examination of the hybrid nanofluid's thermophysical properties. In Chapter 7, the heat transfer behaviour of the developed hybrid nanofluid for laminar flow in the solar receiver is investigated numerically. Chapter 8 discusses the performance study on the effects of the secondary reflector on the designed PTC's and presents the results obtained during the thermal performance outdoor experiments. Furthermore, a correlation has been developed to predict the performance of the proposed PTC using either daily, monthly, and annual average meteorological data. Chapter 9 deals with the numerical modelling of the constructed PTC with a secondary reflector and presents the results obtained by the thermal performance analysis of the hybrid nanofluid. Moreover, this chapter covers the life-cycle cost analysis of the proposed PTC. Chapter 10 provides the general conclusions drawn from this investigation and recommends future work.

3.6 Summary

This chapter provides a concise definition of the problem as well as insight into the objectives, approach, and methodology used to conduct this research. The chapter also presents the conceptual framework of the investigation that explains the specific objectives and their relationships with each other. The next chapter describes the design of the PTC with a secondary reflector, which has a better heat flux distribution than the PTC without a secondary reflector.

Chapter 4

Design of Parabolic Trough Collector With Secondary Reflector for Uniform Heat Flux Distribution

This chapter envisages a detailed novel design approach for a PTC that incorporates a secondary parabolic reflector to homogenise the concentrated solar flux distribution on the receiver tube with the desired total output power.

4.1 Theoretical background

A literature review of the heat flux distribution enhancement around the PTC receiver tube reveals that using a secondary reflector integrated with the conventional PTC is beneficial. An accurate design of the PTC with the secondary reflector is necessary to have a desirable heat flux distribution for the desired output power from the system. Designing a PTC system with a secondary reflector for a targeted output power with the optimum heat flux distribution around the receiver tube is a complex problem. As such, it includes both optical and structural parameters. The former are mostly related to concentrated sun rays which miss the receiver tube, profile error of the trough, and thermal distortion of the receiver and the latter mainly concerns about the location of the receiver tube, structural deformation of the collector under extreme wind loads and location and size of the secondary reflector. This chapter presents a simple design procedure and an overview of Tonatiuh, the optical simulation tool suitable for modelling CSP technologies. The system's performance is investigated by developing a

comprehensive procedure that uses the Central Composite Design method (CCD), Monte Carlo Ray Tracing (MCRT), Response Surface Methodology (RSM), Analysis of Variance (ANOVA), and Computational Fluid Dynamics (CFD) to efficiently build the system with the most desirable parameters.

In PTC systems, the bottom side of the receiver tube wall receives large amounts of concentrated solar radiation from the parabolic concentrator. The upper half receives nearly global radiation from the sun, as shown in Fig. 4.1. Hence, the solar flux distribution on the receiver tube is highly non-uniform. As per the literature survey, the circumferential non-uniform distribution of the heat flux is the leading cause of PTC receivers' failures and its lower performance [101]. Designing a PTC with a uniform heat flux distribution around the circumference of the receiver tube is challenging. Many studies have been published that focus on the effective heat transfer from the receiver to the HTF, utilising various ways to reduce the temperature gradient on the receiver tube. Flow pattern modification by modifying the geometry of absorber tubes, for an enhanced temperature gradient over receiver tubes surface, has been studied [57]. However, these methods result in increased pumping power and hence the higher auxiliary power usage. The schematic diagram of a PTC's receiver tube is shown in Fig. 4.2. Bending of the absorber tube induced by the surface temperature gradient can result in the rupture of the glass envelope and consequent vacuum loss.

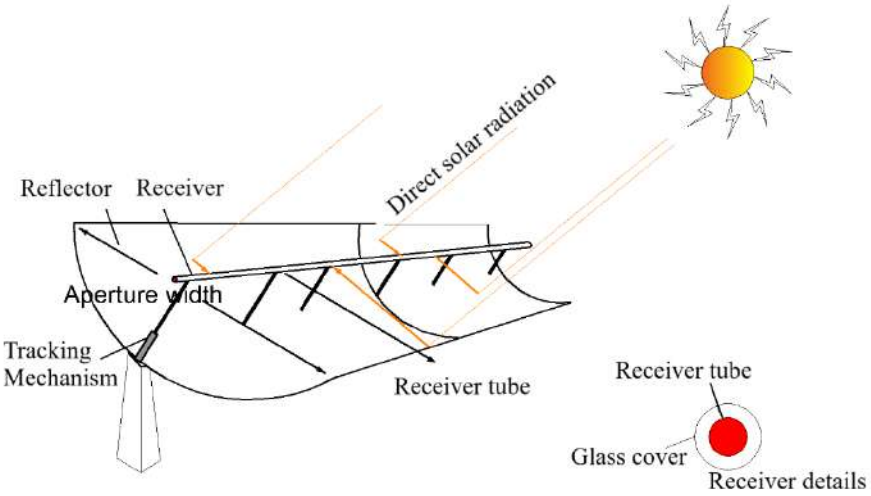

Fig. 4.1: Schematic of a conventional parabolic trough collector

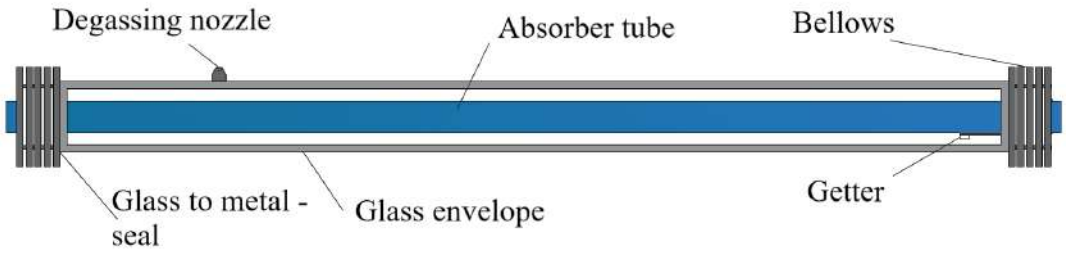

Fig. 4.2: Receiver tube of a PTC

Only a few researchers have reported using secondary reflectors that homogenise the heat flux distribution over the receiver and achieve optical improvements. In this context, there remains considerable scope for diminishing optical losses and improving the homogeneity of heat flux of PTCs. The detailed literature reveals that there are no well-established design procedures for determining the secondary reflector's size and location and the receiver tube's modified position for a particular PTC for optimal heat flux uniformity with the required power output. Therefore, this study investigates the application of a novel secondary parabolic reflector for homogenising the concentrated solar flux distribution on the receiver tube to achieve a uniform flux distribution with maximum total power and proposes a detailed design approach for it.

The effect of receiver tube position and secondary reflector width on heat flux distribution is analysed in this study, and the optimal values for a targeted output power are proposed. This chapter also discusses the characteristics and models of MCRT and the models and assumptions used in the DOE and RSM. Additionally, a numerical analysis using CFD is performed to determine the effect of the improved heat flux distribution on the temperature field of the receiver tube wall and the HTF.

4.2 Methodology

The optimal configuration of a PTC system with a secondary reflector is designed in two stages. The first phase discusses simulating the system's heat flux distribution around the receiver tube and predicting the power output for various configurations using the

MCRT analysis. The design points for the optical simulations of the PTC configurations are developed using a classical DOE approach based on CCD. The PTC is ray-traced using the MCRT-based optical simulation software Tonatiuh. In the second phase RSM is used to investigate the effect of the receiver tube and a secondary reflector configuration on the power output and heat flux distribution of the PTC system. The ANOVA procedure is used to determine the significance and adequacy of the mathematical models developed by RSM to describe the relationship between PTC system parameters and outputs. Additionally, a random ray-tracing analysis is performed to validate the MCRT and DOE results. Furthermore, a desirable functional analysis is performed to determine the system's optimal configuration for optimum heat flux uniformity without compromising the total power. The temperature distribution across the HTF and the pipe is then evaluated using ANSYS Fluent 2020 R1. The study compares PTC without a secondary reflector to PTC with the most desirable parameters. The addition of a secondary reflector results in a shadowing effect, which may impact the heat transfer fluid's temperature. As a result, the average temperature of the fluid is sought for comparison purposes. The methodology is summarised in Fig. 4.3.

4.2.1 Parameters of the primary concentrator and the receiver tube

The experimental setups of PTCs include parabolic profile surface, GI pipe structs, MS support structure and absorber tube supports. The incident radiation, falling on the rim of the PTC, makes an angle with the central plane of the PTC, which is known as rim angle. The PTC geometry is determined by the following parameters: a 70° rim angle (φ_r) and a 1 m focal length (f) of the parabola. Most PTCs operating with 100°C to 200°C have an area of 5 to 10 m^2; therefore, the area of the present PTC is selected as 7 m^2. The system's physical characteristics are determined using the following equations [102].

The aperture width of a parabola is a function of the focal length and rim angle as,

$$W_a = 4ftan\frac{\varphi_r}{2} \tag{4.1}$$

$$W_a = 4 * 1 * tan\frac{70}{2} = 2.8\ m$$

Length of the collector, $L = \frac{A_a}{W_a} = \frac{7}{2.8} = 2.5\ m$

The radius of the parabola at the rim angle corresponding to the focal length is:

$$r_r = \frac{2f}{1+cos\varphi_r} \tag{4.2}$$

$$r_r = \frac{2 * 1}{1 + cos70} = 1.49\ m$$

The diameter of the receiver tube for a perfect and aligned collector with an intercept of unity can be related to the incident angle as,

$$D = 2r_r sin\theta_m \tag{4.3}$$

where θ_m is the half-angle subtended by the sun on the earth.

Equation (4.3) is valid for perfect reflectors without profile and fabrication errors. Furthermore, the equation assumes that the beam radiation hits normal (zero incidence angle) to the concentrator surface. Various studies reported that the minimum half-sun beam angle is 0.265°, which gives the maximum concentration. From Eq. (4.3), the theoretical diameter of the receiver is determined as 0.013866 m. In actual practice, the incidence angle cannot be zero. This implies that the diameter of the absorber should be larger than the calculated value in order to maintain a high intercept when the incidence angle is high. Considering the changes in incidence angle, reflector profile errors, and manufacturing flaws, the receiver tube diameter must be greater than the estimated value. In addition, considering the possible deformations of the 2.5 m long absorber tube with simple supporting structure, and the pressure losses at smaller absorber diameters, the commercially available absorber tube with 0.02665m is considered for this study.

With this, the geometric concentration ratio of the concentrator can be expressed as [102],

$$C_c = \frac{W_a}{\pi D} \tag{4.4}$$

$$C_c = \frac{2.8}{\pi * 0.02665} = 33.46$$

The parameters of the parabolic trough and receiver tube of the PTC system used in this study are shown in Fig. 4.4. The physical parameters of the primary collector and the receiver tube are summarised in Table 4.1.

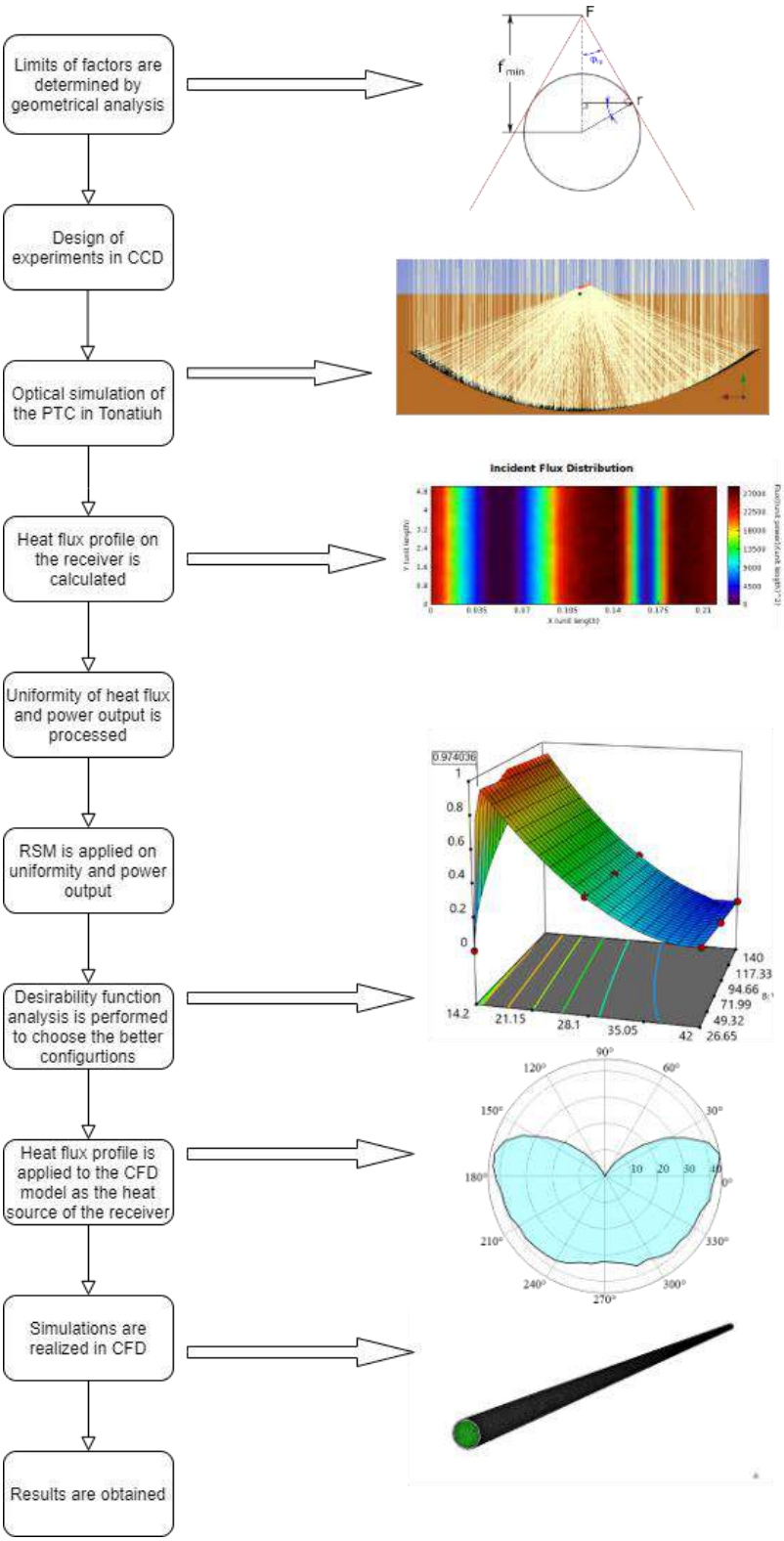

Fig. 4.3: Summary of the design procedure

Table 4.1 Physical parameter of the primary collector and receiver

Item	Numerical Value
Aperture area of the collector (A_a)	7 (m^2)
Aperture width (W_a)	2.8 (m)
Collector length (L)	2.5 (m)
Focal distance (f)	1 (m)
Rim angle (φ_r)	70°
Diameter of the receiver (D)	0.02665 (m)
Thickness of the receiver	0.00165 (m)
Geometric concentration ratio (C_c)	33
Receiver tube absorptivity	0.98
Concentrator reflectivity	0.98

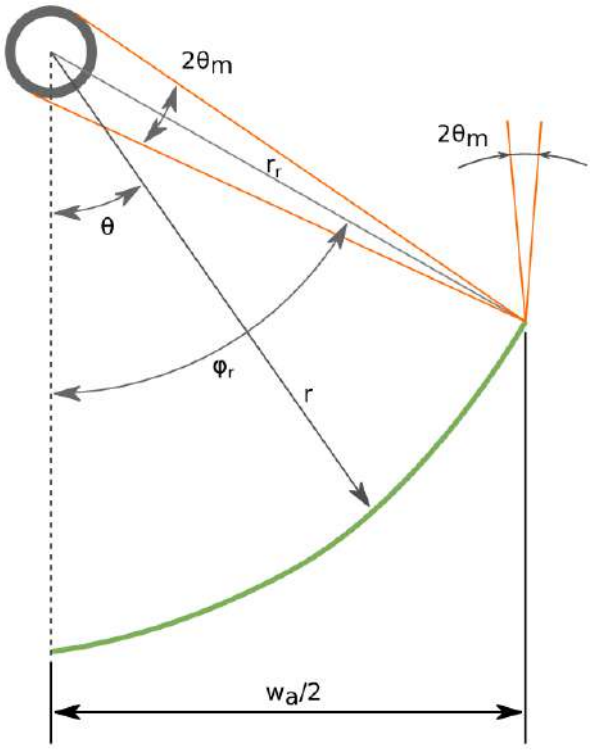

Fig.4.4: Parameters of a PTC

4.2.2 Parameters of secondary reflector and design of experiment

The absorber tube is positioned at the focal axis in conventional PTCs, as illustrated in Fig. 4.5(b). Under ideal conditions, the entire concentrated radiations should be

intercepted on the bottom circumference of the absorber surface along the rim angle. However, in practice, because the top periphery is exposed to direct solar radiation, the receiver experiences a non-uniform heat flux. When the absorber tube is positioned above the collector's focal axis, the majority of the concentrated radiations are intercepted by the tube's small surface area, as illustrated in Fig. 4.5(a). This increases the circumferential temperature gradient and, as a result, the thermal stress on the receiver tube [22]. When the absorber tube is positioned below the concentrator's focal axis (see Fig. 4.5(c)), heat flux is distributed over a larger surface area, but a portion of the reflected radiations are lost.

The absorber tube is positioned at the focal axis in conventional PTCs, as illustrated in Fig. 4.5(b). Under ideal conditions, the entire concentrated radiations should be intercepted on the bottom surface of the receiver along the rim angle. However, in practice, the top periphery is exposed to direct solar radiation and hence the receiver tube experiences a non-uniform heat flux. When the absorber tube is positioned above the collector's focal axis, most of the concentrated radiations are intercepted by the tube's small surface area, as illustrated in Fig. 4.5(a). This increases the circumferential temperature gradient and, as a result, the thermal stress on the receiver tube. When the absorber tube is positioned below the concentrator's focal axis (Fig. 4.5(c)), heat flux is distributed over a larger surface area, but a portion of the reflected radiations are lost.

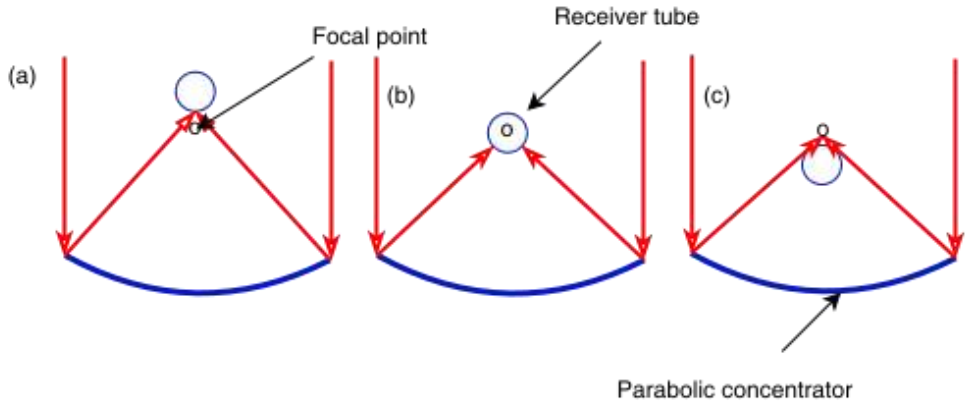

Fig. 4.5: Receiver tube positions (a) above the focal axis (b) at the focal axis (c) below the focal axis

Typically, the intercept factor is used to estimate the concentrator's imperfections. The intercept factor is the ratio of solar insolation intercepted by the receiver to that reflected by the collector (concentrator). A slight deviation of the receiver tube from the focal axis results in a larger change in the intercept factor. The intercept factor decreases as the deviation increases when the receiver is mounted below the exact focal axis. Neverthless, by using a secondary reflector, most of the escaped rays on the absorber tube are re-intercepted. A simple way to uniformize the heat flux over the circumference is to place the absorber tube below the focal axis of the primary collector and a secondary reflector above the tube [103]. The schematic diagram of a PTC with a secondary booster reflector is shown in Fig. 4.6.

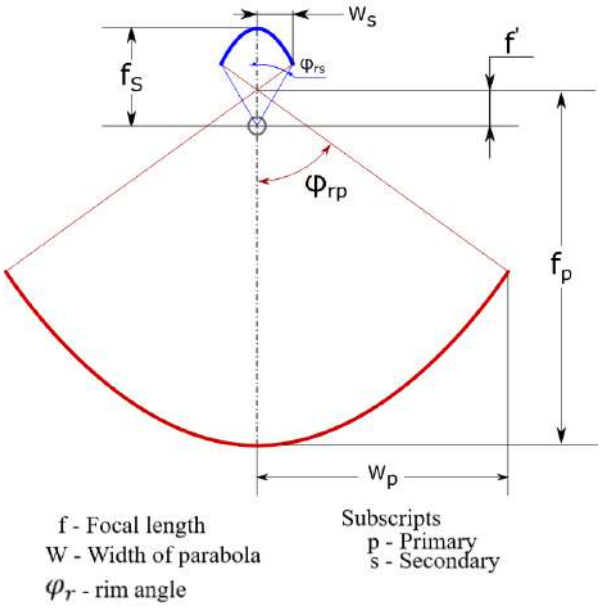

Fig. 4.6: Schematic diagram of a PTC with a secondary booster reflector

The design points are derived from a CCD with two factors and two levels. CCD is a collection of statistical and mathematical techniques for establishing a series of design points that will yield adequate response predictions. To begin, a geometric study is conducted to determine the minimum and maximum locations of the absorber tube (f') relative to the focal axis of the primary collector. Additionally, the study establishes the aperture (*W-s*) limits of the secondary reflector for the purpose of designing experiments

to perform desired analyses. The absorber's minimum distance from the primary reflector's focal axis is determined by the position of the rays reflected from the outer edge of the aperture rendered tangential to the tube, as illustrated in Fig. 4.7(a). The maximum limit is calculated by assuming that at least 50% of reflected rays intercept the receiver tube, as shown in Fig. 4.7(b). The maximum and minimum values can be calculated using Eq. (5), which can be found in Figs. 4.7(a) and (b).

$$f' = \frac{r}{sin\varphi_{rp}} \tag{4.6}$$

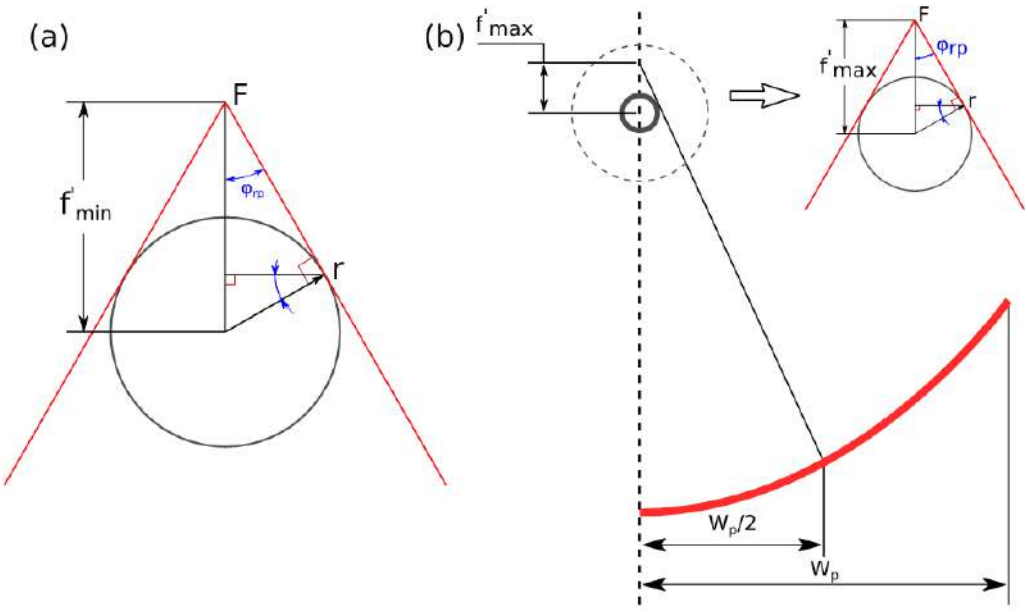

Fig. 4.7: Geometry to determine the location of the receiver tube (a) minimum limit, (b) maximum limit

where $\varphi_{rp} = 70^{\circ}$ for the maximum limit and $\varphi_{rp} = 19.29^{\circ}$ for the minimum limit for this configuration as obtained from the trigonometry. The secondary reflector's minimum width is limited by the diameter of the receiver tube. The maximum aperture of the secondary reflector is limited to 5% of the aperture of the primary reflector, as a large secondary reflector width is superfluous and results in significant optical loss due to the shading effect. As illustrated in Table 4.2, these limits are used to design ray-tracing analyses to determine the secondary reflector's effect on heat flux distribution around the receiver and total power.

Table 4.2 Coded levels of experimental design

Factors	Variables	Unit	Type	Low coded	High coded	Low actual	High actual
A	f'	mm	Numeric	-1	+1	14.2	42
B	*W-s*	mm	Numeric	-1	+1	26.650	140

4.2.3 MCRT Model of PTC

The ray-tracing analysis is critical for the geometric and optical design of CSP systems because it affects their optical and thermal performance and enables more detailed test results with fewer experimental requirements. The optical simulation tool Tonatiuh, based on MCRT, is used in this study to simulate the various configurations of the PTC with a secondary reflector as designed by CCD. The MCRT method is efficient for evaluating the performance of concentrating solar collectors. Based on the collector configurations, as shown in Table 1 and receiver position (*f'*) and secondary reflector configurations (*Ws*) obtained through CCD [Table 4.3], thirteen ray-tracing analyses are conducted to investigate the uniformity of heat flux over the absorber surface and the system's power output.

Table 4.3 Experimental configurations for ray tracing

Exp. No.	f'(mm)	*W-s* (mm)	$f_p - f'$ (mm)	φ_{rs}(rad)	f_s (mm)	W_s (mm)
1	14.2	140	985.8	1.05512568	60.071	70
2	28.1	83.325	971.9	0.766543956	51.663	41.6625
3	28.1	83.825	971.9	0.766543956	51.663	41.6625
4	42.0	26.650	958.0	0.277101669	47.779	13.325
5	14.2	83.325	985.8	0.95685326	40.167	41.6625
6	28.1	26.650	971.9	0.384295257	34.246	13.325
7	28.1	83.325	971.9	0.766543956	51.663	41.6625
8	28.1	83.325	971.9	0.766543956	51.663	41.6625
9	28.1	83.325	971.9	0.766543956	51.663	41.6625
10	42.0	83.325	958.0	0.62981096	63.95	41.6625
11	42.0	140	958.0	0.803741478	82.353	70
12	28.1	140	971.9	0.917512604	70.864	70
13	14.2	26.650	98.58	0.610375955	21.149	13.325

When viewed from earth, the sun appears to be a disc rather than a point source. The radiation flux distribution within the disc is expressed as a normalised radiance profile, referred to as sunshape. The sunshape is mathematically defined as the radiation energy rate per unit solid angle in a given direction and per unit projected area that is normal to that direction. The Pillbox, Neumann, and Gaussian models are frequently used to describe sunshape. The Pillbox model assumes a constant rate across the disc angle, whereas the Gaussian model is the accepted model. A Gaussian function is a bell-shaped curve, and any random trial will eventually follow a normal distribution as the number of trials increases.

None of the models mentioned above accounts for the broadening effect of the solar beam caused by its interaction with the earth's atmospheric particles. Due to the large size of the particles (between 0.1 and 1.0 m), these interactions scatter the light, forming the solar aureole. This results in a circumsolar region or aureole ranging from 4.65 to 50 mrad around the sun. Thus, the Circum Solar Ratio (CSR) is defined as the fraction of apparent beam radiation that originates in the circumsolar region. Figure 4.8(a) illustrates a comparison of normalised intensity as a function of angular displacement from the centre for the various sunshape models. Without taking CSR into account, models tend to overestimate the power output and underestimate the flux distribution in imaging concentrators. The limb-darkened solar disc with circumsolar radiation produces the most realistic sunshape because it incorporates the effects of interaction with the earth's atmospheric particles. The Neumann and Buie models are the most frequently used limb-darkened solar disc models.

Tonatiuh is a cutting-edge open-source ray-tracing software developed by Spain's National Renewable Energy Center (CENER) to design and analyse CSP systems. Tonatiuh provides the Buie sunshape, the most realistic and widely used model of the solar disc with limb-darkened limbs and circumsolar radiation. The system's geographical location has no bearing on this model, which exhibits both axial and central symmetry. The distribution of the rate of energy per unit solid angle in a specified direction and per unit projected surface area normal to the specified direction can be calculated using this model [104] as,

$$\hat{L}_{Biue}(\theta) = \begin{cases} \frac{cos326(\theta)}{cos308(\theta)}, & 0 \le \theta \le \theta_{disk} \\ e^{\kappa}(10^3\theta)^{\gamma}, & \theta_{disk} < \theta \le \theta_{aureole} \end{cases} \quad (4.5)$$

where θ is the radial angular displacement, κ and γ are the functions of circumsolar ratio (χ) and are expressed as

$$\gamma = 2.2ln(0.52\chi)\chi^{0.43} - 0.1 \quad (4.6)$$

$$\kappa = 0.9ln(13.5\chi)\chi^{-0.3} \quad (4.7)$$

In optical simulations, $\theta_{disk} \approx 4.65$ mrad is the annual averaged angular width of the solar disk, and $\theta_{aureole} \approx 43.6$ mrad the angular extent of the halo considered.

The reflectivity and absorptivity of the receiver are assumed to be 0.98 in this study. Each ray tracing run considers samples of 2 million rays with an irradiance of 1 kW/m^2. The rays are chosen based on the results of the ray-independent test shown in Fig. 4.8(b). The number of rays used varies between 1000 and 10000000, and the MCRT analysis is performed accordingly. The total power is plotted against the number of rays in Fig. 4.8(b) using a log plot. As can be seen, the total power varies by only 0.05% beyond 2 million rays.

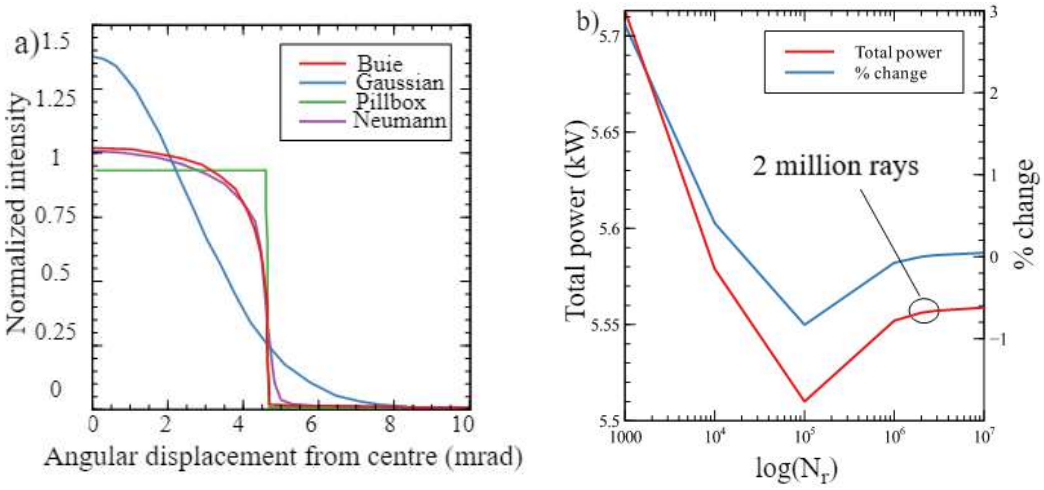

Fig. 4.8:(a) Comparison of different sunshapes, (b) Ray independent study

4.2.4 Modelling paradigm

Tonatiuh's computational structure is based on two models: one for incoming solar radiation and another for the radiation's interaction with the surface. A bounding volume,

an aperture, and a collection of surfaces with varying optical properties are used to model the entire system. The bounding box serves as the computational boundary. Only rays passing through the bounding box are taken into account when computing the energy equation, while rays departing from the bounding box are assumed to have no interaction with the system. Solar radiation enters the bounding box is specified as the energy per unit area per unit solid angle to the direction of the surface at the input aperture of the bounding box. The vector of the sun's direction is defined as a function of four variables: latitude, declination, hour angle, and solar azimuth angle. Geometrical optics is used to determine the interaction between the incoming radiation and the surface.

In Tonatiuh, the input solar flux will be mathematically transformed into a probability density function. This is accomplished through the use of the MCRT algorithm. Here, the input radiation is computed at each point to obtain the radiative flux's spatial distribution. The probability density function can be used to improve convergence and decrease variance. The function indicates the likelihood that a given photon bundle will pass through a particular point on the inlet aperture. The interaction between the photon bundle and the surface is similarly modelled. Using this approach, the flux map over the surface can be easily computed as a fraction of photon bundles available per unit area and unit time relative to the total bundles analysed.

The optical modelling is carried out with the following assumptions:

(i) Only direct radiation is considered
(ii) Buie sunshape is considered for modelling the sun
(iii) Solar irradiation is considered as parallel beams
(iv) All the properties considered are independent of wavelength and beam direction
(v) The reflective surface considered are perfectly specular without any deformation
(vi) The tracking error of the receiver tube is not considered

4.2.5 Validation of MCRT methodology

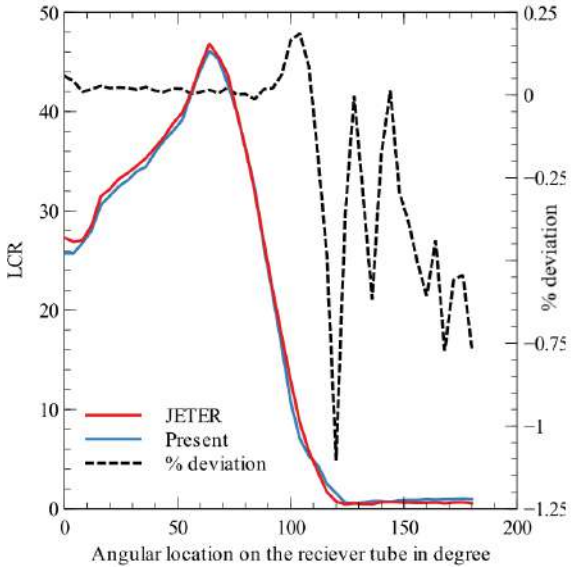

Fig. 4.9: Comparison of LCR profile for a round receiver tube

Due to the lack of measured flux distributions around the demonstrative receiver tubes, the proposed methodology is validated using Jeter's analytical model [105]. The receiver tube chosen in Jeter's study has a geometrical concentration ratio of 20 and a 90^{o} rim angle corresponding to LS2 and LS3. A uniform sun with an angular radius of 7.5 mrad is assumed to be the source with a DNI of 1kW/m^2. The Local Concentration Ratio (LCR) obtained from the ray-tracing analysis is plotted in Fig. 4.9 in relation to the angular location between 0 and 180^{o}. Figure 4.9 clearly shows that a maximum deviation of 1.15% exists beyond the angular location of 120^{o}. However, the deviation is negligible when the flux value is significant. Additionally, the current model overestimates the effect of shading when compared to the Jeter profile.

4.2.6 Computational Fluid Dynamic (CFD) analysis

The effect of heat flux distribution over the receiver and the heat transfer to the HTF has been numerically investigated by CFD analysis. Two 3D steady-state conjugate heat transfer CFD models are performed using the Ansys Fluent 2020 R1: one for the receiver without a secondary reflector and one for the receiver with a secondary reflector in the most desirable position. The following are the general governing equations for the incompressible HTF flow in the receiver tube [106]:

Continuity equation

$$\frac{\partial u_j}{\partial x_i} = 0 \tag{4.8}$$

Momentum equation

$$\rho \frac{\partial (u_i u_j)}{\partial x_i} = \frac{\partial}{\partial x_j}\left[-\rho \delta_{ij} + \mu\left(\frac{\partial u_i}{\partial x_j} + \frac{\partial u_j}{\partial x_i}\right)\right] + \rho g_i \tag{4.9}$$

Energy equation

$$\rho \frac{\partial (u_i C_p T)}{\partial x_i} - \frac{\partial}{\partial x_j}\left(\lambda \frac{\partial T}{\partial x_j}\right) = S_T \tag{4.10}$$

S_T represents the source term. Due to the incompressible nature and the absence of internal heat generation, the source term is considered zero. For the solid domain (the pipe), the first term in the energy equation is not relevant as it contributes to the convection of temperature. At the boundary nodes, the source term is contributed by the boundary heat flux. For modelling the effect of turbulence in HTF, two equation-based realisable k-ε turbulent models with standard wall function are used. This model solves two equations, one for turbulent kinetic energy and another specific dissipation rate for evaluating the Reynolds stress terms. These equations are as follows:

Turbulence kinetic energy (k) equation:

$$\rho \frac{\partial (k u_j)}{\partial x_j} = \frac{\partial}{\partial x_j}\left[\left(\mu + \frac{\mu_t}{\sigma_k}\right)\frac{\partial k}{\partial x_j}\right] + G_k - Y_k + S_k \tag{4.11}$$

Specific dissipation (ε) equation:

$$\rho \frac{\partial (\varepsilon u_j)}{\partial x_j} = \frac{\partial}{\partial x_j}\left(\left(\mu + \frac{\mu_t}{\sigma_\varepsilon}\right)\frac{\partial \varepsilon}{\partial x_j}\right) + G_\varepsilon - Y_\varepsilon + D_\varepsilon + S_\varepsilon \tag{4.12}$$

The governing equations are discretised using the finite volume-based Fluent solver. The 3D geometry representing the PTC receiver's models is discretised for optimum grid sizes in Ansys Fluent meshing. The Second-order Upwind scheme is used to discretise the convection term in all the equations mentioned above, while the least square gradient scheme is used to approximate the gradient terms. The coupled algorithm is used to solve the discrete equations. Water is used as the HTF, and copper is used as the material for

the pipe. The fluid velocity of 0.1 m/s and a temperature of 300 K are used as the inlet boundary condition. Since the analyses are carried out at normal atmospheric pressure, the useful working temperature of the water is selected as 303 to 368K. The outlet is set to be at a zero pressure gradient and the operating pressure selected is the ambient pressure. The actual heat flux distribution obtained through the MCRT analysis is converted to a profile file and applied as the receiver wall's thermal boundary condition for the CFD analysis. The ambient temperature is taken as 300K.

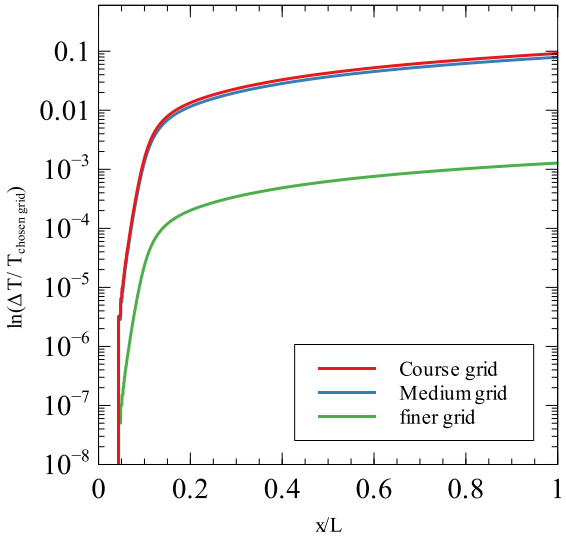

Fig. 4.10: Grid convergence test

Four different grid qualities selected are course grid, medium grid, fine grid and finer grid. For the validation of the model, a uniform heat flux of 33 kW/m^2 is applied and the Nusselts number is calculated from the CFD results using the mean temperature and surface temperature in the axial direction. The value 33 kW/m^2 is considered here based on the concentration ratio of the current PTC (33), and the standard flux intensity, 1kW/m^2, that is usually considered in the analysis of solar collector analyses. The energy losses happening from the solar irradiation to the useful heat gain in the receiver tube is categorized as either optical loss or thermal loss. Two distinct thermal loss modes that occur at the receiver tube are convection and radiation loss. Optical losses are due to the imperfections in the reflector surface and its geometry. It is typically estimated using the intercept factor, which represents the fraction of direct solar radiation that reaches the receiver tube concerning the reflected radiation from the concentrator mirror. The various factors considered for providing the optical loss are given in Table 4.4.

Table 4.4 Optical errors considered in the present study

Sl. No	Parameter (λ_i)	Numerical Value
1	Shadowing factor	0.97
2	Tracking error	0.95
3	Collector mirror imperfection	0.96
4	Mirror cleanliness	0.93
4	Miscellaneous factors	0.95
5	Shading factor	0.96

A user-defined function is developed to include the optical and thermal losses mentioned here. The CFD results have all the sources of losses applicable to the receiver tube without a cover tube. A fine mesh having 350 thousand elements is selected for the study. Figure 4.10 shows the log plot for a fraction of deviation from the chosen grid with grid size tested. It is evident that the deviation of the fine and finer grid is insignificant when compared to the computational cost. In contrast, the deviation is much more significant, while considering medium and coarse meshes. The final mesh after the grid convergence study is shown the Fig. 4.11. With the grid size selected, analysis is performed by varying the inlet velocity with constant heat flux to verify the validity of the model. Three different inlet velocities (0.1 m/s, 0.25 m/s and 0.5 m/s) are used to analyze the model. The velocities are corresponding to transition flow and turbulent flow. The results are then compared with Gnielinski's modification of the Petukhov–Popov formula for the Nusselt number as explained by J.P. Abraham *et al.* [107] and are presented in Table 4.5. The maximum deviation between the numerical analysis and correlation obtained is only 2.174%. The deviation is within an acceptable range.

Table 4.5 Validation of numerical study

u (m/sec)	0.1	0.25	0.5
Re	2646.025	6615.0625	13230.125
$Nu_{claulated}$	15.88	55.1656	105.7268
Nu_{CFD}	15.34	53.976	103.802
% deviation	2.174	2.156	1.823

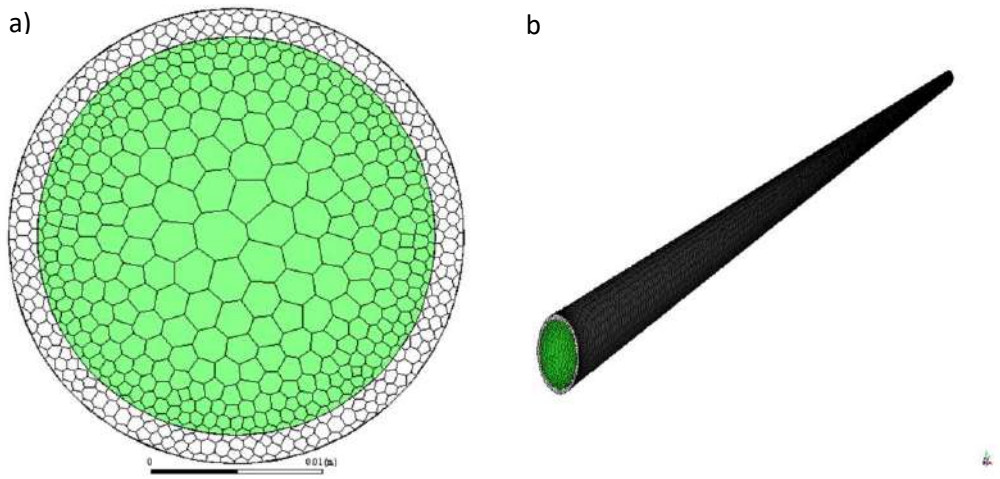

Fig. 4.11: Final mesh obtained after mesh convergence study (a) cross section, (b) lateral view

4.3 Results and Discussion

This section presents and analyses the effects of introducing a secondary reflector in a conventional PTC. As suggested by CCD, the ray-tracing simulations are carried out with different receiver positions and reflector widths. The design is performed by considering the better heat flux distribution against the targeted output power. Finally, the effect of the desirable uniform heat flux distribution is numerically studied by considering the temperature profile of the receiver tube wall and HTF.

4.3.1 Ray tracing and heat flux analysis

The concentrator, receiver and secondary reflector parameters, as illustrated in Table 1 and Table 3, are used in the Tonatiuh simulations. Figure 4.12(a) demonstrates the rays' path reflected by the collector on the receiver tube when the tube is mounted at the focal axis. The bottom half of a conventional PTC's receiver surface receives the concentrated radiations, while the top half is subject to the direct solar beam. It can be seen from Fig. 4.12(b) that most of the lost rays that are not received on the receiver are re-reflected on

the tube with the aid of the secondary reflector when the tube is mounted below the focal axis. The heat flux distribution on the receiver tube's outer surface without and with a secondary reflector is demonstrated in Figs. 4.13(a) and 4.13(b), respectively.

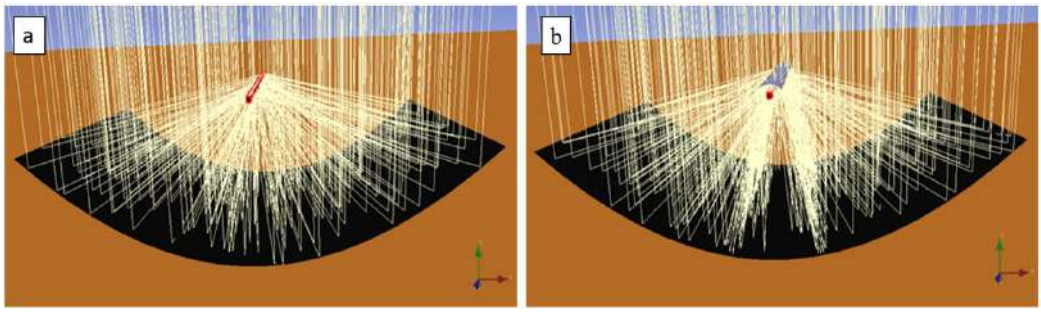

Fig. 4.12: PTC with concentrated radiations (a) without secondary reflector (b) with secondary reflector

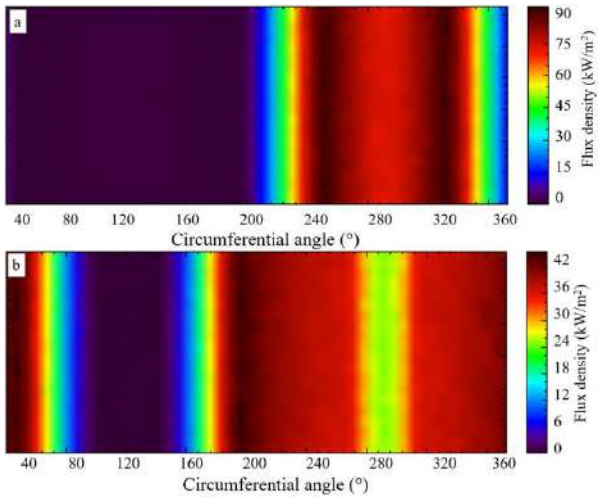

Fig. 4.13: Radiation flux (W/m^2) in receiver's surface (a) without secondary reflector (b) with secondary reflector

It can be observed that the circumferential distribution of radiation flux distribution around the receiver in the PTC without a secondary reflector (Fig. 4.13(a)) is exceptionally non-uniform with a significant gradient. This non-uniformity in heat flux around the tube wall results in the receiver's deflection, loss of vacuum and is one of the leading reasons for PTC failure. On the other hand, the PTC with a secondary reflector can significantly improve the uniformity of heat flux distribution around the receiver with a small gradient, as shown in Fig. 4.13(b). The maximum heat flux of the PTC with and without a secondary reflector is in the range of 42 kW/m^2 and 90 kW/m^2, respectively.

Therefore, it can be concluded that using a secondary reflector will decrease the heat flux non-uniformity and enhance the PTC receiver's lifetime. As per the design matrix generated by CCD, the ray-tracing numerical analyses are performed, and the results are shown in Table 4.6.

4.3.2 Development of model and statistical testing

Mathematical and statistical techniques such as predictive experiments, regression models, and optimization techniques are part of RSM. After the results obtained from MCRT runs, RSM is used to establish an appropriate model through statistical analysis of the experimental data. The objective of RSM is to choose the most desirable receiver tube misalignment from the primary focal axis and the secondary parabolic reflector width based on the system's uniformity of heat flux and power output. Researchers found that RSM has a significant role in the design, development, and formulations of mathematical models as well as in the enhancements of current systems.

Table 4.6 CCD matrix and results for uniformity and total power

Run	Factor 1	Factor 2	Response 1	Response 2	Average
	f'(mm)	W_s (mm)	Uniformity	Total Power (kW)	Heat flux (kW/m^2)
1	14.2	70	0.592628	5.56027	0.7943
2	28.1	41.6625	0.82163	2.33787	0.3339
3	28.1	41.6625	0.81487	2.33918	0.3341
4	42.0	13.325	0.887638	1.60674	0.2295
5	14.2	41.6625	0.572282	5.69872	0.8141
6	28.1	13.325	0.791166	2.51064	0.3586
7	28.1	41.6625	0.822295	2.33832	0.3340
8	28.1	41.6625	0.822464	2.33995	0.3342
9	28.1	41.6625	0.822632	2.33896	0.3341
10	42.0	41.6625	0.949518	1.42862	0.2041
11	42.0	70	1.00475	1.28354	0.1833
12	28.1	70	0.853023	2.19612	0.3137
13	14.2	13.325	0.560564	5.84575	0.8351

The eccentricity of the absorber tube from the focal axis of the primary reflector (f') and width of the secondary reflector (W_s) are the key parameters of the PTC system that determine the heat flux distribution and power output. The response surface analysis, including four factorial points, four axial points, and five replicates at the central points, as shown in Table 4.6 and is applied using central composite design to develop an empirical relationship for predicting heat flux distribution and power output.

The RSM can establish mathematical models for the input variables and the responses through the statistical analysis of numerical results. The stability of the model is tested by using ANOVA. Using the quadratic polynomial model, the final mathematical model for uniformity and total power for the PTC-secondary reflector system obtained is as follows:

$$Uniformity = 0.211873 + 0.028670f' - 0.000186W_s + 0.000027f'W_s - 0.000312f'^2 + 2.86362E - 07W_s^2 \quad (4.13)$$

$$Totalpower = 11.80149 - 0.503154f' - 0.001310W_s - 0.000123f'W_s + 0.006254f'^2 - 4.56763E - 06W_s^2 + 1.57091E - 06f'^2W_s + 5.09967E - 07f'W_s^2 - 6.63711E - 09f'^2W_s^2 \quad (4.14)$$

In this study, ANOVA has also been used to investigate the significance and adequacy of empirical models generated by RSM. The results are illustrated in Tables 4.7 and 4.8. The results of the analysis show that factors such as A, B, A^2, and the interaction factor A * B have significant effects on the response surface model of uniformity, where A and B represent f' and W_s, respectively. The important factors for the total power, as shown in Table 4.8, includes A, B, A^2, B^2, A*B, A^2*B, A*B^2, and A^2*B^2. The F-value of 2707.44 and p-values of less than 0.001 from the uniformity model indicate the significant model terms. The lack of fit of 2.3 implies that the lack of fit is not substantial, and a non-significant lack of fit is good.

The large model F-value of 6.271E+06 for total power response indicates that the model is significant. The associate p-values, which are less than 0.05, indicate that the model terms are statistically significant. ANOVA analysis shows that a second-order

model fit the analysis results for uniformity and total power. Hence, the mathematical equations developed can predict the uniformity of heat flux and power output of the considered PTC.

Table 4.7 ANOVA for uniformity

Source	Sum of Squares	df	Mean Square	F-value	p-value	
Model	0.2286	5	0.0457	2708.44	< 0.0001	significant
A-f'	0.2077	1	0.2077	12307.80	< 0.0001	
B-Ws	0.0074	1	0.0074	439.76	< 0.0001	
AB	0.0018	1	0.0018	107.14	< 0.0001	
A^2	0.0100	1	0.0100	594.49	< 0.0001	
B^2	2.337E-06	1	2.337E-06	0.1384	0.7208	
Residual	0.0001	7	0.0000			
Lack of Fit	0.0001	3	0.0000	2.23	0.2271	not significant
Pure Error	0.0000	4	0.0000			
Cor Total	0.2287	12				

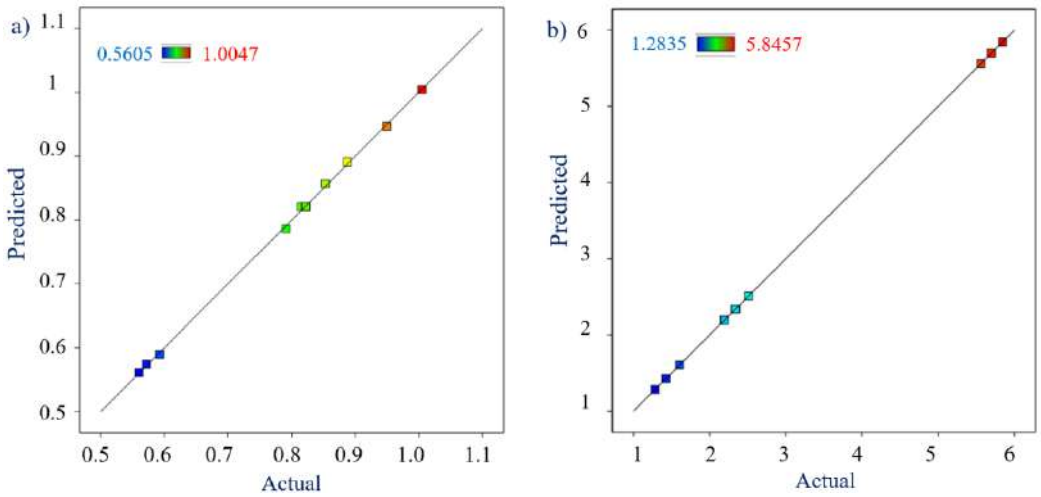

Fig. 4.14: Experimental results and predicted values (a) uniformity (b) total power

Figures 4.14(a) and (b) illustrate the comparison of predicted results of uniformity and total power developed by the RSM with the Tonatiuh results. It is observed that there

is an acceptable quantitative and qualitative conformity between predicted and Tonatiuh results.

Table 4.8 ANOVA for total power

Source	Sum of Squares	df	Mean Square	F-value	p-value	
Model	32.26	8	4.03	6.271E+06	< 0.0001	significant
A-f'	9.12	1	9.12	1.418E+07	< 0.0001	
B-Ws	0.0495	1	0.0495	76919.30	< 0.0001	
AB	0.0004	1	0.0004	553.16	< 0.0001	
A^2	2.14	1	2.14	3.333E+06	< 0.0001	
B^2	0.0003	1	0.0003	468.64	< 0.0001	
A^2B	0.0000	1	0.0000	53.72	0.0018	
AB^2	0.0000	1	0.0000	77.54	0.0009	
A^2B^2	0.0000	1	0.0000	18.20	0.0130	
Pure Error	2.572E-06	4	6.430E-07			
Cor Total	32.26	12				

4.3.3 Validation of the model

A confirmation ray-tracing analysis is also conducted for the parameters of *f'* = 29 mm and *Ws* = 83 mm. The predicted and numerical results are compared and given in Table 4.9. It has been found that the percentage of error for uniformity is -0.257 and 1.91 for total power. Hence, the developed models can accurately predict the uniformity and power output of the PTC within the range of investigation.

Table 4.9 Confirmation between experimental and predicted results

Response	Experiment result	Predicted result	% error
Uniformity	0.83461	0.83247	-0.257
Total power (kW)	2.2488	2.2066	1.91

4.3.4 Parametric Effects

The individual effects of the receiver tube position (f') and width of the secondary reflector (W_s) on the uniformity of heat flux distribution over the receiver tube is illustrated in Fig. 4.15. Uniformity close to zero implies a uniform heat flux distribution around the receiver tube. As shown in Fig. 4.15(a), the receiver tube's location to the primary reflector's focal axis has more influence on the uniformity of heat flux distribution than the secondary reflector width (see Fig. 4.15(b)). Due to the receiver tube's significant misalignment, the majority of reflected rays cannot reach the receiver. For the minor deviations of receiver tube locations, the secondary reflector can lead to a more uniform heat flux distribution over the receiver tube's entire periphery. It can be observed from Fig. 4.15(a) that the uniformity of heat flux distribution has improved up to 0.58, while it is 1.0836 for the PTC without secondary reflector. Thus, the achievable improvement factor on heat flux distribution is 1.868.

The combined influence of the receiver tube position (f') and configuration of the secondary reflector (W_s) on the uniformity of distribution of heat flux over the receiver tube is demonstrated using the three-dimensional and contour response surfaces as shown in Figs. 4.16(a) and (b), respectively. It can be seen that the heat flux distribution becomes non-homogenised when the receiver tube location from the focal axis increases with the increase in width of the secondary collector.

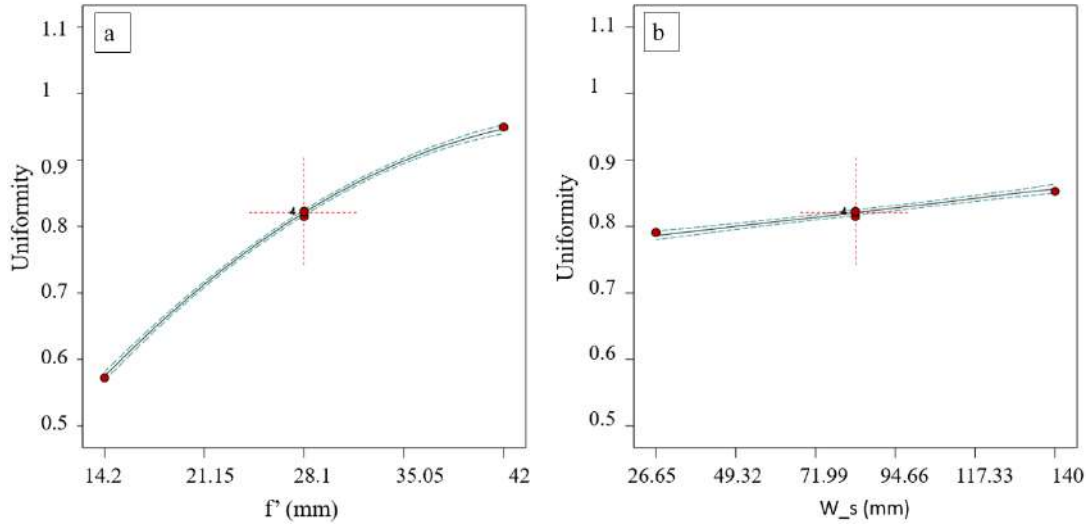

Fig. 4.15: Uniformity of heat flux distribution with (a) receiver tube position (b) width of the secondary reflector

Among the thirteen ray-tracing analyses conducted, the heat flux distribution of three configurations is depicted in Fig. 4.17. As shown in Fig. 4.17, the heat flux distribution over the receiver tube periphery follows the same trend as illustrated in Fig. 4.16. The gradient of a PTC without a secondary reflector is 90 kW/m^2 (see Fig. 4.13(a)). The gradient is reduced to 42 kW/m^2 with improved heat flux distribution, as seen in Fig. 4.17(a). Thus, the gradient of heat flux over the circumference of the receiver is enhanced, and the gradient is reduced by 73.33 %. Gong *et al.* [108] used an adaptive method to design a parabolic trough solar concentrator with a secondary reflector. The improvement factor of heat flux distribution achieved by this design is around two, but it is 1.868 in the present study, which is comparable. Reda and Abdelylah [103] investigated the solar flux distribution of a parabolic trough solar collector with a secondary reflector numerically. They observed a 70.37% reduction in the gradient of heat flux over the circumferential angle, while the current study showed a 73.33% reduction in the heat flux gradient.

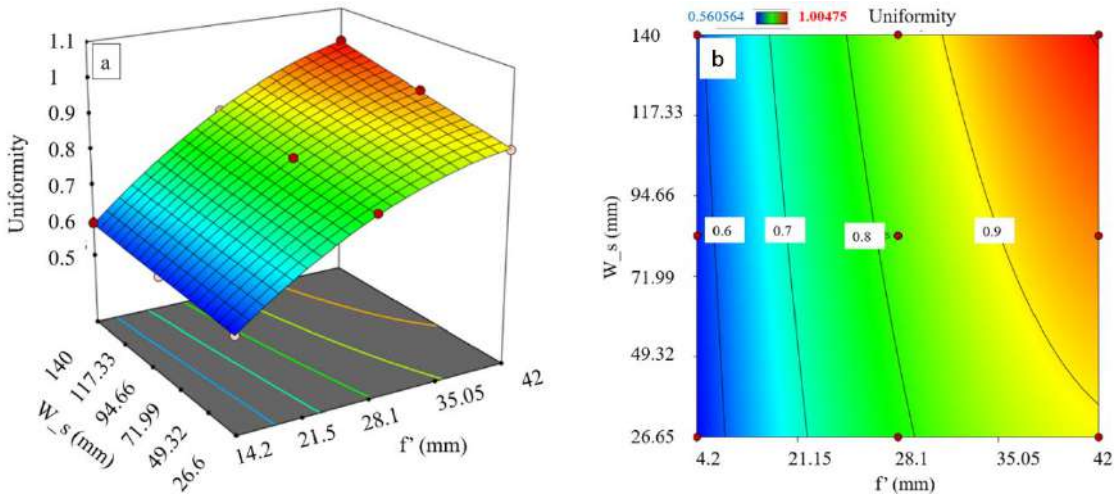

Fig. 4.16: Interaction effect of receiver position and secondary reflector configuration on heat flux uniformity (a) response surface plot and (b) contour plot

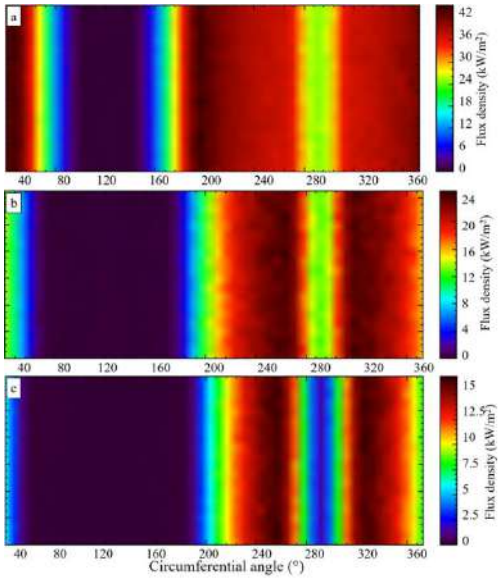

Fig. 4.17: Distribution of heat flux when (a) f'=14.2 mm and W_s=13.225mm (b) f'=28.1 mm and W_s=41.6625 mm (c) f'=42.0 mm and W_s=70.0 mm

The individual effects of the receiver tube position (f') and configuration of the secondary reflector (W_s) on the power output are illustrated in Figs. 4.18(a) and (b). Figures 4.19(a) and (b) show the response surface and contour plots for the combined effect of parameters. The minimum reflector size and deviation of the receiver from the focal axis increase the system's power output. A non-uniform illumination due to the significant deviation of the receiver tube position and the shading effect of a large secondary reflector on the primary reflector significantly reduces the PTC system's output power.

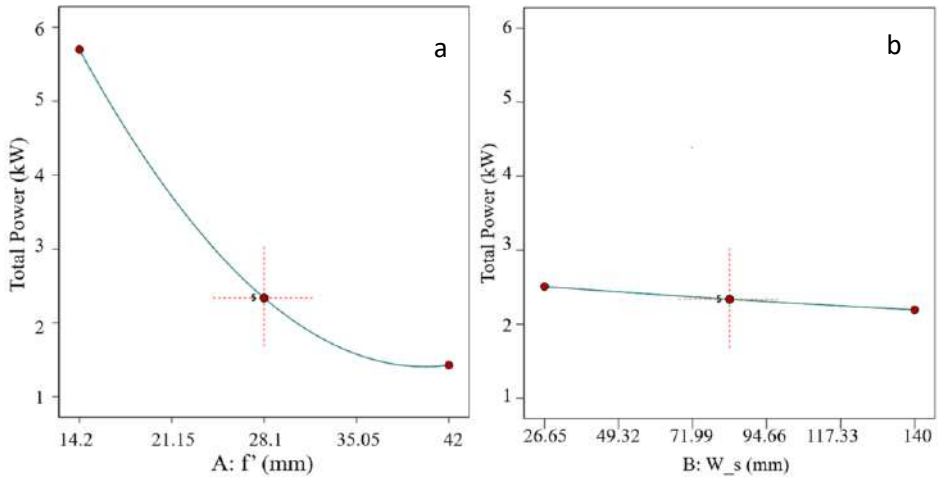

Fig. 4.18: Effect of power output with (a) receiver tube position and (b) width of secondary collector

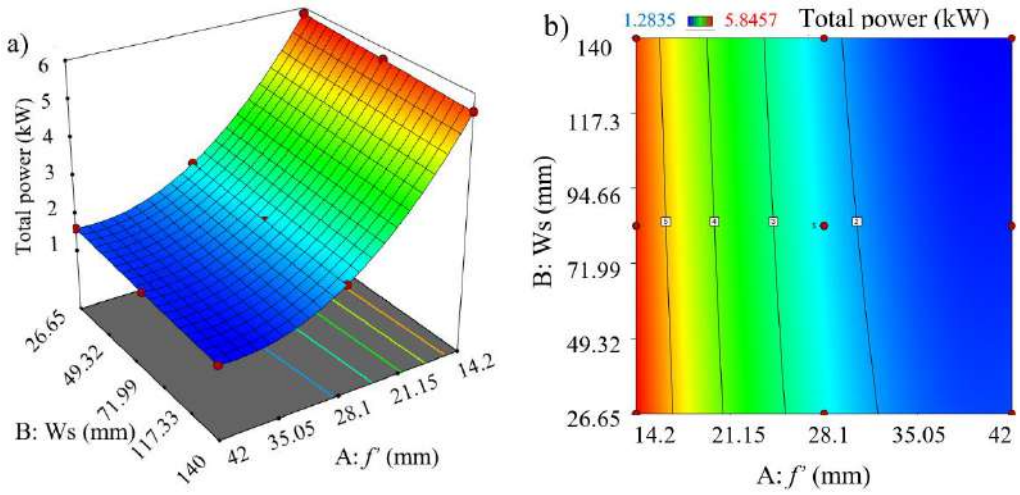

Fig. 4.19: Interaction effect of receiver position and secondary reflector configuration on power output (a) response surface plot and (b) contour plot

4.3.5 Response optimisation

A desirability function analysis is performed to identify the most desired parameters that improve the uniformity in flux distribution. The desirability analysis is found better to produce good outputs in deciding the optimal input conditions. The uniformity value nearer to zero represents the better uniform distribution of the flux around the receiver tube. Placing a secondary reflector above the tube will shadow a portion of the radiation from the primary reflector. This will leads to a reduction in total power received at the reflector. Eventually, a trade-off is required to choose the desired parameters with better uniformity and less power loss. This necessitates the objective function (desirability function) with maximising the total power and to minimise the non-uniformity. The set of parameters corresponding to the maximum value of the overall desirability function, subjected to 95% of total output power, is identified and selected as the desirable PTC configurations.

To minimise the heat flux gradient without much effect on the total power, a desirability functional analysis is performed as mentioned above. The optimal level of absorber tube position and the secondary reflector width have been identified. The large flux gradient on the outer tube periphery is the major reason for PTC failures [95]. The optimal level could reduce the circumferential temperature difference on the receiver,

thereby improving the reliability and life cycle of the PTC.

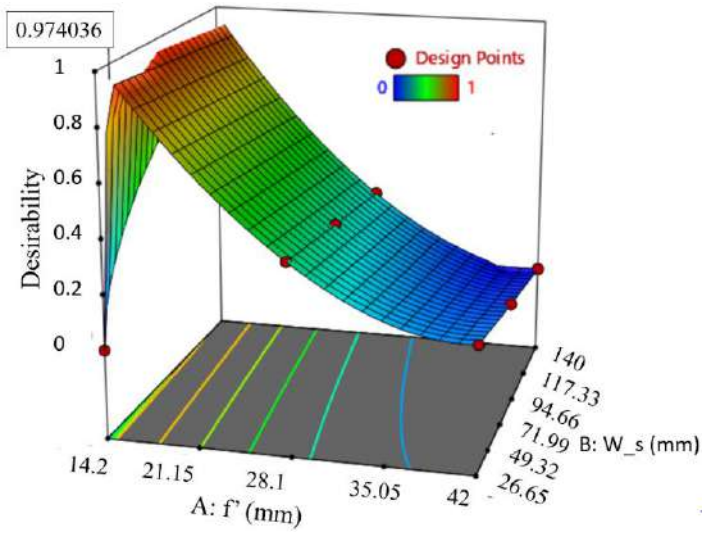

Fig. 4. 20: Response surface plot showing the desirable parameter values

Table 4.10 shows the constraints for desirability for receiver tube position and secondary reflector width. The results of RSM desirability are *f'* = 15.278 mm and *W_s* = 26.850 mm and have optimal desirability of 0.974, as depicted in Figs. 4.20 and 4.21. The desirability value closer to unity is considered to be the most desirable.

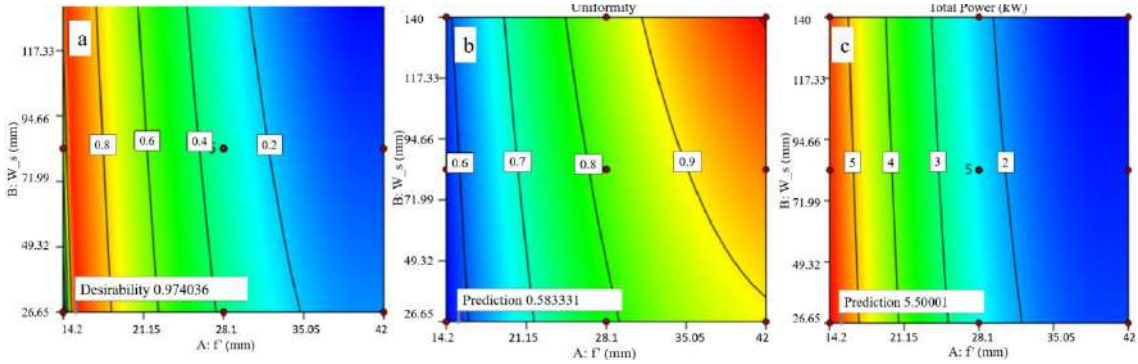

Fig. 4.21: Contour plots for desirability predictions (a) desirability (b) uniformity (c) total power

Table 4.10 Objectives and constraints for the desirability of parameters and responses

Factor and Response	Goal	Lower limit	Upper limit
Receiver location, f’	In range	14.2	42
Width of sec. reflector, W_s	In range	26.65	140
Uniformity	Minimize	0.560564	1.00475
Power output	Target » 5.5 kW	1.28354	5.84575

4.3.6 CFD simulation

A comparative analysis of the thermo-hydraulics of HTF is performed for the receiver in the most desirable location to the receiver tube without the secondary reflector. Figures 4. 22(a) and (b) depict the heat flux distribution at the receiver tube’s surface without and with the secondary reflector, respectively, as obtained from MCRT analysis. This flux distribution is converted to a profile file and applied as the CFD analysis’s thermal boundary condition

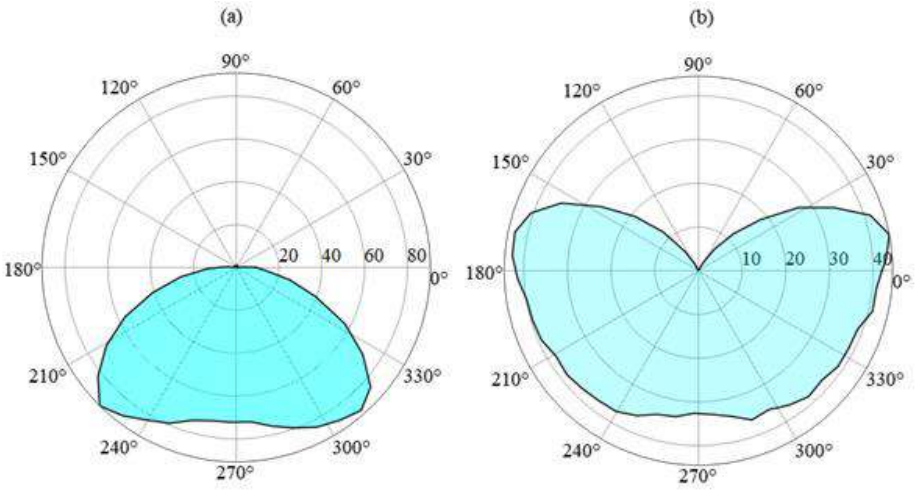

Fig. 4.22: Heat flux distribution (kW/m^2) on the receiver tube’s surface, (a) without secondary reflector (b) with secondary reflector, at the outlet of the tube

From Fig. 4. 22(a), it is observed that the heat flux distribution on the receiver’s bottom side is high, and in the upper half, it is null. This is due to most of the radiation reflected directly onto the bottom periphery of the receiver without re-reflection, which

leads to the chances of the formation of local hot spots, thermal stresses and hence deformation of the tube. Figure 4. 22(b) shows the heat flux distribution on the receiver tube with a secondary reflector. The flux gradient reduces and becomes significantly uniform. This enhanced heat flux distribution results from re-reflected radiations from the secondary reflector. It is also noted that the polar axis maximum value of the receiver with the secondary reflector is 50 kW/m^2. In contrast, it is 100 kW/m^2 for the receiver without the secondary reflector, as depicted in Fig. 4. 22. This implies that using additional reflectors can significantly reduce the peak flux intensity, which avoids PTC failures due to the uneven heat flux distribution. Thus, the non-uniform heat flux distribution can be kept at lower levels to ensure the longer service life of the receiver tube with a negligible reduction in fluid temperature.

The temperature distribution on the surface of the receiver with a secondary reflector, as shown in Fig. 4.24, is considerably more uniform than that of a receiver without a secondary reflector (Fig. 4.23). A significant reduction in the peak temperature of the wall can be seen from the study. This also signifies the reduction of heat loss from the receiver tube as the radiation loss is of the fourth power of temperature.

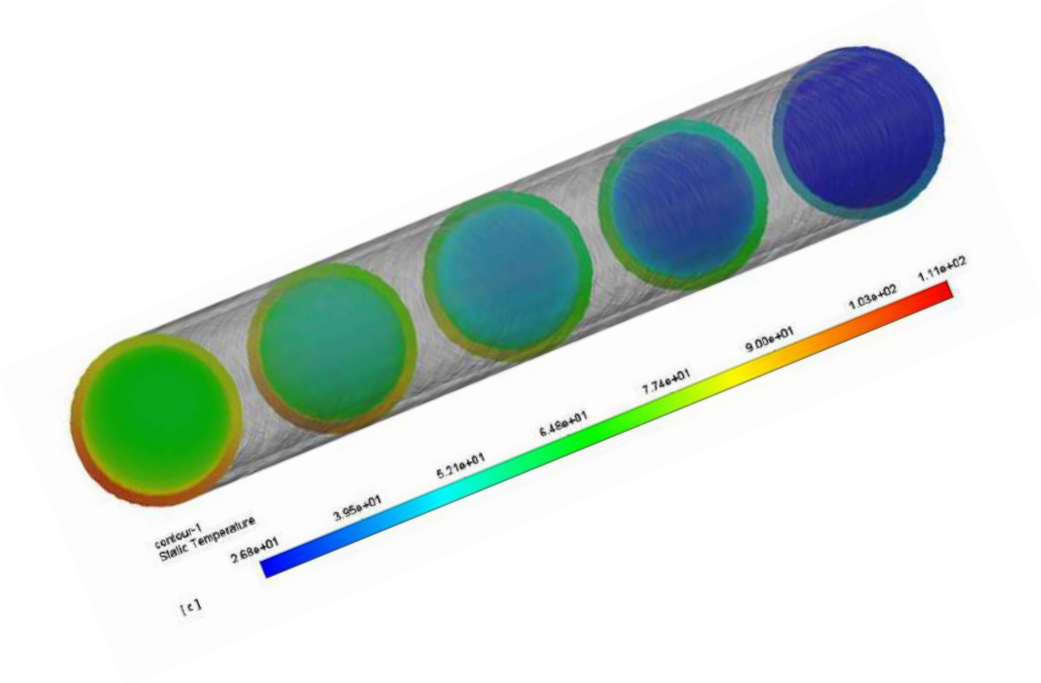

Fig. 4.23: Temperature contour at different cross sections of the receiver tube without secondary reflector for 3 lpm

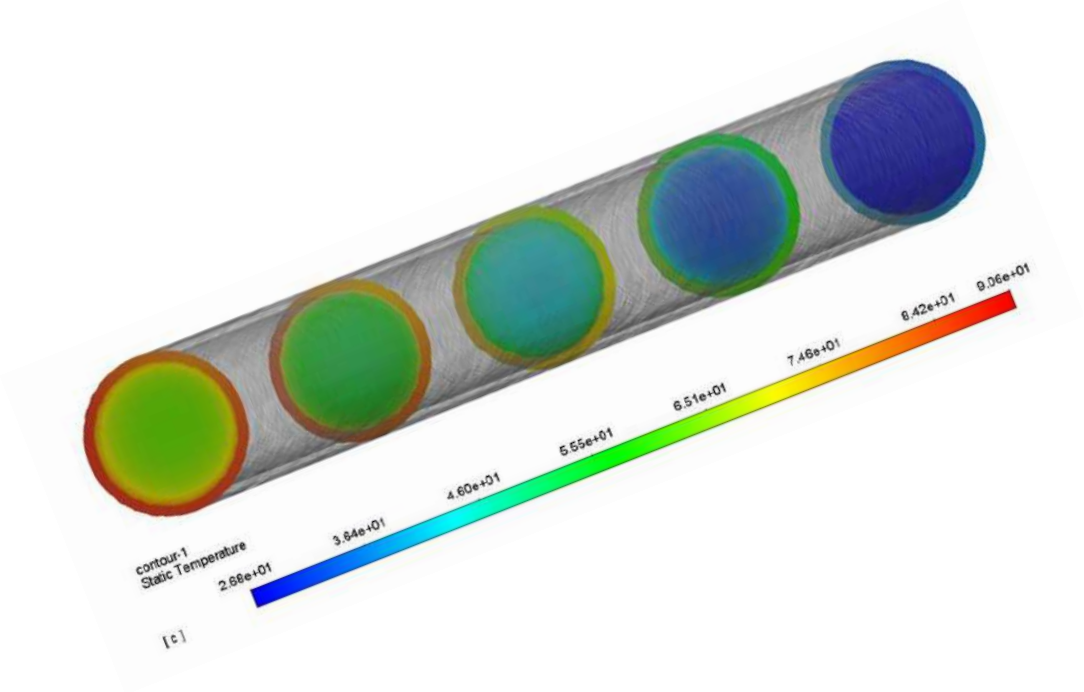

Fig. 4.24: Temperature contour at different cross sections of the receiver tube with secondary reflector for 3 lpm

The simulation results indicate that for the flow rate of 3 lpm, the peak temperature obtained at the surface of the receiver with a secondary reflector is 90.6°C, and that of the receiver without the secondary reflector is 111°C. The corresponding bulk mean temperatures of the fluid at the outlet are 65.8°C and 68.8°C, respectively. Even though the maximum wall temperature of the receiver tube with the secondary reflector is around 20°C less than that of the receiver placed on the actual focal axis without a reflector, the difference in bulk mean temperature is only 3°C. The same trend of improving the circumferential distribution of heat flux accompanied by a slight fluid temperature reduction was reported in the literature [95]. Due to non-uniform heat flux encountered in traditional PTC receiver tubes, thermal distortion is expected, which results in significant radiation loss. This radiation loss may further drop the outlet temperature of the convectional receiver down below that of the receiver tube's HTF when a secondary reflector is used. Additionally, receiver deflection is a significant cause of PTC failures and affects the reliability and lifetime of the PTCs [95]. As a result, the design and application of a secondary reflector can be seen as a necessary choice.

A new step-by-step design procedure of a parabolic trough solar thermal collector

system for medium temperature applications is investigated in this chapter. The design suggests the most desirable receiver tube location and the size and location of the secondary reflector for the targeted output power with the optimum heat flux distribution. By homogenising the flux distribution, secondary reflector PTC systems can be configured to meet the required output power as well as the system's prolonged service life. In addition, the current research has developed mathematical correlations for uniformity of flux distribution and output power in terms of distance of receiver centre from the focal axis (f') and width of the secondary reflector (Ws). These correlations are independent of the primary concentrator and only depend on the receiver tube's position. Hence these are applicable to any PTCs. The studies of PTC with a secondary reflector described above are extremely useful in creating actual systems and providing a better knowledge of the design of optimum PTC.

4.4 Summary

The main focus of this chapter is the design of a PTC with uniform heat flux distribution over the receiver tube. This chapter proposed a new systematic procedure for designing a PTC with a secondary reflector, which cannot be found elsewhere, together with the CFD analysis of the PTC receiver tube with the obtained heat flux profile as the boundary condition to alleviate problems caused by unequal heat flux distribution. Using the methodology proposed by the present study, one can easily design and evaluate the performance of PTCs using the absorber tube material of their choice. The design suggests the most desirable receiver tube location and the size and location of the secondary reflector for the targeted output power with the optimum heat flux distribution. A uniformity value of 0.58 is attained with the secondary reflector in its most desired placement. It is 46.47% less than for the receiver without a secondary reflector. The heat flux distribution is enhanced by a factor of 1.868. By homogenising the flux distribution, secondary reflector PTC systems can be configured to meet the required output power as well as the system's prolonged service life. In addition, the current research has developed mathematical correlations for uniformity of flux distribution and output power in terms of distance of receiver centre from the focal axis (f') and width of the secondary reflector (Ws). These correlations are independent of the primary concentrator and only depend on the receiver tube's position. Hence these are applicable to any PTCs. The studies of PTC

with a secondary reflector described above are extremely useful in creating actual systems and providing a better knowledge of the design of an efficient PTC. The construction of the PTC with the secondary reflector is described in Chapter 5 in detail.

Chapter 5

Structural Analysis and Construction of the PTC With Secondary Reflector

The design of a PTC with a secondary reflector with enhanced heat flux distribution are detailed in the previous chapter. This chapter describes the method used to construct the designed PTC. The numerical study on the effects of wind load on the parabolic concentrator and its support structure are also presented.

5.1 Materials and Methodology

The designed PTC has a length of 2.5m, an aperture width of 2.8 m, and 1.0 m in focal distance is considered for the study. The PTC concentrator comprises of a 2mm thick mirror-polished stainless steel sheet. As per the design of PTC for enhanced heat flux distribution, the receiver tube position is obtained as 15.278 mm below the focal axis of the main concentrator, and the additional reflector of 2.5 m in length, 26.85 mm in width, and 35° rim angle. The secondary reflector is mounted above 21 mm from the centre of the receiver tube.

The support structure is constructed with simple materials readily available in the commercial market. However, before construction, the rigidity of the design is ensured by structural analysis of the support structure against gravity and extreme wind load

conditions. Figures 5.1 and Table 5.1 illustrate the detailed information of the support frame. Three mild steel parabolic trusses are placed at an equal distance of 1.19 m, and these trusses are connected by using 5 GI pipes to achieve stability and strength. The structural framework of the PTC is constructed using steel rods and a central steel torque tube. A geometric model of the concentrator and its support structure is created using Solidworks.

Table 5.1 Bill of materials

Part number	Part name	Material	Dimensions
1	Concentrator	Stainless steel	2 mm thickness
2	Longitudinal beams	Cylindrical pipe	Φ31.75mm, 3mm gauge
3	Truss elements	Square rod	20 x 20 mm
4	Torque tube	Square pipe	75 x 75 mm, 4.31 mm gauge

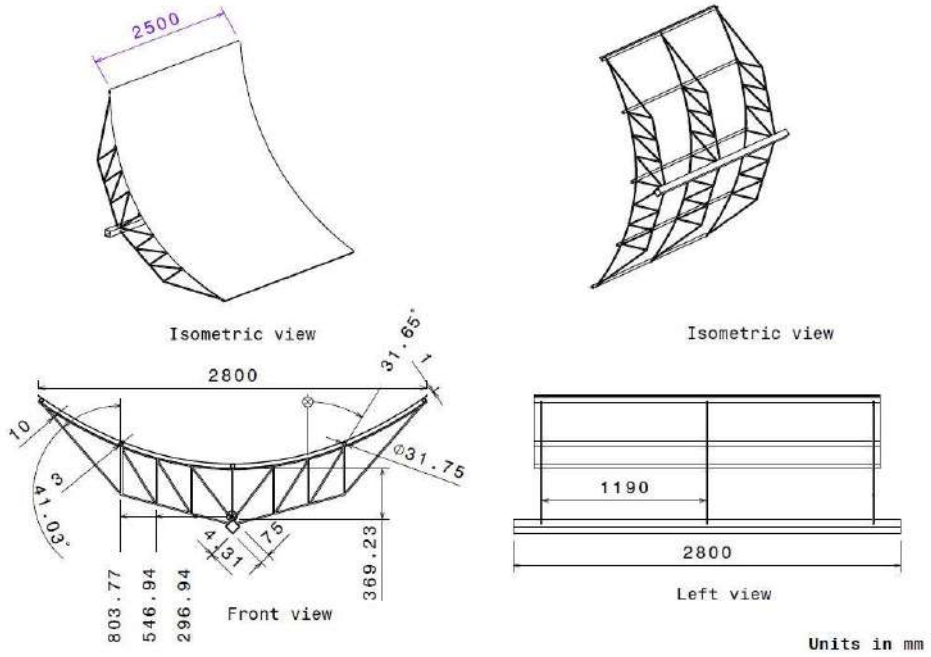

Fig. 5.1: Support structure of the PTC

5.2 Wind load

Since PTCs are erected outdoors, gravity loads and external forces, particularly wind loads, can cause considerable stresses and deflection on the members and corresponding distortion of the parabola, resulting in optical losses as well as structural failures. Therefore, the support structure has been subjected to a mechanical study, which is essential to evaluate the structural failures of the elements. The basic equation as given by Eq. (5.1) for the impact of wind speed could be used to compute the force exerted by wind (F_w) on the trough structure [109].

$$F_w = \frac{1}{2}\rho_a C_d A_a V_w^2 \tag{5.1}$$

where ρ_a is the density of air taken as 1.2 kg/m^3, C_d the drag coefficient, A_a the aperture area of the concentrator (7 m^2), and V_w the velocity of the wind in m/s. The drag coefficient C_d is determined by the CFD analysis corresponding to 38 m/s based on the predicted extreme wind loads in Kerala [110]. According to Eq. (5.1), the only variable that can be considerably modified is the drag coefficient because the density of air and the aperture area of the concentrator are constants, and the wind velocity does not fluctuate much under normal conditions.

5.3 Determination of Drag coefficient

The calculation of the drag coefficient in the flow is significant for estimating the wind-induced forces on the PTC structure, as shown in Eq. (5.1). A steady-state analysis is performed to investigate the flow pattern and the drag coefficient. The CFD analysis is performed in Ansys Fluent 2020 R1. The upstream wind velocity is considered using the empirical power law for the vertical extrapolation of the wind velocity, as given in Eq. (5.2) [111].

$$V_z = V_r * \left(\frac{Z}{Z_r}\right)^{\alpha} \tag{5.2}$$

where V is the wind velocity, Z the height, subscript $r = 10m$ represents the reference level, and α the Hellmann exponent, that can be chosen based on the terrain [16]. It can have value ranging from 0.05 to 0.6 signifies, rough to flat bottom terrain. For normal ground level, an α value of 0.14 is preferred. Fig. 5.2 depicts the wind shear corresponding to different Hellmann exponent values.

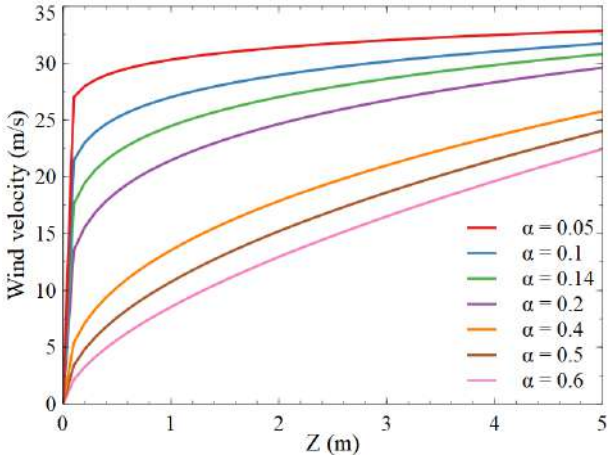

Fig. 5.2: Wind shear corresponding to different α values

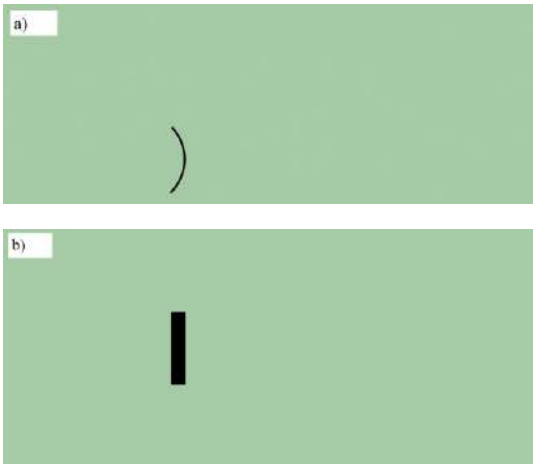

Fig 5.3: Computational domain (a) front view (b) top view

To eliminate the artificial acceleration of the flow in the region of interest, the size of the computational domain is made sufficiently larger than that of the parabolic concentrator as per the European cooperation in science and technology guidelines [112]. The computational domain around the parabolic collector has 25 m in length, 9 m in width and 6 m in height, where the collector is placed exactly at a distance of 8 m from the upstream side. The front and top views of the domain along the flow direction are shown

in Figs. 5.3 (a) and (b), respectively. The collector's highest drag coefficient is measured when subjected to the normal incident wind (at an incidence angle of 90°) [113]. Hence, the collector orientation is -90° upstream to the flow (opening of the collector facing normal to the wind flow).

The discretisation of the computational domain is crucial in fluid dynamics analysis. Poly mesh has been recommended for stability and to reduce the number of iterations necessary to get the converged solution [114]. In this study, poly hex-core mesh is considered for discretising the domain. Poly hex-core is a hybrid meshing scheme consisting of poly mesh at the boundary and hexagonal mesh at the interior. The mesh size at the reflector surface is taken as 20 mm. The mesh at the collector surface is shown in Fig. 5.4. Since boundary layer separation significantly affects drag, boundary elements with five layers with a maximum layer thickness of 1mm are considered to resolve the boundary layer adequately. This ensures the Y^+ value at the mesh is one.

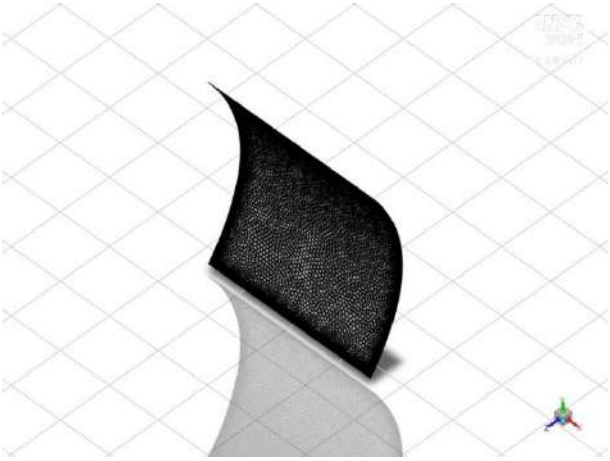

Fig. 5.4: Mesh at the collector surface

Mesh concentration around the collector is employed to facilitate the boundary-layer type of flow structure applicable to wind engineering. As illustrated in the mesh in the central plain (Fig. 5.5), the domain has a different number of grids and sizes. The mesh elements are accurately extended in the required directions to provide sufficient computational elements for numerical solutions. In order to check the quality and consistency, different meshes are created and tested. The final mesh of the discretised domain is shown in Fig. 5.6. With this, the total element count is 4.5 million.

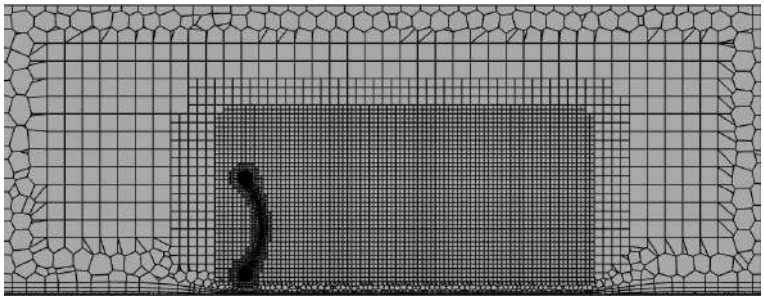

Fig. 5.5: Mesh at the central plane

The solver is set up to be pressure-based, and the analysis has been done in a steady state. A velocity boundary condition is assumed at the inlet, while a wall is assumed at the bottom face. All other four faces of the enclosure are imagined as outlet boundaries with zero gauge pressure. For the inflow conditions, an open terrain type atmospheric wind is used. The wind power law (Eq. (5.2)), illustrated in Fig. 5.7, can be used to define the velocity profile. The 3D steady RANS (Reynolds-averaged Navier-Stokes) equations are solved with the Shear-Stress Transport (SST) k-ω model [115]. The k-ω SST model is used here since it has been shown to be more accurate and dependable than the standard k-ω model for a wide range of flow regimes. The k-ω SST model is a hybrid technique for modelling turbulent flow that can resolve wall-bounded flows. A coupled solver is considered to solve the pressure velocity coupling. A second upwind scheme is considered to discretise the turbulent transport and momentum equations. More information on the governing equations and solution methodology is accessible in [115].

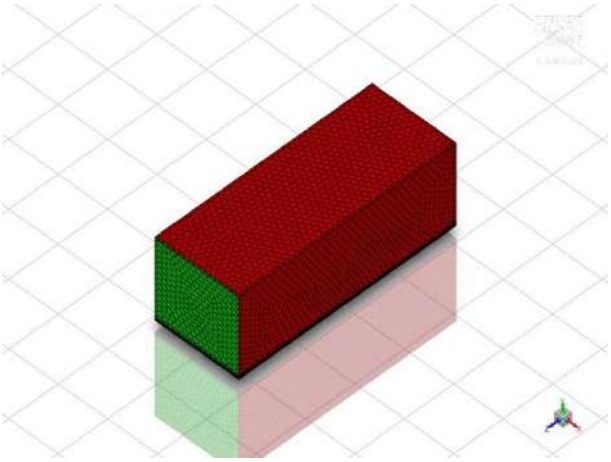

Fig. 5.6: Discretised computational domain of the wind flow

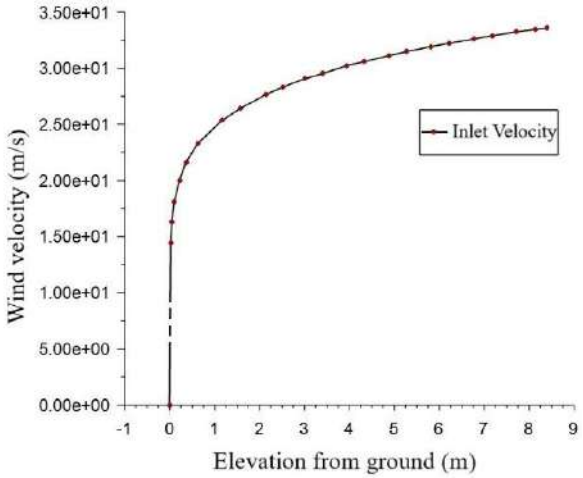

Fig. 5.7: Inlet velocity based on wind power law

5.3.1 Pressure and velocity field around the collector

The velocity of air around the parabolic collector is shown in Fig. 5.8. The velocity vector plot in Fig. 5.9 reveals two recirculation zones (vortex) on the collector's leeward side. This is most likely to occur over a blocked barrier or when the flow make a sudden curve. The presence of recirculation zones implies the pressure drag, which must be considered while designing an aerodynamically thin component like parabolic solar concentrators.

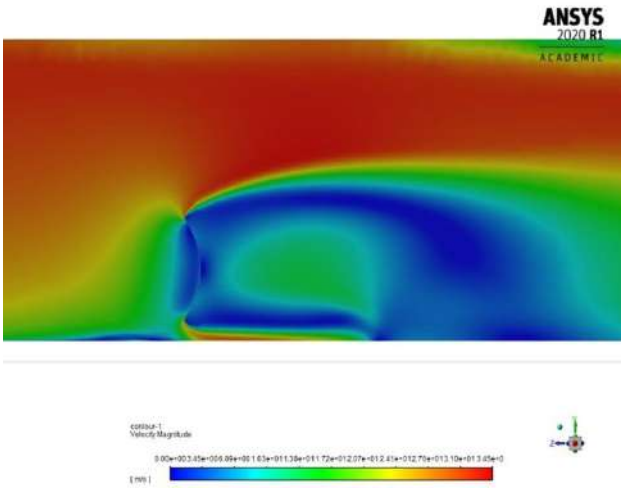

Fig. 5.8: Variation of velocity around the collector

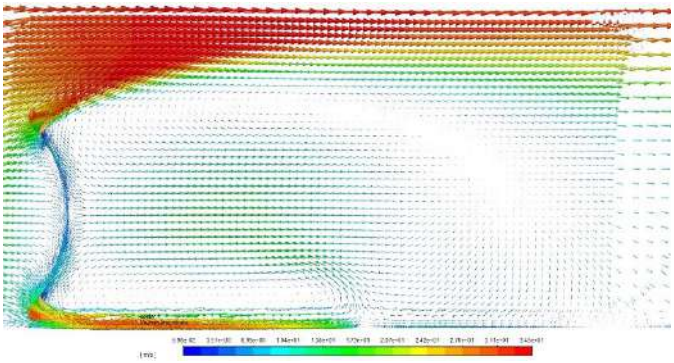

Fig. 5.9: Velocity vector around the collector

Figure 5.10 shows the variation of pressure field over the PTC concentrator, and Fig. 5.111 shows the variation of pressure coefficient contour on the windward and leeward sides of the PTC concentrator. As shown in Fig. 5.10, the pressure in front of the collector is much higher than the behind because of the velocity difference as depicted in Fig. 5.9. The pressure field is highest at the opening aperture of the concentrator. The highest pressure is determined as 5.37 x 10^2 Pa at the opening of the parabola aperture. The maximum positive pressure coefficient in the flow is 1.88 on the windward side. While the maximum negative pressure coefficient has been found as 0.0905 on the leeward side. This unequal pressure distribution causes the drag force on the collector. Here the effect of viscous force is negligible as the fluid in interaction is air.

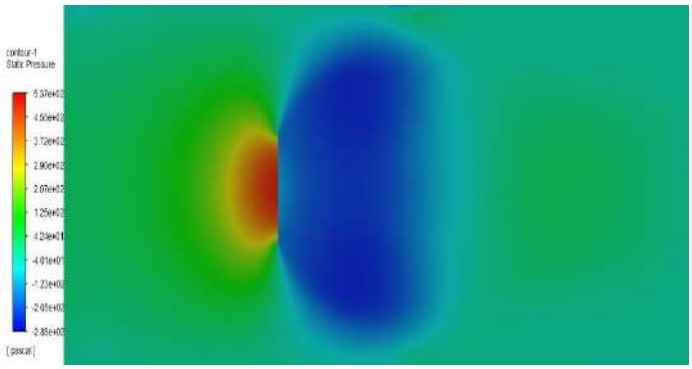

Fig. 5.10: Contours of static pressure (top view)

The drag coefficient is evaluated as the ratio of the total force acting in the direction of the wind to the force available in the wind, $\frac{1}{2}\rho A_c V^2$. Here A_c is the aperture area, and the velocity is calculated as the area-weighted average velocity of the free stream. Using this, the coefficient of drag for the PTC is obtained as 1.9795. Moreover, the drag

coefficient of parabola profiles reported by Jaramillo *et al.* (2013) [109] and Paetzold *et al.* (2014) [116] lie between 1.6 to 2.3, which closely matches the result of the current study.

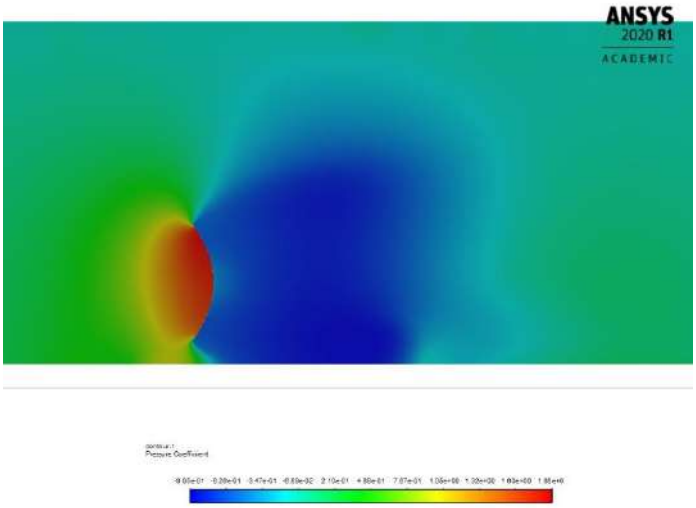

Fig. 5.11: Pressure coefficient contour around the PTC collector

5.4 Structural stability analysis of the PTC

The mechanical stability and optical accuracy of PTCs are connected to the structural stiffness and the applied stress level. From a structural standpoint, it should be noted that the parabolic-trough concentrator is primarily made of three systems: the focussing, the torque tube, and the support truss. The main focus of the current investigation is the design of a PTC with a secondary reflector for better heat flux distribution and the development of a nanoparticle-based HTF for its application. When designing the support structure of the system, mechanical functionality, safety, and optical performance are the prime requirements. Hence, the present study aims to verify the structural stability of the PTC support structure under extreme wind load conditions.

5.4.1 Wind load calculation

The design loads can be subdivided into permanent and variable loads. The self-weight of the elements due to the gravity force is the only permanent load and can be determined from the density of the components. The main variable load of a PTC is the effect of wind load on the structure, which can be applied as a pressure distribution on

the concentrator surface. Wind load effects on the PTC are connected with the parabolic trough's aerodynamics in their different solar tracking positions.

Static structural analysis of PTC trough and support structure is done using ANSYS workbench package to verify the mechanical stiffness of the PTC. In this analysis, the wind velocity (V_w)is chosen as 38 m/s based on the design wind velocity and extreme cyclonic conditions of Kerala [110]. Eq. (5.1) could be used to compute the wind force induced on the PTC, as given below. The corresponding pressure (load) distributed on the structure can be calculated as follows;

$$P_w = \frac{F_w}{A_a} = \frac{1}{2}\rho_a C_d V_w^2 \tag{5.3}$$

$$P_w = \frac{1}{2} * 1.25 * 1.9795 * (38)^2$$

$$P_w = 1786.48\ Pa$$

5.4.2 Modelling of the PTC support structure

Initially, the PTC support structure modelling is done using SolidWorks modelling software and imported into the Ansys workbench. Since the thickness of the parabolic trough is only 2 mm, the shell element, SHELL281, is used for meshing the trough. SHELL281 is a kind of 8-noded isoparametric element capable of considering bending and twisting simultaneously. The remaining structure is modelled using 20 noded isoparamtric 3D brick elements compatible with the SHELL281 elements.

5.4.3 Boundary conditions

The PTC structure is subjected to wind load. The self-weight of the entire structure is considered based on the standard earth gravity. The present structural performance analysis of the PTC structure considers real material properties, i.e. properties of stainless steel and mild steel for reflector and trusses, respectively. The two ends of the torque tube are fixed as the essential boundary condition, which leads to the simple condition of zero displacements at the ends of the tube. The static structural analysis is carried out with combined gravity and wind loads, acting at different angles such as 30°, 45°, 60°, and 90° with the normal of the concentrator surface as given in Fig. 5.12. In this study, the safety

factor is identified along with parameters such as equivalent stress, shear strain, and deformation.

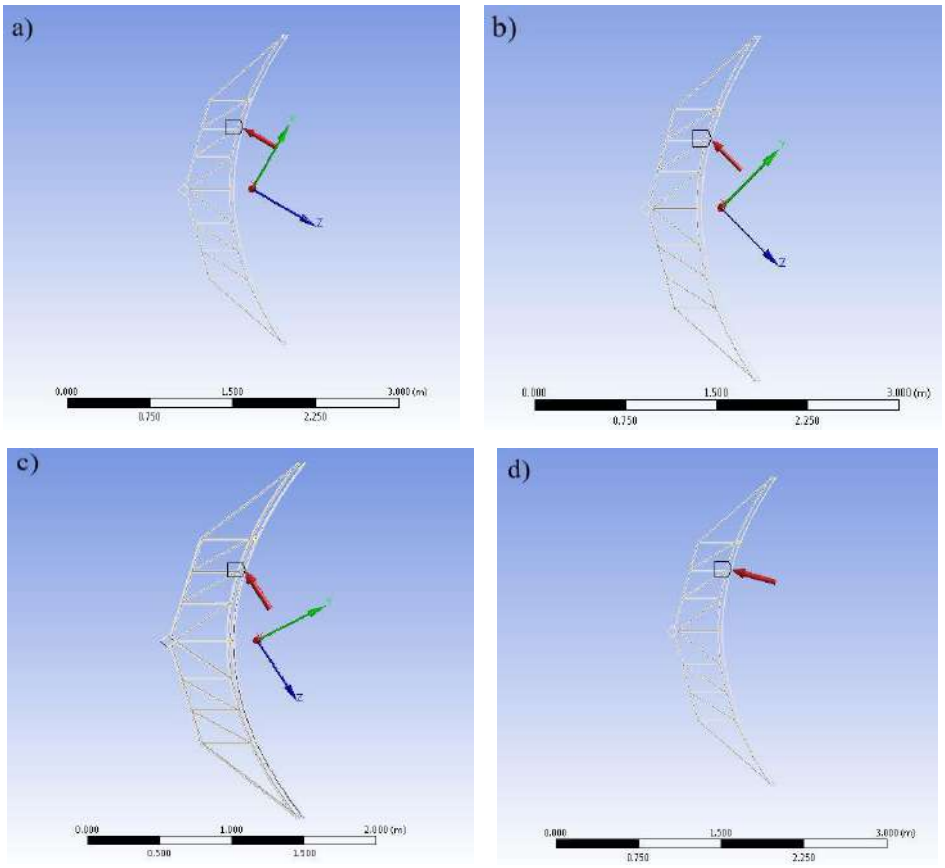

Fig. 5.12: Wind directions for the analysis (a) 30°, (b) 45°, (c) 60°, (d) 90°

5.4.4 Mesh convergence study

The mesh convergence study for the geometry is conducted using a proper mesh convergence tool. The element size is refined by lowering the aspect ratio at maximum load condition, and the safety factor and maximum principal stresses are monitored. During mesh convergence analysis, it is observed that, as the number of nodes increases, the maximum principal stress increases and the minimum factor of safety decreases. Figure 5.13 illustrates the variations in the maximum principal stresses and the minimum factor of safety for the examined meshes. From Fig. 5.13, it is observed that as the number of nodes increases beyond 68706, the variation in maximum principal stress and the minimum factor of safety becomes insignificant. Hence, 68706 is selected as the optimum

number of nodes for the analysis, and the corresponding number of elements is 32499. The discretised computational domain is shown in Fig. 5.14.

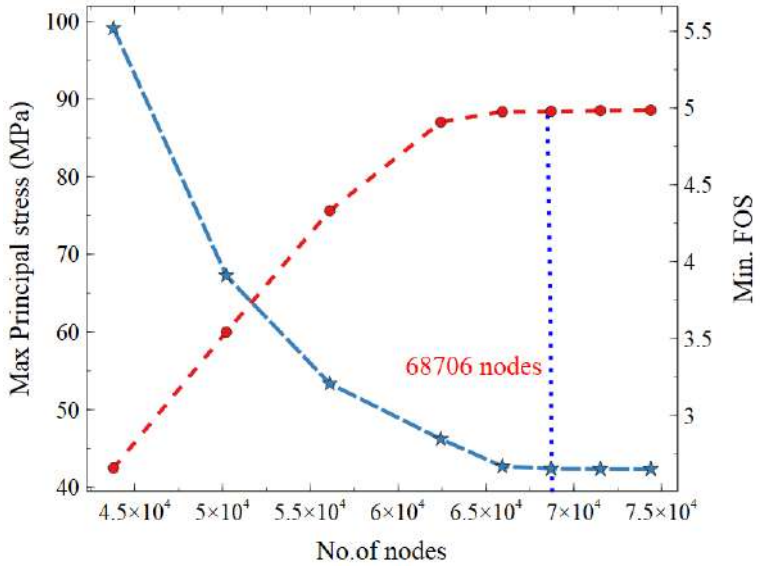

Fig. 5.13: Mesh independence study

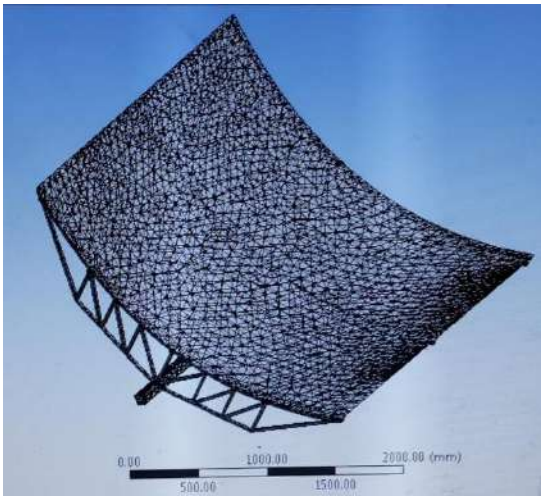

Fig. 5.14: Discretised computational domain of the PTC structure

5.4.5 Numerical analysis with varying load conditions

Based on the ANSYS Workbench simulation of the static structure under extreme wind loads, the mechanical behaviour of the support structure has been determined. The analysis is carried out for wind directions 30°,45°,60°, and 90° (normal) to the surface of

the trough surface. Figure 5.15 shows the pressure applied along 90° to the Parabolic trough surface.

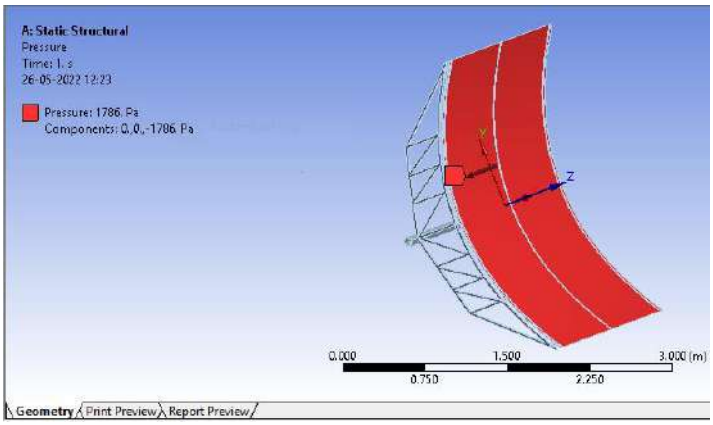

Fig. 5.15: Pressure applied on the PTC surface when wind direction is 90°

5.4.5.1 Analysis of mechanical behaviour at different wind angles

For the wind directions of 30°, 45°, 60°, and 90°, the support structure suffered deformations of 0.0325mm, 0.0339mm, 0.0341mm, and 0.276mm, respectively. Parabolic reflector structure deformed most when the angle of attack is 90° or normal to the parabolic surface, as can be seen in Fig. 5.16(a). The variation of shear strain for the different wind directions is between 5.6376 x 10^{-5} m/m at 45° to 5.477 x 10^{-4} m/m at 90°. The shear elastic strain experienced by the structure at 90° wind direction is depicted in Fig. 5.16 (b).

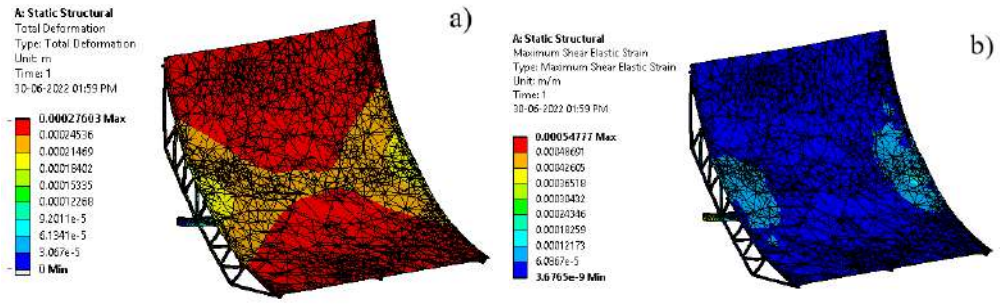

Fig. 5.16: (a) Deformation of the collector, and (b) max. shear elastic strain, for wind direction is 90°

The equivalent stress or von-Mises stress can be used to evaluate whether a material will yield or fracture. Figures 5.17 (a)- (d) show the equivalent stresses over the surface of the collector and the support structure for the four evaluated wind directions. The results depicts that the equivalent stress acting on the structure ranges between 7.7099 x 10^6 Pa to 7.5857 x 10^7 Pa. The maximum stress is observed for the wind direction of 90°, i.e wind attacks normal to the parabolic surface, which is under safe limit.

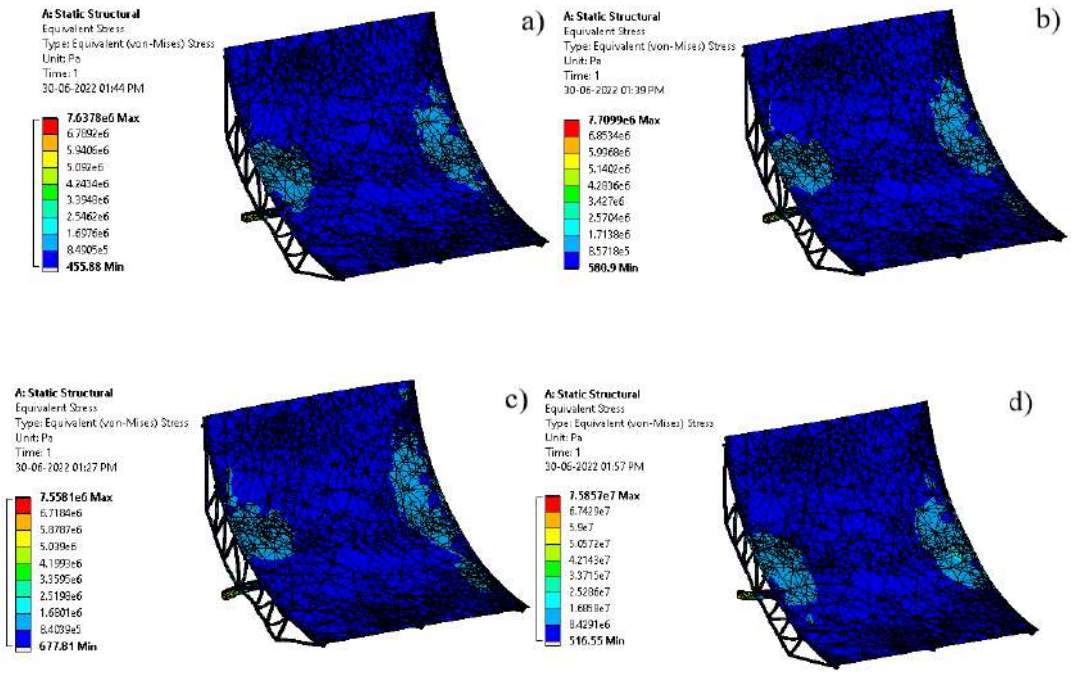

Fig. 5.17: Equivalent stress for different wind directions (a) 30°, (b) 45°, (c) 60°, and (d) 90°

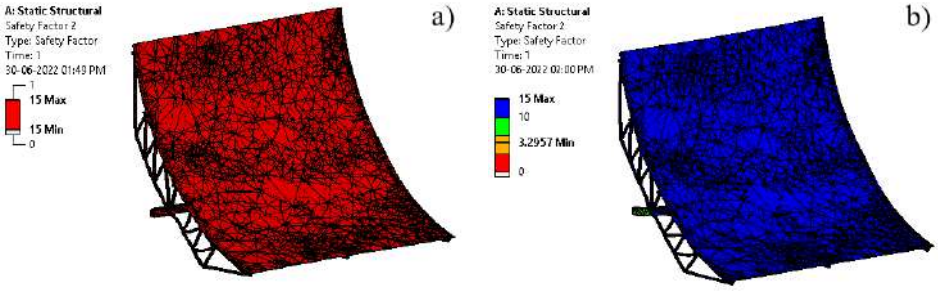

Fig. 5.18: Factor of safety for wind direction (a) 45°, (b) 90°

The factor of safety offered by the support structure for all the cases is determined and found that at 90° wind direction, the factor of safety is dominant, while in all other cases the minimum factor of safety is around 15. Results for the factor of safety for 45°, 90° wind directions are shown in Figs. 5.18 (a)-(b). At an attack angle of 90°, the factor of safety is found to be 3.29. For the present investigations since the extreme wind conditions and drag coefficient that the parabolic collector would experience is considered, the safety factor of 3.29 guarantees its reliability.

5.5 Construction of the PTC

The PTC has been constructed at the Mechanical Engineering Workshop of the TKM College of Engineering, located in Kollam city of Kerala, India.

5.5.1 Support structure

The PTC structure is constructed based on the structural analysis described in the section 5.4. It comprises three parabolic trusses connected by five mild steel cylindrical beams with outer diameters of 31.75 mm and gauge thicknesses of 3 mm. The mild steel truss elements employed are 20mm square rods. The parabola reference template ensures the profile accuracy of the parabolic trusses, which are digitally machined on a high-density fibreboard with a CNC milling cutter. The torque tube is a 75 mm square hollow section of mild steel with a thickness of 4.31 mm. The two ends of the torque tube are extended with steel shafts of a diameter 70 mm to accommodate ball bearings. The fabrication of the support structure is carried out in the Mechanical workshop of TKM College of Engineering, Kollam.

5.5.2 Main base

The main base is designed like a cradle. Hence, it is more stable under varying wind loads. The main base of the PTC is made of mild steel angle sections of size 90 mm x 90mm x 10mm and aligned in the North-South direction. The main base frames are connected to the PTC support structure through ball bearings. They are anchored to the

terrace by foundation bolts and concrete. The photograph of the base frame and support structrure is shown in Fig. 5.19.

Fig. 5.19: Main frame and support structure

5.5.3 Solar tracking

The current PTC is employed with a single-axis manual tracking system that moves the collector about a horizontal axis. The parabolic concentrator is rotated in an East-West direction to track the sun throughout the day. For this, a gearbox assembly comprising bevel and worm gear pairs is attached to the torque tube of the PTC. A handwheel with a dial indicator enables easy concentrator navigation and allows sunlight to fall normally on the concentrator surface. The gear arrangement and dial indicator arrangement for the solar tracking are depicted in Figs. 5.20 (a)- (b), respectievely.

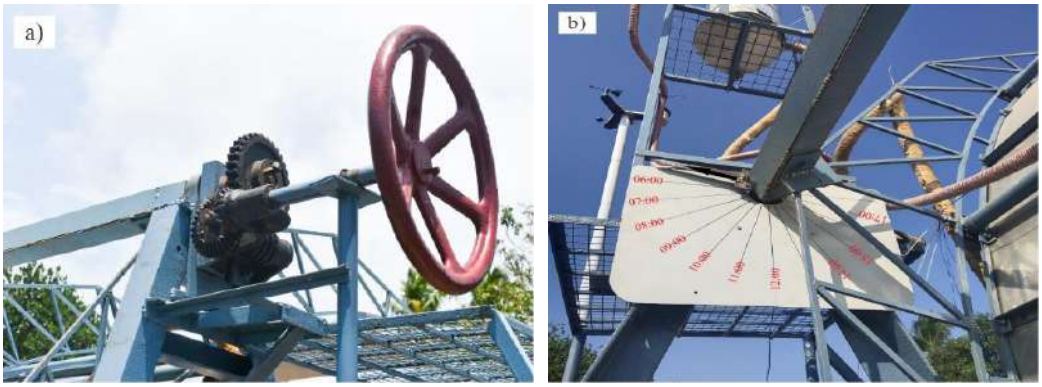

Fig. 5.20: (a) Gear arrangement and (b) dial indicator for solar tracking

5.5.4 Receiver tube and secondary reflector

For PTC evaluations without secondary reflectors, the copper receiver tube is located at the focal axis, while when a secondary reflector is used, it is below 15.278mm of the focal axis. The receiver tube support frame has a provision for adjusting the tube position with respect to the focal axis. A parabolic secondary reflector of size (2.5m x 0.2685m) determined from ray-tracing study (Chapter 4) is constructed using mirror-polished stainless steel.

5.5.5 HTF storage system

The thermal storage system consists of a 50-litre stainless steel tank. The heat transfer fluid is transferred from or to the collector through the outlet and inlet tubes using a regulated motor. A flow regulator and a control valve are used to control the HTF. The storage tank is connected to the inlet and outlet of the receiver tube by means of silicon tubes. Polyurethane insulations are used to reduce thermal energy losses as low as possible. The photograph of the storage tank is given in Fig. 5.21.

Fig. 5.21: HTF storage tank and weather station

5.6 Apparatus and Instrumentation

A total of eight T-type thermocouples are used to record temperatures at various points throughout the PTC system. Out of these, five T-type thermocouples are welded on the outer surface of the receiver tube at 50 cm intervals. Two T-type thermocouples are inserted into the flow to measure the receiver tube's HTF inlet and outlet temperatures. A T-type thermocouple is positioned at the center of the storage tank, and all thermocouples are connected to the digital electrical reader. The thermocouples have an accuracy of ±1°C and are calibrated before installation.

The working fluid is circulated from the storage tank to the PTC receiver. A regulated pump placed at the outlet of the storage tank is used to circulate the working fluid. The pump is mounted on a mounting base with an inlet and delivery line of 3/4 inch. A magnetically coupled regulator, pumps the HTF at the required flow rates, and the pump employs silicon-made shaft sleeve packing and glands for high-temperature applications. The flowrate measurement has been calibrated, and the measurement accuracy is found to be ±1.5%.

The weather conditions, including outdoor ambient temperature, wind speed, wind direction, solar flux and other weather conditions, are recorded by the ambient weather station WS-2902A. The sensor array of the weather station is installed near the PTC system's location. Weather station data (global radiation) is calibrated with a high-performance research grade pyranometer and variations are found to be within 2%.

The experimental setup is mounted on the terrace of the Energy Research Lab of TKM College of Engineering (8.9142°N latitude, 76.6320E longitude) Kollam. The assembly is shown schematically in Fig. 5.22, and the photograph of the fabricated setup is shown in Fig. 5.23. It consists of (a) PTC, (b) a 50 litre HTF storage tank, (c) a single axis manual solar tracker, (d) a regulated circulating pump, and (e) a control system. The present investigation uses a closed loop system for oil circulation. Flexible silicon tubes are connected to the receiver tube to convey the HTF. Therminol® 55 (TH55) oil is used as the HTF. The pump circulates HTF from the storage tank through the absorber tube of the PTC back to the storage tank. The HTF temperatures at the storage tank, inlet and

outlet of the absorber, surface temperatures of the receiver tube at five equal distances, global solar radiation and ambient temperature, and wind velocity are measured during the experiment. The specifications and measuring accuracy of the measuring devices and listed in Table 5.2.

Table 5.2 Measuring instruments specification

Equipment	Range	Parameter measured	Accuracy
Thermocouples, T-type	-250°C to 350°C	HTF Temperature	±1°C
Pyranometer, CM21, Kipp and Zonen	-40°C to 80°C operating temperature	Global Solar radiation	±0.01% of the measured quantity
Temperature sensor, Ambient Weather WS 2902A	-30°C to 60°C	Outdoor temperature	±0.5°C after calibration
Light Sensor, Ambient Weather WS 2902A	0 W/m^2 to 1578 W/m^2	Glubal Solar radiation	±2% after calibration

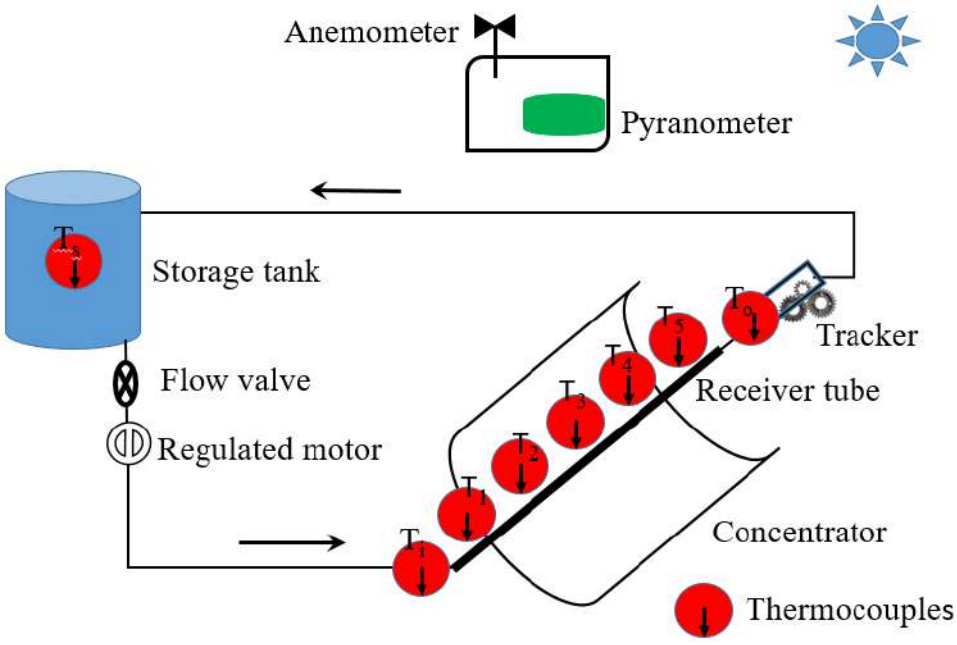

Fig. 5.22: Schematic of the experimental setup

Fig. 5.23: Constructed PTC experimental setup

5.7 Summary

The optical and thermal efficiency of a PTC is significantly reduced by the deflection of the structure with wind loads. Hence, this chapter presents the structural strength analysis and the fabrication of the experimental PTC system with a mechanically stable support frame. This chapter outlined the drag force analysis, mechanical strength investigation, fabrication of PTC subsystems and assembly of the physical PTC experimental test rig. As a result of the drag force analysis, the coefficient of drag that the PTC experience is equal to 1.9795, which is consistent with literature findings. ANSYS Workbench simulations of the static structure under extreme wind loads determined the factor of safety offered by the support structure for all case scenarios and found a dominant factor of safety at 90° wind directions. It is found that the factor of safety is 3.29 at 90° of attack angle. Since the extreme wind conditions and drag coefficient the parabolic collector would experience is considered in this investigation, the safety factor 3.29, is considered sufficient to guarantee its reliability. The next chapter discusses the synthesis of a hybrid nanofluid suitable for medium-temperature solar collector applications.

Chapter 6

Preparation and Experimental Characterisation of Hybrid Nanofluid

This chapter aims to develop a hybrid nanofluid with enhanced thermophysical properties suitable for medium-temperature solar collector applications. The thermal conductivity, viscosity, and specific heat of the nanofluids have been measured, and models for the thermal conductivity, viscosity, and specific heat have been presented.

6.1 Nanofluid preparation methods

The development of heat transfer fluids with considerably greater thermal conductivities and improved heat transfer characteristics can enhance the thermal performance of concentrating solar collectors. Accordingly, this chapter focuses on selecting relevant constituents and developing a thermal oil-based hybrid nanofluid ideal for medium-temperature PTC and similar applications. After choosing the nanoparticles and the base fluid through a critical literature review, the optimum synthesis procedure (ultrasonication time) and the influence of a dispersant/surfactant on the long-term dispersion stability of the hybrid nanofluid are investigated. Then the experimental investigation of the thermophysical properties of the developed hybrid nanofluid as a function of nanoparticle volume concentration and temperature is done to assess the augmentation of properties over the conventional fluid.

It should be noted that the synthesis of nanofluids includes more than just mixing and dispersing solid nanoparticles in a base liquid. The so-called one-step and two-step techniques are the most common procedures for producing nanofluids. The one-step technique is a single-step procedure that simultaneously makes, synthesises, and distributes nanoparticles in the base fluid, as illustrated in Fig. 6.1. The nanofluids prepared by this approach have improved dispersion stability and lowered particle agglomeration by eliminating nanoparticles' drying, shipping, storage, and other dispersion processes [73]. However, the one-step procedure only develops a limited amount of nanofluids, and the obtained nanofluids are costly. Moreover, in the single-step method, the mass concentration of the solid particles is significantly less than in the two-step approach.

In the two-step procedure, nanoparticles are first prepared as powders by physical or chemical methods and then suspended in a base fluid. The commonly used nanopowder preparation methods include grinding, Chemical Vapour Deposition (CVD), chemical precipitation, laser ablation, micro-emulsions, inert-gas condensation, thermal spray, spray pyrolysis, and so on. This approach is the most commonly used, as the production of large-scale nanoparticles has already been developed on an industrial scale. The nanoparticles are then dispersed in the base fluid using mechanical stirring and ultrasonic agitation using a high-frequency ultrasonic bath.

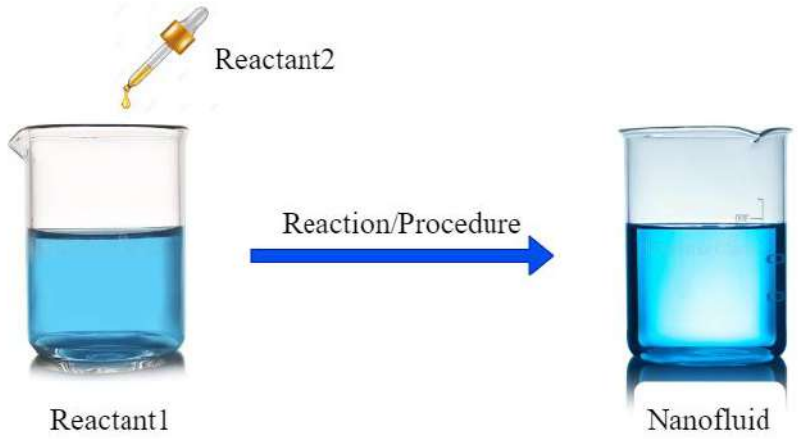

Fig. 6.1: One-step preparation process of nanofluids

Stability is a significant concern intrinsically linked to this operation because of the high Van der Walls force between nanoparticles. Research suggests that for

developing nanofluids of oxide nanoparticles the two-step technique is more effective than single step method [117]. Mohammadpoor *et al.* [63] developed Cu-based nanofluids using both one-step and two-step techniques and investigated the fluids' thermophysical characteristics and dispersion stability. They reported that nanofluids developed in the one-step process were more stable than fluids produced in the two-step process. Still, the nanofluids developed in two-step technique have better heat transport properties. In general, the two-step method is preferred over the one-step method because it is more cost-effective in the large-scale production of nanofluids. The most common two-step preparation process of nanofluids is depicted in Fig. 6.2.

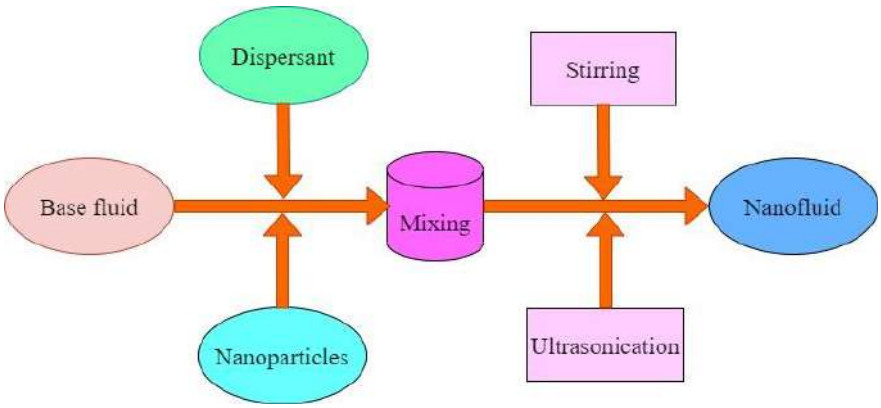

Fig. 6.2: Two-step preparation process of nanofluids

6.2 Stability of nanofluids

The development of long-term, stable and uniform nanoparticle dispersions in the base fluids is still a technical problem, and this challenge must generally be tackled in nanofluid preparation. Because of their immense surface energy, nanoparticles agglomerate gradually over time. Brownian motions of the nanoparticles lead to Van der Walls's forces of attraction between the particles, causing clustering and agglomeration. The aggregation of nanoparticles leads to sedimentation, which reduces the thermal conductivity of nanofluids. Some widely used approaches for the long-term stability of nanofluids include nanoparticle functionalisation, surfactant addition, ultrasonic agitation, surface modification of nanoparticles, and pH control of the nanofluid [118]. Meanwhile, certain techniques have been observed, such as nanoparticle functionalisation

or dispersant supplementation, to cause detrimental effects on thermal conductivity and dynamic viscosity, limiting the possible improvement of heat transfer. In light of this, nanofluids should be engineered to achieve a compromise between good stability and enhanced thermophysical properties. The dispersion stability of nanomaterials in nanofluids can be assessed using various techniques, including zeta potential, light scattering methods, and UV-vis spectroscopy.

6.3 Thermophysical and transport properties of nanofluids

Many ideas have been proposed in the literature for enhancing the thermal and thermodynamic performance of thermal oil-based PTC collectors. With the promising advancements in nanotechnology, nanofluid-based liquids have recently attracted increased interest in improving the thermophysical properties of HTFs by adding various nanoparticles. Many investigations have indicated that heat transport can be improved by modifying the thermophysical properties of HTFs with the aid of nanoparticle dispersion [119]. They also play a crucial impact in HTFs, such as improving specific heat capacity.

On the other hand, since density of most widely used nanoparticles is higher than the base liquids, the density of the nanofluids usually increases with the addition of nanoparticles. The presence of solid nano-additives within a liquid will also influence the viscosity and, therefore, the flow regime, leading to reduced pumping power and pressure drop. Thus, a comprehensive thermophysical profile is necessary to adequately assess the fluid's thermal performance. The dependence of the thermophysical properties, nanoparticle characteristics, and its dispersion are illustrated in Fig. 6.3 [120].

6.4 Selection of materials for the present study

The metal oxide nanoparticles, such as SiO_2, CuO, ZnO, Al_2O_3, and TiO_2, are reported to be stable and are well dispersed in working fluids. In addition, Al_2O_3 nano-powders exhibit superior heat transport properties. Furthermore, Al_2O_3 nanofluids maintain excellent chemical stability even at high temperatures. Moreover, because of its desirable thermophysical properties as compared to other metal oxide nanoparticles, Al_2O_3 is considered to be a potential nanoparticle for solar thermal applications. Furthermore, the thermal conductivity of Al_2O_3 at room temperature is around 36

W/(m.K) which is about 60 times higher than that of water (0.598 W/(m.K)). However, the thermal conductivity of Al_2O_3 is lesser than metal-nanoparticles such as silver, copper and gold, carbon-nanoparticles like graphene, CNTs and diamond. The literature reveals that Al_2O_3 nanoparticles have superior heat transfer properties and are ideal for applications in solar thermal technologies. Al_2O_3 is selected as, one of the nanomaterial for the present study.

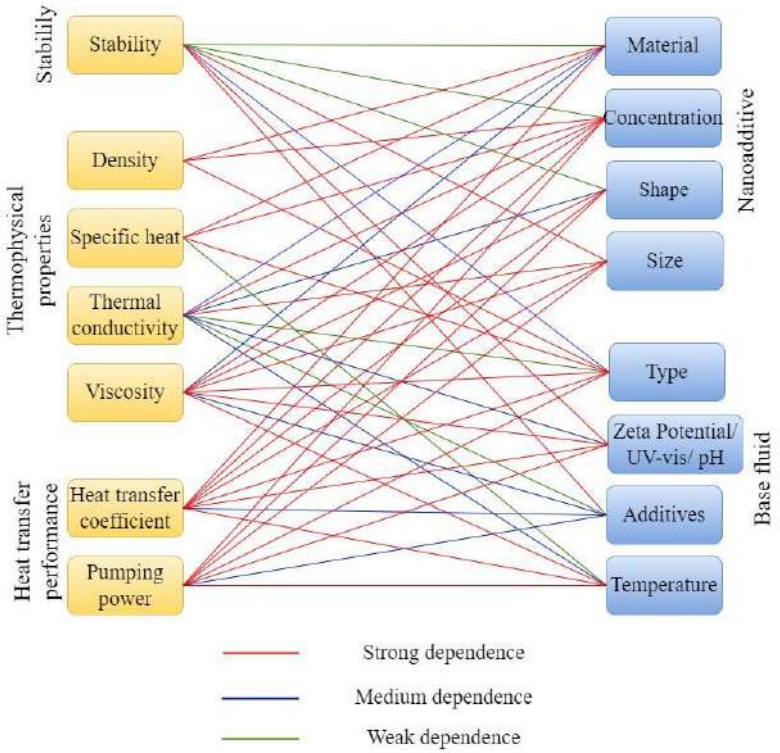

Fig. 6.3: Relations between nanofluid properties and design parameters of nanoparticles and base fluid

Graphene, atom-thick monocrystalline graphite, exhibited remarkable heat transport properties [121] and was proven to be a promising nanomaterial for HTFs for thermal energy storage and direct absorption solar collectors. Graphene Nanoplatelets (GNP) possesses a large surface area, high thermal conductivity, better stability, and low specific gravity than metal oxide nanoparticles. These materials have an outstanding thermal conductivity of around 5000 W/(m.K) [122], higher than the thermal conductivity of carbon nanotubes (3000 W/(m.K)). Further, since GNP is a 2D material, the heat transfer properties are supposed to be very distinct from the 0-dimensional nanoparticles and 1-dimensional carbon nanotube. Some of the nanoparticles such as copper, have

thermal conductivities of about 393 W/(m.K) at 400K, while silver has a thermal conductivity of about 425 W/(m.K) at 400K, which is very low in comparison to graphene [123]. The results reported by various investigators recommended that GNP can be a potential candidate for solar thermal energy harvesting applications. Hence, using GNP as the second nanoparticle for the hybridisation could be more efficient and helpful in the thermal energy absorbing and dissipating ability of the solar HTFs significantly.

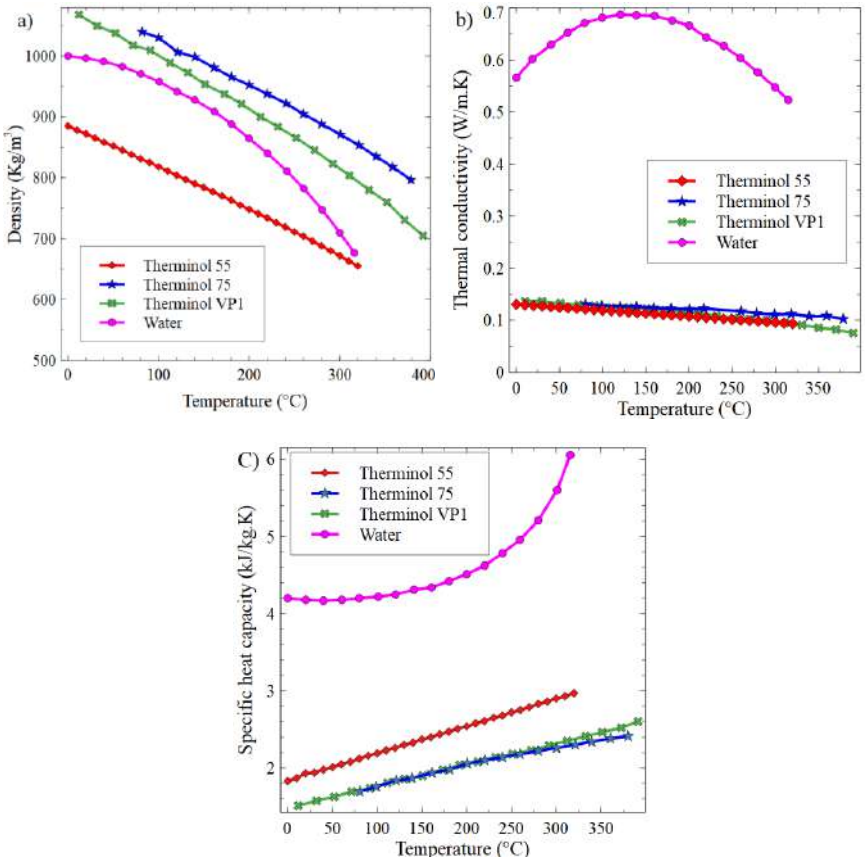

Fig. 6.4: Comparison of thermophysical properties of therminol oils and water (a) specific heat, (b) thermal conductivity and (c) density

Most commercial parabolic solar collector plants use Therminol as their HTF. A brief comparison of desirable thermophysical properties of different Therminol oils and water is illustrated in Figs. 6.4 (a)-(c). Although Therminol VP1 has a higher heat transfer efficiency as compared to Therminol® 55 (TH55), adequate heat would be needed to avoid clogging of pipes below 12°C [81]. On the other hand, Therminol 75, designed for typical liquid phase HTF systems, operates at low pressure. TH55 is reported to be very

reliable, cost-effective, durable and suitable for solar concentrators operating continuously at 300°C. The thermal conductivity value of TH55 oil is around 0.115 W/(m.K) at 400 K [124], which is quite low as compared to GNP. Hence, GNP loading in TH55 would significantly improves the effective thermal conductivity of the resulting nanofluid. As a result, the rise in thermal conductivity for Therminol-based nanofluids would be greater than the conventional HTFs based nanofluids. Thus, a hybrid nanofluid comprising of Al_2O_3 and GNP in TH55 oil base fluid could produce a long-time stable hybrid nanofluid with desirable thermal properties. In summary, Table 6.1 shows the desired bulk thermophysical property-based preference for selecting nanomaterials. TH55 is chosen because of its excellent physical and thermal properties over the temperature range of interest (<200°C) [125], Al_2O_3 because of its desirable thermal properties and chemical stabilities [126], and GNP for its outstanding thermal conductivity and desirable thermophysical properties [127].

Table 6.1 Thermophysical property-based preference position of nanomaterials

Sl. No	**Materials**	**Shape**	**Thermal conductivity, k [W/(m K)]**	**Density, ρ [Kg/m^3]**	**Specific heat, cP [J/(kg K)]**	**Rank**	**Ref.**
Metal oxides							
1	CuO	Spherical	33	6000	551	2	[128]
2	Fe_2O_3	Spherical	6.9	5180	670	4	
3	TiO_2	Spherical	8.4	4230	692	3	
4	Al_2O_3	Spherical	40	3960	773	1	
5	SiO_2	Spherical	1.4	2200	765	5	
Carbon derivatives							
1	SWCNT	Cylinder	2725	1800	720 [129]	2	[123]
2	MWCNT	Cylinder	1500	2500	630	3	[130]
3	GNP	Platelets	5000	2272	700	1	[131]

A comprehensive review of the literature on nanofluid-operated solar thermal collectors indicated that Al_2O_3-GNP hybrid nanoparticles in TH55 oil as base fluid had not previously been investigated in detail. Hence, this chapter discusses the preparation

of TH55 oil-based hybrid nanofluids with GNP and Al_2O_3 nanoparticles with different concentrations for the first time. Thermophysical properties such as thermal conductivity, dynamic viscosity, and specific heat are determined experimentally for the different concentrations of hybrid nanoparticles in TH55 as base fluid.

6.5 Materials and methodology

The experimental techniques and measurement of properties are detailed in this section. The characterisation of nanoparticles and the steps for preparing nanofluids are first described. Subsequently, steps to measure the thermal conductivity, dynamic viscosity, and specific heat are discussed in detail.

6.5.1 Materials used

The sample of TH55 from *Eastman Chemical Company, USA*, provided by *Solutia Chemical India Private Limited,* is utilised as the base fluid for the present study. Its chemical name is benzene, C14-30-alkyl derivatives, and its molecular formula is $C_{28}H_{50}$. The characteristics of TH55 oil are given in Table 6.2.

Table 6.2 Chemical and physical data of TH55 oil

Composition	Synthetic hydrocarbon mixture
Appearance	Clear, yellow liquid
Odour	Odourless
Average Molecular weight	350 (g/mol)
Density (@ 20°C)	872 (kg/m^3)
Viscosity (@ 20°C)	47.7 (cSt)
Flashpoint	177 (°C)
Boiling point	351 (°C)
Extended maximum use temperature	315 (°C)
Thermal conductivity (@ 20°C)	0.1284 (W/(m.K))
Specific heat	1.91(kJ/(kg.K))

Al_2O_3 and GNPs are acquired from *Alfa Aesar, UK*. The chemical and physical properties of Al_2O_3 and GNP are summarised in Table 6.3. The meteorological content and characteristic structural study of the nanoparticles are very significant. X-Ray Diffraction (XRD) on a *LynxEye diffractometer* with CuKα radiation (40 kV, 20 mA, λ = 1.54060 Å) is used to analyse the mineralogical content of the dry Al_2O_3 nanoparticles

and GNP. The 2θ analysis is carried out in the range of 5° to 80° with a step of 0.02°. Scanning Electron Microscopy (SEM) by a *JEOL JSM6370* is used to investigate the morphological characterisation of the nanomaterials. The Transmission Electron Microscopy (TEM) imaging system (*JEOL/JEM 2100*) has been used to characterise the structure of the nanomaterials in the hybrid suspension.

Table 6.3 Characteristics of selected nanomaterials

	Al_2O_3	**GNP**
Purity (%)	99.5	95
Morphology	Nearly spherical	Platelets
Size (nm)	40 -50	-
Molecular weight (g/mol)	101.96	12.011
Colour	white	Black
Specific surface area (m^2/g)	36	500
Density (g/cm^3)	3.965	2
Melting point (°C)	2030	2760

6.5.2 Experimental study

The suspensions are dispersed with magnetic stirring at 1600 RPM for 1 hour to separate the particle agglomeration. Then the influence of the ultrasonic agitation period on its properties such as thermal conductivity and dynamic viscosity is monitored by varying the ultrasonication time. The ultrasonication is conducted at 4000 Hz with the BRANSON-3800 sonication homogeniser. After that, mono and hybrid nanofluids are prepared using the optimised two-step method with GNP and Al_2O_3 nanoparticles dispersed into the TH55 base fluid.

The mineralogical and morphological features of the nanoparticles are evaluated using XRD patterns and SEM images. TEM and UV-spectroscopy techniques are utilised to verify the uniform dispersion and stability of the hybrid suspension. Thermophysical properties such as thermal conductivity, dynamic viscosity, and specific heat are determined experimentally over different temperatures and solid concentrations. Densities of nanofluids are determined using the correlations based on the classical theory of mixing available in the literature. The transient hot-wire technique, cone-and-plate rheometer, and T- history methods are used to evaluate nanofluids' thermal conductivity, viscosity, and specific heat. Moreover, based on the experimental data, correlations for

predicting the hybrid nanofluid's thermal conductivity, dynamic viscosity, and specific heat capacity are proposed in terms of solid concentration and temperature.

6.5.3 Nanofluid preparation

The two-step dispersion process and ultrasonic agitation are the most commonly used nanofluid preparation methods. The schematic of the hybrid nanofluid preparation by the two-step method is shown in Fig. 6.5. The two-step method aimed to prevent the accumulation and agglomeration of the particle clusters and obtain a stable and homogeneous nanofluid. The two-step method prepares the nanofluids with TH55 as the base fluid. Before dispersing the nanoparticles, a specific amount of Oleic Acid (OA) is added to TH55 to ensure stability. The choice of OA (0.5 ml for 1 g of nanoparticle) [62] is inspired by its outstanding miscibility and comparable density with TH55, as well as its superior high-temperature stability [132].

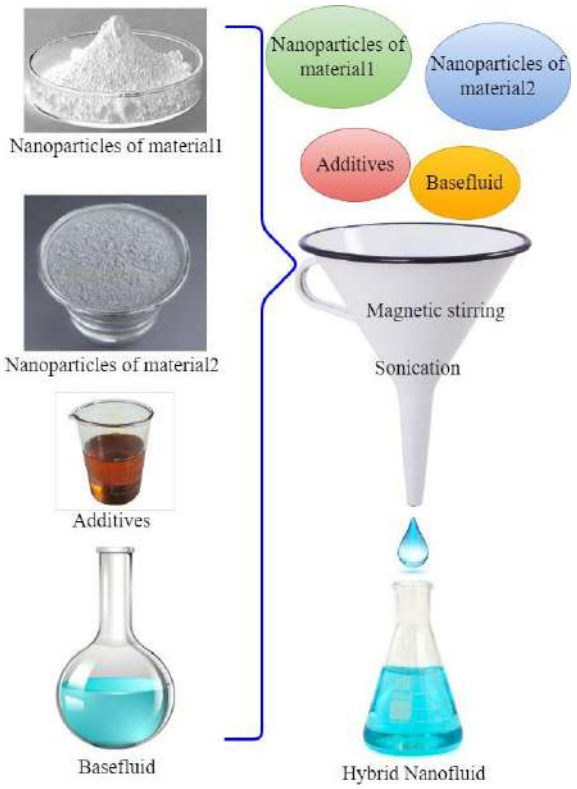

Fig. 6.5: Schematic diagram of the hybrid nanofluid preparation

Before developing the hybrid nanofluids, the optimum procedure for preparing the nanofluid with better thermal conductivity has been studied. Before ultrasonication, the samples are stirred for 1 hour at 1600 RPM. To obtain a homogeneous suspension, ultrasonication is performed in an ultrasonication homogeniser (BRANSON-3800) at a frequency of 4000 Hz. The impact of different ultrasonication times and OA addition on the viscosity and thermal conductivity of the hybrid nanofluids are investigated by varying the ultrasonication period from 1 hour to 5 hours.

To study the individual effect of nanoparticles on the thermophysical properties of the base fluid, Al_2O_3 dispersed mono-nanofluids at weight fractions of 0.1%, 0.5% and 1.0%; and GNP dispersed mono-nanofluids at weight fractions of 0.01%, 0.05% and 0.1% are prepared separately using the optimised synthesis procedure. Three samples of GNP-Al_2O_3 hybrid nanofluids are prepared by varying the weight fractions of GNP as 0.01%, 0.05%, and 0.1%, with the weight fraction of Al_2O_3 remaining constant at 1.0% for all samples. All the processes are conducted at ambient temperature.

6.5.4 Thermal conductivity measurement

The thermal conductivity of nanofluids plays a vital role in the thermal performance of PTC. In this study, the KD2 pro thermal property analyser (*Decagon Devices Inc., USA*), which meets the ASTM standard's D5334 regulations, is used to evaluate the thermal conductivity of both base fluid and prepared samples within the working temperature. The schematic arrangement of the thermal conductivity measurement system is illustrated in Fig. 6.6. Measurement is carried out by the transient hot-wire method with the help of the KS-1 sensor of the analyser. The KS-1 sensor has a 60 mm long and 1.3 mm diameter stainless steel probe, and the maximum deviation is ±5%. The measuring range of the KS1 sensor is 0.2 to 2 W/(m. K) with an accuracy of ±0.001%. The transient hot-wire method is considered the most accurate thermal conductivity measurement. KD2 can detect the thermal conductivity of oil-based nanofluids at temperatures up to 110°C and the temperature of water-based nanofluids at temperatures up to 70°C. Oils can retain thermal energy for much longer than water, making it possible to test the thermal conductivity of oil-based nanofluids at around 70°C with more accuracy than water-based nanofluids [132]. Before measuring the thermal conductivity of the samples, the analyser is calibrated using verification standard

(Glycerine, CAS 56-81-5) at 28°C and atmospheric pressure. The measurement error has been calculated as the difference between the thermal conductivity of the standard and the recorded thermal conductivity during calibration. The thermal conductivity values reported in the study are an average of five measurements with an estimated error of ±1.6. Figure 6.7 illustrates the comparison between the experimental and the reported values of thermal conductivity of TH55. The thermal conductivity values of the base fluid are in good agreement with the manufacturer's data for temperatures between 25°C and 65°C.

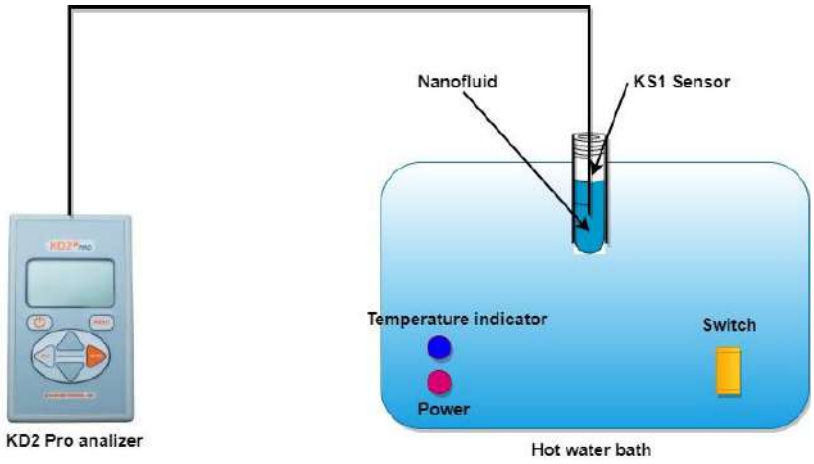

Fig. 6.6: Schematic diagram of the thermal conductivity measurement setup

After calibration, a 30 ml test sample is carefully weighed and kept in a test tube placed vertically in an isothermal water bath. The KS1 probe is kept completely immersed in the centre of the sample. Before the measurement, the sample and the sensor temperature are kept the same for 15 minutes to ensure equilibrium. The thermal conductivity of the sample is obtained based on the following equation:

$$k = \frac{q(lnt_2 - lnt_1)}{4\pi(\Delta T_2 - \Delta T_1)} \qquad (6.1)$$

where q is the consumed heat rate (W/m^2), ΔT_1 and ΔT_2 are the change in temperatures at times t_1 and t_2, respectively.

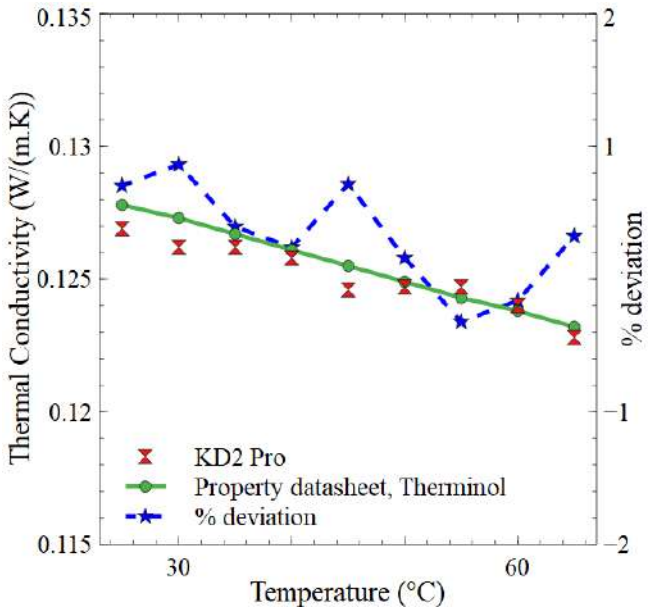

Fig. 6.7: Comparison of the experimental and reported values for thermal conductivity of TH55

6.5.5 Viscosity measurement

The viscosity plays a vital role in the natural convection heat transfer process of PTCs. The Al_2O_3-GNP/ TH55 nanofluid's viscosity at different weight fractions is measured with a Brook-field LVDV-II + Pro cone-and-plate rheometer having a measurement range between 1.0 cP and 2000 cP and spindle speeds 0-150 RPM. The rheometer has a PC-controlled constant temperature circulator bath (Julabo F25 HE Refrigerated/Heating circulator, Germany) for regulating the temperature. The spindle used in this study is calibrated with the standard fluid provided by Brookfield Engineering Laboratories. The measurement uncertainty is found to be less than 2%. All the measurements are made under steady-state when the imposed twisting moment is between 10% and 100%. The operation of the viscometer and data collection is carried out using the Rheocalc software. To minimise the measuring errors and obtain reliable experimental results, each measurement is repeated three times and the mean is recorded.

6.5.6 Specific heat measurement

Knowing the specific heat capacity of the HTFs used for solar thermal collectors is essential since the heat transfer rate between the receiver tube and the HTF depends on

the fluid properties. In most cases, specific heat capacity has been determined by using conventional calorimetry, Differential Thermal Analysis (DTA), Differential Scanning Calorimetry (DSC), and the T-History method. The well-known DSC is the most used method to determine these parameters. This method, however, usually uses an inconvenient sample size, typically 1 mg to 50 mg, making it difficult to obtain representative results for HTFs [133]. In contrast, the T-history method can handle large samples of the order of 15000 mg, representing the bulk material's correct chemical and physical composition [134]. In addition, DSC requires an expensive laboratory setup, and examining one specimen at a trial can become highly time-consuming. For these reasons, Yinping *et al.* [90] developed the T-history method to investigate the thermophysical properties of thermal materials. The comparison of four common thermal analysis techniques is given in Table 6.4 [134].

6.5.6.1 Temperature history (T- history) method

The T-history method is inexpensive and is based on comparing the temperature versus time curves of the sample and reference material (of established thermal properties) during the cooling against ambient temperature. This method can also simultaneously determine the properties of several samples in a single experiment. Heat capacity, thermal conductivity, enthalpy of fusion, and phase change temperatures can be estimated primarily using the T-history approach [134]. Unlike other methods, this approach permits larger sample sizes and requires less maintenance and evaluation time. The experimental system for this approach is not commercially available but can be easily installed using standard laboratory components.

Table 6.4 Comparison among four common thermal analysis methods.

	Sample size (mg)	**Measurement time (min)**	**Maintenance**	**Equipment cost**	**phenomenon**	**Properties**
Thermogravimetric analysis (TGA)	10 -150	100	++	++	Thermal stability/ decomposition, sublimation/evaporation/dehydration	% sample mass loss $f(T,t)$
Differential Thermal analysis (DTA)	10 - 150	100	++	++	Decomposition, glass transition, melting	$\Delta T\ f(T,t)$ $H\ f(T,t)$
Differential scanning calorimetry (DSC)	1 - 50	100	++	++	Melting, glass transition, subcooling degree, reaction (curing/polymerisation)	$C_p\ f(T,t)$ $H\ f(T,t)$ T_m
T-history	15000	40	+	+	Melting, visual phase change, subcooling degree	$C_p\ f(T,t)$ $H\ f(T,t)$ T_m k

6.5.6.2 Method of measurement and analysis

The basic principles involved in the original T-history method developed by Yinping *et al.*[135] are summarised below. The uniform temperature distribution over the whole cross-section of the material to be investigated is a significant prerequisite in the T-history experiment. If the Biot number is less than 0.1, this requirement can be accomplished and ensure the application of the lumped capacitance model [135]. Mathematically,

$$\text{Biot number}, Bi = {}^{hr}/_{(2k)} \tag{6.2}$$

where r is the radius of the test tube, h the natural convective heat transfer coefficient between the tube and the surrounding air, and k the material's thermal conductivity. Generally, if the test tube has an L/D ratio of more than 15 with a narrow wall, it is reasonable to assume that the heat transfer is approximately one dimension [135]. Using a sample of reference material whose thermophysical properties are very well-known and no phase changes under the test conditions is another prerequisite of this method. Figure 6.8 shows the schematic of the experimental setup used for the T- history method.

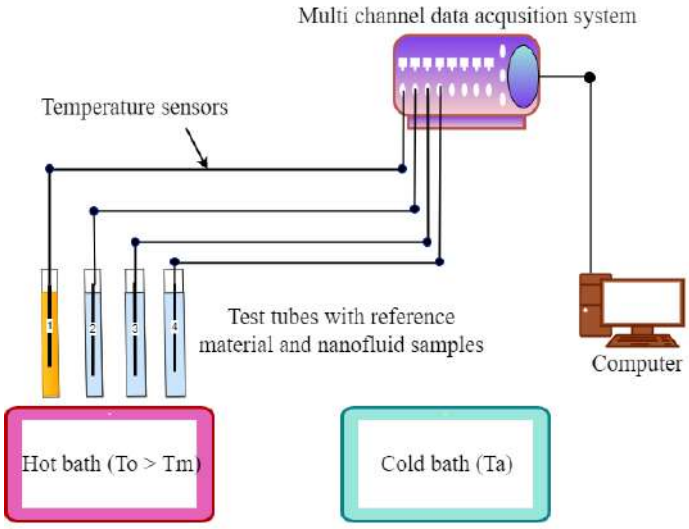

Fig. 6.8: Schematic of the experimental setup for the T-history method

It consists of smaller diameter and long length glass tubes filled with nanofluid samples and suitable reference material. The identical initial temperatures of each material are needed to be higher than the freezing temperature of the samples. The samples and the reference material inside the tubes are then heated in an oil bath to a suitable temperature (T_o) above the melting point of the samples (T_m). Afterwards, as soon as a steady-state is achieved, the glass tubes are simultaneously taken out of the hot bath and exposed to sudden cooling by dipping them into a water bath maintained at ambient temperature T_∞. During cooling, the temperature of both materials concerning the time has to be recorded, which can make it possible to determine the thermophysical properties of the nanofluid. According to the original T- history method, typical cooling curves of a phase change material and a reference fluid are shown in Fig. 6.9. The sensible heat transfer balancing from the reference to the ambient can be expressed in Eq. (6.3). The

natural convective heat transfer coefficient can be calculated using Eq. (6.4) and taking into account the recorded *T* versus *t* curve of the reference fluid.

$$\left(m_r C_{p,r} + m_t C_{p,t}\right)(T_o - T_i) = hA_c A_{1r} \tag{6.3}$$

$$h = \frac{(m_r C_{p,r} + m_t C_{p,t})(T_o - T_i)}{A_c A_{1r}} \tag{6.4}$$

where $C_{p,r}$, $C_{p,t}$ are the mean specific heats of the reference fluid and glass tube; m_r, m_t the masses of the reference fluid and tube; A_c the convective heat transfer area of the tube, and dA_{1r} the area under the curve within the recorded reference temperature and ambient temperature as shown in Fig. 6.9.

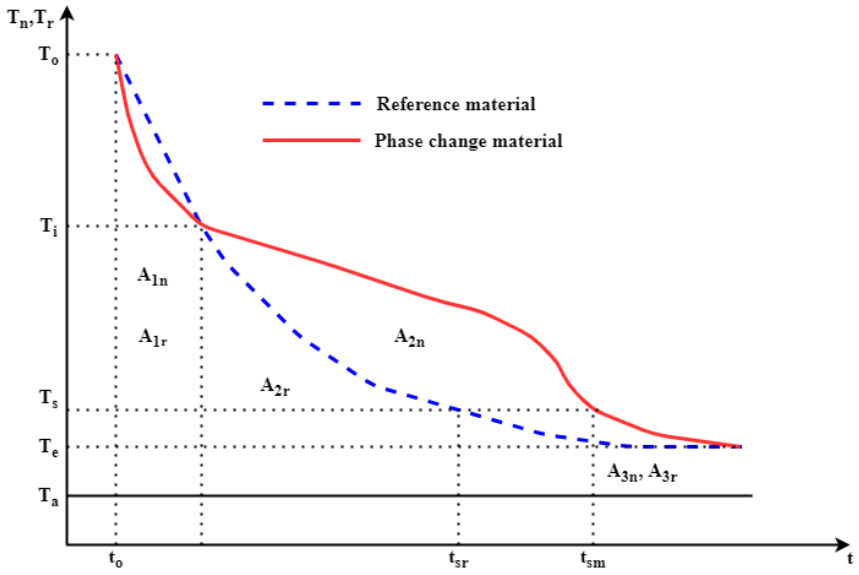

Fig. 6.9: Cooling curves of phase change material and reference fluid, according to the original T-history method

In the liquid phase of the sample, the heat transfer equilibrium between the nanofluid and the reference sample and the atmosphere is expressed by the following two equations [135].

$$\left(m_{tn} C_{p,t,n} + m_n C_{p,n,l}\right)(T_o - T_i) = h_1 S_{t,n} A_{1n} \tag{6.5}$$

$$\left(m_{tr} C_{p,t,r} + m_r C_{p,r}\right)(T_o - T_i) = h_1 S_{t,r} A_{1r} \tag{6.6}$$

where m_{tn} and m_{tr} are the masses of the glass tubes containing nanofluid and reference liquid, respectively; m_n and m_r the masses of nanofluid and reference sample, respectively; $C_{p,n,l}$ and $C_{p,r}$ the heat capacities of nanofluid and reference fluid,

respectively; T_o and T_i the initial temperature during cooling and temperature at a particular time interval, respectively, h_1 the mean convective heat transfer coefficient between the tube surfaces and ambient for the temperature limits; $S_{t,n}$ and $S_{t,r}$ the surface areas of nanofluid and reference glass tubes, respectively, A_{1n} and A_{1r} the areas below the cooling curves of the nanofluid $T_n(t)$, and reference fluid $T_{r(t)}$, respectively, between temperatures T_o and T_i. In the above equations, $A_{1n} = \int_{t_0}^{t_{1n}} \left(T_{n(t)} - T_a\right) dt$, that represents the area under the curve in the liquid region of the nanofluid in Fig. 6.9 and $A_{1r} = \int_{t_0}^{t_{ir}} \left(T_{r(t)} - T_a\right) dt$, corresponds the same for the reference fluid.

As described above, the original T-history method based on time delay at a specified temperature needs a curve fitting to the data set $T_n(t)$ and $T_r(t)$ for developing the nanofluid and reference sample cooling curves as well depicted in Fig. 6.9. Kravvaritis *et al.*[136] modified this method by using the thermal delay approach (temperature difference) between nanofluid and reference fluid at any specified time. An advantage of this method is the ability to determine the effective heat capacity as a function of temperature $C_{p,eff}(T)$ without having to proceed with determining the enthalpy function. Furthermore, in the thermal delay method, the need for curve fitting to the data and integration of the area under the curve can be eliminated by directly calculating the area, thus considerably reducing the duration of the experiment.

6.5.6.3 Thermal delay method

The main advantage of the thermal delay method relative to the original T-history method is in the way of measurement processing. For example, in the original T-history method, the same reference fluid and nanofluid temperature T_s are obtained at different times t_{sr} and $t_{sn,}$ respectively, as displayed in Fig.6.9. On the other hand, the thermal delay method examines the reference fluid temperature $T_{n,i}$ and nanofluid temperature $T_{r,i}$ at the same time t_i as shown in Fig. 6.10. At time t_{i+1}, the corresponding temperatures would be $T_{n,i+1}$ and $T_{r,i+1}$.

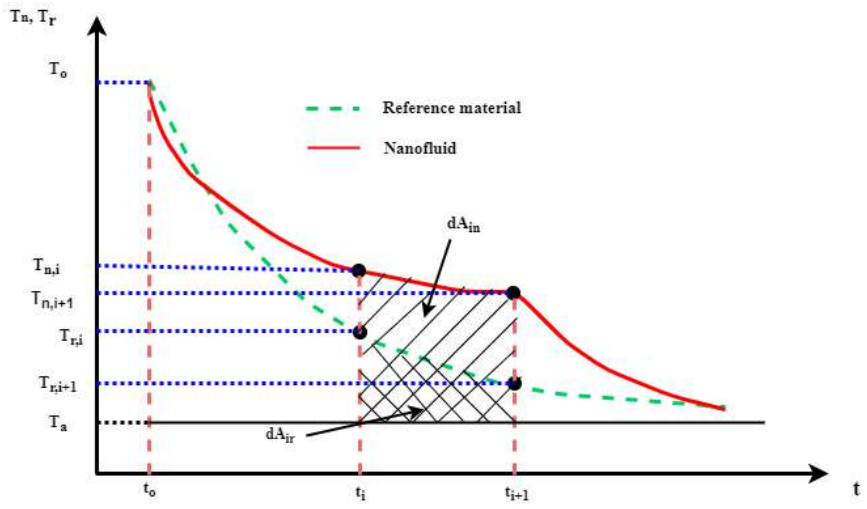

Fig. 6.10: Schematic diagram of measurement processing in thermal delay method

The energy balance between the nano and reference fluid with the environment with the ambient during the time interval (t_{i+1}- t_i) can be expressed by referring to the following two relationships.

$$\left(m_{tn}C_{ptn} + m_m C_{p,eff}\right)\left(T_{n,i} - T_{n,i+1}\right) = hS_{tn}dA_{in} \tag{6.7}$$

$$\left(m_{tr}C_{ptr} + m_r C_{pr}\right)\left(T_{r,i} - T_{r,i+1}\right) = hS_{tr}dA_{ir} \tag{6.8}$$

where $C_{p,eff}(T)$ is the effective nanofluid thermal capacity at temperature $T = \left(T_{n,i} + T_{n,i+1}\right)/2$ and dA_{in} and dA_{ir} are the areas below the cooling curves of the nanofluid and the reference fluid, respectively, between times t_i and t_{i+1}.

$$dA_{in} \cong \frac{\left(T_{n,i}+T_{n,i+1}-2T_a\right)\left(t_{i+1}-t_i\right)}{2} \tag{6.9}$$

$$dA_{ir} \cong \frac{\left(T_{r,i}+T_{r,i+1}-2T_a\right)\left(t_{i+1}-t_i\right)}{2} \tag{6.10}$$

Effective nanofluid heat capacity, $C_{p,eff}(T)$, can be determined by dividing the Eqs. (6.7) and (6.8) and eliminating the heat transfer coefficients, *h*, as they are equal to each other during the time step $t_{i+1} - t_i$.

$$C_{p,eff}(T) = \frac{M\left(T_{r,i}-T_{r,i+1}\right)dA_{in}}{\left(T_{n,i}-T_{n,i+1}\right)dA_{ir}} - N \tag{6.11}$$

where M and N are given by Eqs. (6.12) and (6.13), respectively.

$$M = \frac{\left(m_{tr}C_{ptr}+m_r C_{pr}\right)S_{tn}}{m_n S_{tr}} \tag{6.12}$$

$$N = \frac{m_{tn} C_{ptn}}{m_n} \tag{6.13}$$

where m_{tn} and m_{tr} are the masses of the tubes containing nanofluid and reference fluid, respectively; m_n and m_r the masses of nanofluid and reference fluid, respectively; and C_{ptn} and C_{ptr} the heat capacities of tubes containing nanofluid and reference fluid, respectively. Substitution of $dA_{in}$and dA_{ir} from equations (6.9) and (6.10) into equation (6.11) gives a final equation for $C_{p,eff}$ based on the thermal delay method [136].

$$C_{p,eff}(T) = \frac{M(T_{r,i} - T_{r,i+1})(T_{n,i} + T_{n,i+1} - 2T_a)}{(T_{n,i} - T_{n,i+1})(T_{r,i} + T_{r,i+1} - 2T_a)} - N \tag{6.14}$$

6.5.6.4 T-History experimental setup

The photograph of the T-history test setup to determine the specific heat of the samples designed and developed is shown in Fig. 6.11. The system consists of a controlled hot temperature silicon oil bath of size 22cm diameter x 25cm height, 500 W electric heater, T-type thermocouples with an accuracy of ±0.75% integrated with a data acquisition system (*KEYSIGHT 34972A LXI*), and a computer for recording the temperature versus time data. The heating rate of the silicon oil bath can be regulated between 0°C and 400°C by a PID controller and a variac depending on the requirements. The test tubes are designed of pyrex glass with an inside diameter of 0.7cm, a height of 15cm and a wall thickness of 0.1cm. The designed dimensions of the test tubes with the expected natural convective heat transfer coefficient of 5 to 6 W/(m. K) satisfy the Biot number condition. Research grade glycerine is used as the reference fluid.

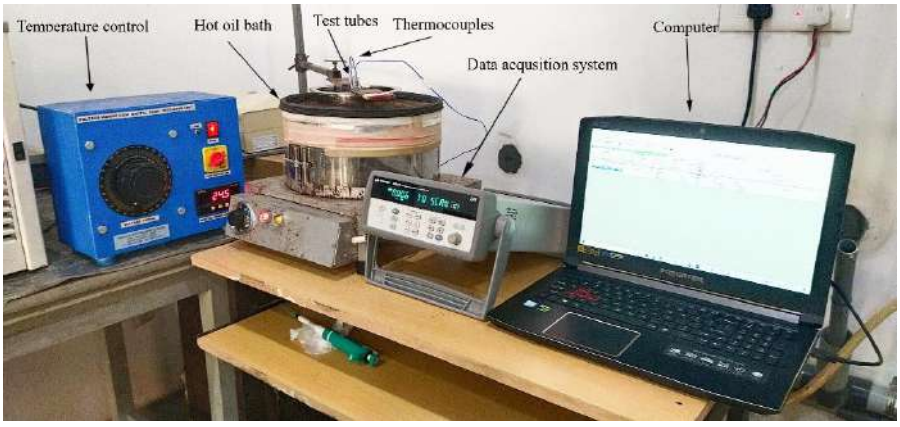

Fig. 6.11: Experimental arrangement of the T-history method

6.5.6.5 Validation of the experimental setup

The experiments are performed carefully to satisfy the condition of the lumped heat capacitance method. The two identical test tubes are filled with pure TH55 oil and the other with a reference fluid (glycerine) whose specific heat is well known. TH55 oil and reference specimen samples are preheated in the hot silicon oil bath. Subsequently, after the temperature is stabilised, they are simultaneously subjected to a sudden change in temperature by exposing them to air. The cooling history of TH55 and Glycerine over a temperature range of 220°C to 25°C [Fig. 6.12(a)] is monitored several times, and the specific heats at different temperatures are calculated. The temperature variations of both materials during cooling are recorded through a data acquisition system (*KEYSIGHT 34972A LXI*). The specific heat of nanofluids is determined by comparing their cooling curves with the cooling curve of glycerine.

The experimental results are in good agreement with the values given by the manufacturer's material property data. The comparison between experimental results and the data obtained from the manufacturer is illustrated in Fig. 6.12(b) indicates that the specific heat values are close. For the experimental setup and the test conditions, the results between 25°C to 110°C are within a percentage error of ±10%.

6.6 Experimental results and discussion

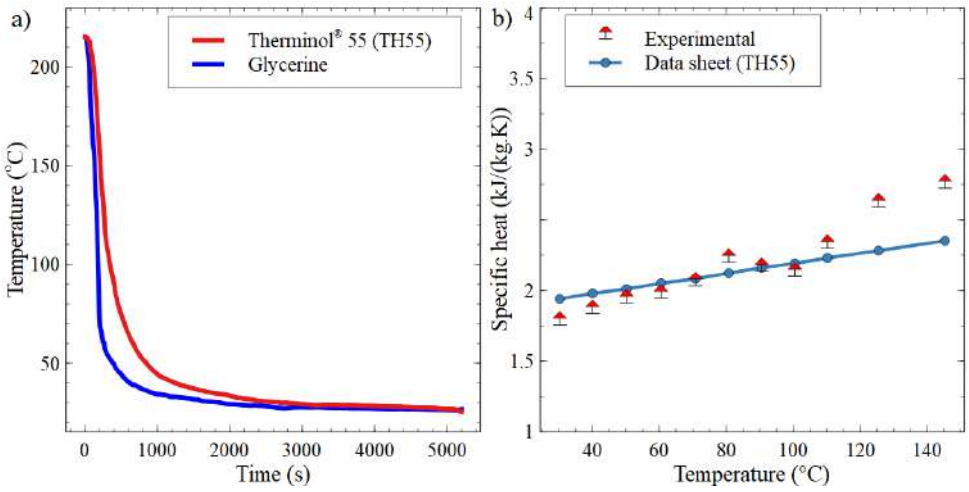

Fig. 6.12: (a) Cooling history of TH55and glycerine (b) Specific heat of TH55

Different samples of nanofluids are prepared and tested for their performance. The meteorological properties of hybrid nanofluids suitable for the PTCs are evaluated by SEM, TEM and XRD techniques. Thermal properties of the prepared hybrid nanofluid combinations are measured and presented here. The thermodynamic properties such as thermal conductivity, specific heat and viscosity of the hybrid fluids are determined and are also discussed in this section.

6.6.1 X-ray powder diffraction (XRD)

Figures 6.13(a) and (b) show the XRD pattern of Al_2O_3 nanoparticles and GNP, respectively. From Fig. 6.13(a), it can be seen that the characteristic peaks at $2\theta = 32.46°$, 36.72°, 38.96°, 45.64°, and 67.06°, which is consistent with the Al_2O_3 crystalline structure according to the JCPDS card number 46-1215[137]. No noticeable reflection crests from other elements are observed from the spectrum. As shown in Fig. 6.13(b), the XRD test revealed a monoclinic structure with the main diffraction peak at $2\theta = 26.465°$ for the graphene confirming that there is no impurity in the structure of the graphene. Furthermore, the structure of the graphene is confirmed by the presence of the exact low-diffraction peaks in the XRD diagram [138].

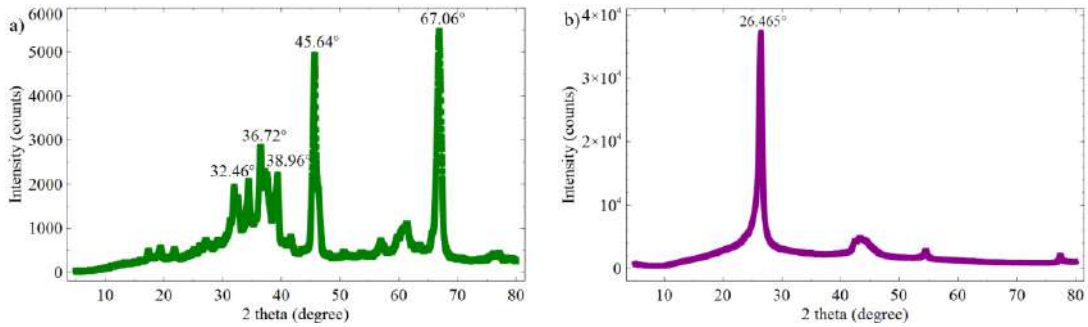

Fig. 6.13: XRD pattern of (a) Al_2O_3 nanoparticles (b) XRD pattern of GNP

6.6.2 Scanning Electron Microscopy (SEM)

SEM images will reveal clear indications of surface morphology and orientation of materials making up the sample. Figures 6.14(a) and (b) provide the SEM images of dry Al_2O_3 nanoparticles, demonstrating the nanostructures' distribution and shape. The images illustrate a fine particulate matter of Al_2O_3, and it can be observed that they form agglomerates of various geometries with rounded edges. These agglomerates are not ready to form stable suspensions. To develop a stable nanofluid, these agglomerates must be broken down using magnetic stirring and ultrasonic agitation.

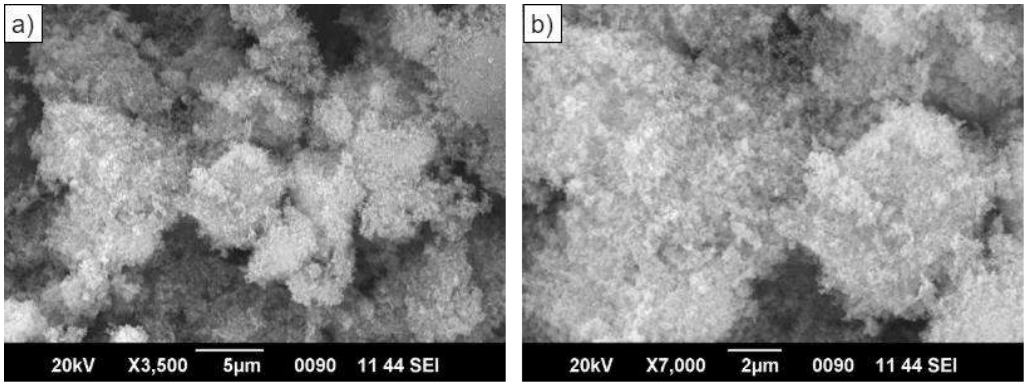

Fig. 6.14: SEM images of Al_2O_3 nanoparticles (a) 3500x magnification (b) 7000x magnification

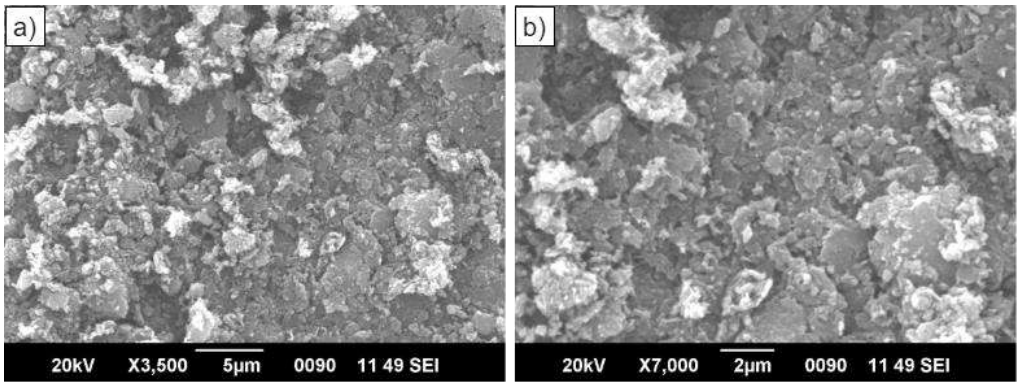

Fig. 6.15: SEM images of GNP (a) 3500x magnification (b) 7000x magnification

SEM images of GNP at two different magnifications are represented in Figs. 6.15(a) and (b). The electron microscopy images of the GNP sample show many individual

platelets on the structure. It is observed from Figs. 6.15(a) and (b) that the platelets are randomly distributed as a flake-like structure.

6.6.3 Optimisation of synthesis procedure of the hybrid nanofluid

Initially, samples of TH55- GNP(0.1 wt.%)/ Al_2O_3(1.0 wt.%) hybrid nanofluids with and without OA are agitated for one hour at 1600 rpm using a magnetic stirrer. Then the influence of ultrasonication time and the addition of OA on viscosity and thermal conductivity of the samples is measured from 1 h to 5 h of ultrasonication time.

6.6.3.1 Influence of ultrasonication time

The optimum time required for ultrasonication is determined by tracking the changes in dynamic viscosity and thermal conductivity of the hybrid nanofluid as a function of ultrasonication time. Figure 6.16 illustrates the variation of viscosity of the hybrid nanofluids at 30°C at different ultrasonication times. As the ultrasonication duration increases, the viscosity of both of the hybrid nanofluids decreases and the difference in viscosity between the three hours and four hours of ultrasonication is negligible. From Fig. 6.16, it is also observed that the addition of OA did not significantly affect the viscosity of the hybrid nanofluid.

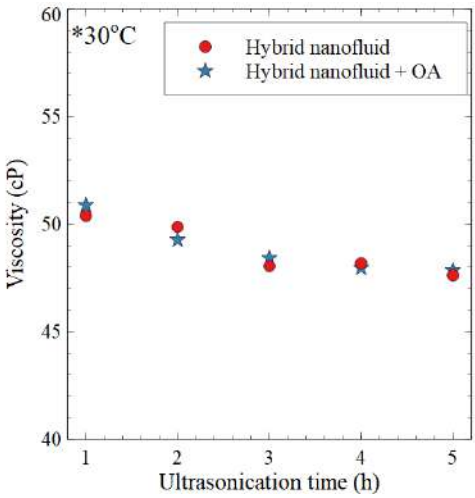

Fig. 6.16: Viscosity as a function of ultrasonication duration for the hybrid nanofluids at 30°C

The effect of the presence of the OA dispersant and the ultrasonication time on the thermal conductivity of the hybrid nanofluid at 30°C is shown in Fig. 6.17. From Fig. 6.17, it is noticed that the thermal conductivity of the hybrid nanofluid without OA is comparable to that of the dispersant-added nanofluid throughout the ultrasonication duration. It is also observed that with very little difference in thermal conductivity for three hours and four hours ultrasonicated hybrid nanofluid samples, the ultrasonication time of three hours seems sufficient.

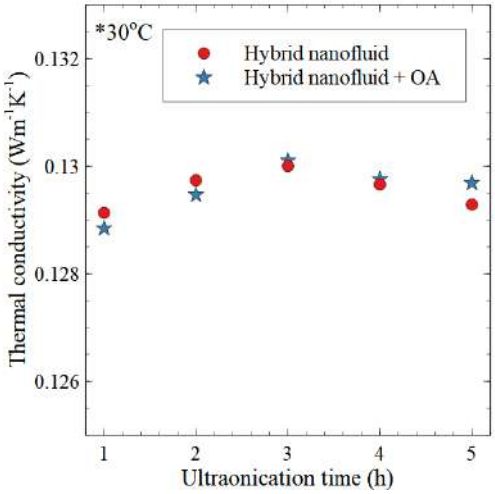

Fig. 6.17: Thermal conductivity of hybrid nanofluids at 30°C for different ultrasonication time

6.6.3.2 Influence of OA dispersant on the stability of the nanofluids

Dispersion stability of nanofluid is a significant concern regarding its heat transfer performance. Zeta potential analysis, UV-Vis spectral analysis, and light scattering methods are some of the important methods employed by several researchers to analyse nanofluids' stability [139]. A nanofluid's dispersion stability can be evaluated using a UV-vis-NIR spectrometer that uses Beer-Lambert's law since absorbance at a particular wavelength depends on the amount of dispersed nanoparticles in the nanofluid. In this study, the dispersion stability evaluation of the hybrid nanofluid has been performed using a Shimadzu UV-3600 series spectrometer over a time span of 14 days. A higher magnitude of absorption is the indication of a stable nanofluid.

The UV-Vis absorption spectra of the hybrid nanofluid with and without adding OA after one day and 14 days of preparation are shown in Fig. 6.18. With the addition of OA, the maximum absorbance peak of the fluid is shifted from 338 nm to 444 nm. Another major difference that appeared due to the addition of OA is the presence of a unique negative absorption at low wavelengths. Negative absorption might be caused by the light excitation of samples at lower wavelengths from ground states to lower molecular states or excited states and then reverted to lower molecular orbits. This light excitation causes an emission with absorbance less than zero or transmission higher than 100%. The negative absorption phenomena of ethanol, chloroform and water were presented in the literature [140].

It is notable that the absorption of both nanofluids after one day of preparation is nearly comparable. That is, the surfactant addition did not significantly affect the initial stability of the hybrid nanofluid. However, it is observed that the absorption of nanofluids is degraded with time. After 14 days of preparation, the maximum absorbance of the hybrid nanofluid with OA is 0.658, while that of the hybrid nanofluid without OA is 0.45. After 14 days of preparation, the absorbance of the hybrid nanofluid with dispersant is nearly 46% higher than that of the hybrid nanofluid without using the dispersant.

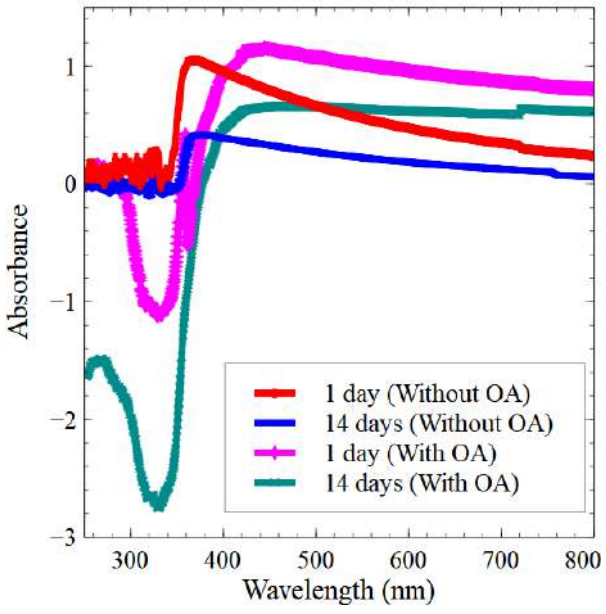

Fig. 6.18: UV-Vis spectrum of hybrid nanofluids with and without OA dispersant

The main reason behind the better dispersion stability of the hybrid nanofluid is the decrease in surface tension and the change of polarity of nanoparticles caused by the addition of OA [61]. The dispersion agent provides sufficient repulsive forces between the particle molecules to counteract the Van der Waals forces of attraction between the particles, resulting in higher stability over the period of observation. Furthermore, the dispersion agent alters the surface charge and enhances the repulsive forces between the nanoparticles, which also adds to enhanced stability.

6.6.3.3 Thermophysical properties

Based on the enhanced properties due to the desirable synthesis procedure, one hour of magnetic stirring at 1600 RPM followed by three hours of ultrasonication duration at 4000 Hz, TH55-Al_2O_3(1.0 wt.%)/GNP(0.1wt.%) hybrid nanofluid is prepared with and without OA. The temperature-dependent viscosity and thermal conductivity variation are investigated to assess the role of OA addition in the hybrid nanofluid.

6.6.3.3.1 Viscosity

The viscosity of the base fluid and the hybrid nanofluids between 20°C to 90°C are measured using the Brookfield cone and plate viscometer. It is observed from Fig. 6.19 that the viscosity of both hybrid nanofluids is higher than that of pure TH55 oil. There is not much variation between the viscosities of the surfactant-added and surfactant-free hybrid nanofluids.

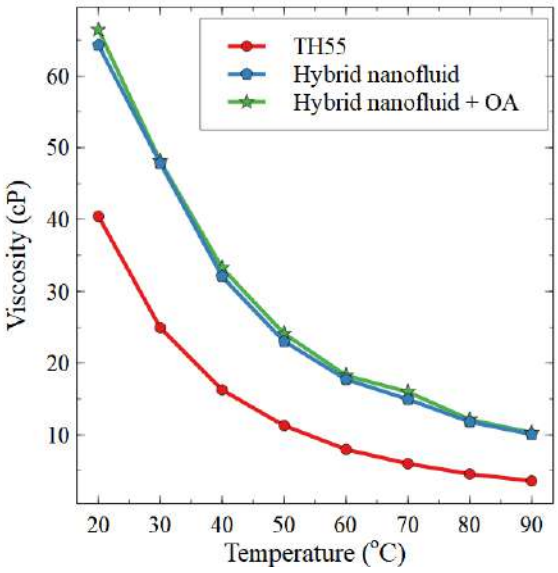

Fig. 6.19: Viscosity of the base fluid and hybrid nanofluids

It can be inferred that OA surfactant does not affect the viscosity of the TH55-Al_2O_3/GNP hybrid nanofluid. Furthermore, the viscosities of all fluids decreases with an increase in temperature. At 20°C, the viscosities of the surfactant-free and surfactant-added hybrid nanofluids are 59% and 64.34% greater than that of the TH55 oil. However, when the temperature increases from 20°C to 90°C, the enhanced viscosities of both hybrid nanofluids are reduced by approximately 84%.

6.6.3.3.2 Thermal conductivity

Thermal conductivities of the fluids between 25°C to 65°C are measured using the KD2 pro thermal property analyser after one day of preparation. Figure 6.20 shows the thermal conductivity of the base fluid, surfactant-free and surfactant-added hybrid nanofluid as a function of temperature. The results shows that, with the increase in temperature the thermal conductivity of TH55 decreases whereas it increases for hybrid nanofluids. Because of the Brownian motion of the nanoparticles in the fluid, the effective thermal conductivity of this suspension is increased. Another reason for the higher thermal conductivity of the hybrid nanofluids is the high aspect ratio platelets of graphene with a high diffusive heat conductivity [141]. Furthermore, the GNPs are interlinked and entwined, as shown in the TEM image (Fig. 6.22). As a result, the GNP can form networks, which might act as a conduction path.

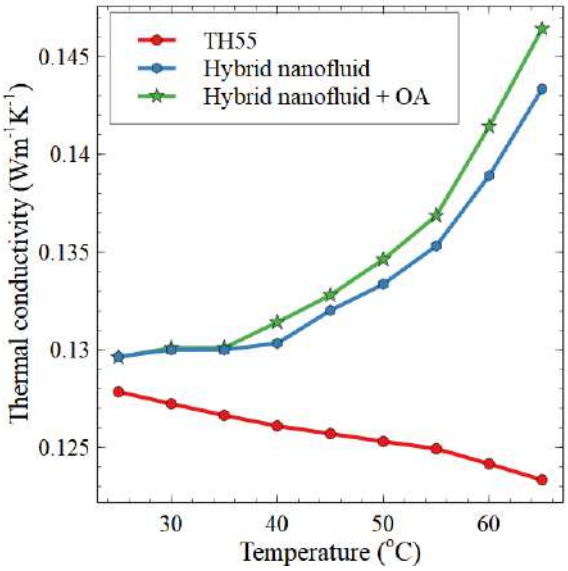

Fig. 6.20: Thermal conductivity of the base fluid and hybrid nanofluids

The results demonstrates that the surfactant-free hybrid nanofluid has thermal conductivity enhancement of 16.22% as compared to TH55 oil at a temperature of 65°C. At 65°C, the surfactant-added hybrid nanofluid has a thermal conductivity enhancement of 18.72% over the base fluid. As a result, the addition of OA contributes 2.5% thermal conductivity to the hybrid nanofluid. This indicates that the uniform dispersion of nanoparticles caused by the surfactant effect leads to enhanced thermal conductivity [142].

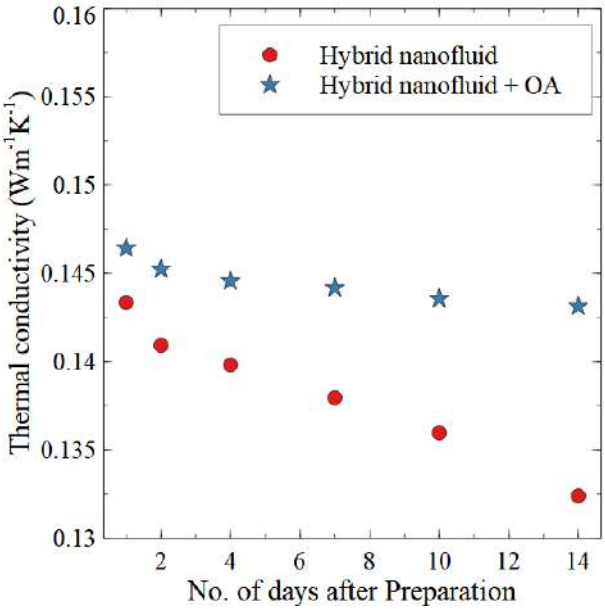

Fig. 6.21: Thermal conductivity of the samples vs storage time at 65°C

The variation of thermal conductivity with time is recorded for the samples, and the results are shown in Fig. 6.21. As illustrated in Fig. 6.21, the thermal conductivity of both hybrid nanofluids diminishes with time, indicating that nanoparticles agglomerate and sediment over time. However, the rate of decrease in thermal conductivity of the surfactant-free hybrid nanofluid with storage time is substantially faster than that of the surfactant-added hybrid nanofluid. The thermal conductivity of the surfactant-added hybrid nanofluid dropped by 2.24 % after 14 days of storage compared to the thermal conductivity after one day of preparation. In contrast, the corresponding reduction in thermal conductivity for the surfactant-free hybrid nanofluid is 7.64%. As a result, adding OA as a surfactant in TH55-Al_2O_3/GNP is highly favourable to the nanofluid's long-term stability and hence thermal conductivity.

Based on the results, magnetic stirring for 1 hour at 1600 RPM followed by ultrasonication for 3 hours at 4000 Hz appears to be optimum for the TH55-Al_2O_3/GNP hybrid nanofluid with OA as a surfactant. So 3 hours of ultrasonication time is chosen as the desirable ultrasonication period for this hybrid nanofluid. Hence, further research is conducted on the nanofluids by developing them through the above synthesis procedure.

6.6.4 Transmission Electron Microscopy (TEM)

The detailed sub-structures of the Al_2O_3-GNP suspension obtained from the TEM images are shown in Figs. 6.22(a) and (b). It is observed that the nanomaterials are clearly suspended in the base fluid and have a size of less than 100 nm. TEM micrographs confirmed the spherical shape of Al_2O_3 nanoparticles with particle sizes ranging from 14.96 nm to 68.86 nm in diameter. The most transparent and featureless regions in Figs. 6.22(a) and (b) are likely graphene mono sheets. GNP are well distributed on the surface of nano-Al_2O_3 particles. The TEM images indicate that the nanoparticles are well dispersed, and the proposed hybrid nanomaterials agree with the desired characteristics.

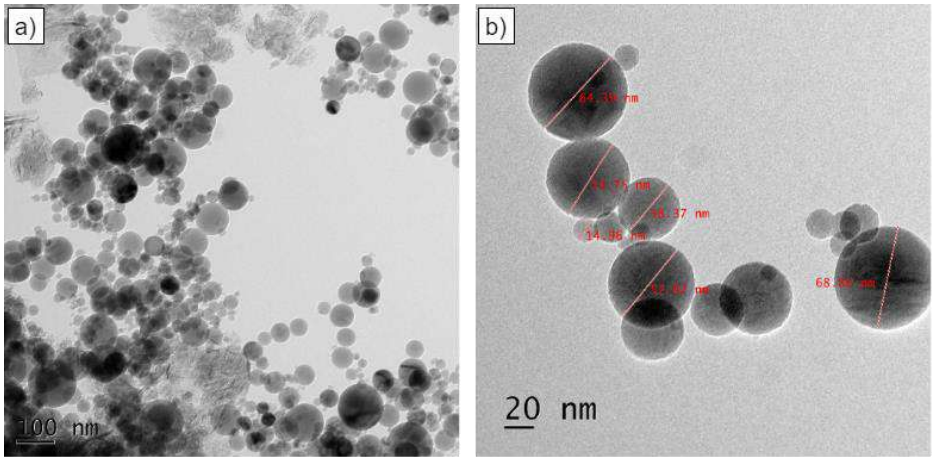

Fig. 6.22: TEM images of Al_2O_3-GNP suspension (a) scale bar is 100nm, (b) scale bar is 20 nm

Figure 6.23 depicts Selected Area Electron Diffraction (SAED) conducted on a particular region of the graphene sheet along with TEM. The well-defined diffraction spots indicate the crystalline structure of GNP. The diffraction pattern shows the typical sixfold symmetry expected for graphene, conforming to the crystalline nature of the graphene sheets and is compared with the previously reported SAED pattern of graphene [143].

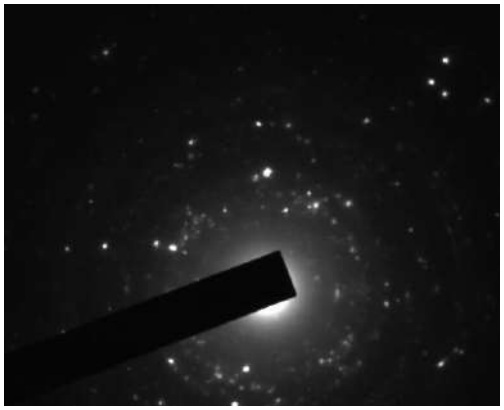

Fig. 6.23: SAED pattern of GNP

6.6.5 Dispersion stability analysis using UV-vis. spectroscopy

Figure 6.24 depicts the absorbance of the TH55- Al_2O_3/GNP hybrid nanofluid after one day, five days, and fourteen days of preparation. The peak absorbance of the hybrid nanofluid occurs at 445 nm wavelength. As shown in Fig. 6.24, the results showed a slow and gradual decreasing suspension stability over time. The peak absorbance of the sample after one day of preparation is 1.154. After five days of nanofluid preparation, the peak absorptance drops to 0.726; after fourteen days, it drops further to 0.658. As increasing the storage time, UV absorption decreases under the higher wavelength. Figure 6.24 clearly shows that UV absorption decreases with greater storage duration. However, the absorbance of 0.658 after fourteen days of the nanofluid preparation is a promising indication of the good stability of the nanofluid. Furthermore, the HTF does not have a long idle time in solar thermal applications, which further lowers the possibility of nanoparticle settling.

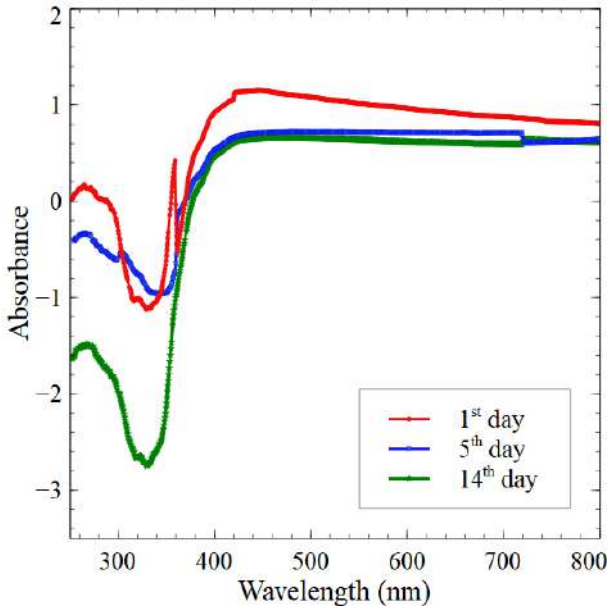

Fig. 6.24: UV spectrographs of TH55-GNP/Al_2O_3 hybrid nanofluid

6.7 Thermophysical properties

This section encapsulates the thermophysical properties of the proposed hybrid nanofluid. Thermophysical properties, including the effective thermal conductivity, dynamic viscosity, and specific heat, are estimated for the base fluid, mono-nanofluids and hybrid nanofluid and are presented.

6.7.1 Thermal conductivity

The thermal conductivities of nanofluids between 25°C to 65°C are measured using a KD2 pro thermal property analyser. GNP and Al_2O_3 nanoparticles are responsible for increasing the thermal conductivity of TH55-GNP/Al_2O_3 hybrid nanofluid. To study the effect of each of these particles on the thermal conductivity of the nanofluid, the thermal conductivity of TH55-Al_2O_3, TH55-GNP mono-nanofluids, and hybrid nanofluid are monitored separately.

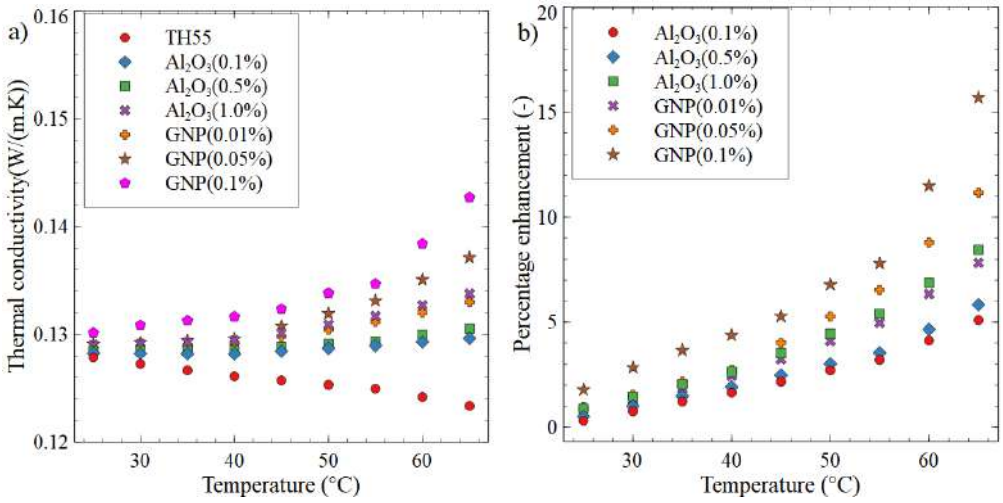

Fig. 6.25: Variations of (a) thermal conductivity of mono-nanofluids and (b) percentage thermal conductivity enhancement of mono-nanofluids at various particle loadings under the influence of temperature

The thermal conductivity increases with the rise in Al_2O_3 and GNP nanoparticles concentrations. The variation of thermal conductivity and percentage of thermal conductivity enhancement of mono-nanofluids at various particle loading under the

influence of temperature is depicted in Figs.6.25 (a) and (b), respectively. The increase in thermal conductivity is due to the solid materials, which have higher thermal conductivity than liquids. GNP and Al_2O_3 nanoparticles, for example, have thermal conductivities of about 5000 W/(m. K) and 40 W/(m. K), respectively, while TH55 has a thermal conductivity of about 0.1284 W/(m. K). Accordingly, the thermal conductivity of GNP nanofluids increases significantly with rising temperature, while the thermal conductivity of Al_2O_3 nanofluids increases only slightly. At 65°C, the maximum thermal conductivity improvement for TH55-Al_2O_3 mono-nanofluid containing 1.0% Al_2O_3 is 8.44%. The results show that mono-nanofluid's maximum enhancement of thermal conductivity is 15.69%, which occurs in a GNP weight fraction of 0.1% and a temperature of 65°C. The higher thermal conductivity is mainly caused by the high specific surface energies associated with the large surface area of GNP per unit volume.

The thermal conductivity ratio (k_{ratio}) as a function of weight fraction and temperature has been used to quantify thermal conductivity enhancement efficiently, as depicted in Fig. 6.26. The thermal conductivity of all the tested mono-nanofluid is observed to be maximum at the highest solid concentration. When temperature increases from 25°C to 65°C, the k_{ratio} increases from 1.009 to 1.084 at 1% weight fraction of Al_2O_3 mono-nanofluid, connoting an augmentation of 7.49%. When GNP wt.% in the mono-nanofluid is 0.1%, as the temperature ascents from 25°C to 65°C, the k_{ratio} also rises from 1.018 to 1.156, which means an increase of 13.66%.

According to Fig. 6.26(b), the temperature of the hybrid nanofluid contains 0.1wt.% GNP rises from 25°C to 65°C, and the k_{ratio} increases from 1.014 to 1.187, indicating that the k_{ratio} growth rate is 17.1%. These improvements in thermal conductivity are due to the positive effect of clustering caused by the Van der Waals forces of the nanoparticles as the number of particles increases [144]. As a result, the nanoparticle solid weight fraction decides the improvement in the thermal conductivity of nanofluids.

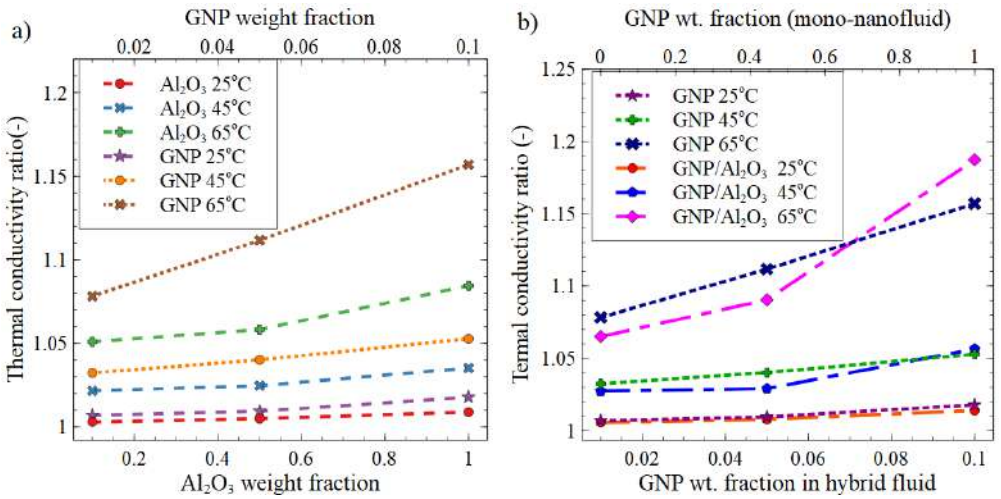

Fig. 6.26: Variations in thermal conductivity ratio and volume fractions (a) mono-nanofluids, (b) GNP mono and hybrid fluids

Figures 6.27(a)-(b) depicts the thermal conductivity of hybrid and mono-nanofluids and their percentage improvements at various temperatures. Figure 6.27(a) shows that the thermal conductivity of all nanofluids increases with an increase in temperature. As shown in Fig. 6.27(b), the percentage raise in the thermal conductivity of mono and hybrid nanofluids in relation to TH55 gives a general overview of the increase in each sample's thermal conductivity. Thermal conductivity of TH55-Al_2O_3 mono-nanofluid increased by 5.09%, 5.83%, and 8.44% at higher temperatures for 0.1%, 0.5%, and 1.0% solid concentrations, respectively. The collisions between the nanoparticles increases due to the induced Brownian motion at higher temperatures. The increase in counts of nanoparticles with the increase in weight concentration also leads to Brownian motion influenced collisions. Thermal conductivity enhancement of TH55-GNP mono-nanofluid is substantially higher than TH55-Al_2O_3 mono-nanofluid. Thermal conductivity of TH55-GNP mono-nanofluid increased by 7.82%, 11.16%, and 15.69% at higher temperatures for 0.01%, 0.05%, and 0.1% mass concentrations, respectively. It is evident that this dramatic increase in thermal conductivity in the TH55-GNP mono-nanofluid occurs at very low mass concentrations as compared to the mass concentrations of Al_2O_3 nanoparticles. So it can be observed that the graphene nanofluids respond more sensitively to the temperature than Al_2O_3 nanofluids. This substantial difference is due to the greater thermal conductivity of GNP than Al_2O_3 nanoparticles. Therefore, the thermal conductivity of nanoparticles plays an important role in increasing the thermal conductivity for the specific base fluid nanofluid.

Additionally, the TEM image in Fig. 6.22 shows that the graphene nanoplatelets are linked and entwined. This indicates that the GNP can constitute networks, which might serve as a conduction channel. In addition to Brownian motion, a nano-layer structure is formed by the liquid interfacial layer between liquid molecules and nanoparticle platelets. These nano-layered structures serve as a thermal path between the solid nanoparticles and bulk liquid molecules. They are present in an intermediate state, leading nanofluids to have higher thermal conductivity than the bulk single-phase base fluid [145].

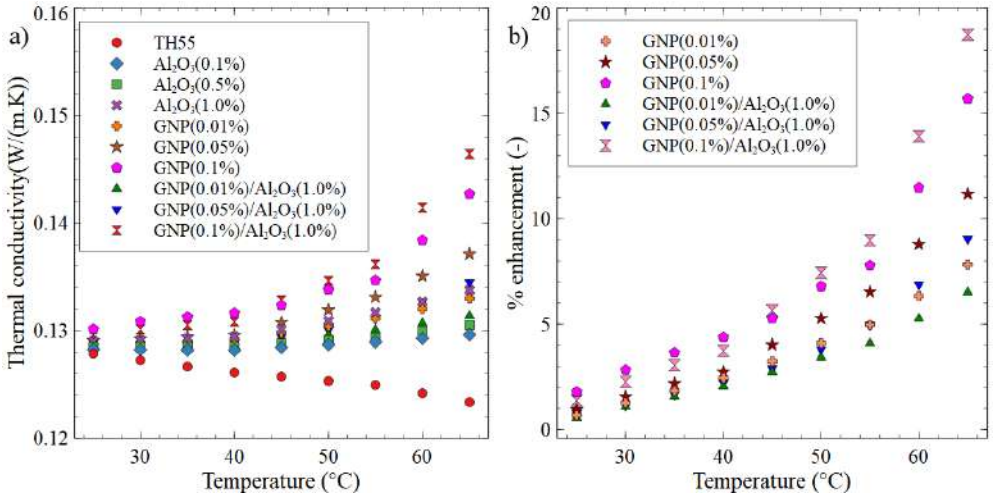

Fig. 6.27: (a) Thermal conductivity of mono and hybrid nanofluids and (b) percentage enhancement in thermal conductivity

Al_2O_3 mono-nanofluids have low thermal conductivity, varying from 0.1282 $Wm^{-1}K^{-1}$ to 0.1337 $Wm^{-1}K^{-1}$ from 25°C to 65°C. While, GNP mono-nanofluids exhibit a higher thermal conductivity value, ranging from 0.1287 $Wm^{-1}K^{-1}$ to 0.1427 $Wm^{-1}K^{-1}$ for the same reference temperature of 25°C to 65°C. This indicates that Al_2O_3 nanoparticles have a relatively low contribution in augmenting the thermal conductivity of the base fluid. The higher surface area of graphene due to its plate structure favours the higher rate of heat conduction in the hybrid nanofluid with GNP particles. It is interesting to note that the thermal conductivity of the TH55-GNP/Al_2O_3 hybrid nanofluids at temperatures ranging from 25°C to 65°C is different from that of the TH55-GNP and TH55-Al_2O_3 mono-nanofluids.

The hybrid nanofluid with the lowest weight fraction of GNP (TH55-GNP(0.01%)/Al_2O_3(1.0%)) showed a lower thermal conductivity than TH55-GNP(0.01%) mono-nanofluid. The thermal conductivity of TH55-GNP(0.05%)/Al_2O_3(1.0%) hybrid nanofluid is in between the values of the mono-nanofluid samples of TH55-GNP(0.01%) and TH55-GNP(0.05%). However, it is much closer to the thermal conductivity of the TH55-GNP(0.05%) mono-nanofluid. The thermal conductivity of TH55-GNP/Al_2O_3 hybrid nanofluids is lower than that of TH55-GNP mono-nanofluids at lower weight concentrations of GNP (0.01% and 0.05%). They are, however, significantly more significant than the thermal conductivity of Al_2O_3 mono-nanofluids.

At room temperature, the thermal conductivities of the TH55 oil, Al_2O_3 nanoparticles and GNP are approximately 0.1273 W/(m.K), 40 W/(m.K), and 5000 W/(m.K), respectively. Accordingly, the thermal conductivity of TH55 enhances with the addition of nanoparticles. Compared to GNP mono-nanofluids, the thermal conductivity enhancement of Al_2O_3 mono-nanofluids is low. At lower particle concentrations (0.01% and 0.05%), the thermal conductivity of GNP mono-nanofluids is higher than that of the hybrid nanofluids containing the same GNP particle concentrations. This indicates that the synergy between the Al_2O_3 and GNP on TH55 is ineffective at lower GNP concentrations. The synergistic effect refers to the combined influence of the distinct phases of solid particles and fluid.

Similarly, at lower temperatures up to 40°C, the thermal conductivity of the hybrid nanofluid with a GNP concentration of 0.1% is smaller than that of the GNP mono-nanofluid at the same concentration of GNP. But, it surpasses at higher temperatures beyond 45°C (Fig. 6.27). The sharp reduction in viscosities with the rise in temperature noted in the study may induce micro-convection through Brownian motion of nanoparticles dispersed in the base fluid [146]. To be more specific, this enhancement of thermal conductivity can be attributed to the enhanced micro-convection accompanied by the synergic effect of combining GNP and Al_2O_3 nanoparticles in the hybrid suspension, which is probably responsible for a substantial increase in its thermal conductivity at temperatures above 45°C. The second factor is related to the particle size and structure effect [147]. There is an adhesive force of attraction between the bigger and smaller nanoparticles. As shown in TEM images (Fig.6.22), the 2D GNP platelets stick over the larger Al_2O_3 nanoparticles and serve as fins. Due to this attachment of more nanoparticles

one over the other, the thermal conductivity enhancement can happen due to the increased conduction and the convection effect.

The maximum thermal conductivity enhancement obtained for hybrid samples of TH55-GNP(0.01%)/Al_2O_3(1.0%), TH55-GNP(0.05%)/Al_2O_3(1.0%), and TH55-GNP(0.1%)/Al_2O_3(1.0%) is 6.5%, 9.04%, and 18.72%, respectively. Compared to the TH55-GNP mono-nanofluid, the hybrid nanofluid has a 3.03% increase in thermal conductivity at 65°C. At the same time, the hybrid nanofluid has a 10.28% increase in thermal conductivity compared to the TH55-Al_2O_3 mono-nanofluid. For the same performance enhancement, a small concentration/wt % of hybrid nanoparticles is sufficient compared to the conventional mono nanofluids. The use of hybrid nanofluids reduces viscosity and hence decreases the pumping power and pressure drop. Because of the reduced particle loading of the GNP and the lower expense of GNP and Al_2O_3 nanoparticles, the use of hybrid nanofluid lowers the cost of nanofluid processing and makes it more profitable. Furthermore, the hybrid nanofluid significantly increases its thermal conductivity compared to the existing Al_2O_3 mono nanofluids, leading to a high heat transfer rate within the flow.

6.7.2 Viscosity

The influence of temperature and solid volume fraction on the viscosity of the base fluid, Al_2O_3 (1.0wt.%) and GNP(0.1wt%) mono-nanofluids, and hybrid nanofluids is depicted in Fig. 6.28, a decrease in viscosity with temperature is observed over the entire temperature range. The measured results also revealed that the dynamic viscosity of the nano-HTFs increases as the nanoparticle concentration increases. This is due to the enhanced Van der Walls force between base fluid and atoms or molecules of nanoparticles [148]. However, the viscosity of the various nanofluid samples decreases by 91.17%, 88.33%, 88.91%, 89.15%, 88.29%, and 84.5% for pure TH55 oil, 1.0wt%Al_2O_3 mono-nanofluid, 0.1% GNP mono-nanofluid, 0.01, 0.05, and 0.1 GNP wt% hybrid nanofluids respectively from 20°C to 90°C.

The results indicate that all nanofluid samples exhibit a common tendency to decrease viscosity. With the increase in temperature, the viscosity of the high

concentration hybrid sample decreases by 26.02 to 6.72 mPa.s compared to pure TH55 oil. Although the particle loading percentage of GNP is much lower than that of Al_2O_3, it should be noted that the viscosity of GNP mono-nanofluid is higher than that of Al_2O_3 mono-nanofluid. This implies that using higher GNP concentrations is particularly undesirable since the effective viscosity of nanofluid increases with concentration.

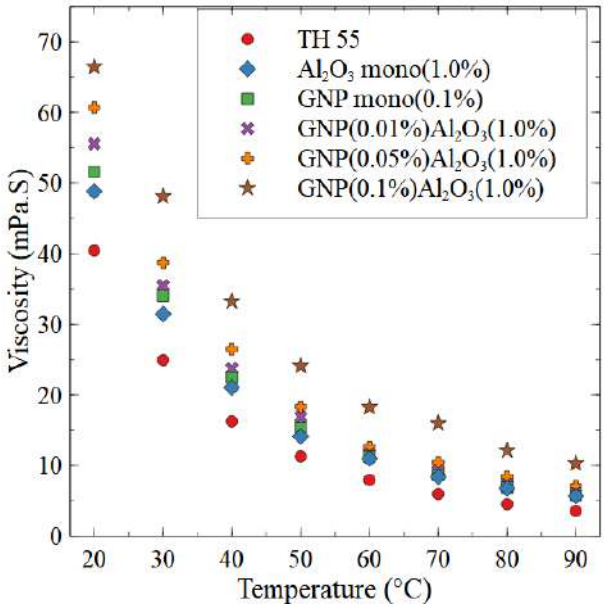

Fig. 6.28: Effect of temperature on viscosity for different nanofluids at 50/s shear rate

Relative viscosity, the ratio between the nanofluid viscosity and base fluid viscosity, is essential in ascertaining the excess pressure drop that would be incurred while pumping them. Lower values of relative viscosities are preferred to reduce the pressure drop and additional power required for pumping nanofluids. Figure 6.29 shows the influence of temperature on the relative viscosity of the nanofluids. The comparatively higher relative viscosity of TH55-GNP(0.1%)/Al_2O_3(1.0%) hybrid nanofluid with temperature, as shown in Fig. 6.29, may be attributed to either increased particle clustering or Brownian motion [149] or both. Hence there might be particle aggregation with a higher concentration of GNP when heated to high temperature.

Figure 6.30 shows the effect of shear rate on the dynamic viscosity of TH55-GNP/Al_2O_3 hybrid nanofluid, Al_2O_3 mono-nanofluid, and its base fluid. The viscosity studies are performed over the range of shear rate from 5 to 150/s at a temperature of

80°C. The viscosity of the TH55 increases with the addition of nanoparticles. This is because the frictional resistance between the neighbouring layers of the TH55 and nanoparticles and between GNP and Al_2O_3 with the development of inter-particle layers increases significantly [150]. In this study, the viscosity enhancement of hybrid nanofluid for the highest graphene concentration of 0.1% is around 66.69% higher in comparison to TH55 at 20°C. Despite a nanoparticle concentration (Al_2O_3+TiO_2) of just 0.5%, Gulzar *et al.* [61] reported a 24% increase in viscosity for TH55-Al_2O_3/TiO_2 (60:40) hybrid nanofluid at 20°C. The 66.69% increase in viscosity obtained in the present study is therefore reasonable, considering that this study employed 1.1% nanoparticle (Al_2O_3+GNP) weight concentration, which is nearly 2.2 times that used by Gulzar *et al.* [61]. Furthermore, due to its platelet structure, GNP could exert higher shear force on liquid molecules than Al_2O_3 and TiO_2 nanoparticles. As demonstrated in Fig. 6.28, the improvements in viscosity are insignificant at higher temperatures, implying that the TH55-GNP/Al_2O_3 hybrid nanofluid's suitability as HTF and broadening its scope for medium temperature applications.

Furthermore, the observations of hybrid nanofluids with 0.01 and 0.05% GNP solid concentration show a slight variation in dynamic viscosity with an increase in shear rate. This confirms that the hybrid nanofluid strongly adheres to the Newtonian character up to a fraction of 0.05% GNP solid concentration. However, as shown in Fig. 6.30, the shear rate slightly influences the dynamic viscosity of the hybrid nano-HTF at 0.1 GNP solid concentration, implying that increasing the GNP concentration further may result in non-Newtonian behaviour. This is due to GNP's high specific surface area, which leads to irreversible agglomerates or Van der Walls interactions between the platelets with increasing GNP concentration.

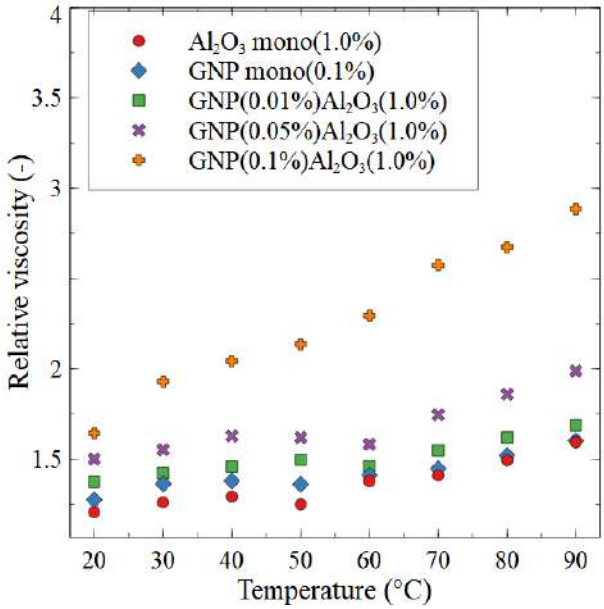

Fig. 6.29: Relative viscosity of nanofluids as a function of temperature

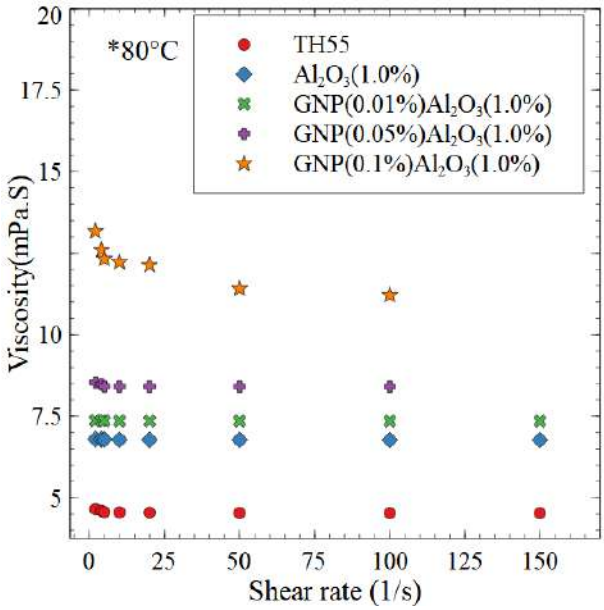

Fig. 6.30: Effect of shear rate on viscosity for different nanofluids at 80°C

6.7.3 Specific heat

Specific heat capacities of TH55 based mono and hybrid nanofluids are measured in the temperature range of 20 to 100°C. As demonstrated in Fig.6.31, each of these nanofluids' specific heat reduction percentage increases as the concentration of solid particles and temperature rise. At 100°C, the heat capacity of the Al_2O_3 (1.0%wt.) and GNP (0.1 wt.%) mono-nanofluids decreased by 2.18% and 3.83%, respectively; as

compared with the pure TH55 oil. Because of its more excellent thermal conductivity and lower specific heat, GNP nanoparticles have been observed to have a more substantial influence on lowering the specific heat of the base fluid. Some researchers have shown a similar tendency for the specific heat of nanofluid to decrease as the volume fraction increases [151]. Ghazatloo *et al.* [152] have also demonstrated a decrease in graphene-water nanofluid's heat capacity, which has been increased by increasing the concentration of graphene nanoparticles.

As shown in Fig. 6.32, the specific heat of nanofluids decreases when the solid concentration of nanoparticles increases. It is observed that when nanoparticles are added to the base fluid, the specific heat of the nanofluid drops as the nanoparticle weight concentration increases. A similar trend for specific heat capacity is presented by Minea *et al.* [72]. Besides, it can be observed that the specific heat capacity of nanofluids increases with temperature, indicating that the temperature impacts the specific heat more strongly than the mass fraction of nanoparticles. For different oil-based nanofluids, a similar pattern of findings is observed in which the specific heat capacity decreased with increasing particle loading and increased with increasing temperature [153]. In addition, it is notable that at higher GNP concentrations (0.05 and 0.1wt%), the specific heat of hybrid nanofluids increases up to 80°C but decreases with further temperature increases.

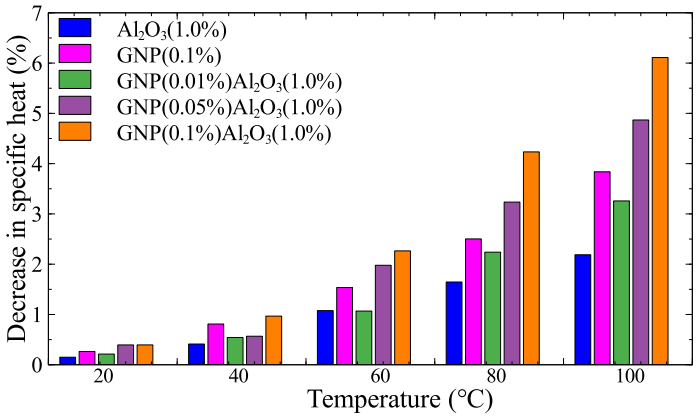

Fig. 6.31: Reduction in specific heat as compared with the base fluid

A similar phenomenon has been reported in the literature [154]. At 100°C, the specific heat capacity of 0.01, 0.05, and 0.1 GNP wt% hybrid nanofluids in the present

study are nearly 3.25%, 4.86%, and 6.11 % less than that of the base fluid. Yarmand *et al.* [155] measured the specific heat capacity of functionalised GNP-Platinum hybrid suspension of distilled water using a differential scanning calorimeter. They observed a 6.26% lower nanofluid specific heat capacity than the base fluid for a nanoparticle concentration of 0.1wt% at 45°C. The heat capacity values of TH55, Al_2O_3 and GNPs at 25°C are around 1.91, 0.765, and 0.79 kJ/kg.K, respectively. Hence, the Al_2O_3 and GNP loading in TH55 would significantly reduce the effective specific heat of the resulting hybrid nanofluid.

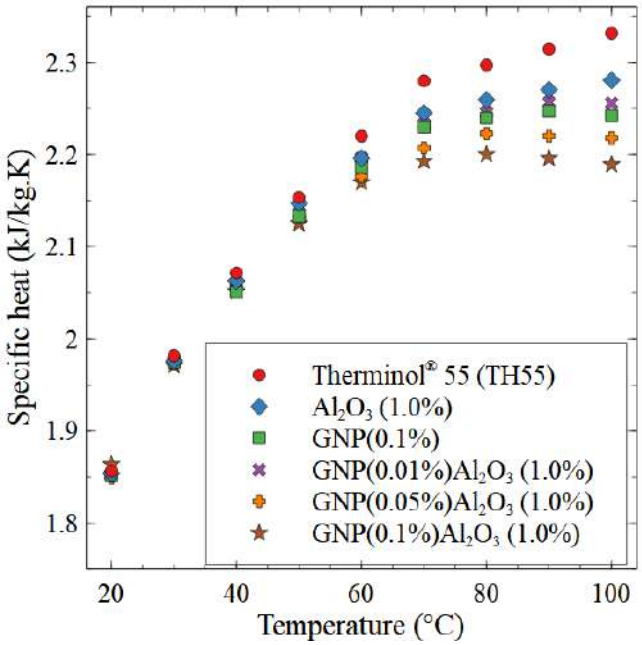

Fig. 6.32: Specific heat of nanofluids at different temperatures

In general, the specific heat of nanofluid can be increased or lowered compared to that of the base fluid. This tendency is influenced by the nanoparticles' nature and size, temperature, and type of base fluid. However, if the heat capacity of nanomaterials is less than that of the base fluid, the heat capacity of nanofluid drops; otherwise, it rises. The specific heat capacity value of TH55, Al_2O_3 and GNPs at 25°C are around 1.91, 0.765, and 0.79 kJ/kg.K, respectively. Hence, the Al_2O_3 and GNP loading in TH55 would significantly reduce the effective specific heat of the resulting nanofluid.

6.7.4 Density of nanofluids

The density of nanofluids has been reported to be consistent with the theory of mixtures [156]. The following is a relationship for the effective density of mono-nanofluids (ρ_{mnf}) based on the mass balance using conventional mixing theory [157].

$$\rho_{mnf} = (1 - \varphi_{np})\rho_{bf} + \varphi\rho_s \tag{6.15}$$

The experimental findings reported by Pak and Cho [158] are consistent with the values estimated with Eq. (6.15). The correlation for effective density of hybrid nanofluid (ρ_{hnf}) as a function of weight fraction (φ), which is derived from the theory of mixing [159], is given in Eq. (6.16). Ho *et al.* [156] and many researchers have confirmed the effective density of hybrid nanofluids by comparing the measured and predicted data from Eq. (6.16).

$$\rho_{hnf} = (1 - \varphi_1 - \varphi_2)\rho_{bf} + \varphi_1\rho_{s1} + \varphi_2\rho_{s2} \tag{6.16}$$

where ρ_{bf}, ρ_s, ρ_{s1}, and ρ_{s2} represent the density of the base fluid and corresponding nanoparticles, respectively, and φ represents the weight fraction of related nanomaterials. The densities of the mono and hybrid nanofluids are computed from the Eqs. 6.15 and 6.16 using the density of TH55 oil for temperatures of 20°C to 100°C [124]. A comparison between the increases in density against the nanoparticle weight fraction at various temperatures is depicted in Fig. 6.33.

The density of TH55 base-fluid increases with the addition of GNP and Al_2O_3 nanoparticles. Density decreases with an increase in temperature for all the fluids. Experimental studies reported in the literature with different base fluids and nanoparticles also show a similar trend [160]. TH55-GNP(0.1%) nanofluid density is slightly higher than that of TH55 oil, but the density of TH55-Al_2O_3 and TH55-GNP/Al_2O_3 nanofluids is considerably greater than that of TH55 oil. The increase in density of TH55 by the addition of Al_2O_3 nanoparticles is significantly higher in comparison with GNP because Al_2O_3 have a higher density (approximately two times) and higher weight concentration (almost ten times) in the base-fluid than GNP.

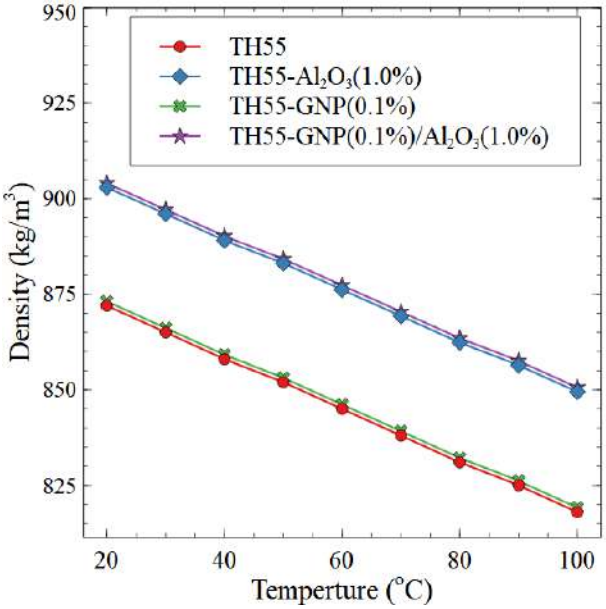

Fig. 6.33: Density variations with temperature

6.8 Thermophysical property models

In general, experiments or simulation results, as well as correlation models, are used to define the thermophysical properties of nanofluids. Due to the lack of models for predicting thermophysical properties of TH55-GNP/Al_2O_3 hybrid nanofluids, correlation models for predicting thermal conductivity, dynamic viscosity, and specific heat of the hybrid nanofluid have been developed in the study. To develop the models, the properties mentioned above of hybrid nanofluids with different GNP concentrations, such as 0.025% and 0.075%, and the current hybrid fluids with 0.01%, 0.05%, and 0.1% have been measured separately. The non-linear least square method is used to develop relationships between nanofluid temperature (T), GNP wt% (φ), and thermal conductivity (k).

6.8.1 Thermal conductivity model

No theoretical correlation is available in the literature for TH55-GNP/Al_2O_3 hybrid nanofluids for designated particle fraction and temperature. A relationship (Eq. (6.17)) between nanofluid temperature (T), GNP wt.% (φ), and thermal conductivity (k) has been developed to estimate the thermal conductivity of the hybrid nanofluid for a wide range of temperatures.

$$k(\varphi,T) = 0.1055 + 0.6761\varphi + 0.001097T - 3.247\varphi^2 - 0.02626\varphi T - 1.515e^{-05}T^2 + 0.08627\varphi^2 T + 0.0002225\varphi T^2 + 7.288e^{-08}T^3 \quad (6.17)$$

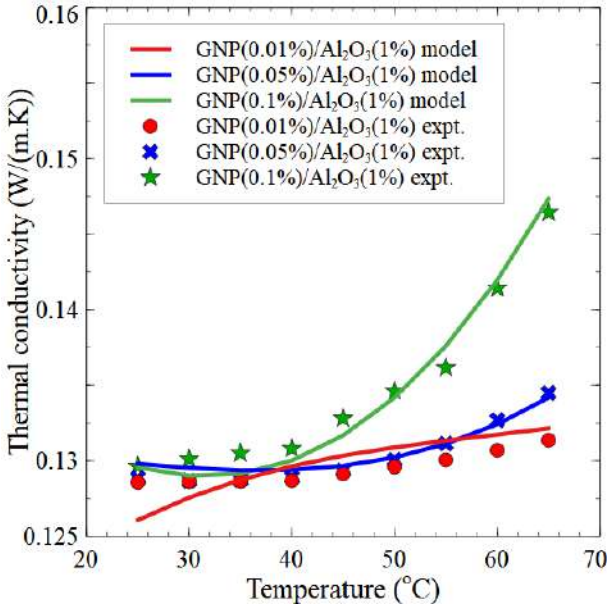

Fig. 6.34: Comparison of hybrid nanofluid thermal conductivity value between present data and proposed model

The correlation has a Root Mean Square Error (RSME) of 0.001155 and R^2 of 0.9961. The model is in good agreement within a 1.94% deviation compared to the experimental data, as shown in Fig. 6.34.

6.8.2 Viscosity model

Compared to single nanomaterial-based nanofluids, only a few empirical correlations were developed for hybrid nanofluids. However, there is no viscosity model for TH55-GNP/Al_2O_3 hybrid nanofluids available in the literature. Hence, in the present investigation, a new accurate correlation to predict the dynamic viscosity of the TH55-GNP/Al_2O_3 hybrid nanofluid in terms of temperature and nanoparticle weight fraction has been proposed as follows.

$$\mu(\varphi,T) = 116 + 106\varphi - 3.992T + 522.5\varphi^2 - 1.676\varphi T + 0.05056T^2 + 1.104\varphi^2 T + 0.002767\varphi T^2 - 0.0002194T^3 \quad (6.18)$$

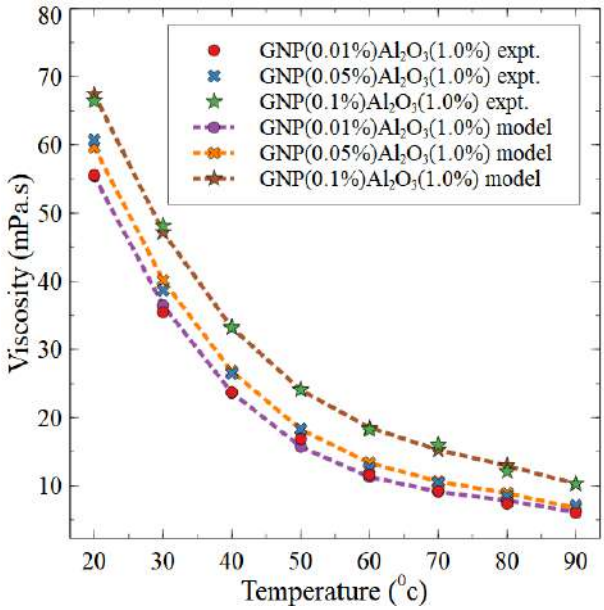

Fig. 6.35: Comparison of viscosity between experimental data and correlation output

For the developed model, the RSME and R^2 are found to be 0.6611 and 0.9989, respectively. As illustrated in Fig. 6.35, the fitting between the measured dynamic viscosity of the hybrid nanofluids and the model is quite good. The results obtained show that the current model viscosity agrees with the experimental data within a gap of 7%.

6.8.3 Specific heat model

The non-linear least square technique has been used to derive a correlation between the GNP weight fraction, temperature, and specific heat for the TH55-GNP/Al_2O_3 hybrid nanofluid, as shown in Eq. (6.19).

$$Cp(\varphi,T) = 1.519 + 0.2849\varphi + 0.01962T - 0.008667\varphi T - 0.0001654T^2 - 1.721e^{-05}\varphi T^2 + 4.318e^{-07}T^3 \quad (6.19)$$

For the developed model, the RSME and R^2 are found to be 0.003304 and 0.9994, respectively. Figure 6.36 compares the experimental data with the predicted results of specific heat for the hybrid nanofluids between the temperatures of 20°C to 100°C. As

shown in Fig. 6.36, there is excellent agreement between the experimental data and predicted values using the developed correlation, with less than 1% deviation.

The purpose of this study is to experimentally examine the impact of dispersing aluminium oxide (Al_2O_3) and graphene nanoplatelets (GNP) in TH55 oil on thermophysical properties like thermal conductivity, viscosity, and specific heat. The effect of GNP concentration and temperature on thermal conductivity, dynamic viscosity and specific heat capacity of the nanofluids has been experimentally determined. Experimental results reveal that the thermal conductivity of nanofluids is significantly more excellent than that of the base fluid and increases with temperature and nanoparticle concentration level. It has also been observed that the viscosity of nanofluids increases with increasing solid percentage and decreases with increasing temperature compared to TH55.

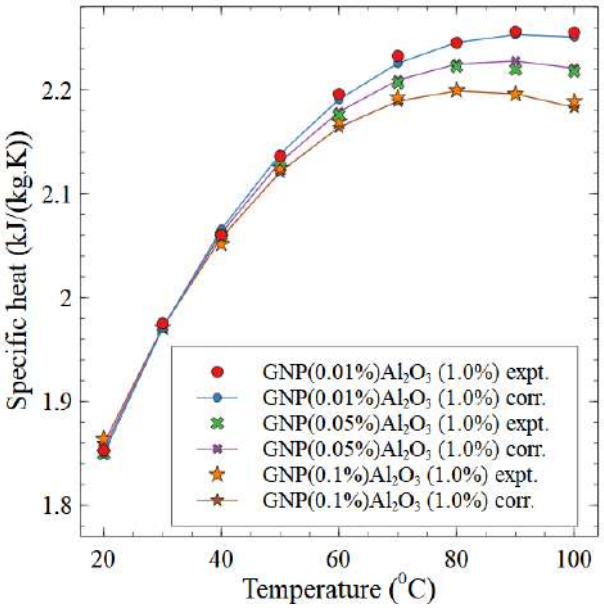

Fig. 6.36: Comparison of specific heat of experimental data and correlation output

The specific heat capacity of the nanofluid reduces as the nanoparticle weight fraction rise. Besides, with temperatures, the specific heat of nanofluids grows remarkably, showing that temperature more strongly affects the specific heat capacity than the solid fraction of nanoparticles. In addition, the developed thermal conductivity and viscosity models are compared with the experiment

results and found that these models can be successfully used to predict these properties of the TH55-GNP/Al_2O_3 hybrid nanofluid.

Table 6.5: Effect of surfactant addition on the hybrid nanofluid

Parameters		**TH55**	**Hybrid Nanofluid**	**Hybrid nanofluid+ OA**	**Hybrid nanofluid+ OA (proposed model)**
Thermal conductivity	W/(m.K)	0.1273	0.1300	0.1301	0.129
	% enhancement	-	2.12	2.19	1.34
Viscosity	cP	24.9326	48.0438	48.1124	47.197
	% enhancement	-	92.69	93.37	89.29
Specific heat	kJ/(kg.K)	1.9815	-	1.9710	1.9714
	% enhancement	-	-	- 0.5	-0.51
Absorbance	After 1 day	-	1.049	1.154	-
	After 14 day	-	0.42	0.658	-

Table 6.5 depicts a comparison of the thermophysical properties of the hybrid nanofluid at 30°C and its stability before and after the addition of the OA as a surfactant. Based on the results, OA appears to enhance both the stability and the thermophysical properties of the hybrid nanofluid. Table 6.6 describes the thermophysical properties corresponding to the evaluated higher temperatures of the base fluid and the mono and hybrid nanofluids determined by the experiments .

Table 6.6 Thermophysical properties of HTFs

HTF	**Thermal conductivity (W/m. K)**	**Viscosity (cP)**	**Specific heat (J/kg.K)**
TH55	0.1233	3.5706	2.3143
TH55-Al_2O_3(1.0%)	0.1327	5.6936	2.2703
TH55-GNP(0.1%)	0.1427	5.7215	2.2841
TH55-Al_2O_3(1.0%)/GNP(0.1%)	0.1433	10.071	-
TH55-Al_2O_3(1.0%)/GNP(0.1%)+OA	0.1464	10.297	2.1961
TH55-Al_2O_3(1.0%)/GNP(0.1%)+OA (Model)	0.1473	10.289	2.1964

Table 6.7: Comparison of thermophysical properties of the proposed hybrid nanofluid with the existing literature

Base fluid	Nanoparticles	Enhancement in Properites			Ref.
		Thermal conductivity	Viscosity	Specific heat	
Water	GNP-Ag(83:17) (0.1wt%)	22.22% at 40°C	30%	-	[161]
Therminol 55	Al_2O_3 -TiO_2 (60:40)(0.5 wt.%)	-	15%	-	[61]
Diathermic oil	Sic-TiO_2 (1 vol.%)	8.39% at 45°C	-	-	[162]
Therminol 55	Al_2O_3-TiO_2 (0.5wt.%)	33.3% at 155°C	-	-	[163]
Therminol 66	Cu (mono) (2 vol.%)	20%		6% increase at 100°C	[164]
Ironic Liquid	Carbon black (mono)	-	-	30% reduction at 200°C	[165]
Water	GNP-Pt	17.77% at 40°C	133%	6.26% decrease at 45°C	[11]
Therminol 55	Al_2O_3(1wt.%)-GNP(0.1 wt.%)	18.75% at 65°C	64%	6.11% decrease at 100°C	Present study

Table 6.7 shows the comparison of thermophysical properties of the proposed hybrid nanofluid with other hybrid nanofluids in the literature. The research revealed that employing this hybrid HTF in medium temperature applications such as solar collectors instead of pure TH55 can be highly beneficial in all particle concentrations examined.

6.9 Summary

Improving the thermal conductivity of TH55 is one of the hopeful ways to enhance the performance of TH55-based systems in order to overcome the drawback of poor efficiency of solar thermal collectors. It has been recommended that nanofluids transfer heat more effectively than traditional fluids. This chapter aimed to experimentally examine the impact of dispersing aluminium oxide (Al_2O_3) and graphene nanoplatelets

(GNP) in TH55 on thermophysical characteristics like thermal conductivity, viscosity, and specific heat. In addition, the developed thermal conductivity, viscosity, density and specific heat capacity models are compared with the experiment results and found that these models can be successfully used to predict these properties of the TH55-GNP/Al_2O_3 hybrid nanofluid. Experimental results reveal that the thermal conductivity of nanofluids is significantly greater than that of the base fluid and increases with temperature and nanoparticle concentration level. The thermal conductivity of TH55-GNP/Al_2O_3 hybrid nanofluids is shown to increase by 6.5%, 9.04%, and 18.72%, as the GNP solid fraction increases from 0.01, 0.05, to 0.10; respectively. It has also been observed that the viscosity of nanofluids increases with increasing solid percentage and decreases with increasing temperature compared to TH55. The specific heat capacity of the nanofluid reduces as the nanoparticle weight fraction rise. Besides, with temperatures, the specific heat of nanofluids grows remarkably, showing that temperature more strongly affects the specific heat capacity than the solid fraction of nanoparticles. In addition, the developed thermal conductivity and viscosity models are compared with the experiment results and found that these models can be successfully used to predict these properties of the TH55-GNP/Al_2O_3 hybrid nanofluid. The research revealed that employing this hybrid HTF in medium temperature applications such as solar collectors instead of pure TH55 can be highly beneficial in all particle concentrations examined. Chapter 7 examines the hybrid nanofluid's thermal performance numerically compared to the base fluid while passing through a solar receiver.

Chapter 7

Numerical Analysis of Heat Transfer Performance of Hybrid Nanofluid

A numerical investigation of the thermal performance of the proposed hybrid nanofluid is detailed in this chapter. This chapter aims to extend on the previous chapter's experimental evaluation of the developed hybrid nanofluid by numerically investigating its heat transfer performance as it passes through a solar receiver tube in a laminar flow.

7.1 Theoretical background

High heat flow requirements have resulted in a substantial demand for advanced HTFs to improve heat transfer. Furthermore, there is a growing need to enhance the performance of existing PTC technologies. The following equation Eq. (7.1) is used to determine the heat transfer in a process [166].

$$Q = hA\Delta T \tag{7.1}$$

where Q is the heat transfer, h the convective heat transfer coefficient, A the heat transfer area, and ΔT the temperature difference that causes heat transfer. Due to the area and minimum temperature constraints, increasing the heat transfer coefficient h is the

viable solution for heat transfer improvements in solar PTCs. The heat transfer coefficient h can be enhanced by employing more efficient heat transfer techniques or by improving the transport characteristics of HTFs. The previous chapter discussed the attempt to develop a hybrid nanofluid for heat transfer enhancement in medium-temperature applications. The experimental results revealed that the developed hybrid nanofluid had much higher thermal conductivity than the TH55 base fluid. However, examining the heat transfer coefficients of the hybrid nanofluid is especially important to confirm the fluid's viability for the specified application.

In a PTC system or any CSP technology, the receiver tube plays a crucial role in converting solar radiation to thermal energy. Heat losses from the receiver should be kept to a minimum to improve their efficiency. As a result, the overall heat loss coefficient, which comprises losses due to conduction, convection, and radiation, is critical to the solar receiver. Many researchers have conducted CFD analysis to assess the convective heat transfer of nanofluids [167]. Sokhansefat *et al.* [168] studied the performance of a PTC using synthetic oil-based alumina nanofluid. The heat transfer coefficient increased up to 14% for Al_2O_3 volume fraction up to 5%. Akbari and Behzadmehr [169] evaluated the influence of water/Al_2O_3 nanofluid in a receiver tube with uniform heat flux. Compared to water, the nanofluid improved the convective heat transfer coefficient by 15% for an Al_2O_3 volume concentration of 4%. Because of the high temperatures achievable in PTC systems, there exists a potential for increasing efficiency with thermal performance enhancement, as demonstrated in the literature [170].

It is clear from the above literature that the CFD method is an effective tool for assessing the heat transfer behaviour of nanofluids. Hence, a CFD analysis of the HTF has been performed to investigate the heat transfer behaviour of the developed hybrid nanofluid (TH55-Al_2O_3(1.0wt.%)/GNP(0.1wt.%)) while passing through the solar receiver and the results are presented in this chapter. The steady-state simulations are conducted using the commercial CFD software Ansys 2020R2. The laminar flow convective heat transfer of the developed hybrid nanofluid with constant heat flux surface boundary condition has been examined. The simulation results identified the heat transfer improvement of the developed hybrid nanofluid compared to pure TH55 oil.

7.2 Model description

The absorber tube considered in this analysis has a length of 2.5m and an inside diameter of 0.02665m, and it is identical to the one for the currently designed PTC, as illustrated in Chapter 4. The schematic diagram of the parabolic concentrator and the absorber/receiver tube is shown in Fig. 7.1. The parabolic trough collector concentrates solar energy around the cylindrical receiver. The focused heat energy is then transferred to the HTF through convection heat transfer in the tube. Figure 7.2 schematically illustrates the flow of HTF in the PTC receiver tube. Since the receiver tube has symmetry about the axis in both geometry as well as the boundary conditions, the model is reduced to 2D axisymmetric by a rectangle with the width equal to the radius of the receiver and length equal to the sum of the tube length and the hydrodynamic entry length. Only the fluid domain is selected for the study as the main goal is to determine how the thermophysical properties of the nanofluid affect heat transfer.

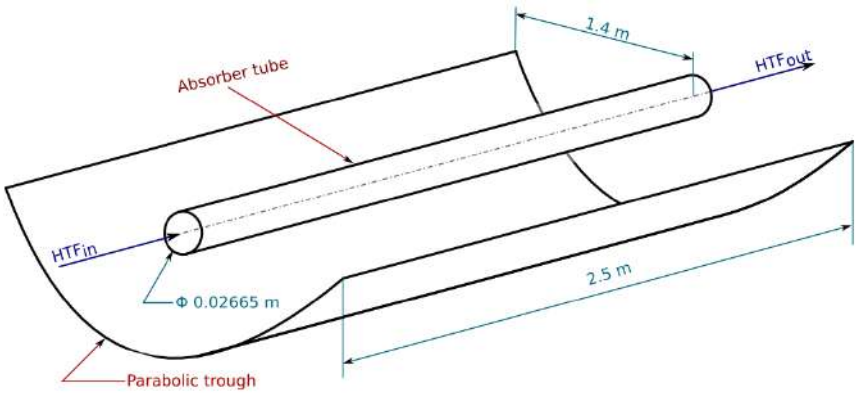

Fig. 7.1: Schematic of the PTC with receiver tube

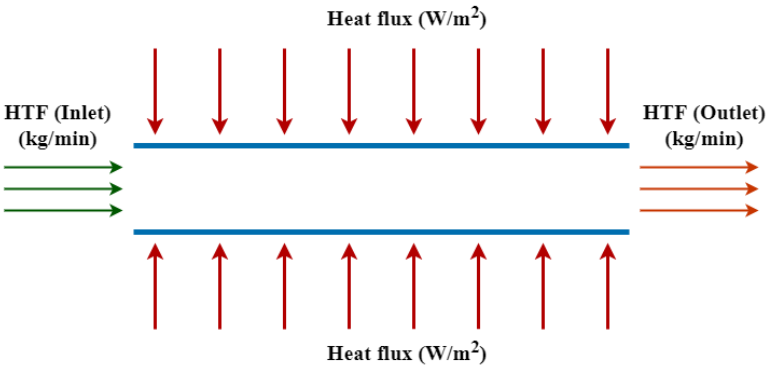

Fig. 7.2: HTF flowing in the receiver tube of PTC

7.3 Governing Equations

The Reynolds number corresponding to the flow condition considered in this study falls below 2000. The flow model chosen here is laminar. With this, the transport equations that govern the flow in polar coordinate are given as [115]:
The continuity equation is given by;

$$\frac{\partial}{\partial x}(\rho v_x) + \frac{\partial}{\partial r}(\rho v_r) + \frac{\rho v_r}{r} = S_m \tag{7.2}$$

where S_m is the mass added to the continuous phase from the dispersed second phase, *x* the axial coordinate, *r* the radial coordinate, v_x the axial velocity, and v_r the radial velocity. In this problem S_m essentially zero, as no mass source is present in the domain of interest.

The axial momentum conservation equation is;

$$\begin{aligned}\frac{1}{r}\frac{\partial}{\partial x}(r\rho v_x v_x) + \frac{1}{r}\frac{\partial}{\partial r}(r\rho v_r v_x) \\ = -\frac{\partial p}{\partial x} + \frac{1}{r}\frac{\partial}{\partial x}\left[r\mu\left(2\frac{\partial v_x}{\partial x} - \frac{2}{3}(\nabla.\vec{v})\right)\right] + \frac{1}{r}\frac{\partial}{\partial r}\left[r\mu\left(\frac{\partial v_x}{\partial r} + \frac{\partial v_r}{\partial x}\right)\right] \\ + F_x\end{aligned} \tag{7.3}$$

The radial momentum conservation equation is;

$$\begin{aligned}\frac{1}{r}\frac{\partial}{\partial x}(r\rho v_x v_r) + \frac{1}{r}\frac{\partial}{\partial r}(r\rho v_r v_r) \\ = -\frac{\partial p}{\partial r} + \frac{1}{r}\frac{\partial}{\partial x}\left[r\mu\left(\frac{\partial v_r}{\partial x} + \frac{\partial v_x}{\partial r}\right)\right] + \frac{1}{r}\frac{\partial}{\partial r}\left[r\mu\left(2\frac{\partial v_r}{\partial r} - \frac{2}{3}(\nabla.\vec{v})\right)\right] \\ - 2\mu\frac{v_r}{r^2} + \frac{2}{3}\frac{\mu}{r}(\nabla.\vec{v}) + \rho\frac{v_z^2}{r} \\ + F_r\end{aligned} \tag{7.4}$$

where

$$\nabla.\vec{v} = \frac{\partial v_x}{\partial x} + \frac{\partial v_r}{\partial r} + \frac{v_r}{r} \tag{7.5}$$

Equation (7.5) is the continuity equation. The nature of flow considered here is truly incompressible. As a result, '$\nabla.\vec{v}$' in the momentum equation is zero.

Energy equation:

$$\rho Cp\left(u_r\frac{\partial T}{\partial r}+u_z\frac{\partial T}{\partial x}\right)=\frac{1}{r}\frac{\partial}{\partial r}\left(kr\frac{\partial T}{\partial r}\right)+\frac{\partial}{\partial x}\left(k\frac{\partial T}{\partial x}\right) \quad (7.6)$$

where ρ, Cp, μ, and k are the fluid density, specific heat, dynamic viscosity and thermal conductivity.

7.4 Thermophysical properties of the fluids

In general, experiments or simulation results, as well as correlation models, are used to define the thermophysical properties of nanofluids. Due to the lack of models for predicting the thermophysical properties of TH55-Al_2O_3/GNP hybrid nanofluids, correlation models for predicting thermal conductivity, dynamic viscosity, and specific heat of the hybrid nanofluid have been developed in the study. To develop the models, the thermophysical properties of hybrid nanofluids with different GNP concentrations, such as 0.025% and 0.075%, and the current hybrid fluids with 0.01%, 0.05%, and 0.1% have been measured separately. Relationships between nanofluid temperature (T), GNP wt% (φ), and thermal conductivity (k) have been developed using the non-linear least square method. As illustrated in the previous Chapter 6, the following developed formulas have been used to compute the thermophysical properties of the nanofluid.

Thermal conductivity:

$$k(\varphi,T)=0.1055+0.6761\varphi+0.001097T-3.247\varphi^2-0.02626\varphi T-1.515e^{-05}T^2+0.08627\varphi^2T+0.0002225\varphi T^2+7.288e^{-08}T^3 \quad (7.7)$$

Dynamic viscosity:

$$\mu(\varphi,T)=116+106\varphi-3.992T+522.5T\varphi^2-1.676\varphi T+0.05056T^2+1.104\varphi^2T+0.002767\varphi T^2-0.0002194T^3 \quad (7.8)$$

Specific heat:

$$p(\varphi, T) = 1.519 + 0.2849\varphi + 0.01962T - 0.008667\varphi T - 0.0001654T^2 - 1.721e^{-05}\varphi T^2 + 4.318e^{-07}T^3 \quad (7.9)$$

The density of the hybrid nanofluid (ρ_{hnf}) is defined based on the theory of mixing [159] :

$$\rho_{hnf} = \left[(1-\varphi_2)\{(1-\varphi_1)\rho_f + \varphi_1\rho_{s1}\}\right] + \varphi_2\rho_{s2} \quad (7.10)$$

where φ_1, φ_2 are the volume fractions of nanoparticles, $\rho_f, \rho_{s1}, \rho_{s2}$ the densities of base fluid and nanoparticles, respectively.

The temperature-dependent properties for TH55 oil have been reported in the manufacturer's material property datasheet [124], and their plots are shown in Fig. 7.3. They are defined by choosing the piecewise-linear interpolation method.

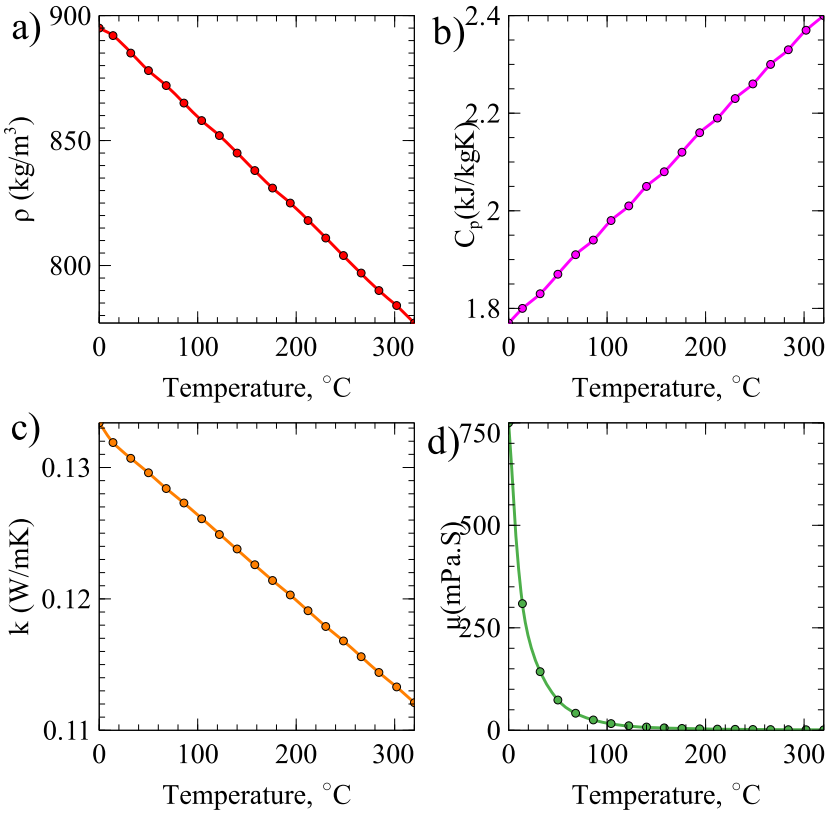

Fig. 7.3: Properties of TH55 (a) density (b) specific heat (c) thermal conductivity (d) viscosity

7.5 Boundary conditions

The computational domain investigated in this analysis and the boundary conditions are illustrated in Fig. 7.4. The receiver tube considered in this study has a length of 2.5m and a diameter of 0.02665m, and it is indented for the previously designed PTC. Because the flow pattern of HTFs for small-size solar PTCs is laminar, an extra entrance length of 0.25m is considered. The entrance length is calculated from the equation, $Le/D = 0.06 * Re,$ [171] where Le is the entrance length, D the diameter of the receiver, and Re the Reynolds number. Due to the simplicity of the geometry, a structured mesh with quadrilateral elements is created to discretise the computational domain. In addition, structured grids are aligned in the flow direction leading to more accurate results and a better convergence [172]. The enlarged view of a small portion of the discretised domain is shown in Fig. 7.5. For thermal boundary conditions, uniform solar heat flux distribution is considered on the outer surface of the fully developed fluid domain, and the wall at the entry region is assumed as adiabatic.

Furthermore, the HTF enters the tube at a given velocity (velocity inlet), and the pressure outlet boundary condition is specified for the outlet flow. A laminar model with SIMPLE method is employed to couple pressure and velocity, and Second-Order Upwind for interpolating convective terms. This study uses TH55 oil and the developed hybrid nanofluid as the working fluids. They have temperature-dependent properties, which are given in the above section 7.4.

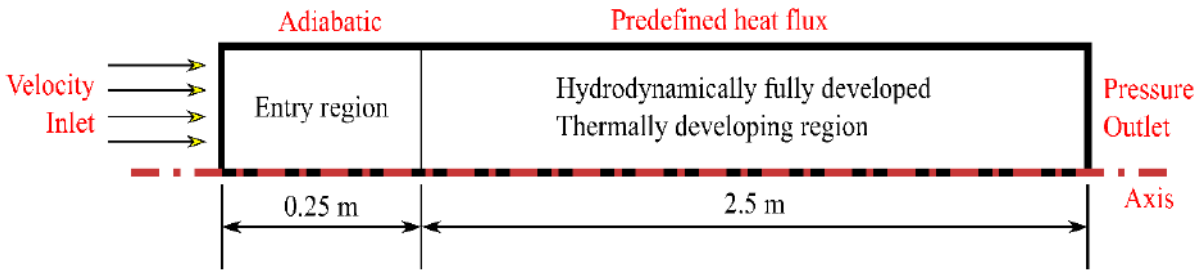

Fig. 7.4: Computational domain and boundary conditions for the analysis

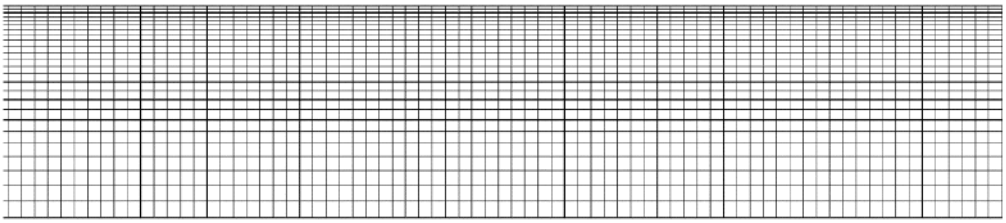

Fig. 7.5: Enlarged view of the discretised domain

7.6 Grid Independence study

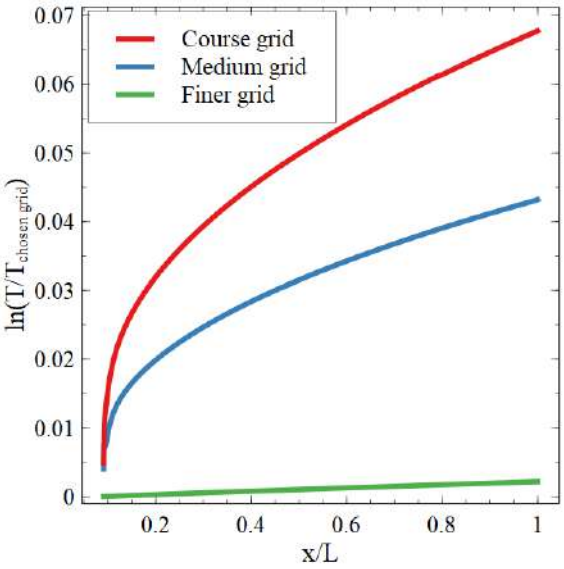

Fig. 7.6: Grid convergence study

For grid independence study, the mass flow rate is kept constant, and uniform heat flux is applied around the fully developed region of the tube while the outlet temperature is monitored. Four different grid sizes selected are coarse grid (10,000 cells), medium grid (34,325 cells), fine grid (68,700 cells), and finer grid (78,750 cells). Figure 7.6 depicts the log plot for the fraction of deviations from the selected grid with the grid sizes examined. Compared to the computing cost, it is clear that the deviation of fine and finer grids is negligible. In contrast, the variation is substantially larger when the medium and coarse mesh is considered. Based on these results, the fine grid with 68700 cells is selected for the numerical analysis.

7.7 Model validation

The numerical model has been validated by comparing the simulation results with the simplified alternative to Graetz's series solution - Nusselt number correlation, as shown in Eq. (1.10) [173]. Water is chosen as the working fluid for validation since Graetz's number is calculated at constant properties. Properties of water used in the analysis are given in Table 7.1. To ensure that Reynold's numbers match those of the nanofluid flow condition, a convenient heat flux (2500 W/m^2) has been used.

$$Nu_{x*} = \begin{cases} 3.302x_*^{-1/3} - 1.00 & x_* \leq 0.00005 \\ 1.302x_*^{-1/3} - 0.50 & 0.00005 < x_* \leq 0.0015 \\ 4.34 + 8.68(10^3 x_*)^{-0.506e^{-41x_*}} & x_* > 0.001 \end{cases} \quad (7.11)$$

where x_* *is* the reciprocal of Graetz's number, which is often used as a non-dimensional form of axial distance in the representation of entrance effect on laminar flow of heat transfer:

$$x_* = \frac{x/D}{Re_D.Pr} \quad (7.12)$$

where x is the axial distance along the pipe, D the diameter of the pipe, Re_D Reynold's number, and Pr the Prandtl number.

Table 7.1 Properties of water [174]

Property	**Numerical Value**
Density	998.2 kg/m^3
Thermal conductivity	0.6 W/(m.K)
Specific heat	4182 J/(kg.K)
Viscosity	0.001003 Pa.s

The convective heat transfer coefficient has been computed by using the equation:

$$Nu = \frac{h.D}{k} \quad (7.13)$$

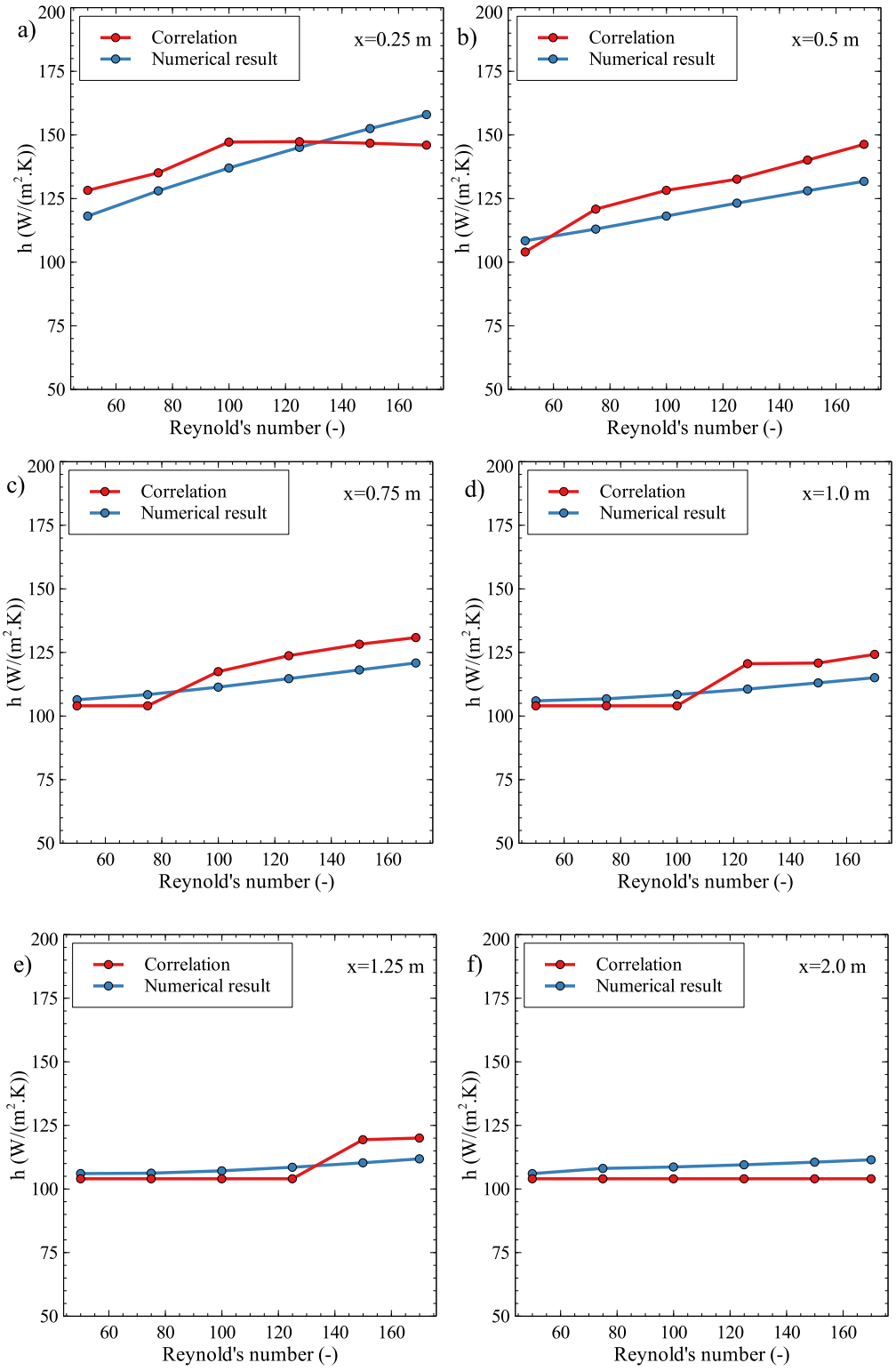

Fig. 7.7: Validation of present model with Graetz's number correlation for convective heat transfer coefficient at (a) x = 0.25m, (b) x = 0.5m, (c) x = 0.75m, (d) x = 1.0m, (e) x = 1.25 m, (f) x = 2.0 m

From numerical simulation results, the convective heat transfer coefficient has been derived by using the formula:

$$h = \frac{q''}{T_s - T_m} \tag{7.14}$$

where q'' is the heat flux, T_s the surface temperature and T_m the mean temperature at the section and obtained by considering the true energy transfer as [175],

$$T_m = \frac{\int \rho c_p u T dA}{\int \rho c_p u dA} \tag{7.15}$$

Figures 7.7(a)-(f) compares the convective heat transfer coefficients computed from the correlation with that obtained from the CFD numerical study for different axial locations of the tube. Figure 7.8 depicts the percentage deviation of the convective heat transfer coefficient between the numerical results and correlation results at various Reynold's numbers and axial locations along the tube axis. It can be observed that the present numerical results correspond quite well with the validation correlation, with a maximum divergence of 9.5% for the convective heat transfer coefficient.

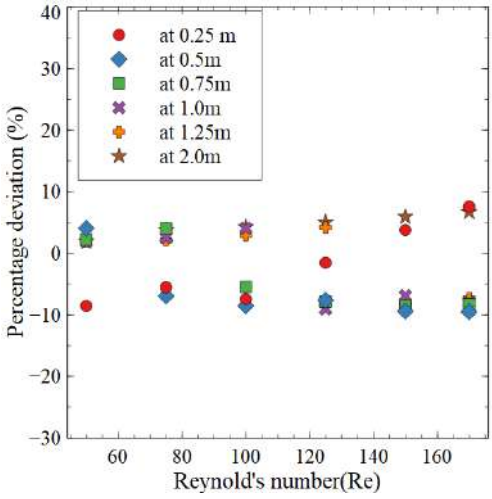

Fig. 7.8: Percentage deviation of convective heat transfer coeficient between the model and correlation results

7.8 Results and discussion

An analysis of numerical simulations of fluid flow is conducted in order to examine the effects of the developed hybrid nanofluid on the heat transfer of the medium

temperature PTC receiver in comparison to the pure TH55 oil. The fluid's thermal and hydrodynamic characteristics, including convective heat transfer coefficient, thermal diffusivity, and surface temperature for various flow velocities, are presented and discussed in detail.

The heat transfer coefficient is a useful indicator of the enhancement in the rate of heat transfer performance with TH55-Al_2O_3/GNP nanofluids as the working fluid. Figure 7.9(a) demonstrates plots of the numerical local heat transfer coefficient of TH55 and hybrid nanofluid versus axial position from the hydro-dynamically fully developed thermally developing region in a constant heat flux of 5000 W/m^2 under different flow rates. The heat transfer coefficient of hybrid nanofluid is superior to TH55 oil at all flow rates, as demonstrated in Fig. 7.9(a) at various points along the tube axis. The high heat transfer coefficient of the nanofluid is due to an increase in the thermal conductivity of the HTF owing to the suspension of high thermal conductivity GNP and Al_2O_3 in TH55. The suspension of nanoscale particles increases the micro-convection due to its low particle momentum and very high mobility. The small size of particles allows for free movement, which promotes heat transfer. It is observed that the heat transfer coefficient falls rapidly with axial distance in the receiver inlet region. Ding *et al.* [176] reported similar phenomena with carbon nanotubes.

Figure 7.9(b) shows the ratio of heat transfer coefficient of hybrid nanoparticles (h_{hnf}) to that of the pure TH55 oil (h_{bf}). It is observed that the heat transfer coefficient ratio is always greater than one for all the discharge rates studied. As shown in Fig. 7.9(b), the heat transfer coefficient increases as the flow rate increases from 0.01 kg/min to 0.1 kg/min. Large increases in the heat transfer coefficient are observed at lower discharge rates due to the poorer performance at these discharges than at high flow rates. The ratio of the heat transfer coefficients does not change substantially as discharge increases, most likely because the HTF no longer can transport more energy at higher discharges due to a much smaller temperature difference between the fluid surface and the average temperature at the section.

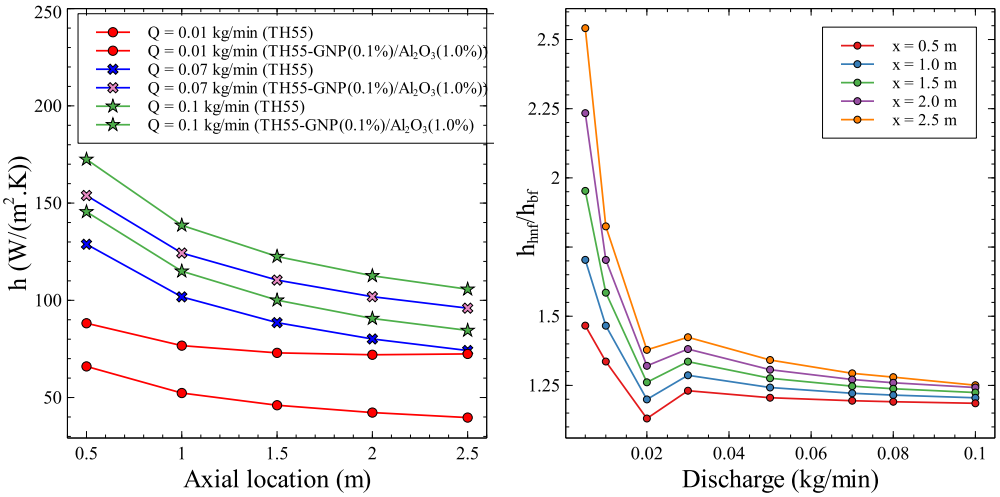

Fig. 7.9: (a) Heat transfer coefficient versus axial location for different flow fates (b) Ratio of heat transfer coefficients with discharge at various points along the tube axis

The variation of average convection heat transfer coefficient with mass flowrates for the base fluid and the hybrid nanofluid along the receiver tube is shown in Fig. 7.10. The heat transfer performance of the hybrid nanofluid is always considerably higher than that of the base fluid, as illustrated in Fig. 7.10. The increase in the heat transfer coefficient with HTF is due to the increase in thermal conductivity of the TH55 with the suspension of high thermal conductivity nanoparticles GNP and Al_2O_3. Significant increases in the heat transfer coefficient are observed at lower mass flow rates due to the lower performance at these discharges than at high flow rates. When the hybrid nanofluid substitutes the conventional TH55 working fluid at a 0.1 kg/min flow rate, the convective heat transfer coefficient increases by 21.88%. That is 29.56% for 0.05 kg/min under the same conditions. Also, this enhancement is 56.08% for the same conditions for a mass flow rate of 0.01 kg/min. This enhancement in heat transfer coefficient is greater in lower mass flow rates. Because of the presence of solid metal nanoparticles, heat transmission via diffusion predominates at lower flow rates. As the flow rate increases, the effect of diffusivity and rate of heat transfer diminishes.

Table 7.2 shows a comparison of the convective heat transfer coefficient enhancement obtained in this study (at 0.1 kg/min) with those available in the literature. The nanofluids described in the literature are mono-nanofluids, and it is evident that the mono-nanofluids requires a significantly higher solid particle concentration than the

hybrid nanoparticles. Furthermore, with a small solid concentration, the current hybrid nanofluid improves the convection heat transfer coefficient by more than 40% as compared to the mono-nanofluids of the previous literature results.

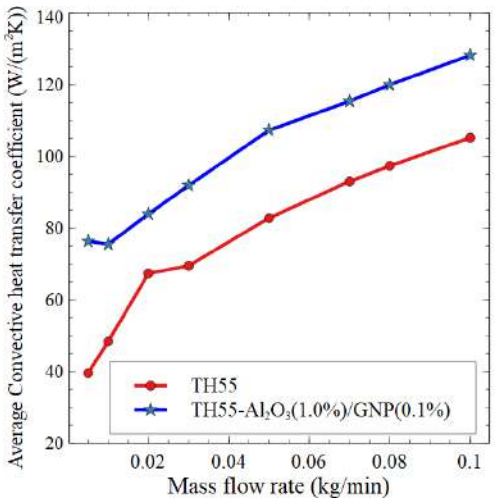

Fig. 7.10: Average convection heat transfer coefficient of the base fluid and the hybrid nanofluid

Table 7.2 Convective heat transfer coefficient enhancements in PTCs

Authors	**Base fluid**	**Nanoparticle**	**Mass concentration (%)**	**Enhancement in h (%)**
Sokhansefat *et al.* [168]	Synthetic oil	Al_2O_3	5	14
Akbari and Behzadmehr [169]	Water	Al_2O_3	4	15
Present study	TH55	Al_2O_3 + GNP	1.1	21.88

The fluid temperature on the surface of the domain of the reciever tube for different flow rates at various points along the tube axis is illustrated in Fig. 7.11. Figure 7.12 depicts the difference in surface temperature between the TH55 and hybrid nanofluid domains in the axial direction for different flow rates. From the Figs. 7.11 and 7.12, it is evident that the surface temperature of the pure TH55 oil is always higher than that of the hybrid nanofluid for the same heat transfer rate. In practice, one of the significant sources of heat loss in a solar thermal application is the radiation heat loss, which is proportional to the fourth power of the temperature. With higher convective heat transfer, the average

temperature of the absorber tube decreases, reducing the receiver's heat loss, resulting in improved system thermal efficiency [170]. Since the given heat input is the same, the lower surface temperature of the nanofluid indicates a lower thermal loss than the base fluid.

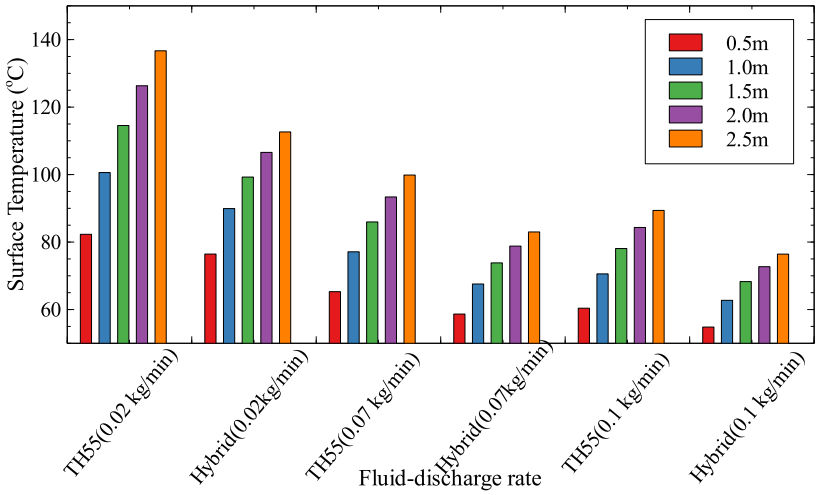

Fig. 7.11: Surface temperature of the fluid along the tube axis

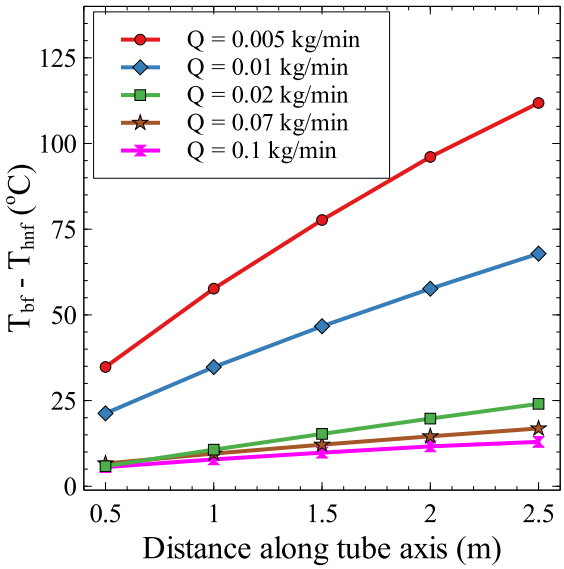

Fig. 7.12: Difference between the surface temperature of TH55 and hybrid nanofluid

As the hybrid nanofluid has a higher diffusivity rate than TH55, this results in a decrease in surface temperature. Based on the results of the previous chapter 6, Fig. 7.13 depicts the thermal diffusivity ($\alpha = k/(\rho C_p)$ of TH55 and hybrid nanofluid as a function of temperature. Although the thermal diffusivity of nanofluid is lower than that of TH55 oil at lower temperatures, it increases rapidly after 40°C. The oil temperature near the

pipe surface is always greater than that of the nanofluid due to the poor diffusivity rate of TH55. On the other hand, due to the higher diffusivity of the nanofluid, incoming heat radiations are easily transported in the radial direction of the fluid, resulting in more heat being transmitted into the fluid. Because of this increased heat transfer, the hybrid nanofluid has a lower surface temperature than TH55 oil. Based on these results, it is evident that the developed nanofluid has the potential to diffuse more energy than pure TH55 oil.

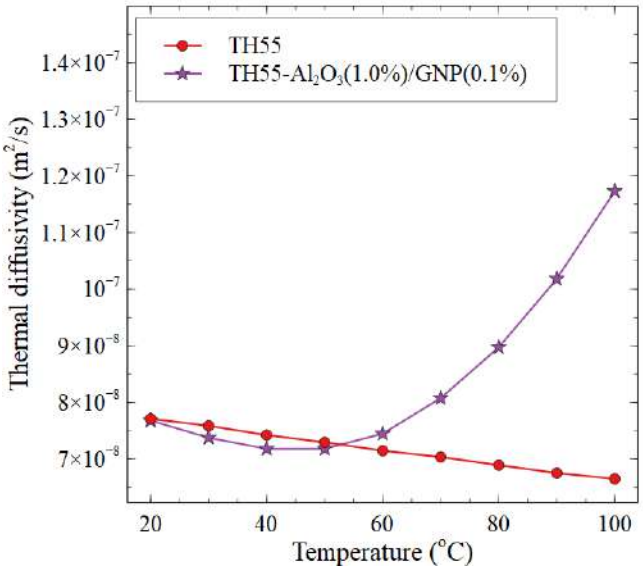

Fig. 7.13: Thermal diffusivity of TH55 and hybrid nanofluid as a function of temperature

Table 7.3 Comparison of thermal properties of TH55 and developed fluid

	k W/(m.K)	**Cp kJ/(kg.K)**	**α m^2/s**	**h_{av} W/(m.K)**
TH55	0.12331	2.3315	6.6484E-08	105.1819
TH55-Al_2O_3/GNP	0.14643	2.1891	1.17289E-07	128.2016
% enhancement	18.72	-6.11	76.42	21.88

The properties of pure TH55 oil and the developed hybrid nanofluid are briefly listed in Table 7.3. According to the results for the hybrid nanofluid, there is a significant increase in thermal conductivity, thermal diffusivity, and average convective heat transfer coefficient; nevertheless, there is a minor decrease in specific heat capacity. In contrast to TH55 oil, the hybrid nanofluid improved thermal conductivity at 65°C by 18.72%,

thermal diffusivity at 100°C by 76.42%, and average heat transfer coefficient at 0.1 kg/min mass flow rate by 21.88%. On the other hand, the specific heat capacity of the hybrid nanofluid at 100°C has decreased by 6.11%, which is also a good sign of the hybrid nanofluid's acceptance since it shows less heat energy is required to raise the fluid's temperature. Specifically, the thermal conductivity significantly increases and the specific heat is slightly reduced. This results in a significant increase in thermal diffusivity for the hybrid nanofluid in comparison with the base fluid.

7.9 Summary

In this chapter, a numerical evaluation of the TH55-Al_2O_3/GNP hybrid nanofluid's heat transfer behaviour is performed, and it is found to have more excellent convective heat transfer than TH55 oil. The results reveal that using the hybrid nanofluid as a working fluid instead of TH55 improves the heat transfer performance. Numerical simulations of 2D axisymmetric steady-state fluid flow have been carried out using ANSYS 2020R2, and the governing equations are discretised by the finite volume method (FVM). From the analysis, the experimentally observed thermal diffusivity of the fluids confirms the significant enhancement of thermal diffusivity of nanofluid over TH55 oil. Furthermore, the lowered surface temperature of the developed hybrid nanofluid compared to TH55 indicates that the nanofluid has improved heat transfer performance. It can be inferred that by dispersing the highly conductive nanomaterials such as GNP and Al_2O_3 in the TH55 oil, the conduction resistance of the fluid has been reduced, which is evident from the higher thermal conductivity measured from the experimental study. That makes the convection heat transfer coefficient the key parameter in heat transfer. The enhancement of 21.88% in the convective heat transfer coefficient of the hybrid nanofluid compared to the pure TH55 oil obtained from the numerical analysis further ensures the better heat transfer capability of the presently developed hybrid nanofluid. It, therefore, suggested that using the TH55-GNP(0.01%)/Al_2O_3 (1.0%) hybrid nanofluid in medium temperature solar thermal applications could potentially lead to an increased rate of heat transfer. The experimental performance evaluation of the PTC system with and without a secondary reflector with TH55 as HTF is described in the next chapter.

Chapter 8

Experimental Study on the Thermal Performance and Heat Transfer Characteristics of the PTC

The present chapter presents the results obtained from the outdoor experiments conducted to study the thermal performance of the designed PTC. The PTC has been evaluated under two configurations via (i) without mounting a secondary reflector and (ii) installing a secondary reflector with TH55 as the HTF. Experimental investigations are carried out for three different flow rates.

8.1 Experimental methodology

The experiments are conducted at the TKM College of Engineering, located in Kollam city of Kerala, India. The geometrical coordinates are 8.9142° North latitude and 76.6320° East longitude. To obtain greater annual collector efficiency and lower auxiliary power requirements, the PTC is oriented in the North-South direction and rotates manually around the horizontal East-West axis. The details of the PTC are described in the Chapter. 4. This experiments are conducted with synthetic oil TH55 as the HTF. TH55's thermophysical properties and stability at medium temperatures are the primary reasons for its selection. The chemical and physical characteristics of TH55 are given in Table 8.1. The inlet and outlet of the receiver tube are connected to a storage tank via silicon tubes. The storage tank has a capacity of 50 litres. The storage tank and the flow lines are thermally well insulated with polyurethane foam.

Table 8.1 Chemical and physical data of TH55

Composition	Synthetic hydrocarbon mixture
Appearance	Clear, yellow liquid
Odour	Odourless
Average Molecular weight	350 (g/mol)
Density (@ 20°C)	872 (kg/m^3)
Viscosity (@ 20°C)	47.7 (cSt)
Flashpoint	177 (°C)
Boiling point	351 (°C)
Extended maximum use temperature	315 (°C)
Thermal conductivity (@ 20°C)	0.1284 (W/m.K)
Specific heat	1.91(kJ/kg.K)

The working fluid is circulated by a pump and a controlling system from the tank through the receiver tube back to the storage tank. The pump gland-packing and coupling seals have been suitably replaced with silicon-based materials to withstand temperature. The oil pump that regulates oil flow is located between the storage tank and the receiver tube's inlet.T-type thermocouples with an accuracy of ±1.0% are used to measure the temperatures at the salient points.

Fig. 8.1: Ambient weather station WS2902A

The ambient temperature, wind speed, and solar radiation during the test have been recorded every 5 minutes using an ambient weather station WS-2902A (Fig. 8.1). The HTF temperature in the storage tank, the temperature at the inlet and outlet of the receiver tube, and the temperature of the receiver surface at five equal intervals have been recorded every 15 minutes. The PTC evaluation has been carried out outdoors, from at 08.00 hrs to at 17.00 hrs local time. To maintain a normal incidence of solar radiation, the manual

sun tracker operated every 15 minutes and rotated the PTC about the horizontal North-South axis.

8.2 Performance analysis of the PTC

The PTC evaluation is carried out on the18th, 19th, and 20th of September 2021 (Day 1, Day 2, and Day 3) for a PTC without a secondary reflector. The evaluation of PTC with the secondary reflector configuration is carried out on the 26th, 27th, and 28th (Day 4, Day 5, and Day 6) of September 2021. The flow rates of the HTF are chosen from the literature review and from the preliminary CFD analysis of the PTC receiver tube for varying flow rates. The flow rate is 2.5 lpm on the 1st and 4th days of testing, 5.0 lpm on the 2nd and 5th, and 7.5 lpm on the 3rd and 6th. The tests on the PTC started at 8.00 hrs and finished at 17.00 hrs local time, as described in Table 8.2.

Table 8.2 Experiment details

Experiment name	**Date**	**Description**	**Flow rate (lpm)**
Day 1	18th Sep. 2021	PTC without Secondary reflector	2.5
Day 2	19th Sep. 2021		5.0
Day 3	20th Sep. 2021		7.5
Day 4	26th Sep. 2021	PTC with Secondary reflector	2.5
Day 5	27th Sep. 2021		5.0
Day 6	28th Sep. 2021		7.5

Fig. 8.2: The photograph of the experimental setup

The photograph of the experimental setup for testing the designed PTC is shown in Fig. 8.2. The configuration of the PTC receiver with and without the secondary reflector is shown in Fig. 8.3 (a) and (b), respectively.

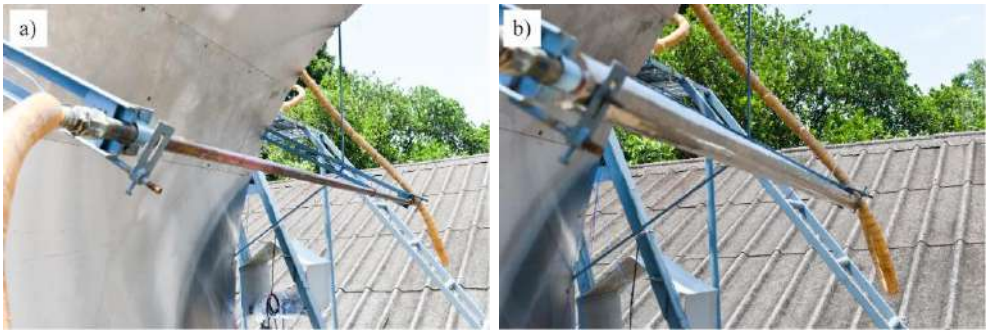

Fig. 8.3: PTC receiver (a) without secondary reflector, (b) with secondary reflector

8.3 Uncertainty analysis

In this experiment, the primary parameter recorded is the temperature for evaluating the thermal performance of the PTC. The major contributor to the uncertainty in experimental results is the uncertainty involved in temperature measurement by thermocouples, the solar radiation measurement by the weather station, and the flow rate value of HTF. The thermocouples used are T-type with an accuracy of ±1°C up to a temperature of 350°C. The weather station has an accuracy value of ±2% in solar radiation and ±0.5°C in ambient temperature measurements. The flow rate measurement has an accuracy value of ±1.5%. The total setup uncertainty value is estimated using the concept of the relative uncertainty estimated with the square root method of the sum of the uncertainties as given by Eq. (8.1) [177].

$$W_R = \left[\left(\frac{\partial R}{\partial x_1} w_1\right)^2 + \left(\frac{\partial R}{\partial x_2} w_2\right)^2 + \cdots + \left(\frac{\partial R}{\partial x_n} w_n\right)^2\right]^{1/2} \tag{8.1}$$

$$U_\eta = \left[\left(\frac{\partial \eta}{\partial \dot{m}} u_{\dot{m}}\right)^2 + \left(\frac{\partial \eta}{\partial \Delta T} u_{\Delta T}\right)^2 + \left(\frac{\partial \eta}{\partial I_D} u_{I_D}\right)^2\right]^{1/2} \tag{8.2}$$

where W_R is the total uncertainty (%) in the result, w the dimensional shape factors, R the uncertainty function of the independent variables $x_1, x_2, \ldots, x_n$.

The total uncertainty estimated for the thermal efficiency is 6.811%. Detailed uncertainty analysis is provided in Appendix I.

8.4 Performance parameters

The performance of the solar collector is determined by direct solar radiations, as well as the inlet and exit temperatures of HTF through the receiver tube for the associated flow rates. The solar beam radiation received by the concentrator is known as the heat received (Q_{tot}) by the PTC and is calculated by Eq. (8.3). The useful heat gained (Q_g) by the working fluid when it flows through the receiver tube is estimated using Eq. (8.4). T_o and T_i represents the entrance and exit temperature of HTF from the receiver. The flow rate of TH55 is represented by $\dot{m}$ in kg/s. The ratio between useful heat gained by the working fluid through the collector receiver tube to the direct normal radiation (I_{DNI}) on the given projected area (A_a) is called the solar thermal collector efficiency (η_{th}).

$$Q_{tot} = I_{DNI} * A_a \tag{8.3}$$

$$Q_g = \dot{m} C_p (T_o - T_i) \tag{8.4}$$

$$\eta_{th} = \frac{Q_g}{Q_{tot}} \tag{8.5}$$

8.5 Determination of Direct Normal Irradiation (DNI)

The solar radiation that falls on earth is composed of two parts, diffuse and direct (beam) radiation. The portion of the radiation that has been incident at various angles after being dispersed by molecules and particles is diffuse radiation. In contrast, the part that has come directly from the sun is direct radiation. As a result, the diffuse flux will be proportional to the total radiation transmitted through the atmosphere. The ratio of global radiation incident on the earth's surface (I_g) to radiation just outside the atmosphere is used to calculate atmospheric transmission (I_o), generally known as the cloudiness index. Direct Normal Irradiation (DNI) is often not recorded due to the high acquisition and maintenance expenses associated with sun tracking. However, it can be calculated as a function of global radiation and clearness index as follows.

The extraterrestrial irradiance incident normal to any surface can be evaluated as,

$$I_o = I_{sc} E_o cos\theta_z \tag{8.6}$$

where I_{sc} is the solar constant taken as 1367 W/m^2, and Eo the eccentricity correlation factor of the earth which is given by Spencer [178] as,

$$E_0 = 1.000110 + 0.034221cos\Gamma + 0.001280sin\Gamma + 0.000719cos\Gamma + 0.000077sin2\Gamma \quad (8.7)$$

with Γ, in radians, called the day angle. It can be expressed as,

$$\Gamma = 2\pi(d_n - 1)/365 \quad (8.8)$$

where d_n is the day number of the year.

In Eq. (8.6), θ_z is the zenith angle which depends on the latitude (ϕ), declination (δ), and the hour angle (ω) is expressed as,

$$cos\theta_z = sin\delta sin\phi + cos\delta cos\omega \quad (8.9)$$

The declination in degrees is evaluated by Cooper correlation [179] as,

$$\delta = 23.45sin\left[\frac{360}{365}(d_n + 284)\right] \quad (8.10)$$

The hour angle is zero at noon and positive in the morning and ranges in between $\frac{\pi}{2} \leq \omega \leq \frac{-\pi}{2}$ with 15° each per hour. With this, the clearness index is obtained as, $k_t = \frac{I_g}{I_o}$. The DNI part is evaluated as the difference between the global and diffuse irradiation. The fraction of diffuse irradiation is obtained using the correlation proposed by Reindl *et al.* [180]. This correlation relates to the diffuse fraction of the clearness index, as shown below. This study adopts this procedure, in which global radiation is measured using a pyranometer.

$$k_d = {I_D}/{I_g} = \begin{cases} 1.02 - 0.2k_t \; for \; k_t \leq 0.3 \\ 1.45 - 1.67k_t \; for \; 0.3 < k_t < 0.78 \\ 0.147 \; for \; k_t \geq 0.78 \end{cases} \quad (8.11)$$

With this, the normal irradiation is evaluated as,

$$I_{DNI} = I_g(1.0 - k_d) \quad (8.12)$$

A sample calculation of the DNI is provided as Appendix III.

8.6 Results and discussion

The fluctuations in hourly solar radiation in terms of global and DNI during the days the tests are carried out are shown in Figs. 8.4 (a)-(f). The ambient temperature and wind speed data for the above days are shown in Figs. 8.5 (a)-(f). By analysing the data,

it can be observed that the solar flux, wind, and ambient temperature exhibits a wide range of variability and nonlinearity during the daily hours. This erratic behaviour of solar flux represents the cloudy weather nature of the region of the location and will influence the instantaneous efficiency of the solar collector.

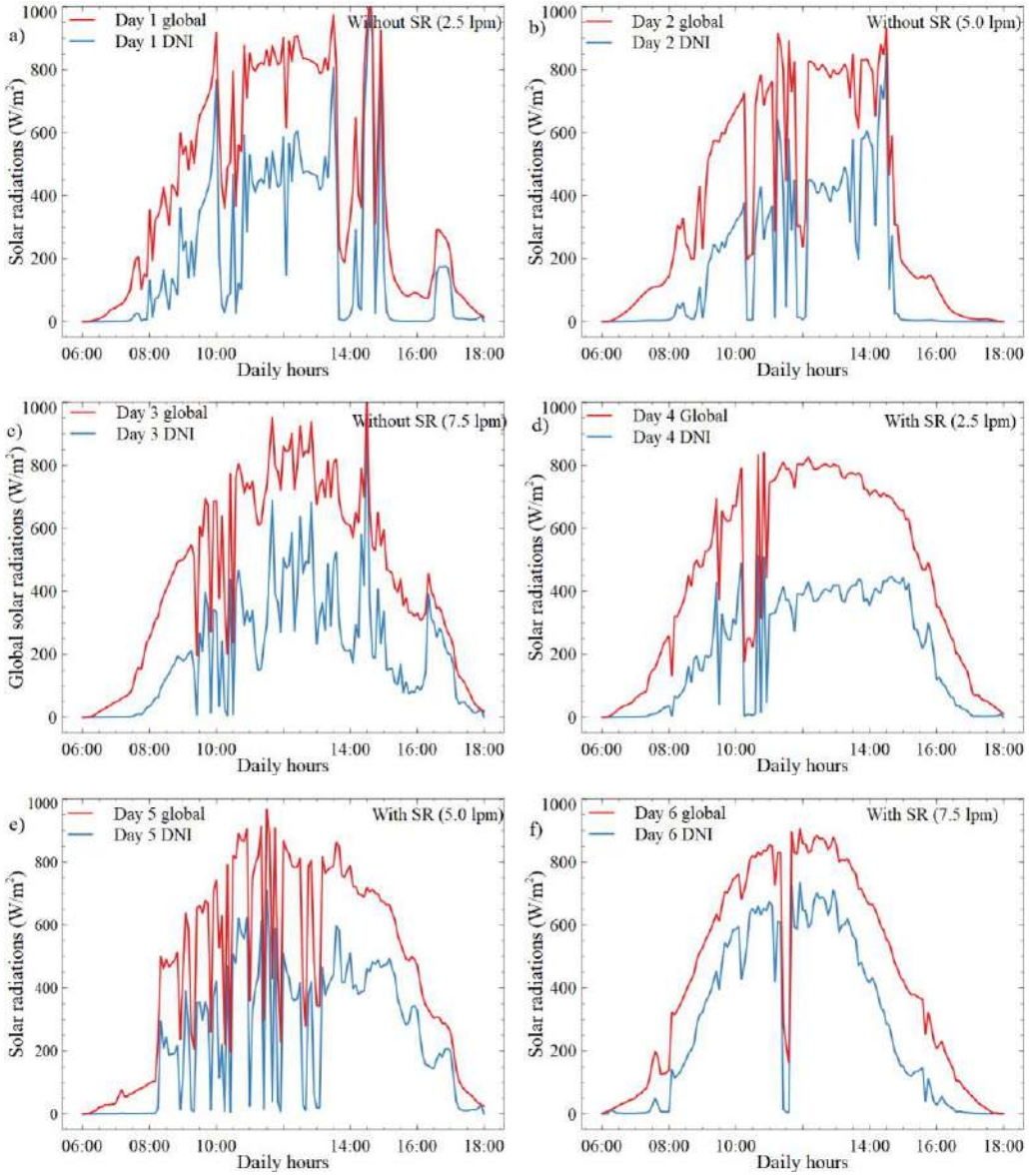

Fig. 8.4: Hourly incident solar radiation on the days of the experiments (a) Day 1 (b) Day 2, (c) Day 3, (d) Day 4, (e) Day 5, (f) Day 6

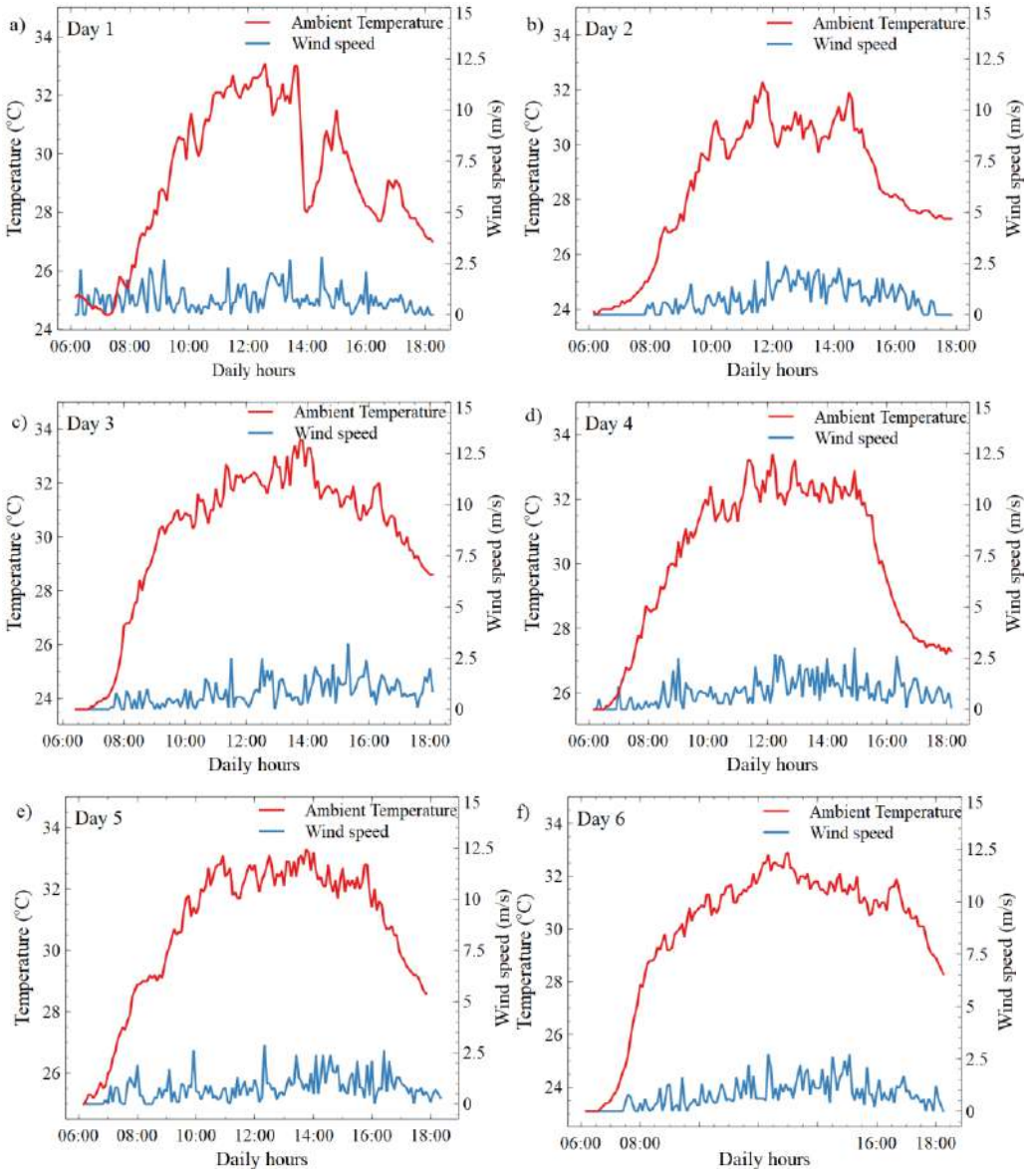

Fig. 8.5: Ambient temperature and wind speed on the days of experiments (a) Day 1, (b) Day 2, (c) Day 3, (d) Day 4, (e) Day 5, (f) Day 6

As shown in Figs. 8.4 and 8.5, the pattern for weather data for the experimental days is almost identical. As shown in Figs. 8.4, global radiation varies from around 400 W/m^2 at 9.00 hrs in the morning to around 250 W/m^2 at 17.00 hrs in the evening. Around noon on all experimental days, global radiation reaches a maximum of above 900 W/m^2. The greatest wind speed measured for the six experimentation days is 3.2 m/s on Day 3, and the average wind speed for these six days is 0.7828 m/s.

8.6.1 Inlet and outlet temperatures

The inlet and outlet temperatures of the HTF passing through the PTC receiver tube, without and with a secondary reflector, are shown in Figs. 8.6 and 8.7. The combined plot of HTF outlet temperature for all the evaluated days is depicted in Fig. 8.8. From the start of the experiments, the inlet and outlet temperatures generally continue to increase up to 15.00 hrs and then begin to fall at a slower rate until the completion of the investigations. It is observed that the temperature rises at a slower rate up to around 10.30 h, then the rise is at a faster rate up to 15.00 hrs. The increased temperature rise from 10.30 hrs to 15.00 hrs is due to the intense radiation during the mid-day hours.

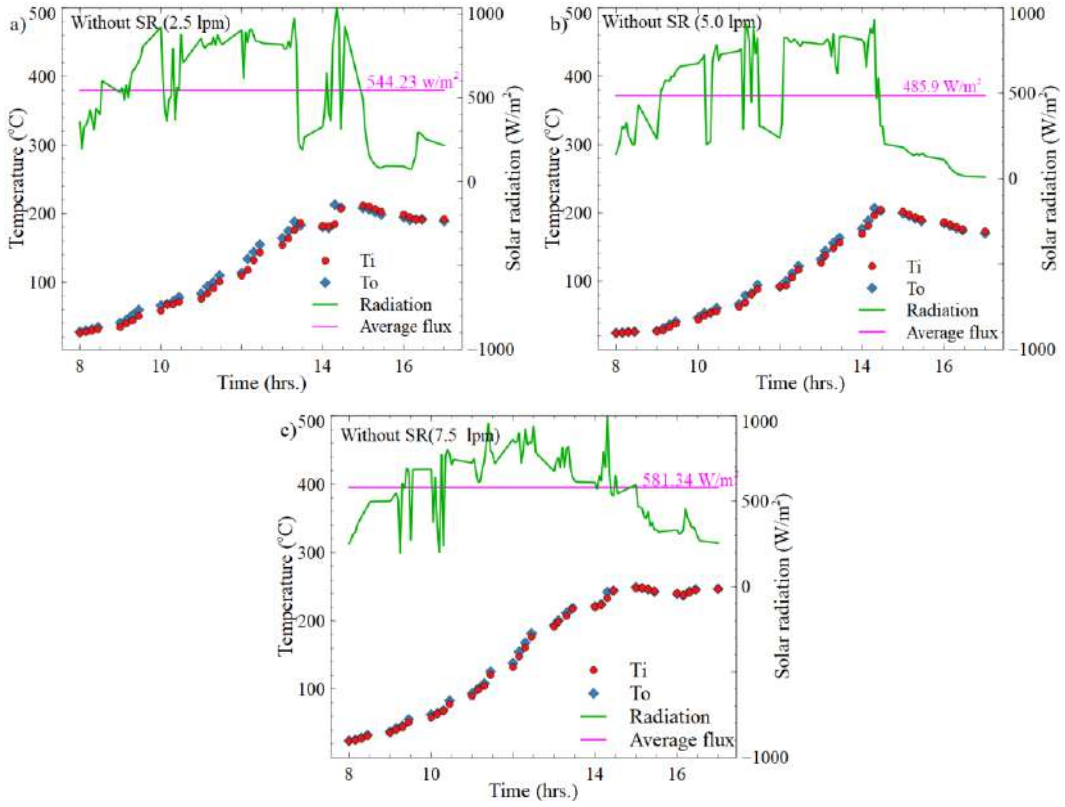

Fig. 8.6: Inlet and outlet temperatures of the HTF (a) Day 1, (b) Day 2, (c) Day 3

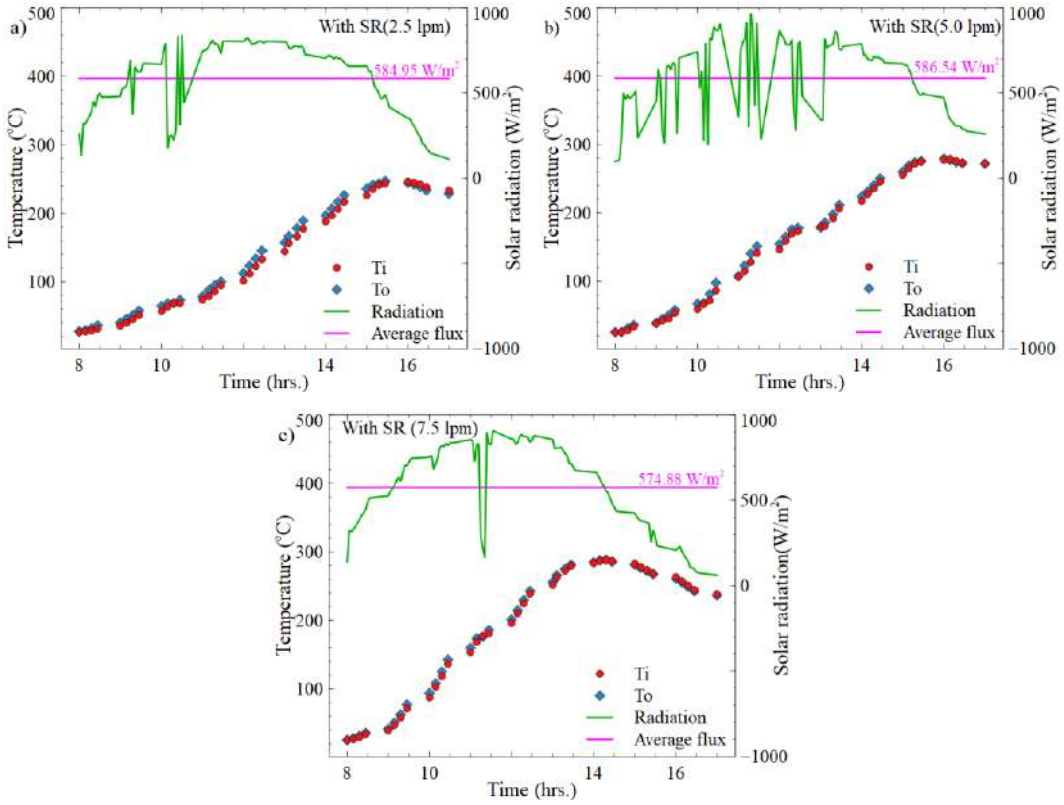

Fig. 8.7: Inlet and outlet temperatures of the HTF (a) Day 4, (b) Day 5, (c) Day 6

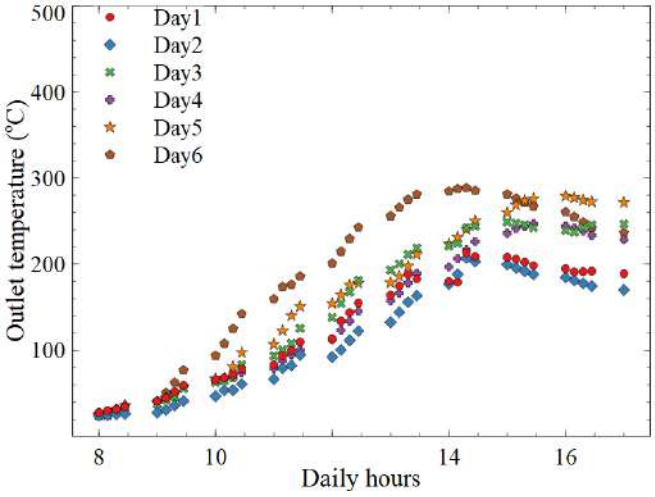

Fig. 8.8: Outlet temperature of the HTF for the experimental days

The daily variations in receiver surface temperature and outlet fluid temperature for the evaluated days are illustrated in Figs. 8.9 (a)-(f). Up to around 14.50 hrs, the absorber surface temperature is generally higher than the fluid temperature, afterwards both temperatures nearly follows the same trend. After 16.00 hrs, the receiver surface

temperature is slightly lower than the fluid temperature, indicating heat loss as the sun intensity decreases. Thus, more significant insolation would be required to compensate for heat losses as the total temperature rises. Since the energy harvested and stored is not consumed, the temperature of the gradually rises with the time. This elevates the temperature differential between the HTF and its surroundings, resulting in greater heat losses.

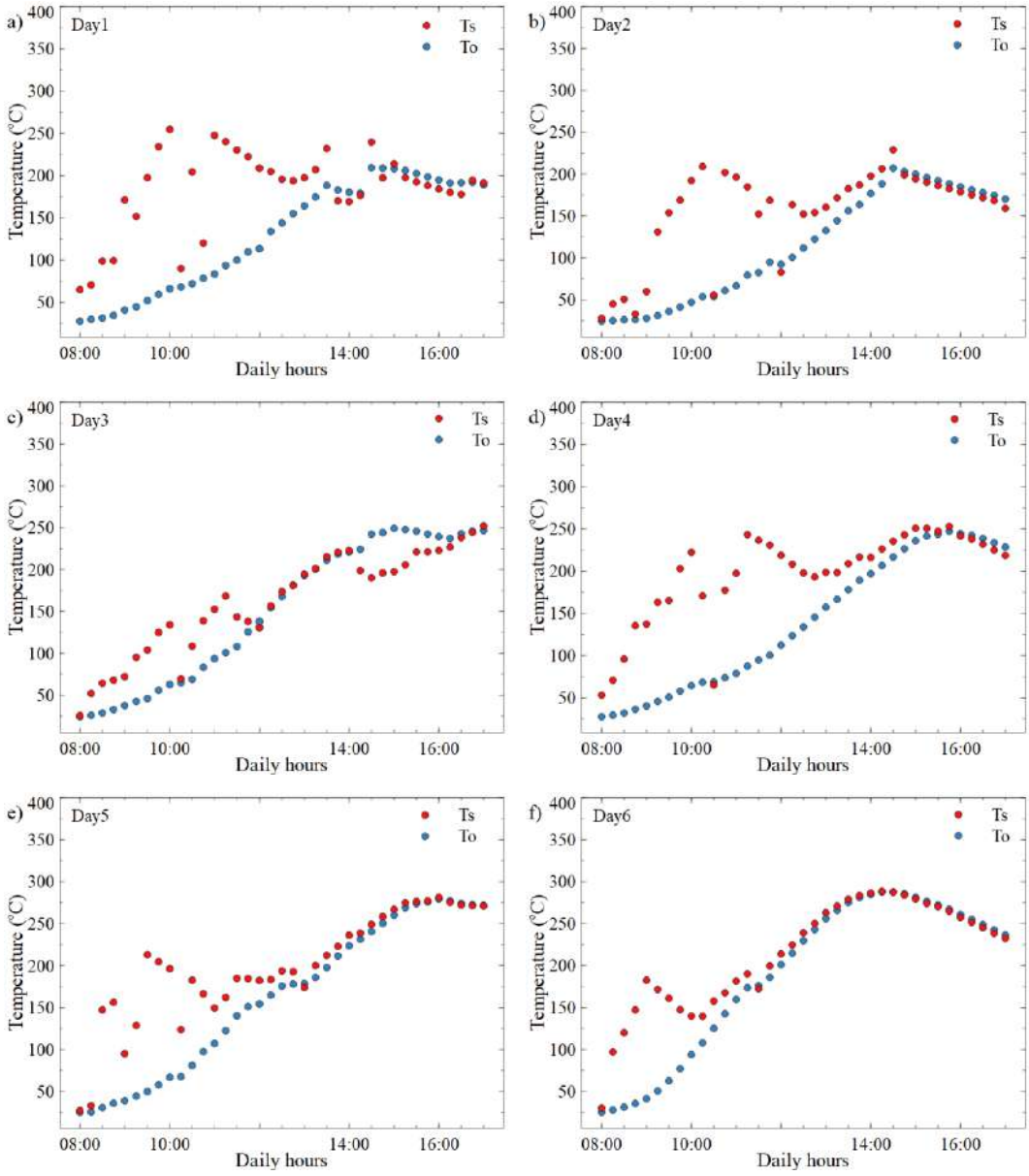

Fig. 8.9: Maximum receiver surface and HTF temperatures (a) Day 1, (b) Day 2, (c) Day 3, (d) Day 4, (e) Day 5, (f) Day 6

The greatest temperature gains obtained for the PTC without secondary reflector are 11.98°C, 10.56°C, and 9.15°C during 12.15-12.30 hrs, 14.15-14.30 hrs, and 14.15-14-30 hrs for the Day 1, Day 2, Day 3 evaluations, respectively. The maximum temperature gains for the PTC with a secondary reflector are 12.73°C, 12.32°C, and 6.75°C during 12.45-13.00 hrs, 11.15-11.30 hrs, and 10.30-10.45 hrs for the Day 4, Day 5, and Day 6 evaluations, respectively. The most significant temperature gains depend on the irradiation's daily distribution, as seen in Figs. 8.4 (a)-(f). The higher instantaneous temperature rises are obtained for lower flow rates in both configurations.

Figure 8.10 compares the average global flux showered by the sun during the experimental hours with the corresponding average inlet (T_{iave}), outlet (T_{oave}), and storage (T_{save}) temperatures of the working fluid. It is noted that the difference in average temperatures of the fluid in the storage tank and absorber tube are relatively close throughout the hours on all the days. The greatest average reservoir temperature obtained for a PTC without a secondary reflector is 150.175°C (Day 3) at a mass flow rate of 7.5 lpm, corresponding to a daily average solar flux of 581.34 W/m^2. The highest average reservoir temperature obtained for the PTC with a secondary reflector is 187.436°C (Day 6), with an average solar flux of 574.88 W/m^2. Hence, the obtained average temperature for the PTC with a secondary reflector is 37.26°C , which is higher than that without a secondary reflector. Furthermore, this rise in fluid temperature is accomplished with an average daily solar flux of 574.88 W/m^2, which is 6.46 W/m^2 less as compared to that in Day 3.

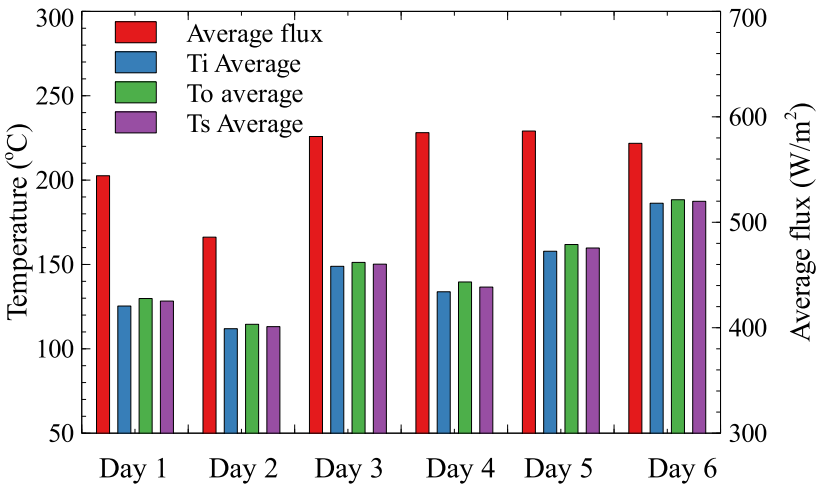

Fig. 8.10: Average irradiation and average fluid temperatures

8.6.2 Heat gain of the PTC with and without secondary reflector

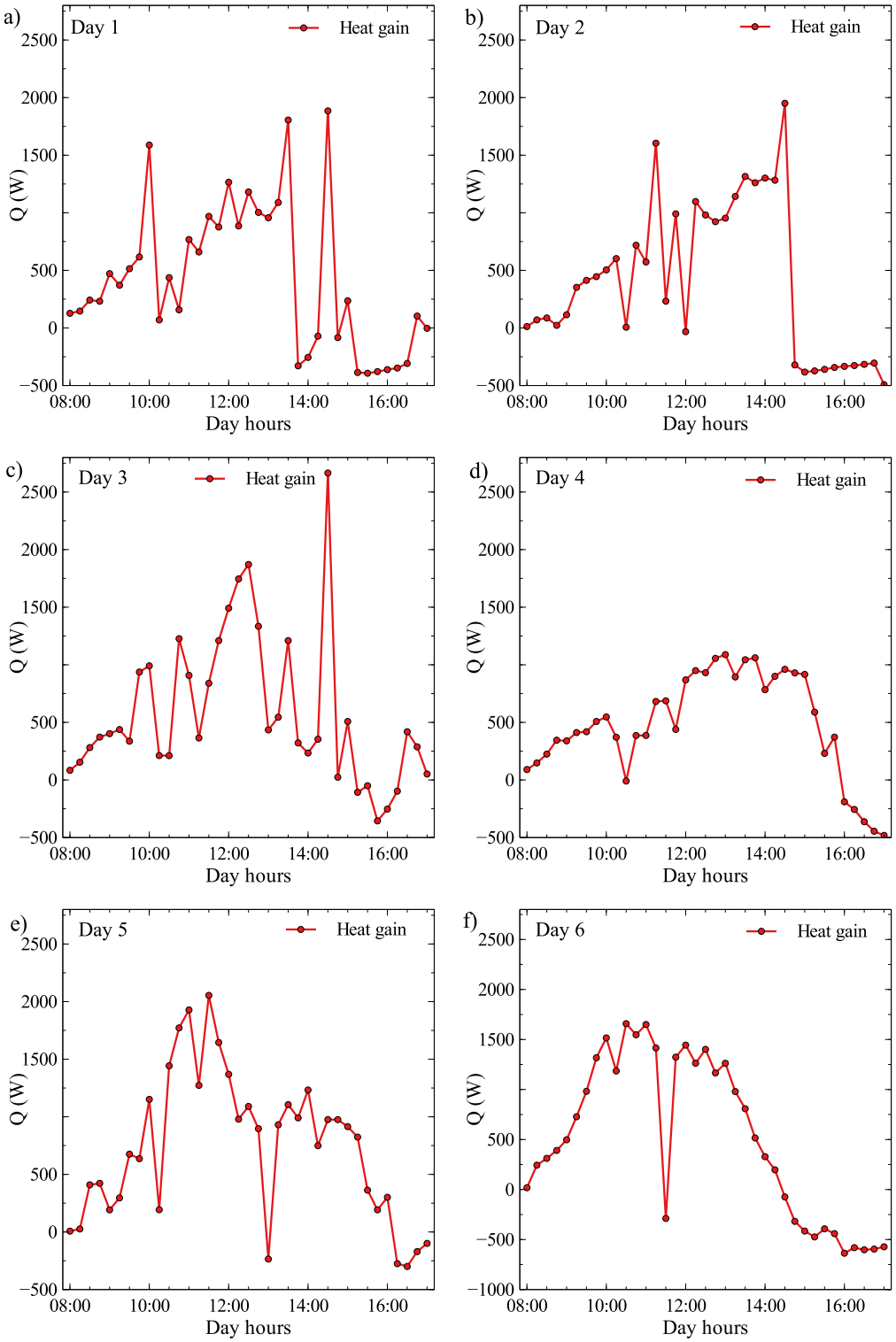

Fig 8.11: Useful heat gain by the HTF (a) Day 1, (b) Day 2, (c) Day 3, (d) Day 4, (e) Day 5, (f) Day 6

The useful energy gain for the evaluated days are shown in Figs. 8.11 (a)-(f). The instantaneous heat gain curves generally demonstrated that significant heat gains are achieved up to 14.00 hrs, after which heat loss is found to be morethan that of heat gain. The total heat gain by the HTF (PTC without a secondary reflector) on Day 1, Day 2, and Day 3 are approximately 14105.5 kW, 14049 kW, and 17130 kW, respectively. The daily heat gains on Days 4, Day 5 and Day 6 (PTC with the secondary reflector) are approximately 30508.6 kW, 22642.3 kW, and 19378.9 kW, respectively. The total heat gain in Day 6 is determined to be 11.36% higher than Day 3's total heat gain. By comparing the average heat flux of Day 3 and Day 6, it is evident that the useful heat gain of a solar collector with an extra reflector is much larger than that of a PTC without a secondary reflector.

According to Figs. 11(a)-(f), the heat gain curve tends to have negative values after 15.00 hrs. The negative heat gains imply heat transfer from the HTF to the surroundings. Thus, the decreasing sun intensity during the afternoon hours is unable to keep the stored energy during the midday hours.

8.6.3 Efficiency of the PTC with and without secondary reflector

The instantaneous and average efficiencies of the PTC with and without the secondary reflectors for the various flow rates are illustrated in Figs. 8.12(a)-(f). The average daily efficiencies for the PTC without a secondary reflector are 18.34 %, 20.94 %, and 19.05 % for 2.5 lpm, 5.0 lpm, and 7.5 lpm flow rates, respectively. The PTC with a secondary reflector has shown 24.52 %, 28.27 %, and 25.84 % efficiency for the same flow rates. According to Figs. 8.12(a)-(f), instantaneous efficiency is merely a function of the corresponding instantaneous incoming solar radiation. Still, the daily average efficiency is dependent on the consistency and amount of light received throughout the day.

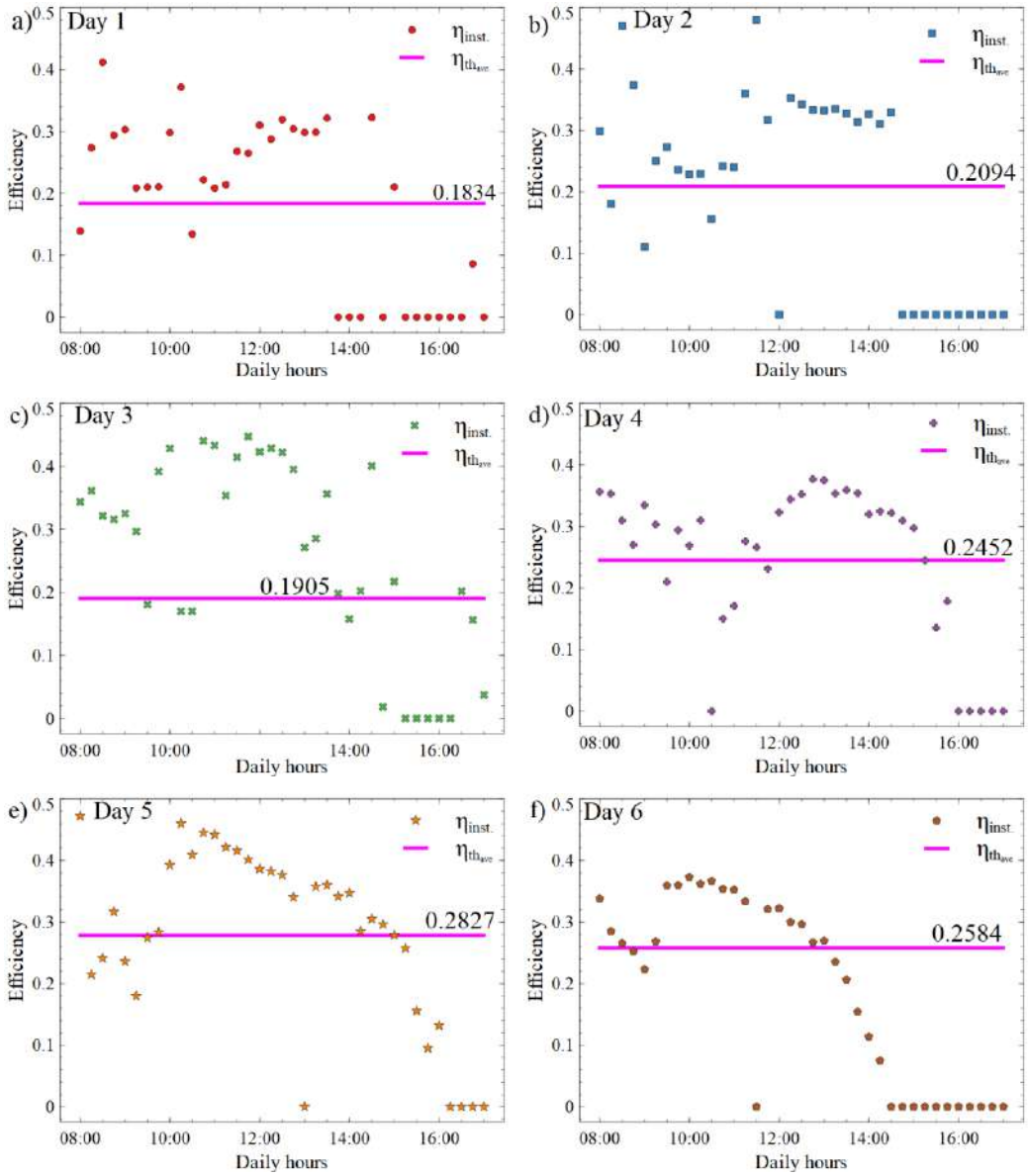

Fig. 8.12: Average and instantaneous efficiencies (a) Day 1, (b) Day 2, (c) Day 3, (d) Day 4, (e) Day 5, (f) Day 6

The comparison of maximum instantaneous efficiencies and average daily efficiencies of the PTC for the different evaluated days are depicted in Fig. 8.13. Although the solar energy received varies, the efficiencies of the PTC with a secondary reflector is on higher side on all evaluated days. The comparison of the PTC with and without the secondary reflector in terms of the daily average efficiency is described in Table 8.3. The PTC with secondary reflector outperformed the PTC without the secondary reflector by 6.18 % efficiency at 2.5 lpm (Day 1 and Day 4). At a 5.0 lpm flow rate, the PTC with secondary reflector (Day 5) has a 7.33% higher daily average efficiency than the PTC

without the secondary reflector (Day 2). For the 7.5 lpm flow rate, the increase in the daily average efficiency of the PTC with a secondary reflector (Day 6) is 6.79% higher than that of the PTC without secondary reflector (Day 3).

Table 8.3: Daily average efficiency of the PTC with and without secondary reflector

PTC (Experimental)	Flow rate (lpm)	HTF	Without secondary reflector		With secondary reflector	
			Average solar radiation (W/m^2)	Average Efficiency (%)	Average solar radiation (W/m^2)	Average Efficiency (%)
	2.5	TH55	544.23	18.34	584.95	24.52
	5.0		485.9	20.94	586.54	28.27
	7.5		581.34	19.05	574.88	25.84

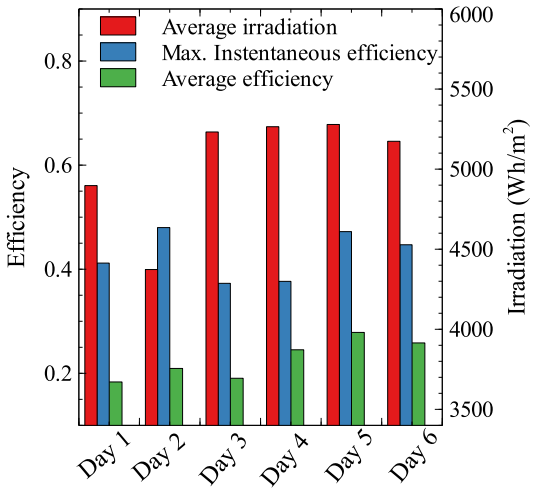

Fig. 8.13: Efficiencies of PTC on evaluated days

The higher efficiencies of the PTCs with the secondary reflector is caused by the re-reflected radiations due to the secondary reflector. On the other hand, the thermal distortion caused by the uneven heat flux distribution on the receiver tube of the PTC without a secondary reflector would significantly reduce the incident radiation on the tube [181]. This reduced flux intensity further decreases the efficiency of the PTCs without the secondary reflector. The thermal distortion is not considered in the analysis of the conventional PTCs design. Hence, the efficiency of the PTCs with and without the

secondary collector is consistent with a slightly higher values for the PTC with a secondary reflector. The literature contains a number of MCRT studies of PTCs with secondary reflectors, but there are few experimental tests of PTCs with secondary reflectors under actual outdoor conditions. A comparison of the maximum thermal efficiencies of PTCs with secondary reflectors in the literature with the present study is shown in Table 8.4. An experiment with a PTC and Therminol VP-1 HTF [94] demonstrated a maximum efficiency of 47%. The maximum thermal efficiency of a PTC with a secondary reflector using water as HTF reported in the literature is 24.3 % [100], whereas our study measured a maximum efficiency of 48.22% with an average efficiency of 28.27 %.

Table 8.4 Thermal efficiency of PTCs with secondary reflectors

Sl No.	**SR type**	**Fluid**	**Experimental hours**	**Maximum Efficiency**	**Reference**
1	Parabolic	Water	9.00-16.00	24.3	[100]
2	Compound parabola	Salt mixture	Numerical	70.1 (4.9% increase)	[108]
3	Compound parabola	Therminol VP-1	Monthly average (March)	47	[94]
4	Nil	Indium tin oxide/EG	Numerical	23.2	[182]
5	Parabolic	Therminol®55	8.00- 17.00	48.22	Present study

On the other hand, the current experimental results revealed that the efficiency of the PTC with the secondary reflector obtained a greater than 6.0 % improvement over conventional PTCs. This higher efficiency is not observed during the design stage since the simulations did not account for the receiver tube deflections for the PTC without a secondary reflector. In practice, the significant disparity in heat flux distribution will induce thermal distortion on the receiver tubes of conventional PTCs, lowering their thermal efficiency further. The experimental results indicate that the designed PTC with the secondary reflector is more suitable for medium-temperature applications with high efficiencies than a PTC without a secondary reflector.

8.7 Performance prediction of the PTC

A correlation has been developed to predict the performance of the proposed PTC based on daily/monthly/annual average weather data of the location. For this, a numerical investigation has been carried out for eight more days considering HTF velocities of 2.5 lpm, 5.0 lpm, and 7.5 lpm on each day. System performance is highly dependent on daily average flux intensity, ambient temperature, and wind velocity. However, they vary throughout the year on a stochastic basis. Hence, these meteorological data is deduced into a dimensionless factor called 'solar day index' (χ) as recommended by Jinsha et al [183].

Here χ is the solar day index defined as,

$$\chi = \frac{0.9096 I_d}{0.039 T_{a-d}^{0.25} + 1.05 U_d^{0.125}} \tag{8.13}$$

where $I_d = {}^{I}/_{I_r}$, $T_{a-d} = {}^{T_a}/_{T_r}$, and $U_d = {}^{U}/_{U_r}$, are the average solar heat flux, average ambient temperature, and average wind velocity for the day, normalised using the corresponding reference values. Take I_r = 650 W/m^2, T_r = 30.88°C, Ur =10.5 m/s and y is the normalized Reynolds number defined as Re/2400 [183]. The solar day indices, normalized Reynolds numbers, and the average HTF temperatures are fitted to obtain a correlation to predict the average fluid temperature as a function of the meteorological data and the flow rate of the HTF.

The proposed correlation is as follows,

$$T = 517.9\chi^2 - 0.2376y^2 + 2.293\chi y - 418.1\chi + 2.962y + 124.2 \tag{8.14}$$

The correlation has a root mean square error of 4.39 and R^2 of 0.9727 at the 95% confidence bounds. The proposed correlation can be applicable for predicting the performance of the PTC by considering either daily, monthly, or annual average meteorological data of the location.

Fig.8.14 shows the average temperatures of the HTF for the PTC with the secondary reflector and the predicted average temperatures for the solar day indices of 0 to 1. Observations show that there is only less than 3% difference between the experimental average temperatures and the expected average temperatures predicted by the proposed correlation.

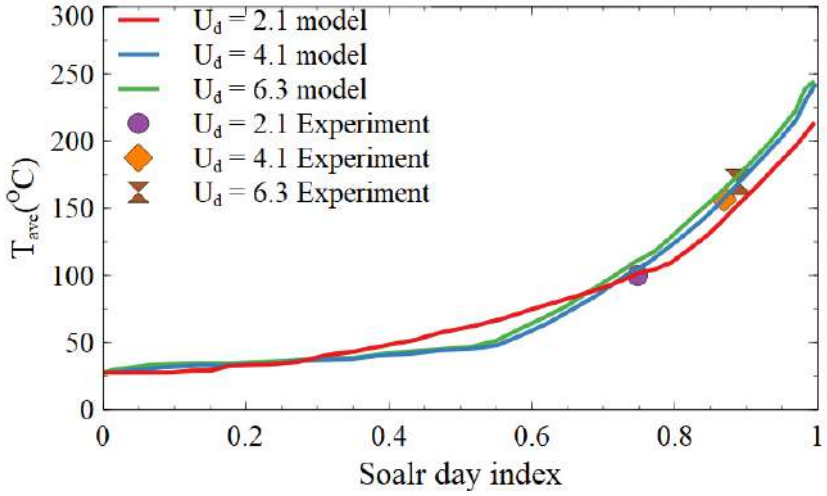

Fig. 8.14 Average HTF temperature of the experimental days and predicted by the model for varying meteorological data.

8.8 Exergy analysis

The PTC has been evaluated exergetically by taking a detailed analysis that includes the exergy of the solar irradiation, the useful exergy produced, the exergy lost, and the exergy destroyed. Solar PTCs use only direct solar radiation, which is assumed to be undiluted. Hence, the rate of exergic flow in the incoming solar energy can be estimated using the Petela model [184]. Equation (8.15) shows the exergy analysis of the solar radiation, where the temperature of the sun's outer layers (T_s) is assumed as 5770 K.

$$E_s = DNI.A_c\left[1-\frac{4}{3}.\left(\frac{T_a}{T_s}\right)+\frac{1}{3}\left(\frac{T_a}{T_s}\right)^4\right] \tag{8.15}$$

The useful exergy output of the collector is given as [185]

$$E_u = Q_u - m.C_p.T_a.ln\left[\frac{T_o}{T_i}\right] - m.T_a\frac{\Delta P}{\rho_{HTF}T_{HTF}} \tag{8.16}$$

In Eq. (8.16), the last term can be ignored since the pressure drop associated with liquid HTFs is small. The useful heat flux can be calculated by the HTF volume's energy balance as indicated in Eq. (8.17).

$$Q_u = m.C_p.(T_o - T_i) \tag{8.17}$$

The ratio of the exergy output of the collector to the solar exergy input is known as the exergy efficiency (η_{ex}) of the PTC.

$$\eta_{ex} = \frac{E_u}{E_s} \tag{8.18}$$

The value of the mean HTF temperature (T_f) is determined using the inlet (T_i) and outlet (T_o) HTF temperatures as given below.

$$T_f = \frac{T_i + T_o}{2} \tag{8.19}$$

The exergy losses (E_l) in solar collectors comprises the optical losses ($E_{l,optical}$) and the thermal losses ($E_{l,th}$). The exergy optical losses and thermal losses are obtained as Eq. (8.20) and Eq. (8.21), respectively:

$$E_{l,optical} = \left(1 - \eta_{optical}\right).E_s \tag{8.20}$$

$$E_{l,th} = Q_l.\left[1 - \frac{T_a}{T_r}\right] \tag{8.21}$$

The total exergy losses are determined as:

$$E_l = E_{l,optical} + E_{l,th} \tag{8.22}$$

The exergy destruction of the system is calculated by the irreversibility, which exists in the heat transfers. In solar PTCs, the exergy destruction occurs between the sun and the receiver (E_{d,s_r}), and the second is in between the receiver and the HTF (E_{d,r_f}). The exergy destruction between the sun and the receiver is given as:

$$E_{d,s\_r} = \eta_{optical}.E_s - Q_r\left(1 - \frac{T_a}{T_r}\right) \tag{8.23}$$

The exergy destruction during the useful heat transport from the absorber to HTF is given as:

$$E_{d,r\_f} = Q_u.\left(1 - \frac{T_a}{T_r}\right) - E_u \tag{8.24}$$

The total exergy destruction (E_d) is obtained as:

$$E_d = E_{d,s\_r} + E_{d,r\_f} \tag{8.25}$$

Finally, the total exergy balance of the system is:

$$E_s = E_u + E_l + E_d \tag{8.25}$$

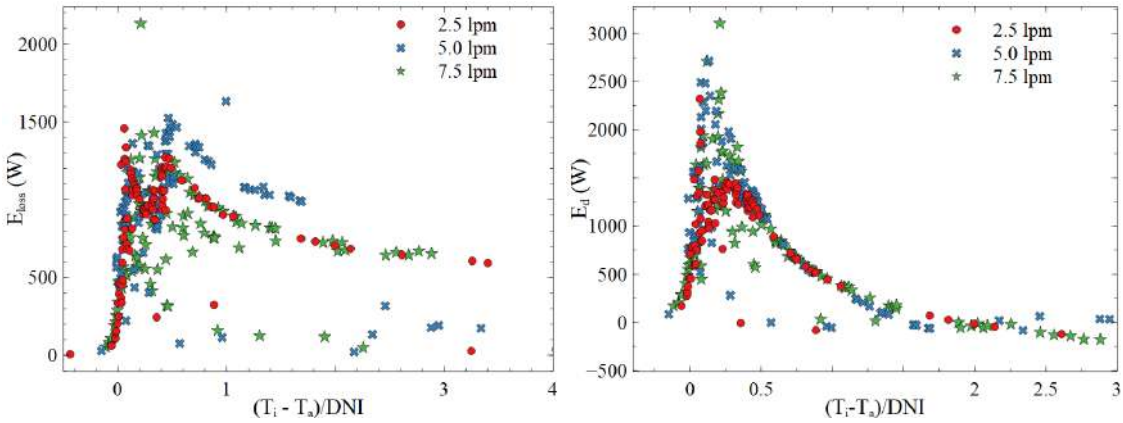

Fig. 8.15(a) Exergy losses for the PTC, (b) Exergy destruction for the PTC

The results of the exergy analysis is given in this section. Figur 8.15(a) and (b) show the exergy losses and destruction for the examined cases. These losses are associated with the optical and thermal losses. To reveal the exergy losses of the PTC, the exergy efficiency values of the PTC with resepect to the HTF inlet temperature and daily hour duration is presented in Fig. 8.16(a) and 8.16(b), respectievely. Figure indicates that a great quantity of exergy is lost/destructed in the solar PTC and the maximum value of exergy efficiency is around 15%. It is found that 53.4% of the energy is destroyed between the sun and the collector. It has been reported that parabolic trough collectors are the primary source of exergy destruction, which destroys more than 50% of the solar inlet exergy [186]. As the HTF inlet temperature rises to 200°C, energy efficiency gradually increases, and then decreases. To assess the PTC's energy performance, Fig. 8.15(a) and (b) demonstrate total exergy losses and destruction, respectievely. The figures show that with increased solar irradiation intensity, the total amount of energy destroyed and the rate of energy loss decrease. Exergy losses and exergy destruction have been observed to increase as temperatures rise. It is expected that these decrements occur due to the increase in exergy efficiency due to the increase in solar radiation intensity and the exergy efficiency is inversely proportional to the rate of exergy loss/destruction, as long as the loss is less than the destruction.

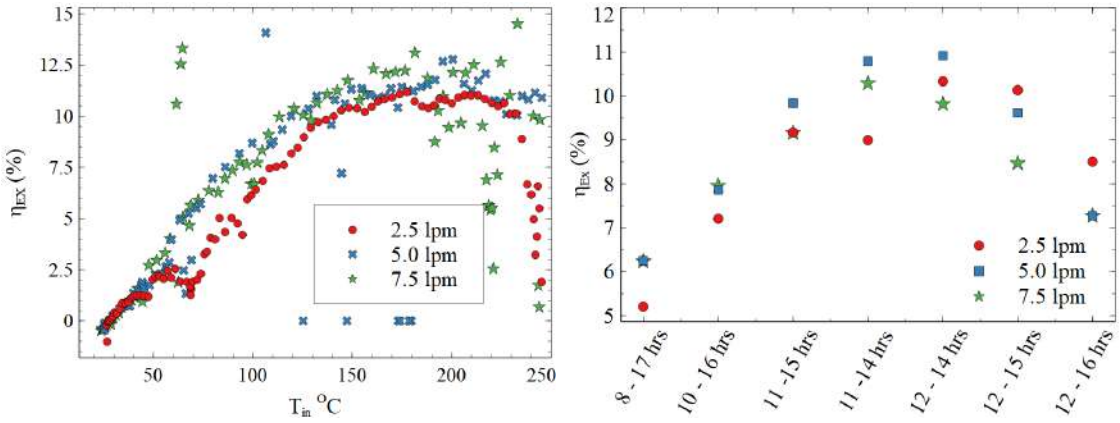

Fig. 8.16 (a) PTC exergy efficiency, (b) Exergy efficiency for different solar hours

The uncertainity of the exergy efficiency has been estimated using Kline-McClintock method using the the following equations (Eq. (8.26-8.28)). Analysis involved uncertainity of thermocouples, flow rate, and solar radiation measurement similar to that used in energy analysis. Result of the uncertainity analysis shows that the average uncertainity of the exery efficiency is below 12 %.

$$U_{Q_u} = \left[\left(\frac{\partial Q_u}{\partial \dot{m}} U_{\dot{m}}\right)^2 + \left(\frac{\partial Q_u}{\partial T_o} U_{T_o}\right)^2 + \left(\frac{\partial Q_u}{\partial T_i} U_{T_i}\right)^2\right]^{\frac{1}{2}} \tag{8.26}$$

$$U_{E_u} = \left[\left(\frac{\partial E_u}{\partial Q_u} U_{Q_u}\right)^2 + \left(\frac{\partial E_u}{\partial \dot{m}} U_{\dot{m}}\right)^2 + \left(\frac{\partial E_u}{\partial T_a} U_{T_a}\right)^2 + \left(\frac{\partial E_u}{\partial T_o} U_{T_o}\right)^2 + \left(\frac{\partial E_u}{\partial T_i} U_{T_i}\right)^2\right]^{\frac{1}{2}} \tag{8.27}$$

$$U\eta_{ex} = \left[\left(\frac{\partial \eta_{ex}}{\partial E_u} U_{E_u}\right)^2 + \left(\frac{\partial \eta_{ex}}{\partial E_s} U_{E_u}\right)^2\right]^{\frac{1}{2}} \tag{8.27}$$

The exergy efficiency of the PTC is highly depends on the intensity of solar irradiation as shown in Fig. 8.16. It is observed that the average exergy efficiency of the PTC is about 11% for the daily hours between 11.00 to 14.00. For the solar irradiation between 11.00 to 15.00 hours, the exergy efficiency of the PTC is found to be greater than 10%. There have been various studies comparing different types of solar collectors and reporting their typical exergy efficiency, which is greatly influenced by the type of collector (glazed, unglazed, coverless), the type of HTF, and the application (i.e., PV/T, air heater) as well as the assumptions and equation models used [187]. Based on the reported results, the best exergy efficiency is achieved by the glazed PV/T water collector, which is equal to 13.30%, followed by the coverless PV/T water collector, which has an

efficiency between 11% and 12.87 %. A double-glazed air heater with an exergy efficiency of 2% was found to have the lowest value. An experiment found that the exergy efficiency of a PTC at medium temperatures varied from 3.5% to 8.5% [188].

8.9 Summary

The effect of using a systematically designed secondary reflector with a PTC is experimentally investigated. The effect of mass flow rate under outdoor ambient conditions on heat gain and efficiency is studied. Compared to the PTC without a secondary reflector, the designed PTC demonstrated better efficiency due to the enhanced heat flux distribution and lower thermal bending of the receiver tube provided by the secondary reflector. The highest daily average fluid outlet temperature for the PTC with the secondary reflector is 188.35^0C for the evaluated days, which is 37.13^0C higher than the PTC without the secondary reflector. For the evaluated days, the maximum daily average efficiency attained by the PTC with the secondary reflector is 28.27%, while it is 20.94% for the PTC without a secondary reflector. The average exergy efficiency varied between 5% to 11% and gets improved more remarkably at peak solar hours.The result shows that using the secondary reflector increases the HTF outlet temperature and efficiency of the PTC. This experimental work revealed that a properly designed PTC with a secondary reflector is highly beneficial for the better performance of the system. Furthermore, a model has been developed to predict the performance of the PTC using average daily, monthly, or annual weather data. Model predictions for daily average meteorological data for the evaluated days have been compared to experimental results and showed good agreement with less than 3% deviation. The numerical modelling of the PTC and the hybrid nanofluid's performance evaluation are shown in the next chapter.

Chapter 9

Numerical Modelling of the PTC and Thermal Performance Evaluation of Hybrid Nanofluid

The present chapter deals with the numerical modelling of the constructed PTC with a secondary reflector and presents the results obtained by the thermal performance analysis of the hybrid nanofluid. The PTC with the secondary reflector has been evaluated under two HTFs: TH55 and the TH55- GNP(0.1%)/ Al_2O_3(1.0%) hybrid nanofluid. Each HTFs has been tested for different flow rates, beginning at 8.00 hrs and ending at 17 hrs.

9.1. Mathematical model of the receiver tube

As shown in Fig. 9.1, the Heat Collecting Element (HCE) considered in this study is a bare absorber tube. The absorber tube is made of copper alloy. Therminol (TH55) and hybrid nanofluid (TH55- GNP/Al_2O_3) selected by the critical study as explained in Chapter 6 is used as the working fluid in this study. Figure 9.1 also represents the control volume and corresponding nodal locations considered for the analysis. The mathematical model governing the flow's physics considered here is based on the energy balance between the HTF and its surroundings.

Figure 9.2 depicts the energy interactions in a segment of the receiver tube. The absorber tube receives solar energy (q_{sol}) reflected by the concentrating mirror. A portion of this energy is transferred to the HTF via convection (q_{htf}). The portion of the

remaining energy absorbed by the absorber is conducted via the pipe ($q_{ap-cond}$), and the remainder is lost as radiation to the sky ($q_{rad(ap-sky)}$) and convection to the ambient ($q_{conv(ap-anu)}$).

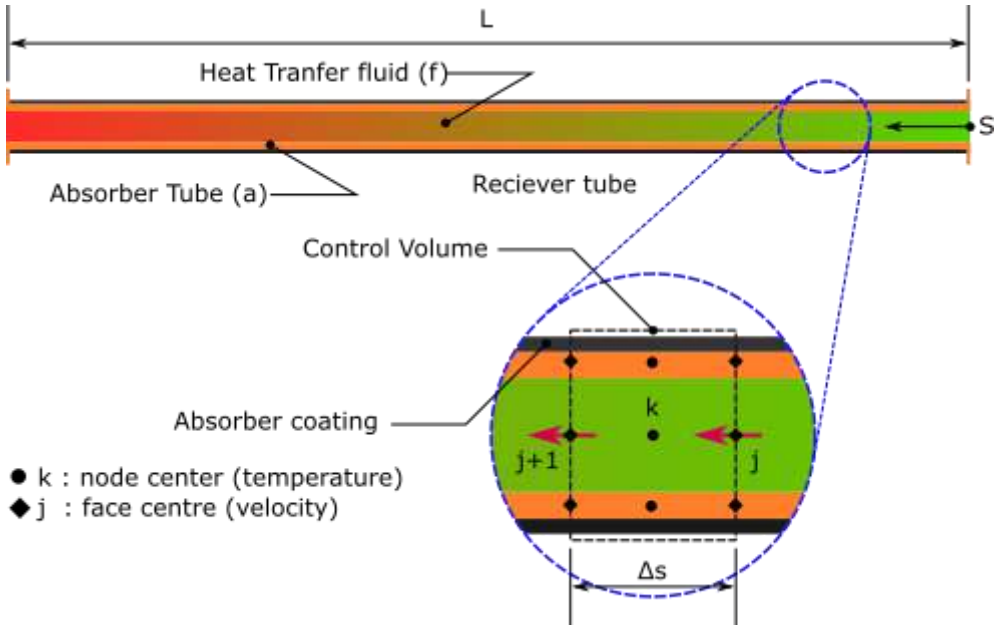

Fig. 9.1: Heat collecting element of the PTC along with the stencil considered for the analysis

Certain assumptions are made here to simplify the mathematical model created without sacrificing the problem's generality.

Assumptions made in the analysis are as follows:

i. Because the length-to-diameter ratio (≈93) is so high, the flow is practically one-dimensional
ii. The influence of viscosity on energy transfer is regarded to be insignificant (since the fluid is a liquid the dissipation and generation due to viscosity is negligible)
iii. In the HCE, the flow regime is the same since the fluid is incompressible
iv. Because the study focuses on area-averaged values rather than local values, uniform heat flux is assumed over the absorber pipe

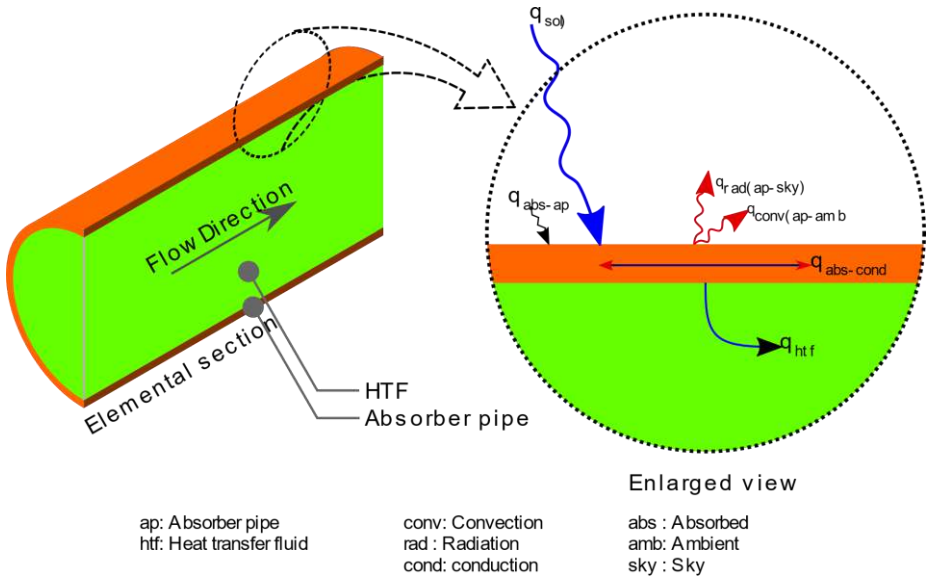

Fig. 9.2: Complete energy interaction for an elemental section of the receiver tube

An energy balance is applied over a segment of the solar receiver in order to derive the partial differential equations that govern the heat transfer processes (Fig. 9.2). The equations for each component are detailed subsequently.

9.1.1 Heat transfer through HTF

On applying the energy balance on the control volume as detailed in Fig. 9.2, assuming an unsteady and incompressible flow, the following partial differential equation is obtained in terms of enthalpy (h):

$$\frac{\partial \rho h}{\partial t} + \frac{\partial \rho u h}{\partial s} = \frac{\partial}{\partial s}\left(k_f \frac{\partial T_f}{\partial s}\right) + \frac{P_i}{A_i} q_{htf} \qquad (9.1)$$

Here enthalpy is considered as a linear function of the temperature as, $h = C_p\left(T_f - T_r\right)$, u is the velocity of the fluid, k_f the thermal conductivity, T_f the fluid temperature, P the perimeter corresponding to the inner diameter of the absorber tube, and A the corresponding cross-sectional area. The reference temperature, T_r is assumed as the absolute temperature for the fluid considered. The velocity u is evaluated using the mass flow rate as,

$$u = \frac{4\dot{m}}{\pi D_i^2} \qquad (9.2)$$

With D_i being the inner diameter of the absorber tube. The convective heat transfer in the Eq. (9.1) is evaluated as,

$$q_{htf} = \frac{Nu_{htf} k_f}{D_i}\left(T_{ab} - T_{htf}\right) \tag{9.3}$$

where, T_{ab} is the absorber tube temperature, and Nu_{htf} the Nusselt number depends on the flow condition, evaluated using empirical correlations. In the case of fully developed turbulent flow ($Re_{D_i} > 2300$), Gnielinski correlation [189] is used, which is valid for Reynolds numbers in the range 2300 to 5×10^6 and Prandtl number in the range of 0.5 to 2000 as,

$$Nu_{htf} = \frac{(\lambda/2)\left(Re_{D_i} - 1000\right)Pr}{1+12.7(\lambda/2)^{0.5}\left(Pr^{2/3}-1\right)}\left[\frac{Pr}{Pr_w}\right]^{0.11} \tag{9.4}$$

with Reynolds number, $Re_{D_i} = \frac{4\dot{m}}{\pi D_i \mu}$. In Eq. (9.4), Pr is the Prandtl number defined as $Pr = \frac{\mu C_p}{k}$. Similar correlations are used to evaluate the Fanning friction factor, λ as follows,

For transition flow, $2100 \leq Re_{D_i} \leq 4000$, Battu and Shah correlation is used as,

$$\lambda = 0.0054 + \frac{2.3\times 10^{-8}}{Re_{D_i}^{-3/2}} \tag{9.5}$$

For the fully turbulent region, $Re > 4000$, Filonenko correlation [189] is used,

$$\lambda = \frac{1}{\left(1.82\log Re_{D_i} - 1.64\right)^2} \tag{9.6}$$

For thermally fully developed, laminar flow ($Re_{D_i} \leq 2300$), the Nusselt number for a constant wall temperature is considered as,

$$Nu_{htf} = 3.66 \tag{9.7}$$

In the case of thermally developing laminar flow, a correlation suggested by Hausen [175] is used for evaluating Nu_{htf} as,

$$Nu_{htf} = 3.66 + \frac{0.0668\frac{D_i}{l} Re_{D_i} Pr}{1.0+0.04\left(\frac{D_i}{l} Re_{D_i} Pr\right)^{0.67}} \tag{9.8}$$

where the above equation is valid till the flow reaches a thermally fully developed state which can be expressed mathematically as, $\frac{l}{D_i Re_{D_i} Pr} \approx 0.05$. Here l is the length from the leading face to the node under consideration. All the properties in the above equations except Pr_w is evaluated at the bulk mean temperature while Pr_w is evaluated at the wall temperature.

9.1.2 Heat transfer in the absorber tube

The absorber temperature is higher than the ambient temperature, and hence the energy is lost to the ambient in two distinct ways: radiation to the sky and convection to the ambient. Apart from that, the absorber interacts with the HTF to exchange heat. The phenomena that governing heat transfer can be well addressed by employing the Fourier Biot equation with radiation and convection boundary conditions as follows:

$$\frac{\partial}{\partial t}\left(\rho C_p T_{ab}\right) = k_{ab}\frac{\partial^2 T_{ab}}{\partial s^2} - \frac{P_i}{A}q_{htf} + \frac{P_o}{A_c}\left[q_{abs} - q_{rad-sky} - q_{conv-amb}\right] \quad (9.9)$$

For convection loss ($q_{conv-amb}$), two distinct cases can be considered: one with wind load and one without wind load. In the presence of wind load, forced convection is considered., whereas natural convection is the mode of heat transfer in the absence of wind. In either mode, a similar relation as of Eq. (9.3) is used, as $q_{conv-amb} = \frac{Nu_{conv-amb}k_{air}}{D_o}(T_{ab} - T_{amb})$. Correlation proposed by Churchill and Chu [173] is recommended for the case of natural convection as,

$$Nu_{conv-amb} = \left[0.6 + 0.387\left\{\frac{Ra_{D_o}}{[1+(0.559/Pr)^{9/16}]^{16/9}}\right\}^{1/6}\right]^2 \quad (9.10)$$

Rayleigh number, Ra_{D_o} is evaluated as:

$$Ra_{D_o} = \frac{g\beta(T_{ab}-T_{amb})D_o^3}{\alpha\nu} \quad (9.11)$$

where α is the thermal diffusivity of the air and ν the dynamic viscosity.

For the forced convection, the correlation for circular cylinder in crossflow suggested by Zukauskas [175] is employed. The correlation is valid for $0.7 \leq Pr \leq 500$ and $1 \leq Re_{D_o} \leq 10^6$, written as,

$$Nu_{conv-amb} = CRe_{D_o}^m Pr^n \left(\frac{Pr}{Pr_w}\right)^{0.25} \quad (9.12)$$

where the constants C, m, and n is depended on Re_{D_o} as listed in Table 9.1.

In practice, either the collector or the sky surrounds the receiver tube. To simplify the analysis, it is assumd that the HCE is surrounded by the sky. With this assumption, radiation loss to the sky is calculated by using the Stefan Boltzmann relation as follows:

$$q_{rad-sky} = \epsilon\sigma\left(T_{ab}^4 - T_{sky}^4\right) \quad (9.13)$$

Table 9.1 Constants in Zukhaskas Correlation

Re_{D_o}	C	m	n
1 - 40	0.76	0.4	0.37
40 - 1000	0.52	0.5	0.37
1000 - 2×10^5	0.26	0.6	0.37
2×10^5 - 1×10^7	0.23	0.8	0.4

This study employs a linearised form of Eq. (9.13) based on the effective heat transfer coefficient as $q_{rad-sky} = \Psi(T_{ab} - T_{sky})$. Where $\Psi = \epsilon\sigma(T_{ab}^2 + T_{sky}^2)(T_{ab} + T_{sky})$.
At any given location, the temperature of the sky is determined by various factors, including altitude, cloudiness, humidity, and the presence of air pollutants. The equivalent sky temperature is calculated in this model using a method described by Al-Sanea *et al.* [190], which was initially proposed by Clark, and T_{sky} is sourced using,

$$T_{sky} = \epsilon_{sky}^{0.25} T_a \tag{9.14}$$

where Berdahl and Fromberg[190] define sky emissivity as a linear function of dew point temperature.

$$\epsilon_{sky} = 0.741 + 0.00062 T_{dpa} \tag{9.15}$$

The dew point temperature is calculated using the ambient air temperature and relative humidity in accordance with Murray's [191] proposed formula:

$$T_{dpa} = \frac{237.3\left[\ln\Phi + \frac{17.27T_a}{T_a+237.3}\right]}{17.27 - \ln\Phi - \frac{17.27T_a}{T_a+237.3}} \ ^\circ C \tag{9.16}$$

9.1.3 Solar energy absorbed

The amount of solar energy collected by the receiver tube is mostly determined by the receiver tube's optical properties and the concentrator's optical efficiency. Imperfections in the concentrator surface can result in a loss of reflected rays relative to the solar irradiation available to the receiver tube. These flaws can be generalised by examining a concept known as the intercept factor (χ). The intercept factor is defined mathematically as the ratio of solar radiation reaching the absorber tube to that reflected by the concentrator. Table 9.2 details the factors contributing to the imperfections and the value assumed in this study. This allows for the mathematical expression of the intercept

factor as,

$$\chi = \prod_{i=1}^{5} \chi_i \qquad (9.17)$$

The factors mentioned above are obtained by assuming the incident radiation as normal to the aperture of the collector. Additional radiation loss occurs as the angle of incidents deviates from zero degrees to the normal to the aperture. The incident angle modifier, K is introduced to correct the additional loss in reflection and absorption with the deviation in incident angle from 0 °. K depends foremost on the optical characteristics as well as the geometry of the mirror, which is typically expressed as an empirical relation of incident angle as follows for the proposed PTC (see Fig. 9. 3),

$$K = 1 + \frac{0.00105\times\theta - 0.00004\times\theta^2}{\cos\theta} \qquad (9.18)$$

here θ is in degree

Table 9.2 Factors affecting intercept factor and optical properties considered

Intercept factors / Optical parameter	Numerical Value
Shadowing factor, χ_1	0.974
Tracking/ Twisting error, χ_2	0.994
Geometric imperfection of collector mirror, χ_3	0.980
Cleanliness of mirror, χ_4	0.950
Miscellaneous factors, χ_5	0.960
Clean mirror reflectivity, ρ_{cl}	0.935

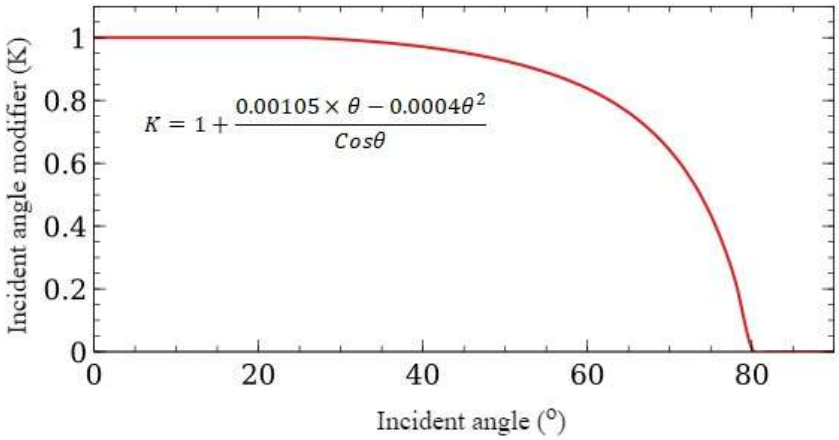

Fig. 9.3: Intercept factor for the proposed PTC

Other geometric factors affecting optical efficiency are the end loss and shading

factors. The shading factor (ζ_{sh}) considers the solar insolation due to the shadow created by other PTCs in the row at low solar altitudes. ζ_{sh} is expressed in terms of the tracking angle (ρ_t), aperture and centre line distance between two rows (L_r) as expressed in the equation,

$$\zeta_{sh} = |\cos\rho_t| \frac{L_r}{W} \tag{9.19}$$

Since only one collector is considered in this study, ζ_{sh} is taken as 1. The sun path is not the same throughout the year. This necessitates the tracking of the concentrator on two axes. Typically PTCs are tracked morning to evening rather than year-round. This makes a small portion of the receiver tube cannot accept the concentrated rays. The end loss factor (ζ_{el}) is introduced to consider this effect. ζ_{el} is expressed as a function of the focal length of the trough, length of the collector and the incident angle as expressed in the equation,

$$\zeta_{el}(i) = 1 - \frac{f}{L}\left(1 + \frac{W^2}{48f^2}\tan(\theta_i)\right) \tag{9.20}$$

with this, q_{abs} in Eq. (9.9) is mathematically written in terms of beam radiation, I_{bn} as,

$$q_{en}^{abs} = \pi D_o \rho_{cl} \chi K \zeta_{sh} \zeta_{el} I_{bn} C_r \tag{9.21}$$

C_r is the geometric concentration ratio, which depends on the trough's geometric characteristics. These parameters include the trough's focal length (*f*), acceptance angle (Θ), and rim angle (Υ_r). The acceptance angle of an ideal collector should be close to the sundisc angle, ensuring higher concentration with less imaging. The minimal diameter of the receiver necessary for a flawlessly aligned specular reflector to intercept all reflected light can be calculated as follows:

$$D_a = \frac{4f sin\theta_m}{1+cos\gamma_r} \tag{9.22}$$

A similar relation can be obtained for the aperture width of the parabola as a function of the rim angle as,

$$W_a = \frac{4f \sin\Upsilon_r}{1+\cos\Upsilon_r} \tag{9.23}$$

The geometric concentration ratio can now be mathematically defined as,

$$C_R = \frac{W_a L}{\pi D_a L} = \frac{\sin\Upsilon_r}{\pi \sin\Theta} \tag{9.24}$$

The collector's efficiency can be calculated using the equation,

$$\eta_{collector} = \frac{h_{HTF-out} - h_{HTF-in}}{I_{DNI} A_{aperture}} \tag{9.25}$$

9.1.4 Heat transfer model for the tank and connecting pipes

In this analysis, the high-temperature fluid from the PTC enters the tank from the top and it leaves from the bottom back to the PTC. A stratified tank model in 1D is considred for the present analysis. The vertical tank is divided into n number of closely arranged control volumes as given in Fig. 9.4. On applying the energy balance to the model, the partial differential equation can be written as,

$$\frac{\partial \rho h_t}{\partial t} + \frac{\partial \rho u h_t}{\partial s} = \frac{\partial}{\partial s}\left(k_f \frac{\partial T_t}{\partial s}\right) + \frac{P_i}{A_i} q_{loss} \tag{9.26}$$

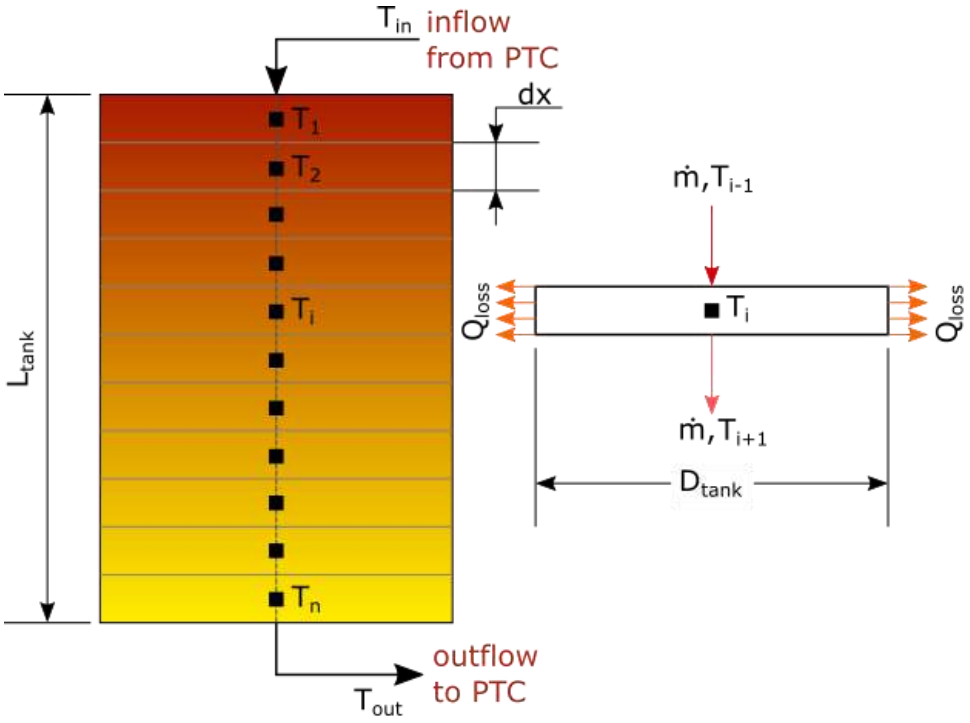

Fig. 9.4: Stratified tank model considered

Here, q_{loss} is utilised to account for heat loss through the tank's surface due to insufficient insulation. The experimental results indicate that the tank's loss is insignificant. Despite this, energy loss is detected in the pipes linking the PTC to the tank, which is a function of temperature differential, pipe length, and mass flow rate. The

experimental data indicate that the inflow temperature at the storage tank is as follows:

$$T_{in-tank} = T_{out-PTC} - 0.156(T_{out-PTC} - Tamb)L * \dot{m} \quad (9.27)$$

9.2 Material properties

This analysis assumes that the absorber material have constant characteristics. It is considered that the thermophysical parameters of the HTF changes with temperature. Figure 9.5 shows the variation of enthalpy, thermal conductivity, density and viscosity of TH55 with the temperature considered here [124]. The data is fitted using nonlinear regression analysis with a minimum R^2 value of 0.985. These equations are as follows.

$$h = 1.8436 \times 10^{-4}T^3 + 1.645175T^2 + 1857.6064T + 31438.1971 \quad (9.28)$$

$$\rho = -8.2737 \times 10^{-7}T^3 + 1.405 \times 10^{-4}T^2 - 0.67915T + 885.1784 \quad (9.29)$$

$$C_p = 2.00854 \times 10^{-6}T^3 - 1.01954 \times 10^{-3}T^2 + 3.67468T + 1832.244 \quad (9.30)$$

$$K = 4.31257 \times 10^{-12}T^3 - 4.98256 \times 10^{-9}T^2 - 1.15789 \times 10^{-4}T + 0.130732 \quad (9.31)$$

$$\mu = 0.1191\exp(-0.07702T) + 0.02367\exp(-0.02033T) \quad (9.32)$$

For the case of hybrid nanofluid, the property models obtained from Chapter 6 are considered.

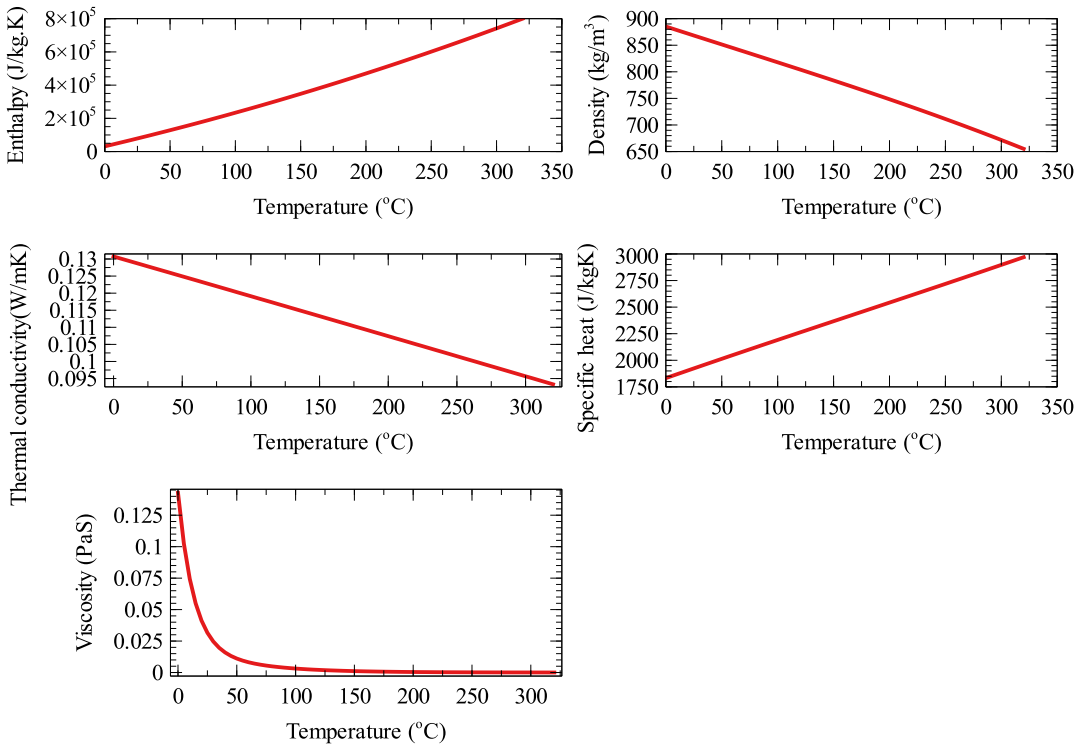

Fig. 9.5: Temperature dependant properties of TH55

9.3 Numerical procedure

The unstable partial differential Eqs. (9.1), (9.9) and (9.26) are discretised using the finite volume stencil. The diffusion terms are discretised using a central difference technique, while the convection term is discretised using a first-order upwind stencil. The time is discretised using a semi-implicit technique in which the diffusion and source terms are considered at the old-time step while the convection terms are considered at the new-time step. Discretised governing equation for the heat transfer fluid is written as,

$$h_i^n = \frac{\rho_i^o h_i^o + \frac{\dot{m}}{V} h_{i-1}^n + (D_t + S_t)\Delta t}{\rho_i^o + \frac{\dot{m}}{V}\Delta t} \tag{9.33}$$

Here the new time step is presented by the superscript n, and the old-time step is presented using o. Also, V is the volume of the control volume considered. D_t and S_t are the diffusion and source terms which are written as:

$$D_t = \frac{k_{j+1}^o T_{f,k+1}^o - \left(k_{j+1}^o - k_j^o\right) T_{f,k}^o + k_j^o T_{f,k-1}^o}{\Delta s^2} \tag{9.34}$$

$$S_t = \frac{P_i}{A_i} \frac{Nu_{htf}^o k_f^o}{D_i} \left(T_{ab,k}^n - T_{f,k}^o\right) \tag{9.35}$$

The above equation is equally applicable for the stratified tank with $S_t = 0$ in that

case. As only two unknowns are available in the discrete equation, the equation can be directly solved with the boundary condition.

Similarly, the discretised equation for the absorber pipe can be written as,

$$AT_{k+1}^{n} + BT_{k}^{n} + CT_{k-1}^{n} = D \tag{9.36}$$

Here the coefficient terms A, B, C and D can be written as,

$$A = C = -\frac{K}{\Delta s^2}$$

$$B = -(A + C) + \frac{\rho C_p}{\Delta t} + \frac{P_i}{A_i}\frac{Nu_{htf}^{o} k_f^{o}}{D_i} + \frac{P_o}{A_o}\left(\frac{Nu_{conv-amb} k_{air}}{D_o} + \Psi\right)$$

$$D = \frac{\rho C_p T_{ab-k}^{o}}{\Delta t} + \frac{P_i}{A_i}\frac{Nu_{htf}^{o} k_f^{o}}{D_i} T_{f-k}^{o} + \frac{P_o}{A_o}\left(\frac{Nu_{conv-amb} k_{air}}{D_o} T_{amb}^{n} + \Psi T_{sky}^{n}\right)$$

The above equation is solved using the tri-diagonal matrix algorithm. An adiabatic boundary condition is assumed at k = 1 and k = n. The detailed procedure for solving the problem is detailed in Fig. 9.6.

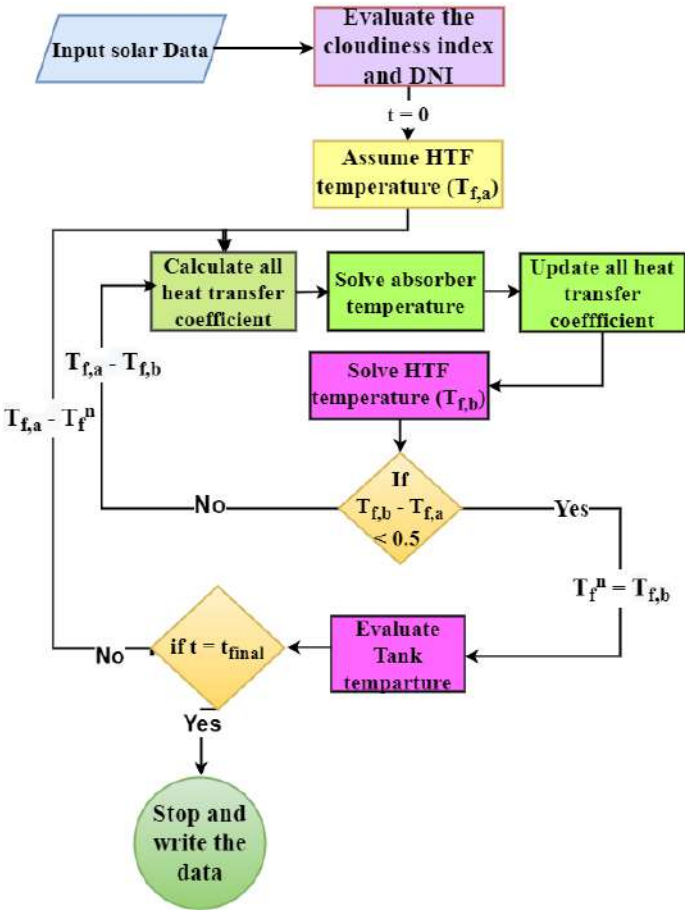

Fig. 9.6: Flow chart for solving the problem

9.4 Model validation

A time-independent study is conducted to observe the effect of time step size on the numerical solution, as portrayed in Fig. 9.7. A flow rate of 5 lpm (Day 5) is considered for the test. The reduction in time step size can increases the computational time. The grid size is chosen as 100, and the time step size is varied through 0.5, 1.0, 2.0 and 5.0 sec. From the result, it is identified that the deviation in outlet temperature is negligible beyond the time step size of 1.0 sec. According to the study, a time step size of 0.5 s has been used in the study.

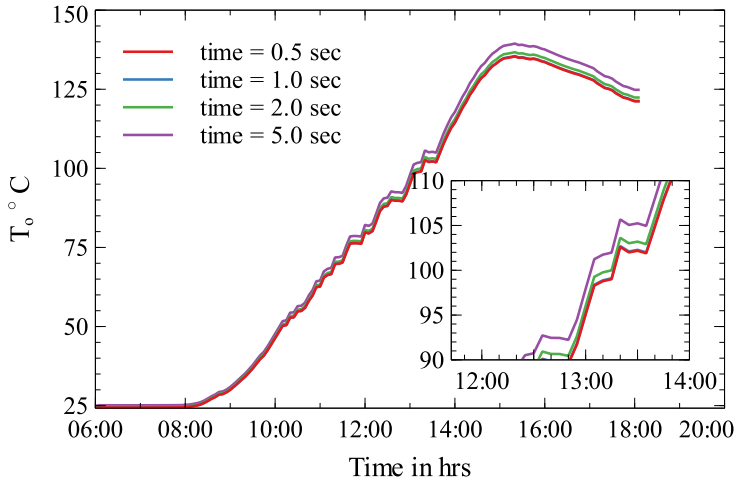

Fig. 9.7: Time-dependent study

Similarly, a grid-independent study is carried out for a mass flux of 5 lpm with the chosen time step. Five different grid numbers of 50, 75, 100, 150 and 250 are selected for the study. The deviation is insignificant among the grid sizes, as observed in Fig. 9.8. Also, the temperature difference is in the order of 0.1 for grid sizes beyond 100. This is due to the semi-implicit nature of the discretisation. In this work, a grid size of 100 is considered further.

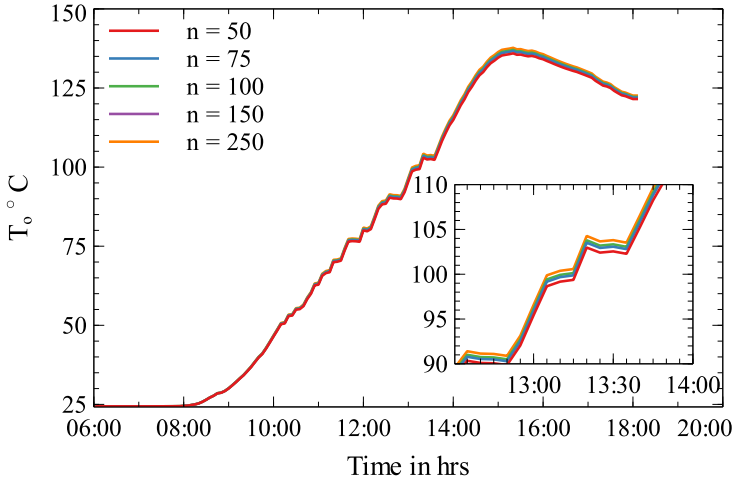

Fig. 9.8: Grid independent study

Figure 9.9 compares the experimental and numerical results for the test Day 5 with the secondary reflector. The representative results represent a flow rate of 5 lpm. The curve follows an exact similar trend for all the days considered. In all the cases, numerical results over predicted the outlet temperature for all the tests. The percentage deviation observed is in the range of 1.5% to 6.3%, and which is in the acceptable limit. The deviation is more with an increase in the absorber surface temperature. This can be due to the underprediction of radiation loss around the receiver by assuming a uniform temperature around the absorber tube. The results suggests that the model can effectively predict the thermo-hydraulics of the PTC with a minimal error (6.3%).

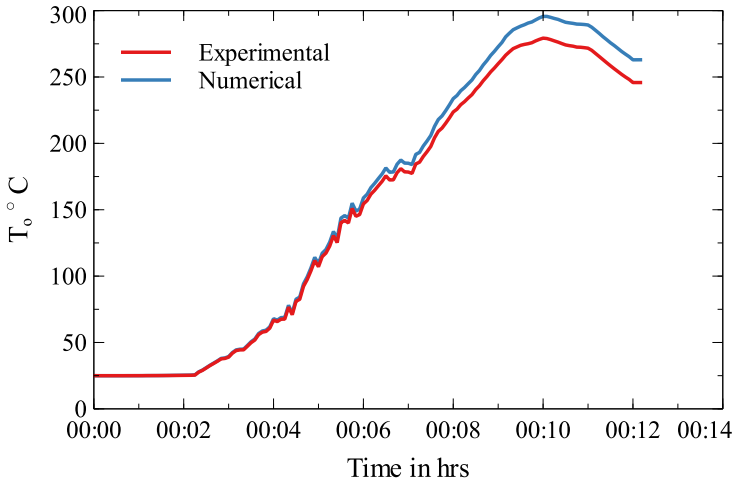

Fig. 9.9: Model validation (Day 5)

9.5 Results and Discussions

For 2.5 lpm, 5.0 lpm, and 7.5 lpm flow rates, numerical simulations are performed for the designed PTC with the secondary reflector, with TH55, and with the TH55-Al_2O_3/GNP hybrid nanofluid as working fluids. The weather data of the day, 07/01/2022, is considered for the analysis. The global solar flux and the DNI of the experimental day are depicted in Fig. 9.10(a). The ambient temperature and the wind speed during the day hours are shown in Fig. 9.10(b). On the evaluated day, the average global radiation flux and the average DNI between 8.00 hrs and 17.00 hrs are detrmined as 424.7 W/m^2 and 169.73 W/m^2, respectively. From 8.00 hrs to 17.00 hrs, the average wind speed and ambient temperatures are found to be 0.799 m/s and 31.35°C, respectively.

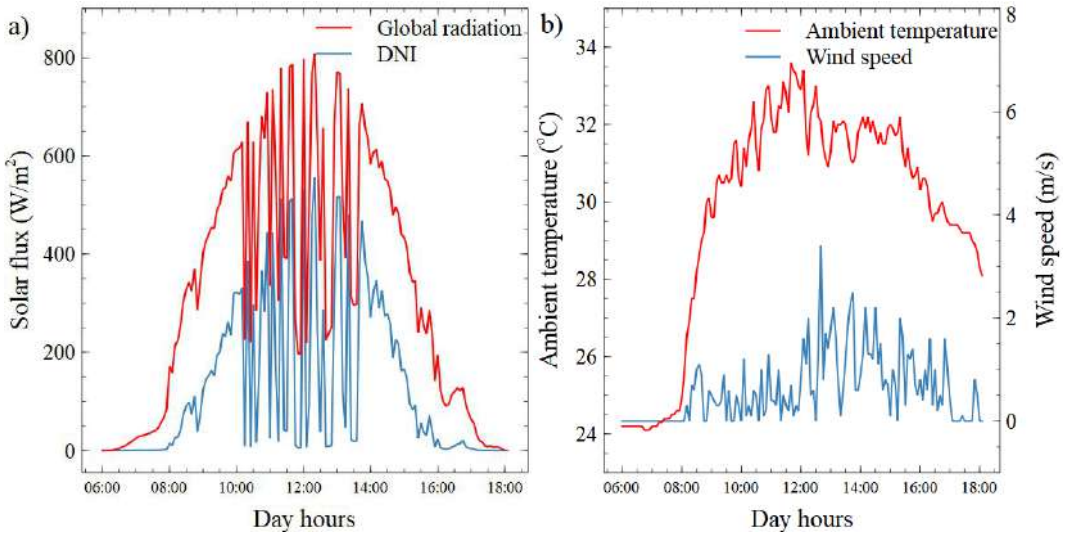

Fig 9.10: Weather data on the evaluated day (a) global and DNI radiation, (b) wind speed and ambient temperature

9.5.1 Inlet and outlet temperatures of HTFs

Figures 9.11(a) and (b) shows the results of the receiver inlet and outlet temperatures of the circulating TH55 and hybrid nanofluid as a function of solar radiation during daily hours. The inlet and outlet temperatures of both HTFs steadily increases from 8.00 hrs to 15.30 hrs, then declines as the intensity of solar radiation diminishes

throughout the afternoon hours. It is observed that the maximum outlet temperatures of TH55 for all flow rates are about 145°C occurring around 15.2 hrs. The daily average inlet temperatures of TH55 for 2.5 lpm, 5.0 lpm, and 7.5 lpm are 76.87°C, 77.32°C, and 77.39°C, respectively. The corresponding average output temperatures for TH55 are found to be approximately 90°C. Hence, the fluid velocities of TH55 do not considerably influence the outlet temperature of TH55.

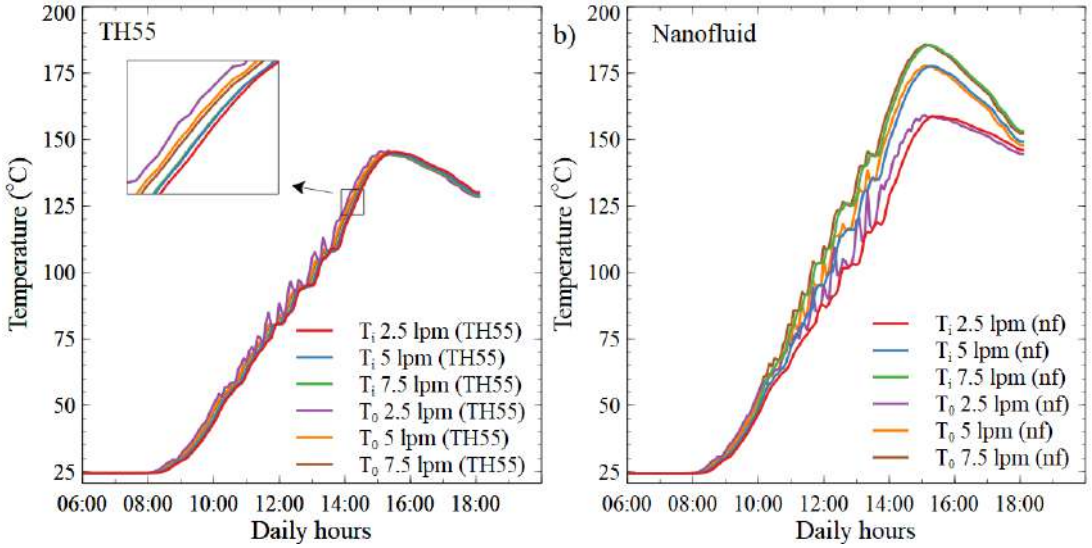

Fig. 9.11: Inlet and outlet fluid temperature of HTFs for different flow rates (a) TH55, (b) nanofluid

The average and maximum temperatures of the hybrid nanofluid, on the other hand, are significantly higher than those of TH55. As shown in Figs. 9.12(a)-(c), at 15.05 hrs, the circulating hybrid nanofluid reaches at the maximum temperatures of 159.36°C, 177.85°C, and 185.68°C, at flow rates of 2.5 lpm, 5.0 lpm, and 7.5 lpm, respectively. The daily average temperatures of the hybrid nanofluid for 2.5 lpm, 5.0 lpm, and 7.5 lpm flow rates of the hybrid nanofluid are 100.31°C, 108.99°C, and 114.35°C, respectively. As the mass flow rate increases from 2.5 lpm to 5 lpm, the hybrid nanofluid showed an increase of 8.68°C in its average outlet temperature. The average outlet temperature of the hybrid nanofluid increased by 5.36°C at 7.5 lpm compared to 5.0 lpm.

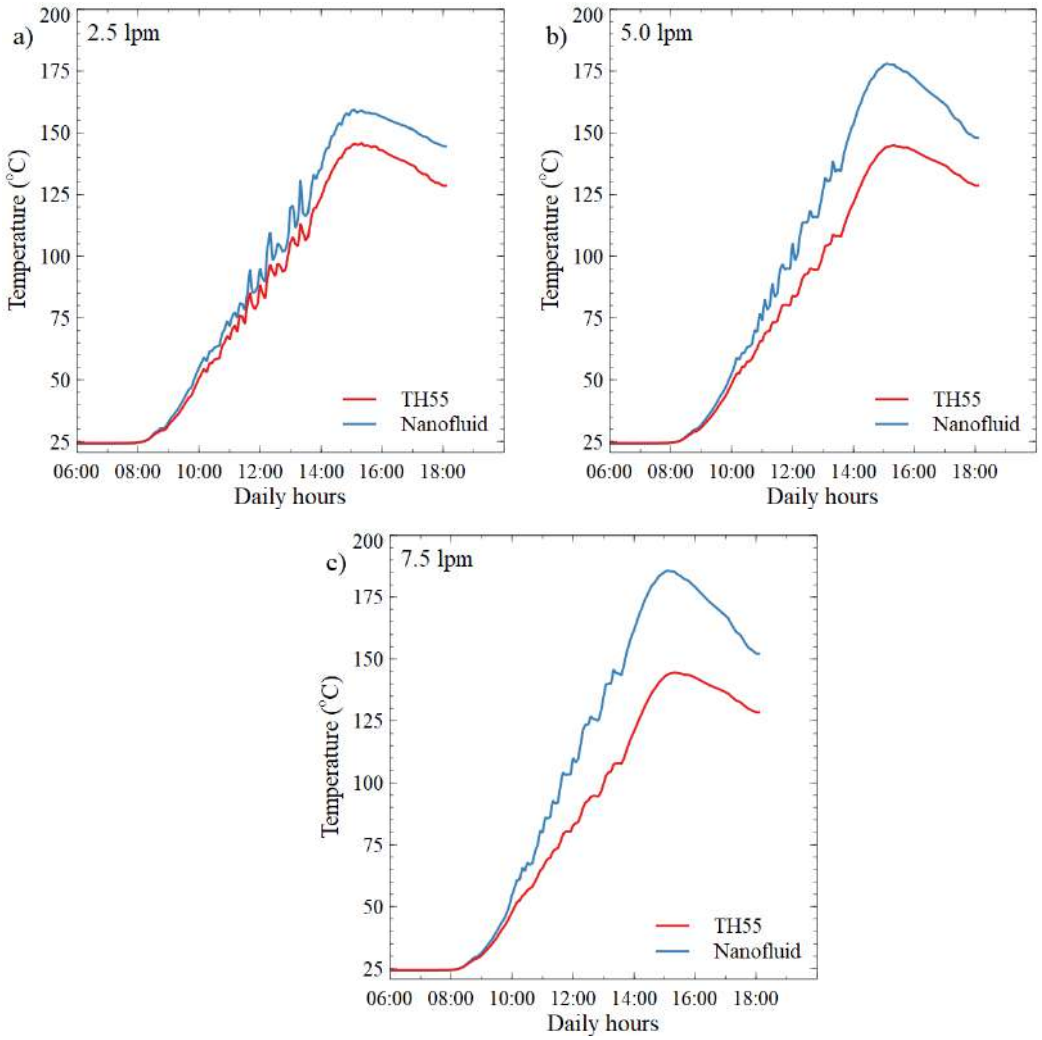

Fig 9.12: Outlet HTF temperatures at different flow rates (a) 2.5 lpm, (b) 5.0 lpm, (c) 7.5 lpm

At 2.5 lpm, the hybrid nanofluid's daily average outlet temperature is 8.3°C higher than the TH55, and at 5.0 lpm, the temperature is 18.23°C higher. The hybrid nanofluid has a maximum average outlet temperature rise of 24.1°C as compared to the TH55 at 7.5 lpm. The outlet temperature of TH55 and hybrid nanofluid during the daily hours is shown in Fig. 9.13. This enhancement of outlet temperature of the hybrid nanofluid can be attributed to the enhanced micro-convection accompanied by the synergic effect of combining GNP and Al_2O_3 nanoparticles in the hybrid suspension, which is probably responsible for a substantial increase in its thermal conductivity at higher temperatures. The enhanced Brownian motion caused by greater velocities improves the thermal conductivity of the hybrid nanofluid, resulting in a significant temperature gain at higher velocities [125].

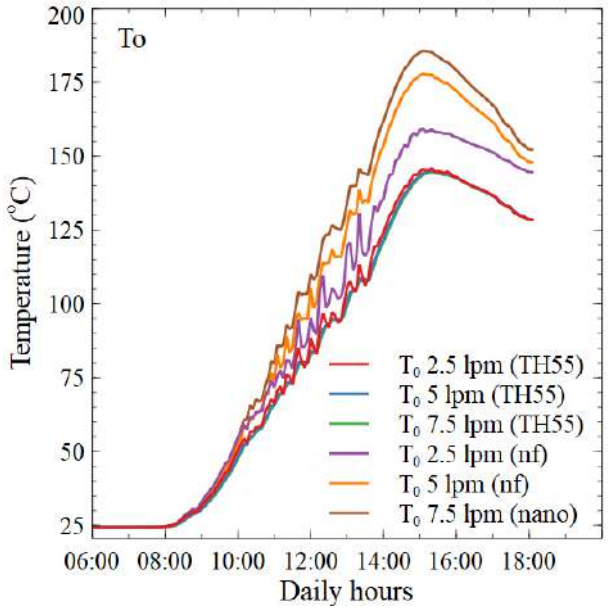

Fig. 9.13: Outlet fluid temperature of TH55 and hybrid nanofluid

9.5.2 Effect of flow rate and nanoparticles on heat gain

Figures 9.14 (a) - (c) compares the instantaneous heat gains of the HTFs and the related DNI during the day hours of the evaluated day. It has been observed that the application of hybrid nanofluid increases the useful heat gain as compared to TH55 oil. It is also evident from Figs. 14 (a)-(c) that the instantaneous heat gain greatly depends on the associated solar DNI.

The heat gain and loss for the TH55 and hybrid nanofluid at various flow rates are depicted in Figs.15 (a) – (c) and 16 (a) –(c), respectively. The results indicated that, the heat loss for both fluids is generally greater than the useful heat gain at all flow rates. The larger heat loss of solar collectors relative to useful heat gain is expected because the heat conversion efficiency of diluted solar energy is still not better with existing technology. The daily average heat gain of TH55 at flow rates of 2.5 lpm, 5.0 lpm, and 7.5 lpm, respectively, is 311.006 W, 310.842 W, and 311.015 W. Under the same flow rates and DNI, the daily average heat gain of the hybrid nanofluid are 320.663 W, 360.175 W, and 367.799 W, respectively.

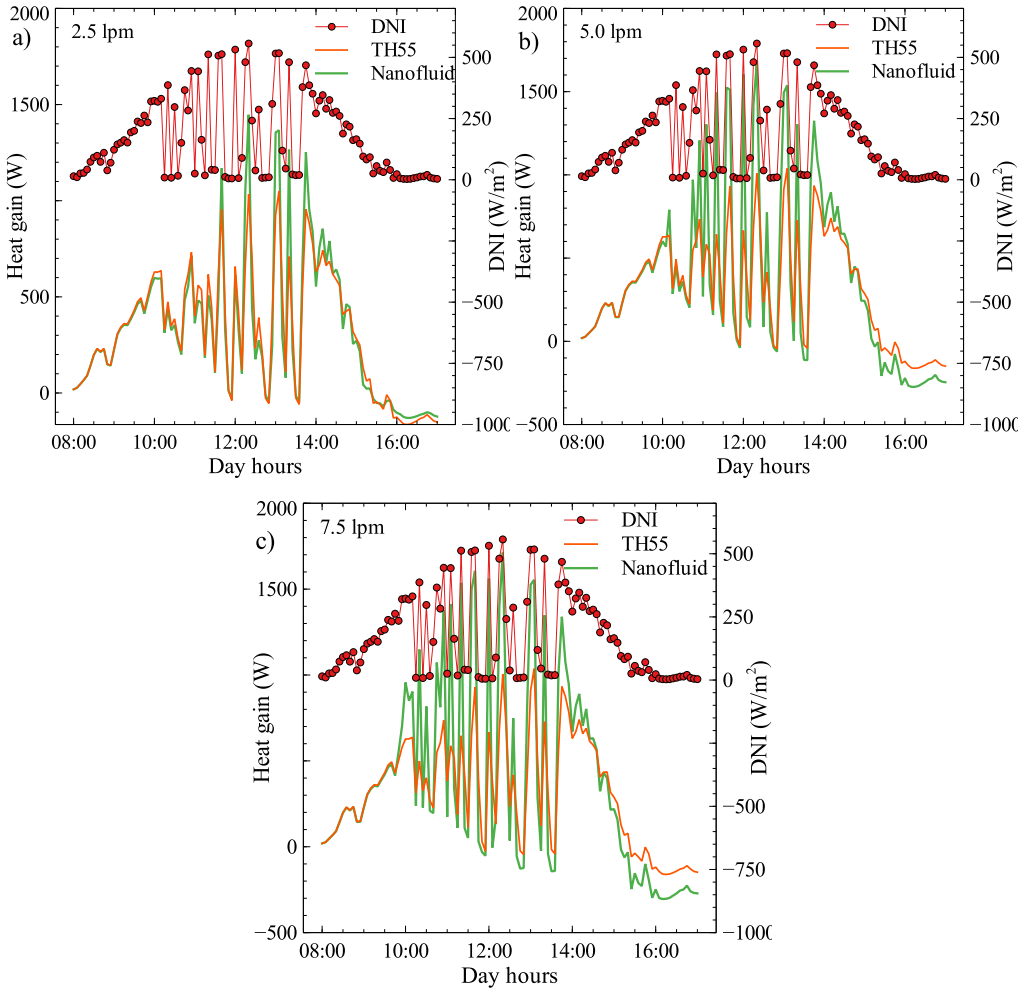

Fig. 9.14: Instantenious useful heat gain of working fluids at different flowrates (a) 2.5 lpm, (b) 5.0 lpm, (c) 7.5 lpm

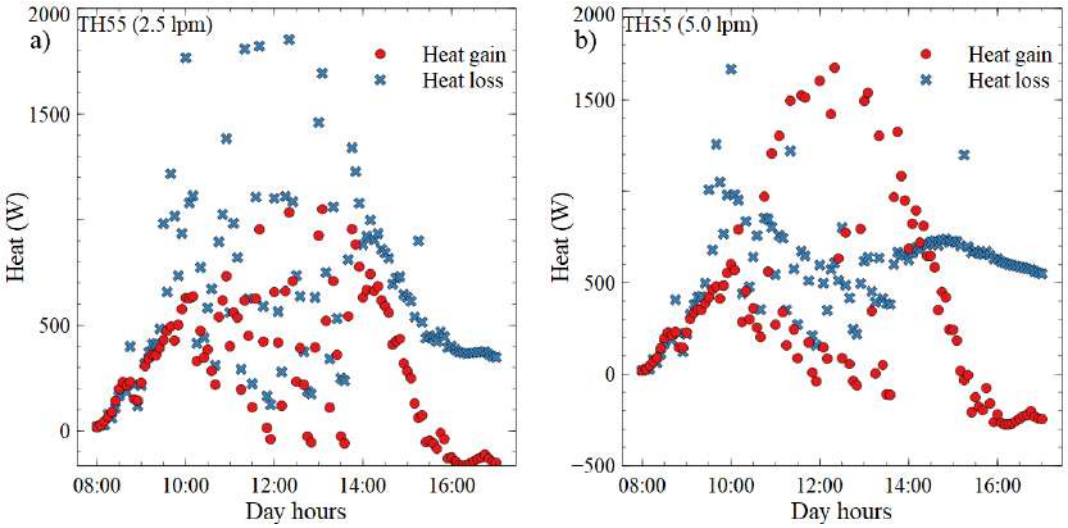

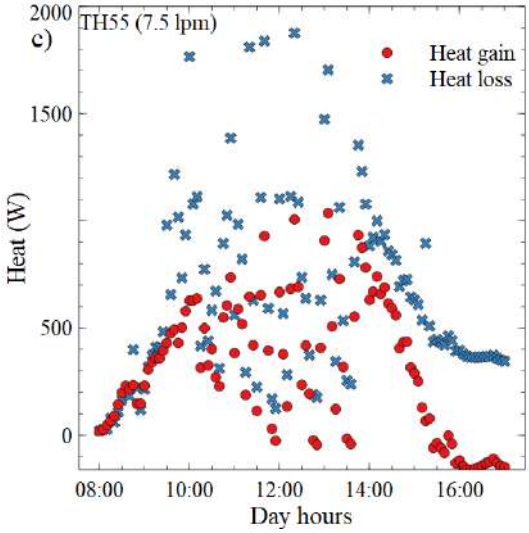

Fig. 9.15: Heat gain and heat loss of TH55 (a) 2.5 lpm, (b) 5.0 lpm, (c) 7.5 lpm

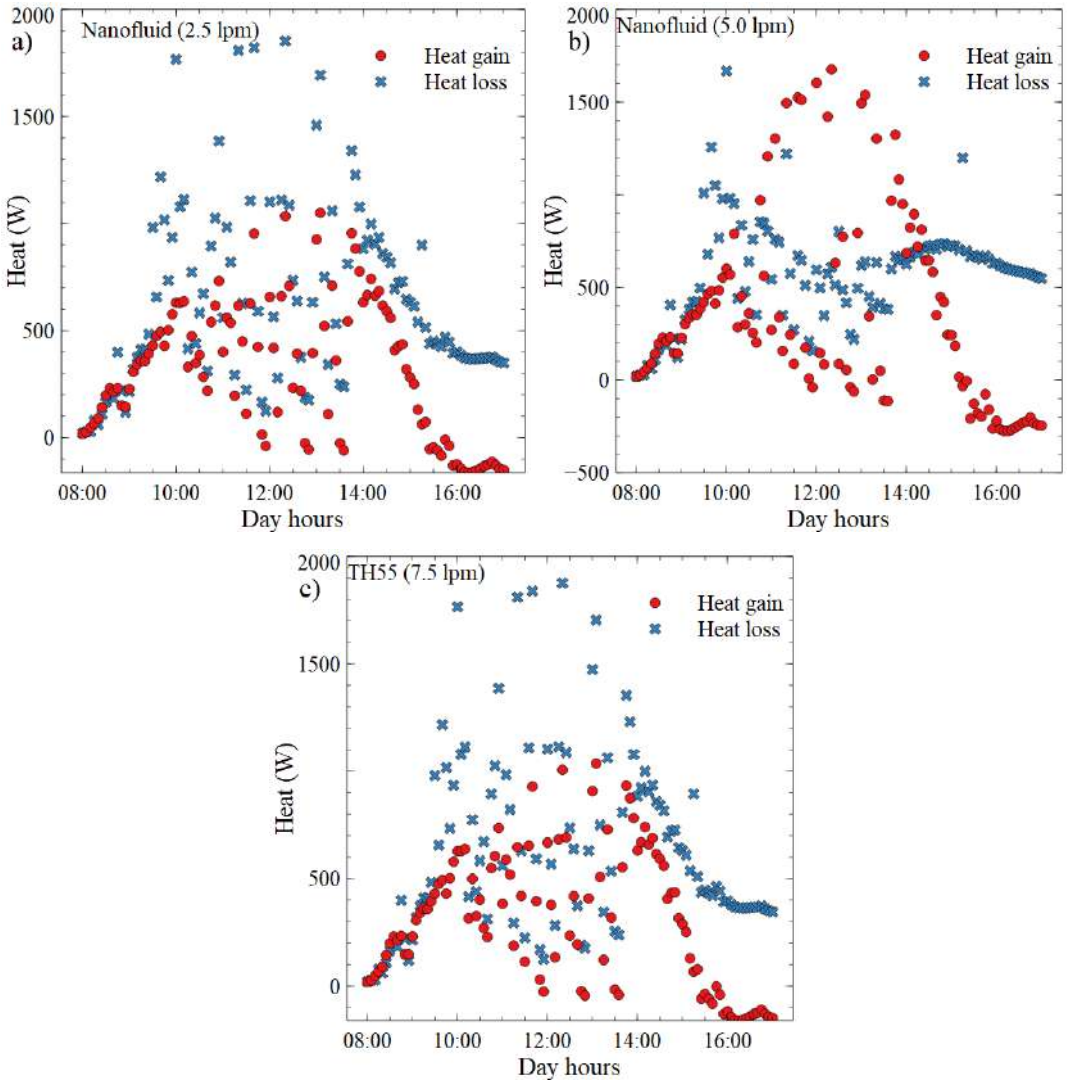

Fig. 9.16: Heat gain and heat loss of hybrid nanofluid (a) 2.5 lpm, (b) 5.0 lpm, (c) 7.5 lpm

Heat gain of TH55-GNP/Al_2O_3 hybrid nanofluid is improved by 3.11 %, 15.87 %, and 18.25 % at 2.5 lpm, 5.0 lpm, and 7.5 lpm flow rates, respectively, as compared to pure TH55 oil. The higher heat gain of the hybrid nanofluid is due to the formed nano-layered structures that serve as a thermal path between the solid nanoparticles and bulk liquid molecules. These structures, which are present in an intermediate state, lead to the higher thermal conductivity of hybrid nanofluid than the bulk single-phase base fluid [144]. The higher mass flow rate shows a greater rate of heat gain due to higher energy collection and relatively lesser thermal losses. It is noteworthy that the heat gain in all cases turns negative shortly after 15.00 hrs. This indicates that the collected heat is lost from the PTC receiver to the ambient due to the lack of intense radiation as the sun approaches the western pole.

9.5.3 Effect of nanofluid and mass flow rate on thermal efficiency

Figures 9.17 (a) - (c) show the instantaneous and average thermal efficiency for both HTFs and different mass flow rates for the evaluated hours. Even though the instantaneous thermal efficiency is dependent on the associated intensity of DNI, the hybrid nanofluid's average efficiency is greater than TH55 at higher mass flow rates. However, at a lower flow rate of 2.5 lpm, the average thermal efficiency of the PTC with TH55 and hybrid nanofluid as HTFs is consistent at 20.52 % and 20.11 %, respectively.

The average efficiency of the PTC with the secondary reflector using TH55 as the HTF is 20.13 % at a 5.0 lpm mass flow rate, whereas the PTC using hybrid nanofluid as the HTF is 22.68 %. The thermal efficiency of the PTC using TH55 as HTF reduces slightly when the flow rate increases from 2.5 lpm to 5.0 lpm. The comparison of the PTC with secondary reflector, with TH55 and the hybrid nanofluid ad the HTF in terms of the daily average efficiency and average outlet temperature is shown in Table 9.3. Compared to PTC using TH55 oil, the PTC with the hybrid nanofluid as the working fluid demonstrated a 2.55 % increase in average thermal efficiency at a 5.0 lpm flow rate. At a 7.5 lpm flow rate, the increase in thermal efficiency of the PTC with the hybrid nanofluid HTF is 4.05%.

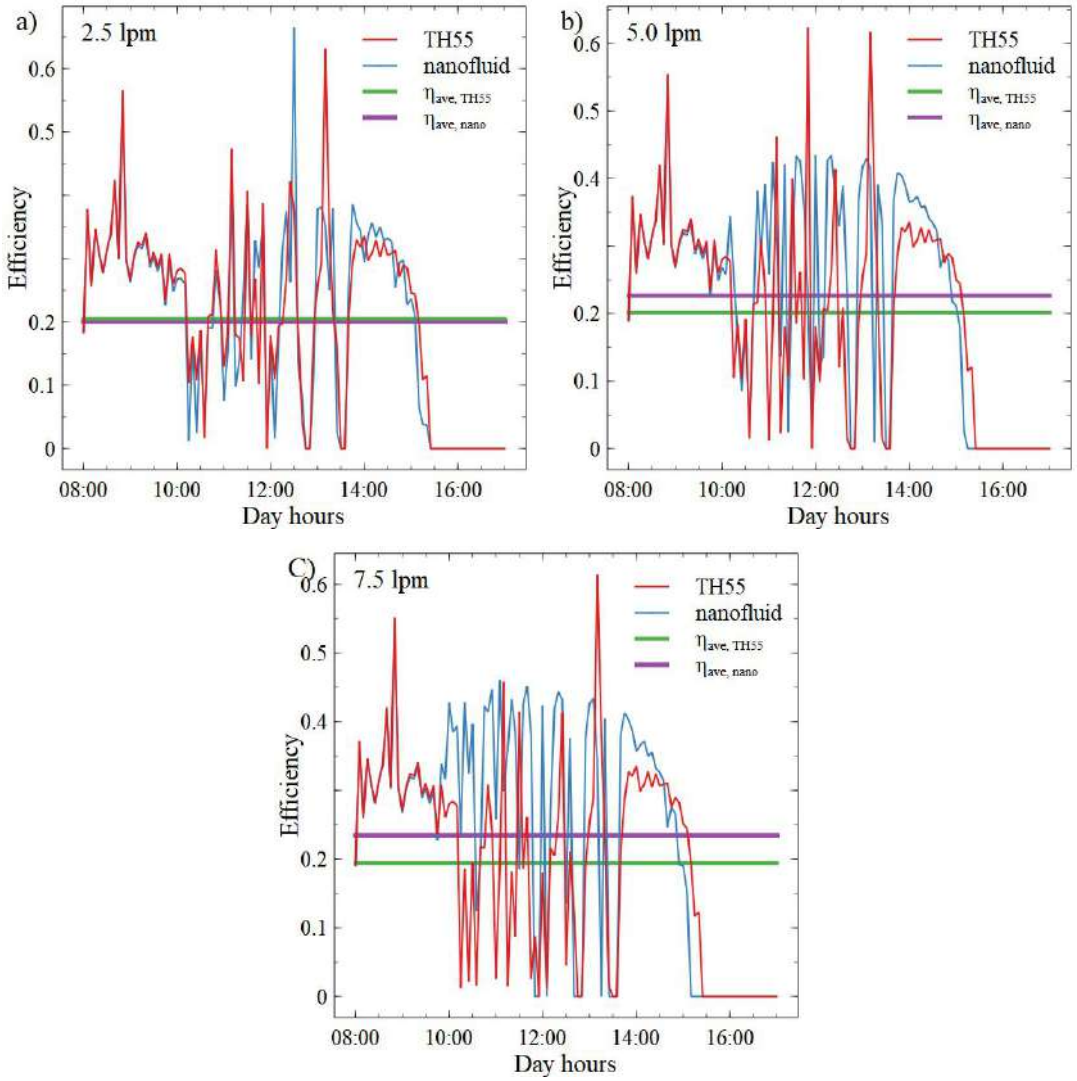

Fig. 9.17: Instantenious and daily average efficiencies for different flow rates (a) 2.5 lpm, (b) 5.0 lpm, (c) 7.5 lpm

Table 9.3: PTC performance with TH55 and hybrid nanofluid as the HTF

PTC with secondary Reflector	Flow rate (lpm)	Average solar radiation (W/m^2)	Average Efficiency (%)		Average outlet Temperature (°C)	
			TH55	Hybrid nanofluid	TH55	Hybrid nanofluid
	2.5		20.52	20.11	92.003	100.31
	5.0	424.7	20.13	22.68	90.76	108.99
	7.5		19.39	23.44	90.25	114.35

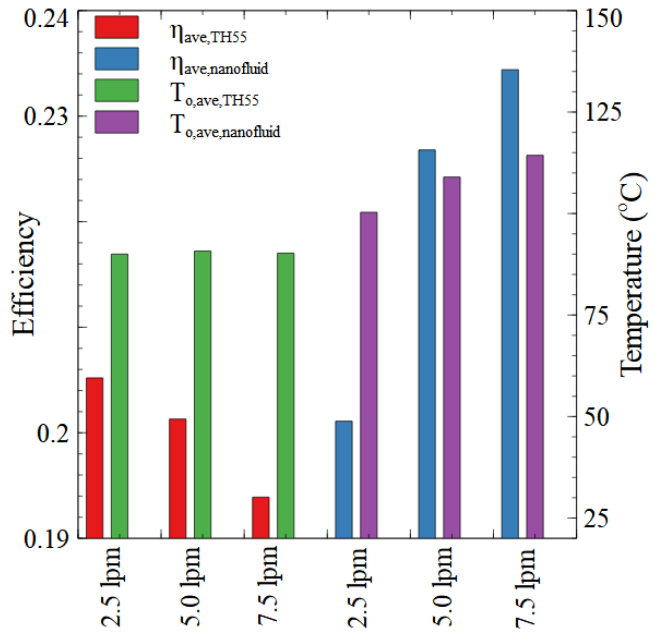

Fig. 9.18: Daily average outlet temperatures and efficiencies for different flowrates

When TH55 is used as the HTF, the average outlet fluid temperature drops from 92.01°C to 90.25°C, as the flow rate changes from 2.5 lpm to 7.5 lpm, as shown in Fig. 9.18. The average outlet temperature rises from 100.31°C to 108.99°C when the flow rate of the hybrid nanofluid increases from 2.5 lpm to 5.0 lpm. As the flow rate of the hybrid nanofluid increases from 5.0 lpm to 7.5 lpm, the average outlet temperature rises to 114.35°C. The temperature rises 8.68°C when the nanofluid flow rates changes from 2.5 lpm to 5.0 lpm, and only 5.36°C as the flow rates increases from 5.0 lpm to 7.5 lpm. According to the observations, the mass flow rate of TH55 has no significant influence on fluid output temperature as compared to that of hybrid nanofluid. The fluid outlet temperature of the hybrid nanofluid, on the other hand, keeps increasing as the mass flow rate increases from 2.5 lpm to 7.5 lpm. To determine the optimum mass flow rate for the hybrid nanofluid, analyses with higher mass fluxes of 10.0 lpm, 12.5 lpm and 15.0 lpm have been performed, and the results are shown in Fig. 9.19.

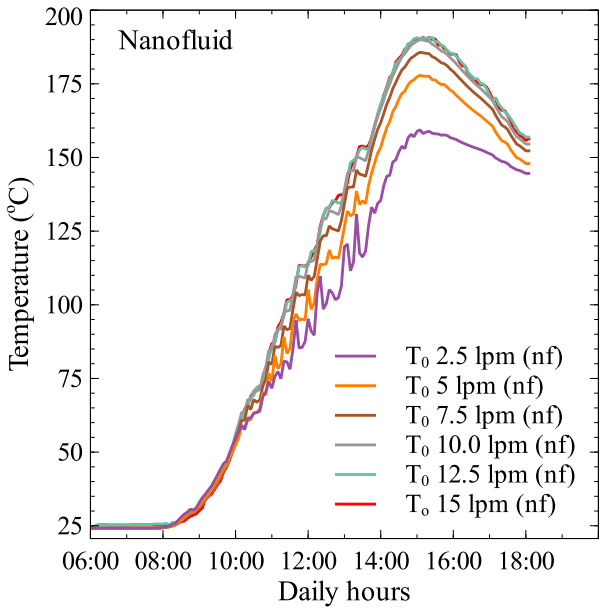

Fig. 9.19: Hybrid nanofluid outlet temperatures for different mass flow rates

As illustrated in Fig. 9.19, as the mass flow rate increases from 7.5 lpm to 10 lpm, the average fluid outlet temperature increases from 114.35°C to 117.82°C, showing a 3.47°C difference. However, when the flow rate is increased further to 12.5 lpm, the rise in fluid temperature is insignificant, with an increase in average outlet temperature of less than 1°C. The further observation is that the daily average temperature of the hybrid nanofluid is the same while the mass flow rate changes from 12.5 lpm to 15.0 lpm, thus indicating that there is no significant change in the temperature. The variation of the average outlet temperature of the hybrid nanofluid as a function of mass flow rate is depicted in Fig. 9. 20. Hence, the optimum mass flow rate of the proposed hybrid nanofluid for considering the average outlet temperature is obtained as 10.0 lpm.

When pure TH55 is utilised as the HTF in the PTC with the secondary reflector, the thermal efficiency and outlet temperature decrease as the mass flow rate increases from 2.5 lpm to 7.5 lpm. On the other hand, when the hybrid nanofluid is employed as its HTF, thermal efficiency and outlet temperature improve as the HTF flow rate increases. According to the results, the hybrid nanofluid can provide a 22.34°C higher average output temperature than pure TH55 under the same solar radiation and meteorological circumstances.

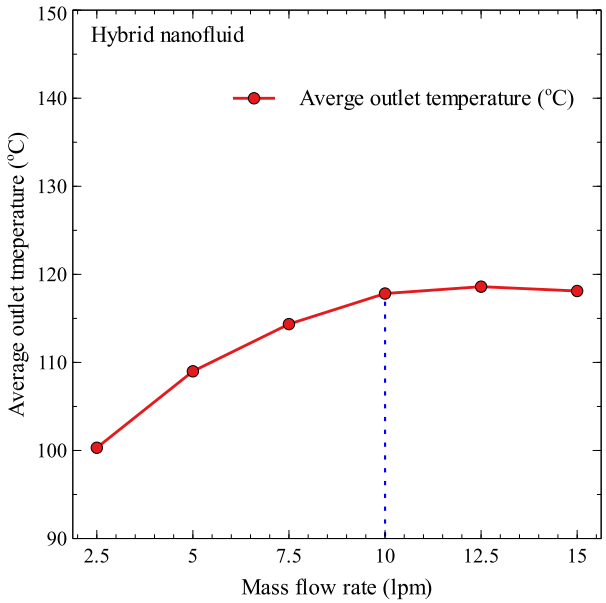

Fig. 9.20: Average outlet temperature of hybrid nanofluid with different mass flow rates

The thermal efficiency enhancement of the PTC with the proposed hybrid nanofluid is presented in Table 9.4 in comparison with PTCs in the literature that use oil-based hybrid nanofluids. The thermal efficiency enhancement obtained in the present study is greater than the other reported literature that uses oil based hybrid nanofluids as their HTFs.

Table 9.4: Themal efficiency enhancement of PTCs with oil based hybrid nanofluids

Base fluid	Hybrid Nanoparticles	Thermal efficiency enhancement (%)	Reference
Therminol VP1	Al_2O_3-WO_3 (50:50) (4 vol.%)	0.26	[192]
Syltherm 800	Al_2O_3(1.5%)&TiO_2(1.5%)	1.8	[193]
Syltherm 800	Al_2O_3-CeO_2 (4% vol%)	1.09	[194]
Therminol 55	Al_2O_3(1wt.%)-GNP(0.1 wt.%)	4.05	Present study

9.6 Economic Evaluation of the PTC system

Levelized Cost of Heat (LCOH) can be used to determine whether a PTC can be economically viable for process heating [195]. The average cost per unit of heat produced by the collector throughout the duration of its lifetime is specified by this index. Mathematically, it is the ratio of the annual amount of heat produced to the entire cost of production over its life, as in Eq.(9.37). Cost incurred in the manufacturing of the PTC is shown in Table 9.5.

Table 9.5: Cost incurred in the manufacturing of the present PTC

Item	Quantity	Cost (Rs/m^2)	Cost ($/m^2)
Stainless steel sheet	8 m^2	932.46	11.32
Copper tube	DN25 x 2m	701.81	8.52
Silicon tube	3/4" x 1-1/8" x 12m	514.83	6.25
Insulation	15mm thick	932.46	11.32
Main frame	2.0 height	1316.31	15.98
Support frame and ribs		4239.71	51.47
Solar tracker	Single axis (Manual)	1199.34	14.56
Circulating pump		1307.25	15.87
Fabrication cost		2018.95	24.51
Miscellaneous	glue, fixtures etc.	959.64	11.65
Total initial cost		**14122.76**	**171.45**
Note. 1 USD ($) = Indian Rupees (₹) 82.19 as on 09.12.2022			

$$LCOH = \frac{C_c C_{rf} + C_{o\&m}}{E_u} \tag{9.37}$$

where C_c is the capital cost, C_{rf} the recovery factor, $C_{o\&m}$ the operation, maintenance cost including the cost of the HTF, and E_u is the heat produced per year. All expenses spent while building the PTC are included in the capital cost. Since they differ depending on location, land and transportation expenses are not taken into account in this computation. The proposed system is simple in construction, and it should last at least n = 15 years [196]. Recovery factor can be calculated using an interest rate of "r = 8%" as follows:

$$C_{rf} = \frac{r(1+r)^n}{(1+r)^n - 1} \tag{9.38}$$

The cost of operation and maintenance for process heating systems is often estimated to be 10% of the overall cost. This covers all expenses related to system upkeep, labour, working fluid and other consumables needed for optimal system performance. The yearly average sun irradiation and the average efficiency of the proposed system have strong correlations with the annual average useable heat energy. According to NREL

meteorological statistics [10], India receives 4.5 kWh/m^2/day and 300 sunny days (*sd*) on average per year.

$$E_u = \bar{\eta}\bar{I_d}n_{sd} \tag{9.39}$$

According to estimates, the planned system will produce 316.44 kWh/m^2 of heat annually. The LCOH of the proposed method, which produces process heat, is roughly 11.74 Cents/kWh. The LCOH reported here is significantly less than that the LCOH of CSPs as reported by NREL which is 18.2 Cents/kWh as on 2021[196]. Furthermore, the present system has a lower LCOH than traditional heating systems, demonstrating its economic viability. It is important to note that LCOH is the only criterion used to compare the cost of technology and that costs are susceptible to change depending on the country.

$$Payback\ period = \frac{Gross\ cost\ - Incentives}{Annual\ Financial\ benefits} \tag{9.40}$$

The payback period identifies the time frame required to recover the investment expenditure. As a longer payback period is not preferable from an investment standpoint, it reflects the project's viability. Here, it is described as the proportion between the project's total cost and the system's yearly financial benefit (F Ba). F Ba is the difference between the LCOH and the nominal cost of the heat, which is assumed to be 92.5 cents/kWh [183]. With a payback period of around 24 months, the proposed PTC is the most promising contender.

9.7 Summary

In this chapter, the numerical model of the designed PTC with the secondary reflector is developed. The numerical model is validated with the experimental results using TH55 as the HTF. PTC performance is then evaluated using the developed hybrid nanofluid as HTF. As compared to PTC using TH55 oil, PTC using hybrid nanofluid demonstrated an increase in thermal efficiency of 4.05 % at a flow rate of 7.5 lpm. As a result, when TH55

and hybrid nanofluid are used under the same solar radiation conditions and meteorological conditions, conventional TH55 provides a 22.34°C higher average output temperature. Based on the average outlet temperature, it is found that 10.0 lpm is the optimum mass flow rate for the hybrid nanofluid. A thorough model for predicting system performance where the meteorological data is used to predict the system's performance is prososed in this chapter. Furthermore, an economic study is carried out to compute the payback period of the PTC, showed a LCOH of 11.74 Cents/kWh, and a payback period of 24 months. The next chapter provides a summary, conclusions, and recommendations for future research.

Chapter 10

Summary, Conclusions and Scope for Future Work

10.1 Summary

PTCs are the most established and economic concentrated solar power (CSP) technology that is used in applications up to 400°C. However, multiple technological improvements and research are ongoing to improve efficiency and increase service lifespan. Augmentation of heat transfer performance by employing hybrid nanofluids and enhancing the distribution of heat flux over the receiver surface are some ways to improve solar collector systems' performance. Uniform heat flux distribution decreases temperature gradient by avoiding severe local temperature peaks. The lack of local temperature peaks eventually improves collector efficiency by reducing heat transfer irreversibility and avoiding thermal distortion in receiver tubes. There is potential for enhanced PTC performance by improving heat flux distribution on the receiver tube's surface by incorporating secondary reflectors.

However, a secondary reflector that homogenises the heat flux distribution over the receiver tube needs to be explored in detail for further improvements in the system's

performance. Therefore, the main focus of this investigation is to design a PTC with a secondary reflector to alleviate the problems associated with the non-uniform heat flux distribution. Construction and experimental and numerical evaluation of the designed PTC with the secondary reflector are also conducted. Moreover, a hybrid nanofluid (TH55-GNP/Al_2O_3) was developed, and its potential for the heat transfer performance of the PTC absorber tube is investigated.

In this study, the optical simulations of the PTC configurations are carried out using a CCD-based classical DoE approach. Actual heat flux distributions on the receiver surface are obtained by the MCRT-based simulations using the tool Tonatiuh. The desirable receiver location and secondary reflector size and position are investigated and selected through RSM, and the results are evaluated by ANOVA. The heat flux distributions obtained from the MCRT analyses are then used in the CFD study to perform further numerical investigations. All numerical investigations are also validated with data available in the literature. Excellent agreement is obtained in all cases. Before constructing the designed PTC with the secondary reflector, its structural stability against extreme wind loads and self-weight is numerically verified using ANSYS Workbench. Performance evaluation of the constructed PTC with and without a secondary reflector under actual outdoor weather conditions is conducted for different flow rates of TH55 oil.

Measurement uncertainty of the experimental results is estimated using the root mean square method and presented. Finally, a numerical code is developed to predict the performance of the PTC using the hybrid nanofluid and compare it to TH55 as the working fluid. The code is developed based on the finite volume method in C++ language. The method assumes a 1-D approach with empirical correlations for modelling the heat transfer coefficient and is validated using the experimental data. Performance indices, including the overall efficiency, outlet temperature, inlet temperature and tank temperature, are compared for both the heat transfer fluids.

10.2 Conclusions

The major conclusions drawn from this investigation for each objective are presented below.

Objective 1: Comprehensive literature review.

The current innovations in applying PTC for heat transfer augmentation methods were reviewed to accomplish this study's primary aim. The study also covered an in-depth review of the application of a secondary reflector from the standpoint of homogenising the heat flux distribution on the receiver tube circumference. Multy-reflective solar concentrating systems showed the potential to reduce the difference in heat flux over the surface of the receiver tube. Recently, the dispersion of two or more nanoparticles (hybrid) in base HTFs has been the subject of numerous heat transfer engineering investigations to improve the heat transfer properties further. The hybrid nanoparticles, a mixture of two or three nanoparticles in correct proportion, will enhance the thermal and rheological properties of the fluid. The enhanced characteristics of hybrid nanofluids make them an appropriate substitute for mono-nanofluids in many applications, including solar energy. Despite the fact that there was an improvement in heat flux distribution by the secondary reflector in the PTC system without sacrificing its thermal efficiency, a worthwhile opportunity existed to utilise hybrid nanofluids to enhance its heat transfer performance.

Objective 2: To investigate the effect of secondary reflector geometry and its desirable location on the optical and thermal performance of the parabolic trough collector

i. The performance of the PTC with a secondary reflector is investigated by developing a comprehensive procedure that uses central composite design, Monte Carlo ray-tracing, response surface methodology, analysis of variance, and

computational fluid dynamics to build the system with the most desirable parameters efficiently

ii. A uniformity value of 0.58 is attained with the secondary reflector in its most desired placement. It is 1.0836 for the receiver without a secondary reflector. The heat flux distribution is enhanced by a factor of 1.868, while total power is reduced by 8%

iii. The new design significantly improved the heat flux distribution of the receiver with a slight increase in thermal efficiency. Models for uniformity and power output have been developed that are independent of the primary collector and can be applied to any PTC

iv. Since the flux is dispersed more evenly, the possibility of a hot spot where the local peak temperature rises dramatically is reduced. Peak surface temperature can be decreased, and heat loss due to convection and radiation can be considerably reduced by homogenising the flux

v. This step-by-step technique introduces a new design approach for establishing the receiver tube position and secondary reflector configuration in order to achieve consistent heat flux distribution and solar collector power output.The studies of parabolic trough collector with a secondary reflector described above are beneficial in creating actual systems and providing a better knowledge of the design of optimum parabolic solar collectors

Objective 3: To identify suitable hybrid nanoparticles for thermal properties and to develop the best combination and composition of hybrid nanoparticles in thermal oil through experimental investigations

i. The thermal conductivity of TH55-Al_2O_3 mono-nanofluids is shown to increase by 5.09%, 5.83%, and 8.44% as the Al_2O_3 solid fraction increases from 0.1%, 0.5%, and 1.0%; respectively. Similarly, TH55-GNP mono-nanofluids are shown 7.82%, 11.16%, and 15.69% enhancements for 0.01%, 0.05%, and 0.1% GNP concentrations.

ii. The thermal conductivity of TH55-GNP/Al_2O_3 hybrid nanofluids is shown to increase by 6.5%, 9.04%, and 18.72%, as the GNP solid fraction increases from 0.01, 0.05, and 0.10; respectively. Compared to the TH55-GNP mono-nanofluid, the hybrid nanofluid appears to have a 3.03% increase in thermal conductivity at 65°C. In contrast, the hybrid nanofluid has a 10.28% increase in thermal conductivity compared to the TH55-Al_2O_3 mono-nanofluid.

iii. The viscosity enhancement of TH55-GNP(0.1%)/Al_2O_3(1.0%) hybrid nanofluid is around 66.69% higher than TH55 at 20°C. However, the viscosity decreases by 84.5% from 20°C to 90°C due to the weakening of the inter-particle adhesive and intermolecular cohesive forces. However, since variation in the viscosity at a constant temperature for the entire shear range from 5 to 150 s^{-1} is small, fluid behaviour can be regarded as Newtonian. Compared to other nanofluids, a marked rise in relative viscosity at higher temperatures of TH55-GNP(0.1%)/Al_2O_3(0.1%) hybrid nanofluid shows that raising the GNP concentration further may result in non-Newtonian behaviour.

iv. Measuring the specific heat capacity of nanofluids as a function of temperature for varying solid concentrations of nanomaterials leads to the conclusion that the specific heat of nanofluids fluctuates with the increase of mass fraction. According to the results, the heat capacity of nanofluids is less than that of the base fluid. The specific heat capacity of 0.1 wt.% GNP hybrid nanofluid is almost 6.11% less than that of TH55 oil at 100°C. Because the nanomaterials dispersed here had lower specific heats than the pure TH55 oil, the dispersion of the GNP and Al_2O_3 reduced the nanofluids' overall specific heat.

Objective 4: To numerically evaluate the heat transfer performance of the hybrid nanofluid employed in PTC with and without secondary reflector

i. At 100°C, the thermal diffusivity of the nanofluid is found to be 76.42% more when compared with the TH55 oil.
ii. Numerical results showed that the nanofluid-based HTF's thermal performance in the solar receiver had improved considerably compared to TH55 HTF.
iii. At 0.1kg/min flow rate, an enhancement of 21.88% in convective heat transfer coefficient has been observed when the developed hybrid nanofluid replaces the conventional TH55 HTF.
iv. TH55-Al_2O_3(1.0%)/GNP(0.1%) hybrid nanofluid in medium temperature solar thermal applications could potentially lead to an increased rate of heat transfer

Objective 5: To design, fabricate and conduct performance investigations of PTC with and without a secondary reflector

Another part of this study focused on the construction and performance evaluation of the designed PTC with and without the secondary reflector. Prior to constructing the PTC, the support structure has been evaluated for its mechanical strength with respect to extreame wind loads and self-weight. The mechanical performance of the PTC has been found satisfactory with simulation in the ANSYS workbench (ANSIS 2020 R2). For the performance evaluation, TH55 oil at three different mass flow rates is used as the working fluid. The experimental results demonstrated that utilising a secondary reflector in combination with the PTC could significantly increase the fluid outlet temperature and system efficiency.

i. For the evaluated day, the obtained average temperature for the PTC with a secondary reflector is 37.26°C higher than that without a secondary reflector
ii. An increase in temperature gain has been observed as the mass flow rate of the TH55 increased from 2.5 lpm to 7.5 lpm

iii. Compared to the traditional collector, the primary collector with the secondary reflector showed substantial efficiency improvement.
iv. In PTCs, over 50% of the solar inlet energy is destroyed, making them a significant source of exergy destruction in thermal systems.

Objective 6: To create a numerical model to predict the performance of the parabolic trough collector using hybrid nanofluid and comparing it to Therminol 55 as the heat transfer oil

The final section of this research focuses on creating a numerical model to predict the performance of the parabolic trough collector with a secondary reflector employing a hybrid nanofluid. The results are compared with the predicted performance of the PTC with TH55 as the HTF. The following conclusions have been drawn from the numerical investigation of PTC with a secondary reflector with TH55 and hybrid nanofluid as HTFs.

i. The thermal efficiency of the PTC increased by 4.05 % when using hybrid-nanofluid HTF compared to TH55
ii. With hybrid nanofluid as the HTF with the same weather and experiment conditions, the average outlet temperature is 24.1°C higher than that of TH55 HTF
iii. The economic analysis of the system showed a LCOH of 11 and a payback period of 24 months, which are appeared to be economically viable.

Overall, this research work has developed a new systematic procedure for designing a PTC with a secondary reflector, which cannot be found elsewhere, to alleviate problems caused by unequal heat flux distribution. It has been shown that, even though the secondary reflector creates a shadow on the primary collector, with better heat flux distribution, the bulk mean temperature at the outlet is found to be greater. It is also observed that the thermal efficiency of the PTC with secondary reflector have significantly greater than that of the PTC without secondary reflector. As a result, the design can significantly enhance the heat flux distribution over the receiver surface by increasing its thermal efficiency and outlet fluid temperature. Moreover, the experimental and numerical analysis results on thermal properties and heat transfer coefficient show

that TH55- GNP/Al_2O_3 hybrid nanofluid has a high heat transfer rate and the potential to be used in medium temperature applications such as PTCs.

10.3 Recommendations for future works

This investigation considered only parabolic secondary reflectors for better heat flux distribution on the receiver tube surface. The use of hybrid nanofluid has only been explored to obtain heat transfer enhancement of the PTC system. The following recommendations should be considered for future research in the area.

- The potential of different secondary reflector geometries for heat flux distribution improvement with increased PTC efficiency should be investigated
- Experimental work may also be carried out on the effect of the movement of the sun throughout the year
- Other possibilities for integrating the PTC system with co-generation systems, such as bio-mass, have not been considered
- Field trials should be undertaken for the use of the PTC system in different applications such as thermal storage, desalination, and space and water heating in domestic applications
- Other heat transfer enhancement techniques such as geometry modifications of the receiver tube and inserting forms should be considered

LIST OF PUBLICATIONS BASED ON THE RESEARCH

International Journals

1. S. Shajan and V. Baiju, “Designing a novel small-scale parabolic trough solar thermal collector with secondary reflector for uniform heat flux distribution,” *Applied Thermal Engineering*, vol. 213, October 2021, p. 118660, 2022.[SCIE indexed, Impact Factor: 6.565]

2. V. Baiju and S. Shajan, “Secondary reflector and receiver positions for uniform heat flux distribution in parabolic trough solar thermal collector,” *Journal of Solar Energy Engineering*: *Transactions of the ASME*, vol. 144, December, pp. 1–24, 2022.[SCIE indexed, Impact Factor: 2.384]

3. S. Shajan, V Baiju *et al.*, “Experimental investigation on thermophysical properties of Therminol® 55 based hybrid nanofluids with alumina and graphene nanoplatelets for medium temperature applications,” *Thermal Science and Engineering Progress*, vol. 26, August, p. 101116, 2021. [SCIE indexed, Impact Factor: 4.946]

4. Shajan. S, V. Baiju. "Experimental and numerical investigation of heat transfer properties of hybrid nanofluid in parabolic trough solar collector receiver." Applied Thermal Engineering, Elsevier (Under review).

5. Shajan. S, V. Baiju. “Experimental Investigation of Secondary Reflector Enhanced Standalone Parabolic Trough Solar Thermal Collector.” Energy, Elsevier (Communicated).

6. Shajan. S, V. Baiju. "A comprehensive review of parabolic trough solar thermal collector component materials." International Journal of Ambient Energy (Under review).

International Conference

Shajan. S, V. Baiju. "Experimental study on ultrasonication, thermal conductivity and dynamic viscosity of Therminol 55-Al_2O_3(1.0wt%)/GNP(0.075wt%) hybrid nanofluid."

International Conference on Aerospace and Mechanical Engineering – ICAME'21, TKM College of Engineering, December 16-18, 2021

National Conference

Shajan. S, V Baiju. "Performance evaluation of small scale parabolic trough solar thermal collector for solar cooling applications." *6th National Conference on Refrigeration and Air Conditioning, Indian Institute of Technology Madras Chennai*, 20-22 Feb 2020

Book Chapter

Shajan. S, V. Baiju. "Advances in Heat Transfer Fluids in Solar Thermal Collectors." *Advances in Renewable Energy Engineering (Volume 3)*, AkiNik Publications, ISBN 978-93-90420-75-9.

APPENDICES

Appendix I

Uncertainty Analysis

The major contributor to the uncertainty in experimental results is the uncertainty involved in temperature measurement by thermocouples, the solar radiation and ambient temperature measurement by the weather station, and the flow rate value of HTF.

The total setup uncertainty value is estimated by using Eq. (*AI.1*) [177].

$$W_R = \left[\left(\frac{\partial R}{\partial x_1} w_1\right)^2 + \left(\frac{\partial R}{\partial x_2} w_2\right)^2 + \cdots + \left(\frac{\partial R}{\partial x_n} w_n\right)^2\right]^{1/2} \qquad (AI.1)$$

where W_R be the total uncertainty (%) in the result, *w* the dimensional shape factors, R the uncertainty function of the independent variables x_1, x_2, ..., x_n.

The thermocouples used are T-type with an accuracy of ±1°C up to a temperature (*T*) of 350°C. The weather station has an accuracy value of ±2% in solar radiation measurement (I_D) and ±0.5°C in ambient temperature measurement. The flow rate ($\dot{m}$) measurement has an accuracy value of ±1.5%. Density of the fluid is provided by the manufacturer. Therefore, the total uncertainty of the thermal efficiency of the collector can be estimated employing the Eq. (*AI. 2*).

$$U_\eta = \left[\left(\frac{\partial \eta}{\partial \dot{m}} u_{\dot{m}}\right)^2 + \left(\frac{\partial \eta}{\partial \Delta T} u_{\Delta T}\right)^2 + \left(\frac{\partial \eta}{\partial I_D} u_{I_D}\right)^2\right]^{1/2} \qquad (AI.2)$$

The sample calculation of measurement uncertainty in the thermal efficiency of the PTC is given below (PTC without secondary reflector, flow rate 2.5 lpm, sample no.19).

Inlet temperature, T_i = 117.834°C

Outlet temperature, T_o = 133.972°C

$\therefore \Delta T = T_o - T_i$ = 16.138 K

Cp (HTF at T≈125°C) ≈ 2280°C

I_D = 592.956 W/m^2

$$\dot{m} = 2.5\ lpm = \frac{2.5}{60}\ lps$$

Density of the HTF for the temperature range of 134°C to 118°C,

ρ = 800.5 kg/m^3 = 0.8005 kg/s

$$\therefore \dot{m} = \frac{2.5}{60} * 0.8005 = 3.3354 * 10^{-2}\ kg/s$$

$$u_{\dot{m}} = \frac{1.5}{100} * 3.3354 * 10^{-2} = 5.0031 * 10^{-4}\ kg/s$$

$$u_{\Delta T} = \pm 1^{o}C$$

$$u_{I_D} = \frac{2}{100} * 592.956 = 11.85912\ w/m^2$$

Thermal efficiency,

$$\eta = \frac{\dot{m} C_p \Delta T}{I_D A_s}$$

$$\eta = \frac{3.3354 * 10^{-2} * 2280 * 16.138}{592.596 * 7} = 0.295675 = 29.56\%$$

$$\frac{\partial \eta}{\partial \dot{m}} = \frac{C_p \Delta T}{I_D A_a} = \frac{2280 * 16.138}{592.596 * 7} = 8.8701$$

$$\frac{\partial \eta}{\partial \Delta T} = \frac{\dot{m} C_p}{I_D A_a} = \frac{3.3354 * 10^{-2} * 2280}{592.596 * 7} = 1.8322 * 10^{-2}$$

$$\frac{\partial \eta}{\partial I_D} = \frac{-1}{I_D^2} * \frac{\dot{m} C_p \Delta T}{A_a}$$

$$= \frac{-1}{(592.596)^2} * \frac{3.3354 * 10^{-2} * 2280 * 16.138}{7} = -4.9864 * 10^{-4}$$

Substituting in Eq. (I.2)

$$U_\eta = [(8.8701 * 5.0031 * 10^{-4})^2 + (1.8322 * 10^{-2} * 1)^2 + (-4.9864 * 10^{-4} * 11.85912)^2]^{\frac{1}{2}}$$

=0.02014

$$\frac{U_\eta}{\eta} = \frac{0.02014}{0.295675} = 0.06811 = 6.811\%$$

The total uncertainty estimated of the thermal efficiency is 6.811%.

Appendix II

Experimental results on Day 2 (27th Sep. 2022)

Day hours (hrs)	Global Radiation (W/m^2)	DNI (W/m^2)	Wind_velocity (m/s)	T_ambient (°C)	Heat gain (W)	Total Heat (W)	T_out (°C)	T_in (°C)	Efficiency
08:00:00	98	2.1647	1.9	27.5	7.08745	15.0079	25.2334	25.1833	0.472248
08:15:00	226.8	17.5037	0	27.9	26.0531	121.353	25.4547	25.2705	0.214688
08:30:00	492.3	244.691	0	28.9	409.264	1696.44	30.752	27.8745	0.241247
08:45:00	488.4	192.266	0.8	29	422.344	1332.98	35.8401	32.8926	0.316841
09:00:00	452.9	117.339	0.6	29.1	192.084	813.511	38.9516	37.6188	0.236116
09:15:00	258.5	13.7358	0.6	29.2	295.829	95.2303	44.4116	42.3745	0.18
09:30:00	662.3	355.304	1	29.9	675.773	2463.32	49.8578	45.233	0.274333
09:45:00	666.7	323.752	0.9	30.7	636.172	2244.57	57.7908	53.4894	0.283425
10:00:00	742.2	423.109	0.6	30.6	1151.2	2933.41	66.8251	59.1269	0.392441
10:15:00	219	6.44996	0.5	31.8	193.066	44.7176	67.6025	66.3191	0.46
10:30:00	822	508.394	0.9	31.2	1442.34	3524.7	81.0351	71.5826	0.409209
10:45:00	870.2	574.294	0.2	31.9	1771.54	3981.58	97.4349	86.0951	0.444932
11:00:00	906.6	629.245	0.7	32.7	1927.73	4362.56	111.689	99.6091	0.441881
11:15:00	816.8	435.275	0.8	32.8	1272.88	3017.76	122.607	114.789	0.421795
11:30:00	968.7	712.085	0.4	32.4	2054.17	4936.89	140.269	127.947	0.416085
11:45:00	909.7	590.992	0.4	31.8	1644.68	4097.35	150.988	141.303	0.401399
12:00:00	869.3	511.324	1.2	31.7	1368.62	3545.01	154.356	146.348	0.386069
12:15:00	789.1	369.491	0.3	32.6	979.3	2561.68	164.637	159.006	0.382286
12:30:00	813.3	417.786	1	32.8	1090.07	2896.51	175.585	169.417	0.376337
12:45:00	785.5	380.019	0.2	32.3	896.698	2634.67	177.94	172.888	0.340344
13:00:00	343.5	19.5318	0.4	33.1	-235.14	135.414	178.41	179.727	0
13:15:00	763.5	375.779	0.9	32.5	930.833	2605.28	185.82	180.637	0.357286
13:30:00	787.4	443.107	1.3	32.1	1105.68	3072.06	197.69	191.636	0.359912
13:45:00	757.9	418.227	1	32.4	990.441	2899.57	211.504	206.19	0.34158
14:00:00	789.1	512.358	0.5	33	1232.54	3552.18	223.647	217.141	0.346981
14:15:00	697.9	379.179	1.3	33.3	749.073	2628.85	231.409	227.503	0.284942
14:30:00	718.7	461.458	1.7	33.2	975.621	3199.29	240.497	235.468	0.304948
14:45:00	700.5	474.868	1.5	32.4	975.488	3292.26	250.349	245.384	0.296296
15:00:00	672.4	472.932	1	32.8	914.492	3278.84	260.006	255.408	0.278906
15:15:00	637.6	461.515	1.3	32.3	823.655	3199.68	268.967	264.87	0.257416
15:30:00	541.8	335.935	2.1	32.7	362.86	2329.04	273.857	272.064	0.155798
15:45:00	486.3	291.195	0.3	32.1	192.132	2018.85	275.802	274.855	0.0951682
16:00:00	472.3	328.865	2.1	32.4	300.979	2280.02	279.275	277.797	0.132007
16:15:00	344.9	156.52	0.8	32.8	-275.28	1085.15	277.198	278.55	0
16:30:00	304	144.976	0.6	31.4	-299.39	1005.12	274.16	275.635	0
16:45:00	286.6	179.238	0.7	31.6	-170.31	1242.66	272.512	273.354	0
17:00:00	259	198.788	1	30.7	-99.229	1378.2	271.709	272.2	0

Appendix III

Calculation of Direct Normal Irradiance (I_{DNI})

Day 5 (27th Sep. 2021)

Day Number, $d_n = 265$

Incident global radiation, $I_g = 906.6\ W/m^2$, Time: 11.00 hrs

Zenith angle θ_z

$$cos\theta_z = sin\delta sin\varphi + cos\delta cos\varphi cos\omega \qquad AIII.1$$

Latitude, ϕ

$$\varphi = 8.8932°$$

Hour angle, ω

$$\omega = -16.25°$$

Declination of the sun, δ

$$\delta = 23.45sin\left(\frac{360}{365}(d_n + 284)\right) \qquad AIII.2$$

$$\delta = -0.59891° \quad \therefore cos\theta_z = 946843°$$

Eccentricity correction factor, E_o,

$$E_o = 1.000110 + 0.034221\cos\Gamma + 0.001280sin\Gamma + 0.000719cos^2\Gamma + 0.000077\sin 2\Gamma \qquad AIII.3$$

where, $\Gamma = 2\pi\frac{(d_n-1)}{365}$ $\qquad AIII.4$

$$\therefore \Gamma = 4.5441644°$$

$$\therefore E_o = 1.035148$$

The extraterrestrial irradiance on any surface normal to the rays, I_o

$$I_o = I_{sc} \times E_o cos\theta_z \qquad AIII.5$$

where Solar constant, $I_{sc} = 1367\ W/m^2$

$$\therefore I_o = 1323.5083\ W/m^2$$

Cloudness index, $k_t = \frac{I_g}{I_o} = 0.685$

Diffusion factor, $k_d = 1.45 - 1.67k_t = 0.3059$

$$I_{DNI} = I_g(1 - k_d) = 629.245\ W/m^2$$

Appendix IV

Sample calculation of thermal efficiency

Day 5 11.00 h,

Direct Normal Irradiation, I_{DNI} = 629.245 W/m^2

Wind speed, V = 0.7 m/s

Ambient temperature, T_a = 32.7°C

Inlet temperature, T_i = 99.6°C

Density of TH55 at 99.6°C, ρ_i [124] = 818.1 kg/m^3

Outlet temperature, T_o = 111.689°C

Flow rate, v = 5.0 lpm

= 5.0 * 1.6667*10^{-5} m^3/s

= 8.3335 * 10^{-5} m^3/s

Mass flow rate, $\dot{m}$ = ρ_i * v

= 818.1 * 8.3335 * 10^{-5}

= 0.068168 kg/s

Aperture area of PTC, A_a = 6.933 m^2

Available solar energy, Q_{tot} = I_b * A_a

= 629.245 * 6.933

= 4362.6199 W

Liquid enthalpy of TH55 at T_o (111.689°C) [124],

h_{out} = 260488.05 J/kg

Liquid enthalpy of TH55 at T_i (99.609°C) [124],

h_{in} = 232208.65 J/kg

Heat gain, Q_g = (h_{out}-h_{in}) * $\dot{m}$

= (260488.05 - 232208.65) * 0.068168

= 1927.750139 W

η_{th} = $\frac{Q_g}{Q_{tot}}$ = $\frac{1927.750139}{4362.6199}$

= 0.442 = 44.2%

Appendix V

Exergy analysis

Experimental Day 6 (DAY 6), Time 12.50 hrs.

Flow rate = 7.5 lpm

DNI = 410 W/m^2

Ambient temperature, T_a = 32.3°C = 32.3 + 273.15 = 305.45 K

Inlet temperature, T_i = 181.5°C = 181.5 + 273.15 = 454.6 K

Outlet temperature, T_o = 188.74°C = 188.74 + 273.15 = 461.9 K

Receiver temperature, T_r = 205.947°C = 205.974 + 273.15 = 479.1 K

Mean HTF temperature, $T_f = \frac{454.6+461.9}{2}$ = 458.25 K

Heat loss, Q_l = 933.499 W

$Cp_{@458.25K}$ = 2490.3 J/(kg.K), $\rho_{@458.25K}$ = 759.0284 kg/m^3

Mass flow rate , $\dot{m} = \frac{0.001}{60}.lpm.\rho = \frac{0.001}{60} * 7.5 * 759.0284$ = 0.0949 kg/s

Useful heat, $Q_u = m.C_p.(T_o - T_i)$ = 0.0949*2490.3*(461.9 - 454.6) = 1715.6 W

Heat energy reached on the absorber, $Q_r = Q_u + Q_l$ = 1715.6 + 933.499 = 2649.099 W

The useful exergy output of the collector,

$$E_u = Q_u - m.C_p.T_a.ln\left[\frac{T_o}{T_i}\right]$$

$$= 1715.6 - 0.0949*2490.3*305.45*\ln\left[\frac{461.9}{454.6}\right] = 565.627 \text{ W}$$

Exergy flow of solar irradiation,

$$E_s = DNI.A_c\left[1 - \frac{4}{3}.\left(\frac{T_a}{T_s}\right) + \frac{1}{3}\left(\frac{T_a}{T_s}\right)^4\right]$$

$$= 410 * 7\left[1 - \frac{4}{3}.\left(\frac{305.45}{5770}\right) + \frac{1}{3}\left(\frac{305.45}{5770}\right)^4\right] = 4365.8 \text{ W}$$

Exergy efficiency,

$$\eta_{ex} = \frac{E_u}{E_s} = \frac{565.627}{4365.8} = 0.12955$$

$$E_{l,optical} = \left(1 - \eta_{optical}\right).E_s = (1 - 0.754) * 4365.8 = 1074 \text{ W}$$

$$E_{l,th} = Q_l.\left[1 - \frac{T_a}{T_r}\right] = 933.499 * \left[1 - \frac{305.45}{479.1}\right] = 338.34 \text{ W}$$

Total exergy losses,

$$E_l = E_{l,optical} + E_{l,th} = 1074 + 338.3434 = 1412.34 \text{ W}$$

The exergy destruction between the sun and the receiver,

$$E_{d,s\_r} = \eta_{optical}.E_s - Q_r\left(1 - \frac{T_a}{T_r}\right)$$

$$= 0.754 * 4365.8 - 2649.099 * \left(1 - \frac{305.45}{479.1}\right)$$

$$= 2331.6 \text{ W}$$

The exergy destruction during the useful heat transport from the absorber to HTF,

$$E_{d,r\_f} = Q_u.\left(1 - \frac{T_a}{T_r}\right) - E_u = 1715.6 * \left(1 - \frac{305.45}{479.1}\right) - 565.627$$

$$= 56.1929 \text{ W}$$

The total exergy destruction,

$$E_d = E_{d,s\_r} + E_{d,r\_f} = 2331.6 + 56.1929 = 2387.7929 \text{ W}$$

Total exergy balance of the system,

$$E_s = E_u + E_l + E_d = 572.043 + 1412.34 + 2387.7929 = 4365.8 \text{ W}$$

List of References

[1] Dr Fatih Birol, “Net Zero by 2050 A Roadmap for the Global Energy Sector,” 2021.

[2] M. Santamouris, “Innovating to zero the building sector in Europe: Minimising the energy consumption, eradication of the energy poverty and mitigating the local climate change,” *Sol. Energy*, vol. 128, pp. 61–94, 2016.

[3] accessed on 03. 12. 2021. Statista, Primary energy consumption worldwide in 2019 and 2020, by fuel type https://www.statista.com/statistics/265619/primary-energy-consumption-worldwide-by-fuel/, “No Title.” p. 265619, 2021.

[4] I. B. E. F. (2021) 1–7. http://www. seda. gov. my/reportal/re-incentive/%0Ahttp://www. seda. gov. my/reportal/. IBEF, Renewable Energy, “Renewable Energy,” no. May, 2021.

[5] I. B. E. Foundation, “Indian Renewable Energy Industry Analysis,” no. April, 2022.

[6] A. Herez, M. Ramadan, and M. Khaled, “Review on solar cooker systems: Economic and environmental study for different Lebanese scenarios,” *Renew. Sustain. Energy Rev.*, vol. 81, no. August 2017, pp. 421–432, 2018.

[7] S. K. Tyagi, S. Wang, M. K. Singhal, S. C. Kaushik, and S. R. Park, “Exergy analysis and parametric study of concentrating type solar collectors,” *Int. J. Therm. Sci.*, vol. 46, no. 12, pp. 1304–1310, 2007.

[8] NREL, “India Solar Resource Data,” *National solar radiation database*, 2012. [Online]. Available: https://www.nrel.gov/docs/fy21osti/78025.pdf.

[9] M. T. Islam, N. Huda, A. B. Abdullah, and R. Saidur, “A comprehensive review of state-of-the-art concentrating solar power (CSP) technologies: Current status and research trends,” *Renew. Sustain. Energy Rev.*, vol. 91, no. April, pp. 987–1018, 2018.

[10] A. Sharma, “A comprehensive study of solar power in India and World,” *Renew. Sustain. Energy Rev.*, vol. 15, no. 4, pp. 1767–1776, 2011.

[11] S. A. Kalogirou, *Solar Energy Engineering: Processes and Systems; Academic Press: New York, NY, USA*. 2014.

[12] A. Fernández-García, E. Zarza, L. Valenzuela, and M. Pérez, “Parabolic-trough solar collectors and their applications,” *Renew. Sustain. Energy Rev.*, vol. 14, no. 7, pp. 1695–1721, 2010.

[13] A. A. Hachicha, I. Rodríguez, R. Capdevila, and A. Oliva, “Heat transfer analysis and numerical simulation of a parabolic trough solar collector,” *Appl. Energy*, vol. 111, pp. 581–592, 2013.

[14] T. Harms, “Design , construction and testing of a parabolic trough solar collector for a developing-country application DESIGN , CONSTRUCTION AND TESTING OF A PARABOLIC TROUGH SOLAR COLLECTOR FOR A DEVELOPING-COUNTRY APPLICATION,” no. January, 2005.

[15] E. Venegas-Reyes, O. A. Jaramillo, R. Castrejón-García, J. O. Aguilar, and F. Sosa-Montemayor, “Design, construction, and testing of a parabolic trough solar concentrator for hot water and low enthalpy steam generation,” *J. Renew. Sustain. Energy*, vol. 4, no. 5, p. 053103, 2012.

[16] P. Forman, S. Mu, K. Hennecke, and J. Kru, “Light concrete shells for parabolic trough collectors – Conceptual design , prototype and proof of accuracy,” vol. 111, pp. 364–377, 2015.

[17] S. Kalogirou, P. Eleftheriou, S. Lloyd, and J. Ward, “Low cost high accuracy parabolic troughs construction and evaluation,” *Renew. Energy*, vol. 5, no. 1–4, pp. 384–386, 1994.

[18] A. Valan Arasu and T. Sornakumar, “Design, manufacture and testing of fiberglass reinforced parabola trough for parabolic trough solar collectors,” *Sol. Energy*, vol. 81, no. 10, pp. 1273–1279, 2007.

[19] A. A. Sagade, S. Aher, and N. N. Shinde, “Performance evaluation of low-cost FRP parabolic trough reflector with mild steel receiver,” *Int. J. Energy Environ. Eng.*, vol. 4, no. 1, pp. 1–8, 2013.

[20] M. Chafie *et al.*, “Experimental investigation of parabolic trough collector system under tunisian climate: design, manufacturing and performance assessment,” *Appl. Therm. Eng.*, 2016.

[21] W. Fu, M. C. Yang, Y. Z. Zhu, and L. Yang, “The Wind-structure Interaction Analysis and Optimization of Parabolic Trough Collector,” *Energy Procedia*, vol. 69, pp. 77–83, 2015.

[22] “Duke Solar, 2000, ‘ Task 2 Report: New Space-Frame Parabolic Trough Structure, ’ Prepared for NREL by Duke Solar, Raleigh, NC,” p. 2000, 2000.

[23] X. Zhu, L. Zhu, and J. Zhao, “Wavy-tape insert designed for managing highly concentrated solar energy on absorber tube of parabolic trough receiver,” *Energy*, vol. 141, pp. 1146–1155, 2017.

[24] A. Morales and G. San Vicente, *A new generation of absorber tubes for concentrating solar thermal (CST) systems*. Elsevier Ltd, 2017.

[25] D. Zhao, E. Xu, Q. Yu, and D. Lei, “The Simulation Model of Flux Density Distribution on an Absorber Tube,” *Energy Procedia*, vol. 69, pp. 250–258, 2015.

[26] M. A. A. Sagade, N. N. Shinde, and M. S. Patil, “Experimental Investigations on Mild Steel Compound Parabolic Reflector with Aluminum Foil as Selective Surface and Top Cover,” *Energy Procedia*, vol. 57, pp. 3058–3070, 2015.

[27] U. Furbo, Simon; Shah, Louise Jivan; Jordan, *Solar energy: state of the art.* 2003.

[28] Z. C. Crnjak Orel and M. Klanjšek Gunde, “Spectrally selective paint coatings: Preparation and characterization,” *Sol. Energy Mater. Sol. Cells*, vol. 68, no. 3–4, pp. 337–353, 2001.

[29] O. Aboelwafa, S. E. K. Fateen, A. Soliman, and I. M. Ismail, “A review on solar Rankine cycles: Working fluids, applications, and cycle modifications,” *Renew.*

Sustain. Energy Rev., vol. 82, no. September 2017, pp. 868–885, 2018.

[30] F. Wang, J. Tan, L. Ma, and C. Wang, "Effects of glass cover on heat flux distribution for tube receiver with parabolic trough collector system," *Energy Convers. Manag.*, vol. 90, pp. 47–52, 2015.

[31] F. Giovannetti, S. Föste, N. Ehrmann, and G. Rockendorf, "High transmittance, low emissivity glass covers for flat plate collectors: Applications and performance," *Sol. Energy*, vol. 104, pp. 52–59, 2014.

[32] A. Kasaeian, R. Daneshazarian, R. Rezaei, and F. Pourfayaz, "Experimental investigation on the thermal behavior of nano fl uid direct absorption in a trough collector," *J. Clean. Prod.*, vol. 158, pp. 276–284, 2017.

[33] F. Burkholder, "Transition Regime Heat Conduction of Argon / Hydrogen and Xenon / Hydrogen Mixtures in a Parabolic Trough Receiver," 2011.

[34] G. Quesada, L. Guillon, D. R. Rousse, M. Mehrtash, Y. Dutil, and P. L. Paradis, "Tracking strategy for photovoltaic solar systems in high latitudes," *Energy Convers. Manag.*, vol. 103, pp. 147–156, 2015.

[35] M. Stern *et al.*, "Development of a low-cost integrated 20-kW-AC solar tracking subarray for grid- connected PV power system applications. Final technical report. NRELISR- 520-2475 9. National Renewable Energy Laboratory, ANational Laboratory of the U.S. Department of Energ," 1998.

[36] J. T. PYTLINSK, "SOLAR ENERGY INSTALLATIONS FOR PUMPING IRRIGATION WATER," vol. 21, pp. 255–262, 1978.

[37] L. C. Spencer, "A COMPREHENSIVE REVIEW OF SMALL SOLAR-POWERED HEAT ENGINES : PART I . A HISTORY OF SOLAR-POWERED DEVICES UP TO 1950," vol. 43, no. 4, pp. 191–196, 1989.

[38] Q. Liu, Y. Wang, Z. Gao, J. Sui, H. Jin, and H. Li, "Experimental investigation on a parabolic trough solar collector for thermal power generation," *Sci. China Technol. Sci.*, vol. 53, no. 1, pp. 52–56, 2010.

[39] E. A. Mohamed, "Desing and Testing of a Solar Parabolic Concentrating Collector," *Renew. Energy Power Qual. J.*, vol. 1, no. 11, pp. 72–76, 2017.

[40] J. Macedo-Valencia, J. Ramírez-Ávila, R. Acosta, O. A. Jaramillo, and J. O. Aguilar, "Design, construction and evaluation of parabolic trough collector as demonstrative prototype," *Energy Procedia*, vol. 57, pp. 989–998, 2014.

[41] M. Rizwan, M. A. Raheem Junaidi, M. Suleman, and M. A. Hussain, "Experimental Verification and Analysis of Solar Parabolic Collector for Water Distillation," *Int. J. Eng. Res.*, vol. 3, no. 10, pp. 588–593, 2015.

[42] Y. Wang, J. Xu, Q. Liu, Y. Chen, and H. Liu, "Performance analysis of a parabolic trough solar collector using Al2O3/synthetic oil nanofluid," *Appl. Therm. Eng.*, vol. 107, pp. 469–478, 2016.

[43] S. A. Murtuza, H. V. Byregowda, M. M. A. H, and M. Imran, "Experimental and simulation studies of parabolic trough collector design for obtaining solar energy," *Resour. Technol.*, vol. 3, no. 4, pp. 414–421, 2017.

[44] J. Subramani, P. K. Nagarajan, S. Wongwises, S. A. El-Agouz, and R. Sathyamurthy, “Experimental study on the thermal performance and heat transfer characteristics of solar parabolic trough collector using Al 2 O 3 nanofluids,” *Environ. Prog. Sustain. Energy*, vol. 37, no. 3, pp. 1149–1159, 2018.

[45] F. R. Bilal, U. C. Arunachala, and H. M. Sandeep, “Experimental validation of energy parameters in parabolic trough collector with plain absorber and analysis of heat transfer enhancement techniques,” *J. Phys. Conf. Ser.*, vol. 953, no. 1, 2018.

[46] D. Mewes and L. Sujessy, “Collector for the Melting of Plastic Waste,” *Adv. Sci. Technol. Innov.*, pp. 169–178, 2019.

[47] N. Abed, I. Afgan, A. Cioncolini, H. Iacovides, A. Nasser, and T. Mekhail, “Thermal performance evaluation of various nanofluids with non-uniform heating for parabolic trough collectors,” *Case Stud. Therm. Eng.*, vol. 22, no. October, p. 100769, 2020.

[48] S. Nain, V. Ahlawat, S. Kajal, P. Anuradha, A. Sharma, and T. Singh, “Performance analysis of different U-shaped heat exchangers in parabolic trough solar collector for air heating applications,” *Case Stud. Therm. Eng.*, vol. 25, no. December 2020, p. 100949, 2021.

[49] M. Sami and H. Parlamıs, “Experimental investigation on the dehumidification performance of a parabolic trough solar air collector assisted rotary desiccant system,” *Case Stud. Therm. Eng.*, vol. 34, no. January, p. 102077, 2022.

[50] B. Shaker, M. Gholinia, M. Pourfallah, and D. D. Ganji, “CFD analysis of Al 2 O 3 -syltherm oil Nanofluid on parabolic trough solar collector with a new flange-shaped turbulator model,” *Theor. Appl. Mech. Lett.*, vol. 12, no. 2, p. 100323, 2022.

[51] P. Wang, D. Y. Liu, and C. Xu, “Numerical study of heat transfer enhancement in the receiver tube of direct steam generation with parabolic trough by inserting metal foams,” *Appl. Energy*, vol. 102, pp. 449–460, 2013.

[52] S. Ebrahim Ghasemi and A. Akbar Ranjbar, “Numerical thermal study on effect of porous rings on performance of solar parabolic trough collector,” *Appl. Therm. Eng.*, vol. 118, pp. 807–816, 2017.

[53] E. Bellos and C. Tzivanidis, “Investigation of a star flow insert in a parabolic trough solar collector,” *Appl. Energy*, vol. 224, no. May, pp. 86–102, 2018.

[54] O. A. Jaramillo, M. Borunda, K. M. Velazquez-Lucho, and M. Robles, “Parabolic trough solar collector for low enthalpy processes: An analysis of the efficiency enhancement by using twisted tape inserts,” *Renew. Energy*, vol. 93, pp. 125–141, 2016.

[55] F. H. Sani, M. Pourfallah, and M. Gholinia, “The effect of MoS2–Ag/ H2O hybrid nanofluid on improving the performance of a solar collector by placing wavy strips in the absorber tube,” *Case Stud. Therm. Eng.*, vol. 30, no. December 2021, p. 101760, 2022.

[56] S. Khanna, V. Sharma, S. Singh, and S. B. Kedare, “Explicit expression for temperature distribution of receiver of parabolic trough concentrator considering

bimetallic absorber tube," *Appl. Therm. Eng.*, vol. 103, pp. 323–332, 2016.

[57] Z. Huang, Z. Y. Li, G. L. Yu, and W. Q. Tao, "Numerical investigations on fully-developed mixed turbulent convection in dimpled parabolic trough receiver tubes," *Appl. Therm. Eng.*, vol. 114, pp. 1287–1299, 2017.

[58] A. Mwesigye, T. Bello-Ochende, and J. P. Meyer, "Heat transfer and entropy generation in a parabolic trough receiver with wall-detached twisted tape inserts," *Int. J. Therm. Sci.*, vol. 99, pp. 238–257, 2016.

[59] E. C. Okonkwo, M. Abid, and T. A. H. Ratlamwala, "Effects of synthetic oil nanofluids and absorber geometries on the exergetic performance of the parabolic trough collector," *Int. J. Energy Res.*, vol. 42, no. 11, pp. 3559–3574, 2018.

[60] M. S. Khan *et al.*, "Comparative performance assessment of different absorber tube geometries for parabolic trough solar collector using nanofluid," *J. Therm. Anal. Calorim.*, vol. 142, no. 6, pp. 2227–2241, 2020.

[61] O. Gulzar, A. Qayoum, and R. Gupta, "Experimental study on stability and rheological behaviour of hybrid Al2O3-TiO2 Therminol-55 nanofluids for concentrating solar collectors," *Powder Technol.*, vol. 352, pp. 436–444, 2019.

[62] O. Gulzar, A. Qayoum, and R. Gupta, "Photo-thermal characteristics of hybrid nanofluids based on Therminol-55 oil for concentrating solar collectors," *Appl. Nanosci.*, vol. 9, no. 5, pp. 1133–1143, 2018.

[63] M. Mohammadpoor, S. Sabbaghi, M. M. Zerafat, and Z. Manafi, "Investigating heat transfer properties of copper nanofluid in ethylene glycol synthesized through single and two-step routes," *Int. J. Refrig.*, vol. 99, pp. 243–250, 2019.

[64] C. Jung, J. Dersch, A. Nietsch, and M. Senholdt, "Technological perspectives of silicone heat transfer fluids for concentrated solar power," *Energy Procedia*, vol. 69, pp. 663–671, 2015.

[65] U. Srivastva, R. K. Malhotra, and S. C. Kaushik, "Recent Developments in Heat Transfer Fluids Used for Solar Thermal Energy Applications Fundamentals of Renewable Energy and Applications," vol. 5, no. 6, 2015.

[66] A. Gil *et al.*, "State of the art on high temperature thermal energy storage for power generation. Part 1-Concepts, materials and modellization," *Renew. Sustain. Energy Rev.*, vol. 14, no. 1, pp. 31–55, 2010.

[67] K. Vignarooban, X. Xu, A. Arvay, K. Hsu, and A. M. Kannan, "Heat transfer fluids for concentrating solar power systems – A review," *Appl. Energy*, vol. 146, pp. 383–396, 2015.

[68] J. Pacio and T. Wetzel, "Assessment of liquid metal technology status and research paths for their use as efficient heat transfer fluids in solar central receiver systems," *Sol. Energy*, vol. 93, pp. 11–22, 2013.

[69] H. Eshgarf, R. Kalbasi, A. Maleki, M. S. Shadloo, and A. karimipour, "A review on the properties, preparation, models and stability of hybrid nanofluids to optimize energy consumption," *J. Therm. Anal. Calorim.*, no. 0123456789, 2020.

[70] E. Bellos, C. Tzivanidis, K. A. Antonopoulos, and G. Gkinis, "Thermal enhancement of solar parabolic trough collectors by using nanofluids and

converging-diverging absorber tube," *Renew. Energy*, vol. 94, pp. 213–222, 2016.

[71] P. Estelle and P. Estelle, "Thermophysical properties and heat transfer performance of carbon nanotubes water-based nanofluids," pp. 2075–2081, 2017.

[72] A. A. Minea and W. M. El-Maghlany, "Influence of hybrid nanofluids on the performance of parabolic trough collectors in solar thermal systems: Recent findings and numerical comparison," *Renew. Energy*, vol. 120, pp. 350–364, 2018.

[73] B. Munkhbayar, R. Tanshen, J. Jeoun, H. Chung, and H. Jeong, "Surfactant-free dispersion of silver nanoparticles into MWCNT-aqueous nanofluids prepared by one-step technique and their thermal characteristics," *Ceram. Int.*, vol. 39, no. 6, pp. 6415–6425, 2013.

[74] O. Bamisile *et al.*, "A brief review and comparative evaluation of nanofluid application in solar parabolic trough and flat plate collectors," *Energy Reports*, vol. 8, pp. 156–166, 2022.

[75] E. Bellos and C. Tzivanidis, "A review of concentrating solar thermal collectors with and without nanofluids," *J. Therm. Anal. Calorim.*, vol. 135, no. 1, pp. 763–786, 2019.

[76] M. Hemmat Esfe, S. Saedodin, O. Mahian, and S. Wongwises, "Heat transfer characteristics and pressure drop of of COOH-functionalized DWCNTs/water nanofluid in turbulent flow at low concentrations," *Int. J. Heat Mass Transf.*, vol. 73, pp. 186–194, 2014.

[77] R. M. Mostafizur, M. G. Rasul, M. N. Nabi, and G. Saianand, "Properties of Al2O3-MWCNT/radiator coolant hybrid nanofluid for solar energy applications," *Energy Reports*, vol. 8, pp. 582–591, 2022.

[78] S. Z. Heris, S. G. Etemad, and M. N. Esfahany, "Experimental investigation of oxide nanofluids laminar flow convective heat transfer," *Int. Commun. Heat Mass Transf.*, vol. 33, no. 4, pp. 529–535, 2006.

[79] R. M. Mostafizur, M. H. U. Bhuiyan, R. Saidur, and A. R. Abdul Aziz, "Thermal conductivity variation for methanol based nanofluids," *Int. J. Heat Mass Transf.*, vol. 76, pp. 350–356, 2014.

[80] Tyagi, "Predicted Efficiency of a Low-Temperature Nanofluid- Based Direct Absorption Solar Collector," *J. Sol. Energy Eng.*, vol. 131(4), no. November 2009, pp. 41004–41007, 2009.

[81] T. Singh, I. W. Almanassra, A. Ghani, T. Al-ansari, G. Mckay, and M. Ali, "Performance investigation of multiwall carbon nanotubes based water / oil nanofluids for high pressure and high temperature solar thermal technologies for sustainable energy systems," *Energy Convers. Manag.*, vol. 225, no. September, p. 113453, 2020.

[82] S. Iranmanesh, O. H. Chyuan, B. C. Ang, E. Sadeghinezhad, A. Esmaeilzadeh, and M. Mehrali, "Thermal performance enhancement of an evacuated tube solar collector using graphene nanoplatelets nanofluid," *J. Clean. Prod.*, pp. 1–40, 2017.

[83] M. M. Sarafraz and M. R. Safaei, “Diurnal thermal evaluation of an evacuated tube solar collector (ETSC) charged with graphene nanoplatelets-methanol nano-suspension,” *Renew. Energy*, vol. 142, pp. 364–372, 2019.

[84] K. Alexander, S. S. Gajghate, A. S. Katarkar, A. Majumder, and S. Bhaumik, “Role of nanomaterials and surfactants for the preparation of graphene nanofluid : A review,” *Mater. Today Proc.*, vol. https://do, 2021.

[85] Fazlay, L. Das, K. Habib, N. Aslfattahi, R. Saidur, and S. Ul, “A comprehensive review on advances of oil-based nanofluids for concentrating solar thermal collector application,” *J. Mol. Liq.*, no. xxxx, p. 116771, 2021.

[86] T. S. Krishnakumar, S. P. Viswanath, S. M. Varghese, and J. P. M, “Experimental studies on thermal and rheological properties of Al 2 O 3 – ethylene glycol nanofluid Études expérimentales sur les propriétés rhéologiques et thermiques d ’ un nanofluide Al 2 O 3 / éthylène glycol,” *Int. J. Refrig.*, vol. 89, pp. 122–130, 2018.

[87] S. S. Sanukrishna and M. J. Prakash, “Experimental studies on thermal and rheological behaviour of TiO 2 -PAG nanolubricant for refrigeration system Études expérimentales du comportement rhéologique et thermique du nanolubrifiant Tio 2 - PAG pour les systèmes frigorifiques,” *Int. J. Refrig.*, vol. 86, pp. 356–372, 2018.

[88] Z. Wang, J. Ni, L. Zhao, S. Deng, and D. Zhao, “Simulation and optimization of parabolic trough receiver with non-uniform heat flux distribution: A review,” *Energy Procedia*, vol. 142, pp. 700–707, 2017.

[89] H. Fathabadi, “Impact of utilizing reflector, single-axis and two-axis sun trackers on the performance of an evacuated tube solar collector,” *Int. J. Green Energy*, vol. 17, no. 12, pp. 742–755, 2020.

[90] Y. Demagh, I. Bordja, Y. Kabar, and H. Benmoussa, “A design method of an S-curved parabolic trough collector absorber with a three-dimensional heat flux density distribution,” *Sol. Energy*, vol. 122, pp. 873–884, 2015.

[91] X. Gong, F. Wang, H. Wang, J. Tan, Q. Lai, and H. Han, “Heat transfer enhancement analysis of tube receiver for parabolic trough solar collector with pin fin arrays inserting,” *Sol. Energy*, vol. 144, pp. 185–202, 2017.

[92] V. Khullar, P. Mahendra, and M. Mittal, “Applicability of Heat Mirrors in Reducing Thermal Losses in Concentrating Solar Collectors,” *J. Therm. Sci. Eng. Appl.*, vol. 10, no. 6, p. 061004, 2018.

[93] E. Bellos and C. Tzivanidis, “Investigation of a booster secondary re fl ector for a parabolic trough solar collector,” *Sol. Energy*, vol. 179, no. December 2018, pp. 174–185, 2019.

[94] M. Abdelhamid *et al.*, “Novel double-stage high-concentrated solar hybrid photovoltaic/thermal (PV/T) collector with nonimaging optics and GaAs solar cells reflector,” *Appl. Energy*, vol. 182, pp. 68–79, 2016.

[95] K. Wang, Y. He, and Z. Cheng, “A design method and numerical study for a new type parabolic trough solar collector with uniform solar flux distribution,” *Sci. China Technol. Sci.*, vol. 57, no. 3, pp. 531–540, 2014.

[96] D. Rodriguez-sanchez and G. Rosengarten, “Improving the concentration ratio of parabolic troughs using a second-stage flat mirror,” *Appl. Energy*, vol. 159, pp. 620–632, 2015.

[97] A. Minaeian, A. Alemrajabi, M. Chavoshi, A. Mostafaeipour, and Z. Seifi, “Effect of secondary reflector on solar flux intensity and uniformity of a Fresnel concentrator,” *J. Renew. Sustain. Energy*, vol. 12, no. 3, p. 033703, May 2020.

[98] M. Hack, G. Zhu, and T. Wendelin, “Evaluation and comparison of an adaptive method technique for improved performance of linear Fresnel secondary designs,” *Appl. Energy*, vol. 208, no. September, pp. 1441–1451, 2017.

[99] S. Balaji, K. S. Reddy, and T. Sundararajan, “Optical modelling and performance analysis of a solar LFR receiver system with parabolic and involute secondary reflectors,” *Appl. Energy*, vol. 179, pp. 1138–1151, 2016.

[100] A. Bharti, A. Mishra, and B. Paul, “Thermal performance analysis of small-sized solar parabolic trough collector using secondary reflectors,” *Int. J. Sustain. Energy*, vol. 38, no. 10, pp. 1002–1022, 2019.

[101] A. Mwesigye, T. Bello-Ochende, and J. P. Meyer, “Heat transfer and thermodynamic performance of a parabolic trough receiver with centrally placed perforated plate inserts,” *Appl. Energy*, vol. 136, pp. 989–1003, 2014.

[102] M. Marefati, M. Mehrpooya, and M. B. Shafii, “Optical and thermal analysis of a parabolic trough solar collector for production of thermal energy in different climates in Iran with comparison between the conventional nanofluids,” *J. Clean. Prod.*, vol. 175, pp. 294–313, 2018.

[103] H. M. Reda and B. Abdelylah, “Numerical investigation and solar flux distribution analysis of parabolic trough solar collector by adding secondary reflector,” *Instrum. Mes. Metrol.*, vol. 18, no. 3, pp. 275–280, 2019.

[104] Y. Wang *et al.*, “Verification of optical modelling of sunshape and surface slope error for concentrating solar power systems,” *Sol. Energy*, vol. 195, no. November 2019, pp. 461–474, 2020.

[105] S. M. Jeter, “The distribution of concentrated solar radiation in paraboloidal collectors,” *J. Sol. Energy Eng. Trans. ASME*, vol. 108, no. 3, pp. 219–225, 1986.

[106] S. Mathew and G. Visavale, “CFD Analysis of a Heat Collector Element in a Solar Parabolic Trough Collector,” no. August, pp. 1–21, 2014.

[107] J. P. Abraham, E. M. Sparrow, and W. J. Minkowycz, “Internal-flow Nusselt numbers for the low-Reynolds-number end of the laminar-to-turbulent transition regime,” *Int. J. Heat Mass Transf.*, vol. 54, no. 1–3, pp. 584–588, 2011.

[108] J. hu Gong *et al.*, “Improving the performance of a 2-stage large aperture parabolic trough solar concentrator using a secondary reflector designed by adaptive method,” *Renew. Energy*, vol. 152, pp. 23–33, 2020.

[109] O. A. Jaramillo, E. Venegas-Reyes, J. O. Aguilar, R. Castrejón-García, and F. Sosa-Montemayor, “Parabolic trough concentrators for low enthalpy processes,” *Renew. Energy*, vol. 60, pp. 529–539, 2013.

[110] K. S. Reddy and H. Singla, “Gravity & wind load analysis and optical study of

solar parabolic trough collector with composite facets using optimized modelling approach," *Energy*, vol. 189, p. 116065, 2019.

[111] S. Emeis and T. Matthias, "Comparison of Logarithmic Wind Profiles and Power Law Wind Profiles and their Applicability for Offshore Wind Profiles Comparison of logarithmic wind profiles and power law wind profiles and their applicability," no. December, 2017.

[112] J. Franke, A. Hellsten, K. H. Schlünzen, and B. Carissimo, "Best Practice Guideline for CFD simulation of flows in the urban environment: A summary," vol. 5, 2007.

[113] A. Agarwal, H. Irtaza, and A. Zameel, "ScienceDirect Numerical study of lift and drag coefficients on a ground-mounted photo-voltaic solar panel," *Mater. Today Proc.*, vol. 4, no. 9, pp. 9822–9827, 2017.

[114] M. Sosnowski, "The influence of computational domain discretization on CFD results concerning aerodynamics of a vehicle," *J. Appl. Math. Comput. Mech.*, vol. 17, no. 1, pp. 79–88, 2018.

[115] ANSYS Fluent Theory Guide, "ANSYS Fluent Theory Guide," *ANSYS Inc., USA*, vol. 15317, no. November, pp. 724–746, 2013.

[116] J. Paetzold, S. Cochard, A. Vassallo, and D. F. Fletcher, "Wind engineering analysis of parabolic trough solar collectors: The effects of varying the trough depth," *J. Wind Eng. Ind. Aerodyn.*, vol. 135, pp. 118–128, 2014.

[117] J. A. Eastman, S. U. S. Choi, S. Li, W. Yu, and L. J. Thompson, "Anomalously increased effective thermal conductivities of ethylene glycol- based nanofluids containing copper nanoparticles Anomalously increased effective thermal conductivities of ethylene glycol-based nanofluids containing copper nanoparticles," vol. 718, no. 2001, pp. 4–7, 2012.

[118] S. Mukherjee and S. Paria, "Preparation and Stability of Nanofluids-A Review," vol. 9, no. 2, pp. 63–69, 2013.

[119] S. Aberoumand and A. Jafarimoghaddam, "Experimental study on synthesis, stability, thermal conductivity and viscosity of Cu–engine oil nanofluid," *J. Taiwan Inst. Chem. Eng.*, vol. 71, pp. 315–322, 2017.

[120] E. V Timofeeva, W. Yu, D. M. France, D. Singh, and J. L. Routbort, "Nanofluids for heat transfer : an engineering approach," *Nanoscale Res Lett 6*, vol. c, pp. 1–7, 2011.

[121] A. K. Geim and K. S. Novoselov, "The rise of graphene," *Nat. Mater.*, vol. 6, no. MARCH 2007, pp. 183–191, 2007.

[122] F. Wang, L. T. Drzal, Y. Qin, and Z. Huang, "Mechanical properties and thermal conductivity of graphene nanoplatelet/epoxy composites," *J. Mater. Sci.*, vol. 50, no. 3, pp. 1082–1093, 2015.

[123] A. Mwesigye, İ. H. Yılmaz, and J. P. Meyer, "Numerical analysis of the thermal and thermodynamic performance of a parabolic trough solar collector using SWCNTs-Therminol®VP-1 nanofluid," *Renew. Energy*, vol. 119, pp. 844–862, 2018.

[124] T. H. T. F. by Eastman, “THERMINOL 55 ® heat transfer fluid, Technical data sheet, Kingsport, TN 37662-5280 U.S.A.”

[125] S. Manikandan and K. S. Rajan, “MgO-Therminol 55 nanofluids for efficient energy management: Analysis of transient heat transfer performance,” *Energy*, vol. 88, pp. 408–416, 2015.

[126] M. Hemmat Esfe, A. Karimipour, W. M. Yan, M. Akbari, M. R. Safaei, and M. Dahari, “Experimental study on thermal conductivity of ethylene glycol based nanofluids containing Al2O3 nanoparticles,” *Int. J. Heat Mass Transf.*, vol. 88, pp. 728–734, 2015.

[127] S. Immanuel, T. K. Aparna, and R. Sivasubramanian, *Graphene – Metal Oxide Nanocomposite Modified Electrochemical Sensors*. Elsevier Inc., 2019.

[128] E. Bellos and C. Tzivanidis, “Alternative designs of parabolic trough solar collectors,” *Prog. Energy Combust. Sci.*, vol. 71, pp. 81–117, 2019.

[129] N. R. Pradhan, H. Duan, J. Liang, and G. S. Iannacchione, “The specific heat and effective thermal conductivity of composites containing single-wall and multi-wall carbon nanotubes,” *IOP Publ. Nanotechnol.*, vol. 245705, no. 20, pp. 1–7, 2009.

[130] M. Fakoor Pakdaman, M. A. Akhavan-Behabadi, and P. Razi, “An experimental investigation on thermo-physical properties and overall performance of MWCNT/heat transfer oil nanofluid flow inside vertical helically coiled tubes,” *Exp. Therm. Fluid Sci.*, vol. 40, pp. 103–111, 2012.

[131] Q. Y. Li *et al.*, “Measurement of specific heat and thermal conductivity of supported and suspended graphene by a comprehensive Raman optothermal method,” *Nanoscale*, vol. 9, no. 30, pp. 10784–10793, 2017.

[132] S. Aberoumand and A. Jafarimoghaddam, “Tungsten (III) oxide (WO3) – Silver/transformer oil hybrid nanofluid: Preparation, stability, thermal conductivity and dielectric strength,” *Alexandria Eng. J.*, vol. 57, no. 1, pp. 169–174, 2018.

[133] D. Jansone, M. Dzikevics, and I. Veidenbergs, “Determination of thermophysical properties of phase change materials using T-History method,” *Energy Procedia*, vol. 147, pp. 488–494, 2018.

[134] A. Solé, L. Miró, C. Barreneche, I. Martorell, and L. F. Cabeza, “Review of the T-history method to determine thermophysical properties of phase change materials (PCM),” *Renew. Sustain. Energy Rev.*, vol. 26, pp. 425–436, 2013.

[135] Z. Yinping and J. Yi, “A simple method, the T-history method, of determining the heat of fusion, specific heat and thermal conductivity of phase-change materials,” *Meas. Sci. Technol.*, vol. 10, no. 3, pp. 201–205, 1999.

[136] E. D. Kravvaritis, K. A. Antonopoulos, and C. Tzivanidis, “Improvements to the measurement of the thermal properties of phase change materials,” *Meas. Sci. Technol.*, vol. 21, no. 4, 2010.

[137] S. Pakrashi, S. Dalai, A. Humayun, S. Chakravarty, N. Chandrasekaran, and A. Mukherjee, “Ceriodaphnia dubia as a Potential Bio-Indicator for Assessing Acute Aluminum Oxide Nanoparticle Toxicity in Fresh Water Environment,” *PLoS*

One, vol. 8, no. 9, 2013.

[138] I. Kazemi, M. Sefid, and M. Afrand, "Improving the thermal conductivity of water by adding mono & hybrid nano-additives containing graphene and silica: A comparative experimental study," *Int. Commun. Heat Mass Transf.*, vol. 116, no. 104648, pp. 1–13, 2020.

[139] N. A. Che Sidik, M. Mahmud Jamil, W. M. A. Aziz Japar, and I. Muhammad Adamu, "A review on preparation methods, stability and applications of hybrid nanofluids," *Renew. Sustain. Energy Rev.*, vol. 80, no. January 2016, pp. 1112–1122, 2017.

[140] Y. Ji, Z. Ji, M. Yao, Y. Qian, and Y. Peng, "Negative Absorption Peaks in Ultraviolet–Visible Spectrum of Water," *ChemistrySelect*, vol. 1, no. 13, pp. 3443–3448, 2016.

[141] Z. H. Han, B. Yang, S. H. Kim, and M. R. Zachariah, "Application of hybrid sphere / carbon nanotube particles in nanofluids," *IOP Publ. Nanotechnol.*, vol. 105701, no. 18, 2007.

[142] K. A. Jehhef, M. Abed, and A. Abas, "EFFECT OF SURFACTANT ADDITION ON THE NANOFLUIDS PROPERTIES : A REVIEW," vol. 2, no. 2, pp. 1–19, 2019.

[143] G. Wang, B. Wang, J. Park, Y. Wang, B. Sun, and J. Yao, "Highly efficient and large-scale synthesis of graphene by electrolytic exfoliation," *Carbon N. Y.*, vol. 47, no. 14, pp. 3242–3246, 2009.

[144] F. Soltani, D. Toghraie, and A. Karimipour, "Experimental measurements of thermal conductivity of engine oil-based hybrid and mono nanofluids with tungsten oxide (WO3) and MWCNTs inclusions," *Powder Technol.*, vol. 371, pp. 37–44, 2020.

[145] A. Arshad, M. Jabbal, Y. Yan, and D. Reay, "A review on graphene based nanofluids: Preparation, characterization and applications," *J. Mol. Liq.*, vol. 279, pp. 444–484, 2019.

[146] A. M. Ajeena, P. Víg, and I. Farkas, "A comprehensive analysis of nanofluids and their practical applications for flat plate solar collectors: Fundamentals, thermophysical properties, stability, and difficulties," *Energy Reports*, vol. 8, pp. 4461–4490, 2022.

[147] C. Jin, Q. Wu, G. Yang, H. Zhang, and Y. Zhong, "Investigation on hybrid nanofluids based on carbon nanotubes filled with metal nanoparticles: Stability, thermal conductivity, and viscosity," *Powder Technol.*, vol. 389, pp. 1–10, 2021.

[148] Simon Furbo;Louise Jivan Shah; Ulrike Jordan, *Solar Energy State of the art*, vol. 14, no. 10. 2003.

[149] L. Chen, H. Xie, Y. Li, and W. Yu, "Nanofluids containing carbon nanotubes treated by mechanochemical reaction," *Thermochim. Acta*, vol. 477, no. 1–2, pp. 21–24, 2008.

[150] S. K. Verma, A. K. Tiwari, and D. S. Chauhan, "Experimental evaluation of flat plate solar collector using nanofluids," *Energy Convers. Manag.*, vol. 134, pp. 103–115, 2017.

[151] R. Strandberg and D. K. Das, “Influence of temperature and properties variation on nanofluids in building heating,” *Energy Convers. Manag.*, vol. 51, no. 7, pp. 1381–1390, 2010.

[152] A. Ghozatloo, A. Rashidi, and M. Shariaty-niassar, “Convective heat transfer enhancement of graphene nanofluids in shell and tube heat exchanger,” *Exp. Therm. FLUID Sci.*, 2013.

[153] I. M. Shahrul, I. M. Mahbubul, S. S. Khaleduzzaman, R. Saidur, and M. F. M. Sabri, “A comparative review on the specific heat of nanofluids for energy perspective,” *Renew. Sustain. Energy Rev.*, vol. 38, pp. 88–98, 2014.

[154] J. Liu, F. Wang, L. Zhang, X. Fang, and Z. Zhang, “Thermodynamic properties and thermal stability of ionic liquid-based nanofluids containing graphene as advanced heat transfer fluids for medium-to-high-temperature applications,” *Renew. Energy*, vol. 63, pp. 519–523, 2014.

[155] H. Yarmand *et al.*, “Study of synthesis, stability and thermo-physical properties of graphene nanoplatelet/platinum hybrid nanofluid,” *Int. Commun. Heat Mass Transf.*, vol. 77, pp. 15–21, 2016.

[156] C. J. Ho, J. B. Huang, P. S. Tsai, and Y. M. Yang, “Preparation and properties of hybrid water-based suspension of Al2O3 nanoparticles and MEPCM particles as functional forced convection fluid,” *Int. Commun. Heat Mass Transf.*, vol. 37, no. 5, pp. 490–494, 2010.

[157] N. Basbous, M. Taqi, and M. A. Janan, “Thermal performances analysis of a parabolic trough solar collector using different nanofluids,” *Proc. 2016 Int. Renew. Sustain. Energy Conf. IRSEC 2016*, pp. 322–326, 2017.

[158] Y. I. C. Bock Choon Pak, “Hydrodynamic and Heat Transfer Study of Dispersed Fluids With Submicron Metallic Oxide,” *Exp. Heat Transf. A J. , Therm. Energy Transp. , Storage , Convers.*, no. January 2013, pp. 37–41, 2013.

[159] S. O. Alharbi, M. Nawaz, and U. Nazir, “Thermal analysis for hybrid nanofluid past a cylinder exposed to magnetic field,” *AIP Adv.*, vol. 115022, no. November 2019, 2019.

[160] A. Mariano, M. J. Pastoriza-Gallego, L. Lugo, L. Mussari, and M. M. Piñeiro, “Co3O4 ethylene glycol-based nanofluids: Thermal conductivity, viscosity and high pressure density,” *Int. J. Heat Mass Transf.*, vol. 85, pp. 54–60, 2015.

[161] H. Yarmand *et al.*, “Graphene nanoplatelets – silver hybrid nanofluids for enhanced heat transfer,” *ENERGY Convers. Manag.*, vol. 100, pp. 419–428, 2015.

[162] B. Wei, C. Zou, X. Yuan, and X. Li, “Thermo-physical property evaluation of diathermic oil based hybrid nanofluids for heat transfer applications,” *Int. J. Heat Mass Transf.*, vol. 107, pp. 281–287, 2017.

[163] R. Gulzar, Ovais;Qayoum, Andan; Gupta, “Experimental study on thermal conductivity of mono and hybrid Al 2 O 3 – TiO 2 nanofluids for concentrating solar collectors,” *Int. J. Energy Res.*, no. October, pp. 1–15, 2020.

[164] D. Singh *et al.*, “Use of metallic nanoparticles to improve the thermophysical properties of organic heat transfer fluids used in concentrated solar power,” *Sol.*

ENERGY, vol. 105, pp. 468–478, 2014.

[165] N. J. Bridges, A. E. Visser, and E. B. Fox, "Potential of Nanoparticle-Enhanced Ionic Liquids (NEILs) as Advanced Heat-Transfer Fluids," pp. 4862–4864, 2011.

[166] Y. Wu, S. Liu, Y. Xiong, C. Ma, and Y. Ding, "Experimental study on the heat transfer characteristics of a low melting point salt in a parabolic trough solar collector system," *Appl. Therm. Eng.*, vol. 89, pp. 748–754, 2015.

[167] S. E. Ghasemi and A. A. Ranjbar, "Thermal performance analysis of solar parabolic trough collector using nanofluid as working fluid: A CFD modelling study," *J. Mol. Liq.*, vol. 222, pp. 159–166, 2016.

[168] T. Sokhansefat, A. B. Kasaeian, and F. Kowsary, "Heat transfer enhancement in parabolic trough collector tube using Al 2O3/synthetic oil nanofluid," *Renew. Sustain. Energy Rev.*, vol. 33, pp. 636–644, 2014.

[169] M. Akbari and A. Behzadmehr, "Developing mixed convection of a nanofluid in a horizontal tube with uniform heat flux," *Int. J. Numer. Methods Heat Mass Flow*, vol. 17, no. 6, pp. 566–586, 2007.

[170] E. Bellos, C. Tzivanidis, K. A. Antonopoulos, and G. Gkinis, "Thermal enhancement of solar parabolic trough collectors by using nano fl uids and converging-diverging absorber tube," *Renew. Energy*, vol. 94, pp. 213–222, 2016.

[171] Q. Ye, Y. Kim, and E. Steudle, "A re-examination of the minor role of unstirred layers during the measurement of transport coefficients of Chara corallina internodes with the cell pressure probe," *Plant, Cell Environ.*, vol. 29, no. 5, pp. 964–980, 2006.

[172] C. L. Jiyuan Tu, Guan-Heng Yeoh, "Practical Guidelines for CFD Simulation and Analysis," in *Computational Fluid Dynamics, Second Edition*, 2013, pp. 219–273.

[173] A. Bejan and A. D. Kraus, *Heat transfer handbook Vol.1*. John Wiley & Sons, 2003.

[174] Y. Cengel and M. Boles, "Heat Transfer A pratical Approach," *McGraw - Hill*, p. 932, 2002.

[175] Lavine; and I. D. Bergman;, *Fundamentals of heat and mass transfer*, Sixth edit., vol. 112. John Wiley & Sons, 2007.

[176] Y. Ding, H. Alias, D. Wen, and R. A. Williams, "Heat transfer of aqueous suspensions of carbon nanotubes (CNT nanofluids)," *Int. J. Heat Mass Transf.*, vol. 49, pp. 240–250, 2006.

[177] A. Ümit, M. Karagöz, S. Sar, and A. Öztürk, "Impact of various metal-oxide based nanoparticles and biodiesel blends on the combustion , performance , emission , vibration and noise characteristics of a CI engine," vol. 270, no. January, 2020.

[178] "Spencer, J.W," in *1971. Fourier series representation of position of the sun, Search 2(5), 172.*

[179] H. L. Zhang, J. Baeyens, J. Degrève, and G. Cacères, “Concentrated solar power plants: Review and design methodology,” *Renew. Sustain. Energy Rev.*, vol. 22, pp. 466–481, 2013.

[180] D. T. Reindl, W. A. Beckman, and J. A. Duffle, “Diffuse fraction correlations,” no. I, 1990.

[181] S. Khanna, S. B. Kedare, and S. Singh, “Analytical expression for circumferential and axial distribution of absorbed flux on a bent absorber tube of solar parabolic trough concentrator,” *Sol. Energy*, vol. 92, pp. 26–40, 2013.

[182] G. Wang, Z. Zhang, T. Jiang, J. Lin, and Z. Chen, “Thermodynamic and optical analyses of a novel solar CPVT system based on parabolic trough concentrator and nanofluid spectral filter,” *Case Stud. Therm. Eng.*, vol. 33, no. March, p. 101948, 2022.

[183] B. S. Jinshah, K. R. Balasubramanian, K. Ravikumar, and S. Divakar, “A dual-mode novel Parabolic Trough Collector for process heating applications in small scale industries—Thermo-hydraulic and performance investigation,” *Appl. Therm. Eng.*, vol. 218, no. January 2022, p. 119287, 2023.

[184] R. Petela, “Exergy of undiluted thermal radiation,” *Sol. Energy*, vol. 74, no. 6, pp. 469–488, 2003.

[185] E. Bellos and C. Tzivanidis, “A detailed exergetic analysis of parabolic trough collectors,” *Energy Convers. Manag.*, vol. 149, pp. 275–292, 2017.

[186] S. Kalogirou, “Design, construction, performance evaluation and economic analysis of an integrated collector storage system,” *Renew. Energy*, vol. 12, no. 2, pp. 179–192, 1997.

[187] S. A. Kalogirou, S. Karellas, K. Braimakis, C. Stanciu, and V. Badescu, “Exergy analysis of solar thermal collectors and processes,” *Prog. Energy Combust. Sci.*, vol. 56, pp. 106–137, 2016.

[188] A. Allouhi, M. Benzakour Amine, R. Saidur, T. Kousksou, and A. Jamil, “Energy and exergy analyses of a parabolic trough collector operated with nanofluids for medium and high temperature applications,” *Energy Convers. Manag.*, vol. 155, no. August 2017, pp. 201–217, 2018.

[189] O. Behar, A. Khellaf, and K. Mohammedi, “A novel parabolic trough solar collector model – Validation with experimental data and comparison to Engineering Equation Solver (EES),” *ENERGY Convers. Manag.*, vol. 106, pp. 268–281, 2015.

[190] B. S. Jinshah and K. R. Balasubramanian, “Thermo-mathematical model for parabolic trough collector using a complete radiation heat transfer model – A new approach,” *Sol. Energy*, vol. 197, no. December 2019, pp. 58–72, 2020.

[191] F. . Murray, “On the computation of saturation vapor pressure., Tech. rep., Rand Corp Santa Monica Calif.,” 1966.

[192] O. Al-oran and F. Lezsovits, “A Hybrid Nanofluid of Alumina and Tungsten Oxide for Performance Enhancement of a Parabolic Trough Collector under the Weather Conditions of Budapest,” *Appl. Phys. Lett.*, vol. 11, no. 4946, pp. 1–21, 2021.

[193] E. Bellos and C. Tzivanidis, “Thermal analysis of parabolic trough collector operating with mono and hybrid nanofluids,” *Sustain. Energy Technol. Assessments*, vol. 26, no. September, pp. 105–115, 2018.

[194] O. Al Oran, F. Lezsovits, and A. Aljawabrah, “Exergy and energy amelioration for parabolic trough collector using mono and hybrid nanofluids,” *J. Therm. Anal. Calorim.*, no. 20 January, 2020.

[195] Y. Bhusal, A. Hassanzadeh, L. Jiang, and R. Winston, “Technical and economic analysis of a novel low-cost concentrated medium-temperature solar collector,” *Renew. Energy*, vol. 146, pp. 968–985, 2020.

[196] O. M. Akinbami, S. R. Oke, and M. O. Bodunrin, “The state of renewable energy development in South Africa: An overview,” *Alexandria Eng. J.*, vol. 60, no. 6, pp. 5077–5093, 2021.